RÉPUBLIQUE FRANÇAISE
*Liberté Égalité Fraternité*

Université de Toulouse

# Doctorat de l'Université de Toulouse

**préparé à l'ISAE-SUPAERO**

---

## Aeroacoustics of thermally choked-flow nozzles in dual-mode ramjets

---

Thèse présentée et soutenue, le 29 janvier 2026 par

**Frédéric OLIVON**

**École doctorale**
MEGEP - Mécanique, Energétique, Génie civil, Procédés

**Spécialité**
Dynamique des fluides

**Unité de recherche**
ISAE-ONERA EDyF Energétique et Dynamique des Fluides

**Thèse dirigée par**
Estelle PIOT et Aurélien GENOT

**Composition du jury**
M. Thierry SCHULLER, Président, Université de Toulouse
Mme Hélène BAILLIET, Rapporteure, Université de Poitiers
M. Alexis GIAUQUE, Rapporteur, Ecole Centrale de Lyon
M. Ronan VICQUELIN, Examinateur, CentraleSupélec
Mme Estelle PIOT, Directrice de thèse, ONERA Toulouse
M. Aurélien GENOT, Co-directeur de thèse, ONERA Toulouse

**Membres invités**
M. Jean-Étienne DURAND, Co-encadrant, ONERA Palaiseau

*À mes parents, à qui je dois tant,*
*et d'abord la curiosité.*

# Acknowledgments

*Mes amis, ce n'est pas à vous de vous incliner.*
**Aragorn [1]**

On pense souvent, à tort, qu'une thèse est un travail solitaire : une longue traversée face à son écran et à ses équations, ponctuée de doutes et de cafés. Pourtant, elle se fait rarement seul. Elle se construit dans les discussions, les conseils glissés au bon moment, les coups de main discrets et ces échanges qui débloquent tout, parfois autour d'un verre (*ndlr* : alcoolisé ou non) : il faut bien le reconnaître, cela favorise les idées. Je tiens donc à remercier ici toutes celles et ceux sans qui ce travail n'aurait jamais pu aboutir.

Je tiens tout d'abord à remercier l'Office National d'Études et de Recherches Aérospatiales (ONERA) pour avoir entièrement financé cette thèse (c'est assez rare pour être souligné), ainsi que le Département Multiphysique pour l'Énergétique (DMPE), qui m'a accueilli du début de mon stage de fin d'études à la fin de mon doctorat (ça en fait, des repas à la cantine). Je remercie également les personnes de l'unité Propulsion Aérobie (PRA), devenue l'unité Modélisation Propulsion Aérobie (MPA) — sans oublier les unités MPF, CMEI et STAT — qui ont toujours su s'intéresser à mon sujet de recherche, poser des questions et se montrer prêtes à aider quand il le fallait. Je remercie tout particulièrement Florent Raynaud, Stéphane Boulal, Jean-Christophe Hoarau (à appeler dès qu'on a un problème avec son ordinateur) et l'inégalable Julien Labaune (responsable officiel du très officieux bureau des plaintes des doctorants : "*Et ça, c'est très important pour la santé du cigare*" [2]) pour les différentes bières partagées lors des soutenances de thèse (la science avance aussi comme ça, ~~parfois~~ souvent). Enfin, je tiens à remercier Tassadite Meksem, qui, telle une héroïne sans cape, m'a si souvent guidé à travers les méandres administratifs de l'ONERA, notamment au milieu de ces magnifiques outils que sont GEDEON2 et GOELAND, et autres interfaces tout aussi incompréhensibles.

Je remercie ensuite les différents membres du jury pour avoir accepté d'évaluer ce travail : Mme Bailliet et MM. Giauque, Schuller et Vicquelin. Merci pour le temps (précieux !) que vous avez consacré à la lecture de ce manuscrit, ainsi que pour vos questions et vos retours, notamment lors de la soutenance, aussi exigeants qu'éclairants, qui ont contribué à l'enrichir. Votre expertise et votre pédagogie forcent le respect, et je tiens à vous remercier pour votre bienveillance lors de nos échanges. J'espère que vous aurez pris autant de plaisir à lire cette thèse que j'en ai eu à l'écrire.

L'encadrement de thèse est le socle sur lequel repose tout le doctorat : une petite équipe dont l'expérience, l'exigence et le soutien permettent d'avancer, même lorsque les résultats se font attendre. Je souhaite donc remercier ses membres, qui m'ont fait confiance et m'ont accompagné depuis ma sortie d'école — où je n'étais encore qu'un étudiant — jusqu'à ma soutenance, où je suis devenu un jeune chercheur : Jean-Étienne Durand, pour ses conseils et son expertise tout

au long de ces trois ans et demi ; Aurélien Genot, devenu mon co-directeur de thèse au cours de cette aventure, pour ta disponibilité sans faille et tes conseils tout au long de ce doctorat, ainsi que pour ton exigence (pour toujours viser plus haut !), tes encouragements et nos discussions (parfois techniques, parfois philosophiques), qui ont été essentiels pour mener ce travail à son terme ; et enfin Estelle Piot, ma directrice de thèse, dont la patience et le calme ont été plus qu'importants pour ne jamais perdre de vue les objectifs que je me fixais, et dont l'expérience et la réactivité (d'aucuns seraient jaloux d'avoir une direction de thèse aussi impliquée) m'ont permis de dénouer nombre de problèmes ! Je ne vous remercierai jamais assez.

En dehors du département, voire même de l'Office, j'ai aussi eu la chance de collaborer et d'échanger avec d'autres chercheurs, qui ont permis d'avancer et de compléter ce travail de thèse. Je remercie Maxime Huet, qui a toujours fait preuve d'intérêt pour mes travaux, qui a très vite saisi les différentes problématiques liées à mon sujet, et qui a su formuler des remarques pertinentes pour répondre aux questions que je me posais. Je me dois également de remercier MM. Hirschberg (père et fils !), dont l'aide a été précieuse : Avraham Hirschberg, pour ses questions, sa pédagogie, son sens physique remarquable et sa bonne humeur, lui qui a su désacraliser le doctorat (je cite : "*il suffit de savoir vendre la camelote et le tour est joué*"). C'est grâce à lui que j'ai pu prendre le recul nécessaire sur ce que j'étais en train de faire (souvent, je n'en avais aucune idée), et avancer. Je remercie enfin Lionel Hirschberg, pour sa rigueur et son enthousiasme face à un sujet aussi novateur que complexe. Ce fut toujours un plaisir d'échanger avec vous. Merci pour tout.

J'en profite pour souhaiter bon courage et bonne route aux anciens et actuels doctorants : Florian G., Thomas D., Margot P., Younès ; mais aussi Ronan, Maxime, Ewen, Sacha, Gabin, Terence (mon co-bureau drippé), Andrea, Baptiste, Emrys, Antoine S., Mathieu et Tanguy M., ainsi qu'aux nouveaux que je n'ai pas eu le temps de connaître. J'ai hâte de voir ce que vous allez faire ! Je remercie aussi mon stagios Antoine Ch., dont l'enthousiasme (et l'inconscience ?) de m'avoir accepté comme tuteur de stage de fin d'études nous a permis de passer de bons moments devant CEDRE (non), devant un tableau, ou même au bar (oui).

Je tiens maintenant à remercier mes amis, si nombreux, qui ont toujours été là et qui comptent tant pour moi : c'est grâce à vous que j'ai réussi à penser à autre chose quand les tempêtes du doctorat faisaient rage.

Merci à mes amis d'enfance, Lilian et Florian L., ainsi qu'à ceux rencontrés plus tard au lycée : Margot C., Margot L. (non, ce n'est pas une erreur), Marilou, Tanguy C. et Rémi, pour m'avoir montré que la vie, ce n'est pas seulement quelques équations, et qu'elle est bien plus vaste que cela. À l'autre bout du monde ou au coin de la rue, je sais que nous serons amis pour la vie, et j'ai hâte de voir la suite.

Merci à mes amis de prépa : Alexis B. (*le bon*), Hélène (*la brute*) et Thomas Ca. (*le truand*). Je n'ai toujours aucune idée de ce qu'on peut vraiment dire d'un polynôme du second degré à discriminant strictement positif (ou négatif ?), mais je sais maintenant ce que c'est d'avoir des amis fidèles comme vous. Je m'excuse aussi de ne pas avoir consigné dans ce manuscrit l'ensemble des choses qui nous énervent : j'en parlerai dans un autre livre. Je suis impatient de continuer à découvrir le reste du monde à vos côtés.

Je continue en remerciant mes amis rencontrés en l'école et qui forment un groupe trop nombreux pour être tous cités (bon, allez, je le fais, sinon je vais avoir des problèmes : Jean-Baptiste, Rémy, Benjamin, Manon, Alexis M., Clément, Romain, Éloi, Krystale, Gauthier, Marion, Lucas, Marius, Quentin, Thomas Ce. et Vincent, ainsi que Léana et Zoé !), mais qui sont toujours partants pour un goûter, une course ou une soirée (on ne sait jamais ce qui nous attend avec eux). Vous savez à quel point ces moments ont compté pour moi. J'espère que cela continuera encore très longtemps : la suite commence maintenant.

Je place ici une petite dédicace à mes amis découverts dans les contrées éloignées et pluvieuses

de Liège : Alice, Nicolas et Lucy. Ce groupe est bien la preuve que, même si nous ne comprenons pas vraiment ce que font les autres, nous sommes toujours heureux de nous retrouver pour papoter de tout et de rien : que ce soit dans le Carré, autour d'une bière, ou de toute autre boisson anisée !

Enfin, merci à l'équipe sans qui mes journées à l'Office auraient eu un goût bien plus fade. Je remercie celles et ceux qui forment aujourd'hui le susnommé Syndicat des Anciens Doctorants de l'ONERA (dont l'acronyme est, je le précise, purement le fruit d'un hasard houblonné) : Jean-Michel (le scientifique fou), Pierre (le prodige), Magdeleine (plus qu'une caution féminine, la maman du groupe — et c'est purement factuel) et Erwin (le grand-frère), les membres les plus expérimentés — chacun dans un domaine très particulier. Merci d'avoir intégré les *bébous* aussi bien à la vie du labo (le feu couloir du bâtiment A, en somme). Votre expérience et votre flegme m'ont permis de relativiser tous les aléas que la thèse pouvait réserver. Je remercie évidemment aussi mes collègues de promo (ou de galère, au choix), Ancelin, Antoine Cl. (mention spéciale à sa grand-mère qui, par le legs d'une paire de chaussons, m'a permis de toujours me sentir comme chez moi au bureau) et Rémy (encore lui), venus compléter cette équipe de choc : c'est grâce à vous que j'ai pu faire tout ça. Finalement, nous n'aurons jamais eu le classement officiel de nos thèses (même si l'ordre des mentions précédentes peut donner un aperçu — et qu'il semble inversement proportionnel au nombre de publications : "$\rightarrow$" mauvaise nouvelle, comme dirait l'autre), mais je suis persuadé que nous avons été les meilleurs. Je suis impatient de compléter notre tour des "mid-cities", des villes plus moyennes les unes que les autres (aucune ne sera nommée ici pour éviter tout désaccord sur la définition), mais qui forgent des amitiés pour la vie.

Pour finir, je remercie évidemment ma famille, qui m'a toujours demandé si je cherchais bien, et qui a compris, une fois le manuscrit finalisé, que faire ce doctorat était vraiment un travail. Merci à mes parents de m'avoir toujours soutenu dans tous mes projets, qu'ils soient étudiants, sportifs ou personnels, et de m'avoir encouragé à m'accomplir à travers ce doctorat. Merci aussi à mon frère d'avoir toujours su trouver les mots pour m'aider à relativiser et de m'avoir, lui aussi, poussé à me donner à 100% dans ce projet (un peu de concurrence entre frères ne fait jamais de mal, sauf dans les jeux vidéo). Je remercie aussi mes grands-parents, où qu'ils soient, pour leur soutien, avant comme maintenant. Je vous aime fort.

Flavie, merci pour tout. Merci pour ta lumière et ton rire qui comblent tous les vides. Je sais que tu n'as jamais vraiment compris ce que je faisais sur mon ordinateur à fond noir, mais, par ta patience et ta gentillesse, tu as su m'aider quand j'en avais le plus besoin. Cette thèse, c'est aussi grâce à toi.

# List of Publications and Communications

*Si votre but c'était de séduire les dames, fallait faire chevalier. C'est tout !*

**Lancelot du Lac [2]**

Publications with peer review:

- **Published**: F. Olivon, A. Genot, L. Hirschberg, S. Moreau, and A. Hirschberg. "On the critical-throat boundary condition in quasi-one-dimensional linearized-Euler equation models". In: *Journal of Fluid Mechanics* 1019 (2025), A4. ISSN: 0022-1120. DOI: 10.1017/jfm.2025.10568.
- **Published**: F. Olivon, A. Genot, J.-E. Durand, A. Hirschberg, and E. Piot. "On the linear aeroacoustic response of a thermally-choked-flow nozzle to acoustic and entropy plane waves". In: *Journal of Sound and Vibration* 626 (2026), 119619. ISSN: 0022-460X. DOI: 10.1016/j.jsv.2025.119619.
- **Published**: F. Olivon, A. Genot, J.-E. Durand, A. Hirschberg, and E. Piot. "A quasi-one-dimensional critical-throat acoustic boundary condition for thermally choked dual-mode ramjet nozzles". In: *Acta Acustica* 9 (2025), 80. ISSN: 2681-4617. DOI: 10.1051/aacus/2025064.
- **Submitted**: F. Olivon, A. Genot, J.-E. Durand, and E. Piot. "Thermoacoustic instabilities linear study of a canonical thermally choked-flow nozzle". In: *Journal of Propulsion and Power* (2026). HAL: hal-05526862
- **Submitted**: F. Olivon, A. Genot, A. Chédin, J.-E. Durand, L. Hirschberg, and E. Piot. "Two-dimensional indirect entropy noise in a thermally choked-flow nozzle". In: *Journal of Sound and Vibration* (2026). HAL: hal-05577111

International communications with proceedings:

- F. Olivon, J.-E. Durand, A. Genot, and E. Piot. "Unsteady Forced Motion of the Thermal Throat in a Low-Mach Dual-Mode Ramjet Nozzle". In: *Proceedings of the 10th European Conference for Aerospace Sciences (EUCASS 2023)*, Lausanne, Switzerland, July 2023. DOI: 10.13009/EUCASS2023-558.
- J.-E. Durand and F. Olivon. "Thermally choked nozzle flow 1D model for low-Mach dual mode scramjet performance assessment". In: *Proceedings of the 3rd International Conference on High-Speed Vehicle Science & Technology (HiSST 2024)*, Busan, Korea, April 2024. HAL: hal-04948424.

- F. Olivon, J.-E. Durand, A. Genot, and E. Piot. "High-Frequency Acoustic Propagation in a Thermally Choked Low-Mach Dual-Mode Ramjet". In: *Proceedings of the 30th AIAA/CEAS Aeroacoustics Conference*, Rome, Italy, June 2024. DOI: 10.2514/6.2024-3114.
- F. Olivon, A. Chédin, J.-E. Durand, A. Genot, and E. Piot. "Sound generation by entropy inhomogeneity within a thermally choked-flow nozzle". In: *Proceedings of the 4th International Conference on High-Speed Vehicle Science & Technology (HiSST 2025)*, Tours, France, September 2025. HAL: hal-05448459.
- K. Elbakly, S. Hulshoff, F. Olivon, A. Genot, F. Bake, C. Venner, and L. Hirschberg. "Entropy-patch choked-nozzle interaction: quasi-steady and inertial modeling regimes mapped and limits of linearization established". In: *Proceedings of the 32nd AIAA/CEAS Aeroacoustics Conference*, Bruxelles, Belgium, May 2026.
- F. Olivon, A. Genot, J.-E. Durand, and E. Piot. "Linear analysis of thermo-acoustic instabilities in a quasi-one-dimensional thermally-choked dual-mode ramjet". In: *Proceedings of the 32nd AIAA/CEAS Aeroacoustics Conference*, Bruxelles, Belgium, May 2026.

# Table of Contents

**List of Publications and Communications** **ix**

**General introduction** **1**
Motivations . . . 1
State of the art and objectives . . . 3
Outline . . . 4

**1 Generalities and challenges of airbreathing engines** **7**
1.1 Airbreathing engine propulsion principle . . . 8
1.1.1 Thrust generation principle . . . 9
1.1.2 Ramjet technology . . . 9
1.1.3 Thermal choking solution . . . 11
1.2 Combustion instabilities in airbreathing engines . . . 12
1.2.1 Direct and indirect combustion noise . . . 12
1.2.2 Thermoacoustic coupling . . . 16
1.2.3 Aeroacoustic response of a thermally choked-flow nozzle . . . 17

**2 Methodology and tools** **19**
2.1 Approach . . . 20
2.1.1 General assumptions . . . 20
2.2 Governing flow-motion equations . . . 22
2.2.1 Euler equations with heat source . . . 22
2.2.2 Equation of state . . . 23
2.2.3 Gibbs relation . . . 23
2.2.4 Speed of sound . . . 23
2.2.5 Thermodynamic gas properties . . . 23
2.3 Dual-mode ramjet geometry . . . 24
2.3.1 Thermal-throat nozzle . . . 25
2.3.2 Inlet flow conditions . . . 25
2.4 Numerical simulation tools . . . 26
2.4.1 CFD code: CEDRE . . . 26
2.4.2 Boundary conditions of the system . . . 27
2.5 Steady volumetric power distribution model . . . 28
2.5.1 Instantaneous heat-release model . . . 29
2.5.2 Determination of the volumetric power profile . . . 30
2.5.3 Validation of the heat-release rate source term model . . . 32

2.6 Equivalent geometric throat nozzle . . . 32

**3 Linear aeroacoustic response of a thermally choked-flow nozzle to acoustic and entropy plane waves 37**
3.1 Objective . . . 38
3.2 Methodology . . . 39
3.2.1 Presentation of choking configuration cases . . . 39
3.2.2 Steady-state volumetric power distribution . . . 39
3.2.3 Linear acoustics forcing at the inlet . . . 41
3.2.4 Computational setup . . . 42
3.3 Aeroacoustic coefficients . . . 43
3.3.1 Quasi-steady limit model for reflection coefficients . . . 45
3.4 Aeroacoustic response of a thermally-choked-flow nozzle . . . 47
3.4.1 Steady-state flow fields . . . 47
3.4.2 Acoustic-reflection coefficient . . . 49
3.4.3 Acoustic-transmission coefficients . . . 50
3.4.4 Effect of the heat-release length on the acoustic-reflection coefficient . . . 53
3.4.5 Entropy-noise coefficients . . . 54
3.5 Critical-throat acoustic boundary condition . . . 57

**4 Development of a quasi-one-dimensional linear acoustic model for thermally choked nozzles with non-uniform flow 61**
4.1 Objective and state of the art . . . 62
4.2 Quasi-one-dimensional Euler equations . . . 64
4.2.1 Quasi-one-dimensional approximation . . . 64
4.2.2 Continuity equation . . . 65
4.2.3 Momentum equation . . . 65
4.2.4 Total energy equation . . . 66
4.2.5 Quasi-one-dimensional Euler system . . . 67
4.3 Linear acoustic model . . . 67
4.3.1 Linearised Euler equations . . . 67
4.3.2 Fourier transform . . . 68
4.3.3 Matrix formulation . . . 69
4.4 Boundary conditions . . . 70
4.4.1 Inlet boundary conditions . . . 71
4.4.2 Critical-throat boundary condition . . . 71
4.5 Resolution algorithm . . . 73
4.6 Validation of the linear acoustic model . . . 75
4.6.1 Validation methodology . . . 75
4.6.2 Critical-throat boundary condition . . . 75
4.6.3 Aeroacoustic-reflection coefficients . . . 77
4.6.4 Aeroacoustic-transmission coefficients . . . 78
4.6.5 Impact of the critical-throat boundary condition on the aeroacoustic response 80
4.7 Impact of the inlet Mach number on the aeroacoustic response . . . 83
4.8 Limit of the linear acoustic regime . . . 87

**5 Influence of a thermoacoustic coupling on the aeroacoustic response of a thermally choked nozzle 91**
5.1 Objective and literature review . . . 92
5.2 Model of the flame–acoustic response for a premixed ducted flame . . . 97

5.2.1 Reformulation of the quasi-one-dimensional linear acoustic model . . . . . 98
5.2.2 Critical-throat boundary condition with FTF . . . . . 99
5.3 Effects of a thermoacoustic model on the aeroacoustic response . . . . . 99
5.3.1 Effect of the flame speed . . . . . 100
5.3.2 Effect of the flame-holder height . . . . . 103
5.3.3 Role of the non-dimensional flame frequency . . . . . 104
5.4 Thermoacoustic stability study of a canonical thermally choked-flow nozzle . . . . 107
5.4.1 Amplification ratio of the aeroacoustic response . . . . . 107
5.4.2 Rayleigh index and potential instabilities . . . . . 108

**6 Sound generation by two-dimensional entropy inhomogeneity in a thermally choked-flow nozzle 113**
6.1 Objective . . . . . 114
6.2 Methodology . . . . . 115
6.2.1 Entropy inhomogeneities injection . . . . . 115
6.2.2 Computational setup . . . . . 116
6.3 One-dimensional entropy-noise response models . . . . . 118
6.3.1 Quasi-steady asymptotic limit model . . . . . 118
6.3.2 Point-mass inertial asymptotic limit model . . . . . 119
6.4 Two-dimensional analysis of the acoustic response induced by entropy non-uniformities 119
6.4.1 Phenomenological description of the acoustic response induced by a circular entropy perturbation . . . . . 120
6.4.2 Comparison of the linear acoustic response to two- and one-dimensional entropy forcing . . . . . 121
6.5 One-dimensional entropy-noise generation mechanism . . . . . 122
6.5.1 Asymptotic scaling of the acoustic response with entropy-shape size . . . 122
6.5.2 Two-dimensional base-flow effects and transverse injection . . . . . 125
6.5.3 Effect of the steady thermal-throat position . . . . . 126
6.5.4 Influence of the inlet Mach number . . . . . 127

**Conclusions and Perspectives 131**
Conclusions . . . . . 131
Perspectives . . . . . 133

**Appendices 135**

**A Acoustic-wave decomposition in a constant-cross-section isentropic-flow nozzle 137**
A.1 Formulation of the acoustic pressure wave equation . . . . . 138
A.1.1 Flow governing equations and assumptions . . . . . 138
A.1.2 Acoustic pressure wave equation . . . . . 138
A.2 Solution of the acoustic wave . . . . . 139
A.2.1 Non-dimensional formulation . . . . . 140

**B A quasi-steady-flow model for reflection coefficients in thermally choked-flow configurations 141**
B.1 Quasi-steady reflection coefficients model . . . . . 142
B.1.1 Objective and motivations . . . . . 142
B.1.2 Flow governing equations and assumptions . . . . . 142
B.1.3 Quasi-steady formulation . . . . . 142
B.1.4 Linearised acoustic relation . . . . . 143

B.1.5 Reflection coefficients . . . 144
B.2 Validation and limits of the present model . . . 144
B.2.1 Results and validation . . . 144
B.2.2 Limits of the model . . . 146

**C A quasi-one-dimensional critical-throat acoustic boundary condition for isentropic nozzles 147**
C.1 Objective . . . 148
C.2 Critical-throat boundary condition for isentropic nozzle . . . 149
C.2.1 Limit of the proposed boundary condition . . . 150
C.3 Validation methodology . . . 150
C.3.1 Presentation of the isentropic nozzle geometries . . . 150
C.3.2 Numerical set-up . . . 153
C.4 Discussion and results . . . 154
C.4.1 Validation and limits of the quasi-one-dimensional model . . . 154
C.4.2 Influence of the boundary condition on the acoustic-pressure distribution . . . 155
C.4.3 Acoustic reflection and transmission coefficients . . . 156
C.4.4 Comparison with experimental measurements . . . 159

**D Validation of the entropy-spot injection methodology 161**
D.1 Objective and validation methodology . . . 162
D.1.1 Isentropic nozzle geometry . . . 162
D.1.2 Numerical set-up . . . 163
D.1.3 Steady-flow fields . . . 164
D.2 Asymptotic acoustic-response models . . . 165
D.2.1 Quasi-steady-state acoustic response . . . 165
D.2.2 Inertial acoustic response . . . 166
D.3 Entropy noise acoustic response . . . 168

**Résumé 171**

**List of Figures 181**

**List of Tables 189**

**Nomenclature 191**

**References 195**

# General introduction

*Je sais pas si ça va être distrayant mais ça va être court, ça c'est sûr.*

**Lancelot du Lac [2]**

## Motivations

A central challenge in the study of combustion instabilities, particularly in ramjet-based propulsion systems, lies in the accurate modelling of acoustic sources and boundary conditions. These aspects are essential for predicting thermoacoustic behaviour and for developing stable and efficient engine designs.

Figure 1 illustrates the ASMP (*Air–Sol–Moyenne–Portée*) and its improved variant, ASMP-A, which are two supersonic air-to-ground missiles developed by MBDA in collaboration with ONERA. Both systems employ a ramjet engine to sustain supersonic flight. To extend the operational flight range beyond Mach 6, scramjet engines are required, in which the flow remains supersonic throughout the combustion chamber. Hybrid propulsion concepts combining ramjet and scramjet engines have therefore attracted significant interest, with thermally choked flow nozzles representing a promising solution for enabling such combustion mode transitions without geometric constraints.

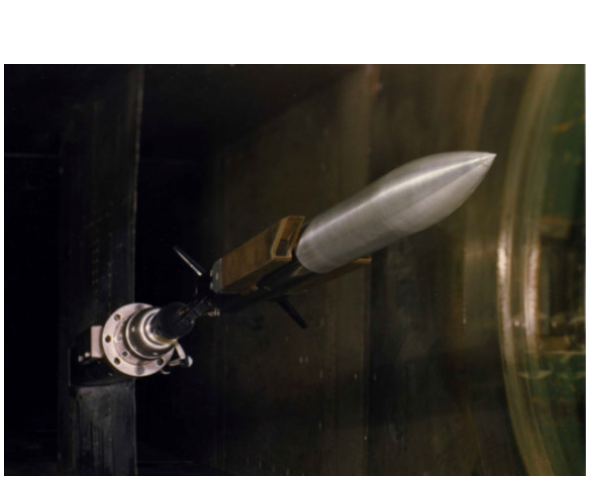

**(a)** Model of the ASMP in the ONERA S3MA wind tunnel.



**(b)** Exhibition of the ASMP-A [3].

**Figure 1** Examples of ramjet-based missiles.

In a thermally choked flow configuration, only a diverging nozzle is required downstream of the combustion chamber to accelerate the flow until a unity Mach number [4], thereby reducing the overall complexity of the engine. This manuscript focuses on this innovative concept in which the flow is choked within the diverging section of the nozzle through heat addition resulting from air–fuel combustion in the combustion chamber. This configuration has been experimentally validated by Dessornes and Scherrer [5].

In ramjet-based engines, unsteady flame dynamics and flow fluctuations can give rise to large-amplitude oscillations in pressure and velocity. Such instabilities may alter the operating regime, trigger flame blowout, accelerate material degradation, and excite damaging structural vibrations. These risks are further amplified by modern trends toward higher volumetric power densities [6], lean combustion regimes, and increasingly compact architectures. Combustion instabilities [7, 8] are particularly problematic in these configurations, which feature complex geometries, high Reynolds numbers on the order of $10^6$ [9], and strong sensitivity to perturbations. Thermally choked configurations are therefore expected to be especially prone to such instabilities. To investigate and control these unsteady phenomena propagating through the engine, a combination of complementary approaches, high-fidelity computational fluid dynamics (CFD) simulations and low-order models, is required as detailed in Fig. 2.

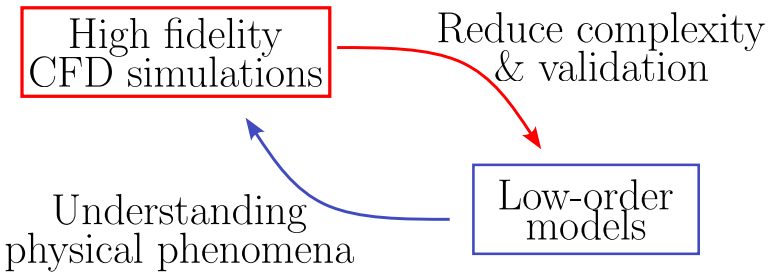


**Figure 2** Sketch illustrating the complementary approaches used to understand combustion instabilities in dual-mode ramjet engine combustors.

High-fidelity CFD simulations provide detailed insight into the coupled acoustic, hydrodynamic, and combustion processes within the engine. They enable the investigation of global stability mechanisms by directly resolving part or all of the relevant physical phenomena involved in such configurations as performed by Roux *et al.* [10] and Bekaert [11]. However, their application to these systems remains computationally demanding due to the complexity of the flow physics (fuel injection, multiphase interactions, shock–boundary-layer coupling, *etc.*). Consequently, low-order models play a crucial role by simplifying the governing physics to isolate and analyse the dominant instability mechanisms before introducing further complexity.

A major challenge for low-order models lies in accurately describing the scattering of perturbations through the nozzle and their interaction with the critical throat, which acts as a natural acoustic boundary for the system. The acoustic behaviour of geometrically choked nozzles has been extensively studied, and several seminal works [12–15] have demonstrated that the predictions of low-order models depend strongly on geometry, flow conditions, hydrodynamic–acoustic coupling, and the representation of reactive zones. These studies highlight the necessity of coupling acoustic modelling with a realistic representation of flame dynamics to capture thermoacoustic feedback mechanisms. However, such flame-dynamics models remain largely unavailable for thermally choked flow configurations. Moreover, the adaptation of acoustic models to flows in which choking is induced by heat addition, characterised by high Mach numbers, elevated

static temperatures, and non-uniform thermodynamic properties, also remains lacking, as the appropriate boundary condition for the thermal throat has yet to be established.

In this context, a detailed understanding of the acoustic behaviour of thermally choked nozzles is essential for the development of dual-mode ramjet technologies. Low-order models, in particular, provide powerful tools for identifying and characterising the physical mechanisms responsible for instability generation in these configurations. Consequently, this thesis focuses on modelling the acoustic response of thermally choked flows and on developing a suitable formulation for the thermal-throat boundary condition.

## State of the art and objectives

Combustion noise originates from both direct and indirect mechanisms. The direct component arises from unsteady heat release and the associated pressure fluctuations generated within the flame region, whereas the indirect component results from the acceleration of entropy and vorticity inhomogeneities through regions of strong mean-flow gradients, such as nozzles. These mechanisms, first identified in aero-engine exhausts, also play a crucial role in airbreathing propulsion systems, where thermal choking and unsteady heat-release rate processes can strongly influence the overall acoustic response. Numerous studies have investigated the propagation of acoustic waves and the generation of both direct and indirect combustion noise in geometrically choked nozzle configurations.

Marble and Candel [16] were among the first to develop an acoustic model for the propagation of acoustic and entropy waves through a nozzle with a geometric throat, building on the earlier works of Crocco [17] and Tsien [18]. Their study characterised the acoustic reflection and entropy-noise-production coefficients in the zero-frequency limit. The formulation relied on the assumption of a quasi-one-dimensional inviscid flow, neglecting vorticity and compositional fluctuations, with planar acoustic and entropy waves. The model was based on the compact-nozzle assumption, in which the characteristic wavelength of the perturbations (acoustic or entropy) is much larger than the nozzle length scale, allowing the nozzle to be treated as a discontinuity. Within this framework, the acoustic response depends solely on the upstream Mach number, rendering the model particularly tractable, though its applicability remains restricted to very low frequencies.

To extend the validity of the compact formulation, finite-frequency effects were progressively incorporated. Early extensions introduced correction terms to the compact model of Marble and Candel [16], as demonstrated by Stow *et al.* [19] and Goh and Morgans [20]. The compact assumption was later removed entirely by Moase *et al.* [21], who adopted a linear velocity profile within the choked nozzle. These developments progressively relaxed the assumptions of the compact-nozzle theory by introducing frequency-dependent corrections and by accounting for spatial variations of the mean flow. An alternative formulation was proposed by Duran and Moreau [22], who recast the quasi-one-dimensional linearised Euler equations into a differential system governing fluctuations in mass-flow rate, total temperature, and entropy. This system was solved using the Magnus expansion, enabling the modelling of choked-flow nozzles, including configurations with diffuser shocks, without assumptions on the steady flow field.

Beyond the linear regime, Huet and Giauque [23] and Huet [24] developed models to investigate non-linear effects within the compact-nozzle framework. Their results showed that the acoustic response becomes significantly non-linear at high Mach numbers, whereas entropy-wave propagation remains only weakly affected. Later investigations by Emmanuelli *et al.* [25] and Huet *et al.* [26] extended these models to two-dimensional axisymmetric configurations and viscous flows, respectively, demonstrating that radial dispersion and boundary-layer effects slightly attenuate the predicted entropy-noise levels.

In relation to thermal-throat configurations, the influence of heat release has also been examined for geometric throat nozzles. Yeddula *et al.* [27] demonstrated that heat release strongly modifies acoustic wave propagation, highlighting its importance in such configurations. Yeddula *et al.* [28] extended this work by considering distributed, fluctuating heat release. Using a simplified flame-transfer function of constant amplitude and phase, they reported a pronounced influence on acoustic propagation, particularly at very low frequencies.

All of the aforementioned studies assume calorically perfect gas behaviour, *i.e.*, constant specific heats independent of temperature. In highly accelerated nozzle flows, such as in thermally choked configurations, large temperature variations may occur, challenging this assumption. Huet [29] addressed this limitation numerically and demonstrated that temperature-dependent specific heats can significantly affect the generation of entropy-induced indirect combustion noise.

More complex perturbation structures have also been investigated. For instance, Emmanuelli *et al.* [25] developed a linear model for two-dimensional nozzle geometries, validated for both acoustic and entropy planar perturbations. Extending further, Hirschberg and Hulshoff [30] proposed a lumped-element model capturing the acoustic response of a choked nozzle to vortex interactions.

Finally, in the specific context of thermally choked flows, Lin *et al.* [31] introduced a model for acoustic feedback loops in a divergent nozzle with a thermal throat generated by a compact heat-release source. However, this formulation does not isolate the specific role of the thermal throat, as it effectively treats the flame and the thermal throat as a single coupled phenomenon.

In summary, while acoustic propagation and indirect noise generation have been extensively studied for geometrically choked nozzles, no study to date has explicitly addressed heat addition as the primary choking mechanism. The present work therefore aims to characterise the aeroacoustic response of thermally choked nozzles, in which flow choking results purely from distributed heat addition, a situation representative of dual-mode ramjet engines operating near the ram-to-scram transition.

## Outline

This manuscript is structured into six chapters.

**Chapter 1** introduces the fundamental concepts of ramjet, scramjet, and dual-mode ramjet propulsion, together with the specific technological challenges associated with these systems. The concept of a thermal throat, used to achieve flow choking in ramjet operation, is then presented. The chapter concludes with a discussion of combustion instabilities and thermoacoustic coupling mechanisms.

**Chapter 2** describes the modelling framework adopted in this work, including the assumptions related to the flow, gas properties, and volumetric heat-release term. The dual-mode ramjet geometry and the computational fluid dynamics solver are detailed. The methodology used to prescribe the steady volumetric power distribution required to thermally choke the flow, as well as to construct an equivalent geometric throat nozzle, is also presented.

**Chapter 3** focuses on the numerical characterisation of the aeroacoustic response of a representative thermally choked nozzle, expressed in terms of reflection, transmission, and entropy–noise–production coefficients. The results are compared with those obtained for alternative thermal-choking conditions and for an equivalent geometric throat configuration. A quasi-steady analytical model is proposed for one of the thermally choked configurations, and particular attention is given to the formulation of the critical throat boundary condition.

**Chapter 4** presents the development of a quasi-one-dimensional linear acoustic model that describes the propagation of acoustic and entropy waves in a non-isentropic, heated flow with temperature-dependent thermodynamic properties. A new boundary condition specifically adapted

to the thermal throat is derived. The model is then validated against the numerical results obtained in Chap. 3. Using this new tool, different steady thermal-throat positions are examined to evaluate their effect on the acoustic behaviour of thermally choked configurations.

**Chapter 5** applies the validated quasi-one-dimensional linear acoustic model to assess the influence of the unsteady volumetric heat-release source term on the aeroacoustic response. The chapter explores thermoacoustic coupling by introducing a flame transfer function from the literature and analysing its impact on the overall acoustic response.

**Chapter 6** investigates the acoustic response induced by two-dimensional entropy perturbations convected through a thermally choked nozzle. The resulting acoustic field is numerically characterised and compared with predictions from one-dimensional linear models. Special attention is given to the asymptotic regimes associated with very small and very large entropy perturbation sizes.

Finally, the **Conclusions and Perspectives** summarize the main findings of the thesis and outline possible directions for future research.

Chapter 1

# Generalities and challenges of airbreathing engines

*Ma parole, des engins comme vous, ça devrait être fourni avec une notice !*

**Léodagan, roi de Carmélide [2]**


## Abstract

This introductory chapter presents the fundamental principles governing airbreathing propulsion systems, with emphasis on dual-mode ramjet engines. The basic mechanisms of thrust generation are first introduced, followed by a detailed discussion of ramjet and scramjet operating modes and their respective limitations. Particular attention is given to the concept of thermal throat choking, which enables smooth transition between subsonic and supersonic combustion regimes without mechanical modification of the nozzle geometry.

The chapter then examines the various instability mechanisms that affect dual-mode ramjets. The origins of combustion noise are discussed, distinguishing between direct noise, resulting from unsteady heat release, and indirect noise, generated by the acceleration of flow non-uniformities such as entropy or vorticity perturbations. The concept of thermoacoustic coupling is introduced to describe the feedback process between the flame and the acoustic field. Finally, the role of the thermal throat as an acoustic boundary is analysed, highlighting its influence on the system's aeroacoustic response and its potential contribution to instability development.

This chapter establishes the physical and theoretical framework for the subsequent analysis of the aeroacoustic behaviour of thermally choked flows, forming the foundation for the detailed modelling and numerical investigations presented in the following chapters.


## Contents


**1.1 Airbreathing engine propulsion principle . . . . . 8**

1.1.1 Thrust generation principle . . . . . 9

1.1.2 Ramjet technology . . . . . 9

1.1.3 Thermal choking solution . . . . . 11

**1.2 Combustion instabilities in airbreathing engines . . . . . 12**
1.2.1 Direct and indirect combustion noise . . . . . 12
1.2.2 Thermoacoustic coupling . . . . . 16
1.2.3 Aeroacoustic response of a thermally choked-flow nozzle . . . . . 17

## 1.1 Airbreathing engine propulsion principle

The airbreathing engine is designed to propel a wide range of vehicles, from civilian aircraft to battlefield fighters and even hypersonic missiles. In contrast to rocket engines, it does not carry its own oxidiser. Instead, the oxidiser, typically air, is drawn directly from the surrounding atmosphere. This substantially reduces the overall weight of the propulsion system and thereby increases the global specific impulse of such engines.

The operation of airbreathing propulsion systems is governed by the fundamental physical laws that convert chemical energy into kinetic energy. Several types of airbreathing engines exist, as shown Fig. 1.1. At low flight Mach numbers, turbofan engines, commonly employed for aircraft propulsion, are used, since the relatively low inlet velocity requires the incoming airflow to be compressed by a fan and subsequent compression stages. At higher flight Mach numbers, such compression stages are no longer required because the ram effect naturally compresses the incoming airflow at the inlet. In this regime, the inlet total enthalpy is sufficiently high for the energy addition from the compressor to be neglected. The use of compression stages is therefore no longer advantageous. Engines operating under these conditions are ramjets or scramjets, depending on the combustion regime in the combustor, and these concepts are therefore employed.

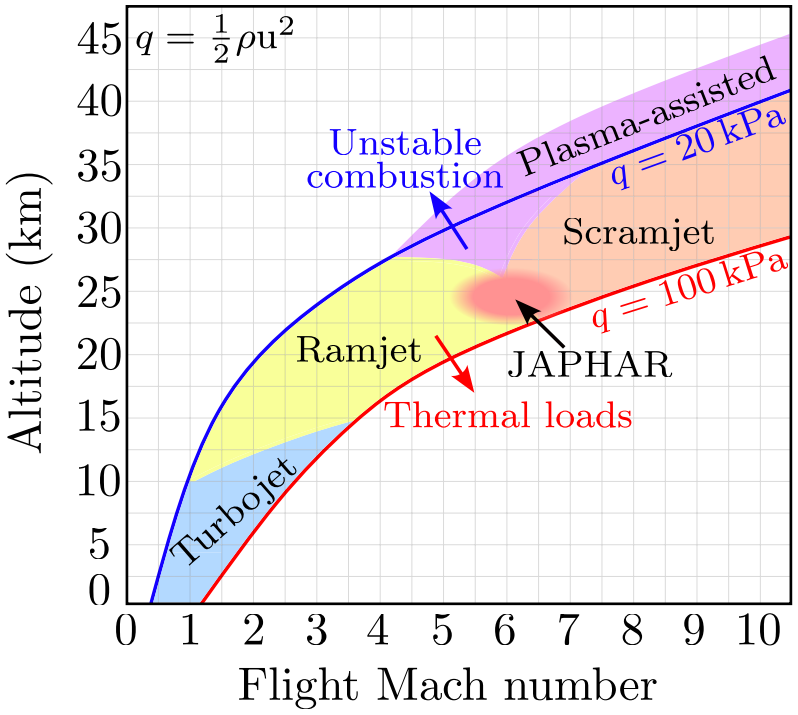


**Figure 1.1** Flight altitude versus flight Mach number for several airbreathing engines (adapted from Laux *et al.* [32]). The JAPHAR [5] operating range is also shown. Two dynamic-pressure isolines, corresponding to $q = \rho \mathbf{u}^2/2$, are shown: $q = 20\,\mathrm{kPa}$ and $q = 100\,\mathrm{kPa}$.

For ramjets and scramjets, the operational range is bounded by two main phenomena. At lower altitudes and high flight velocities (dynamic-pressure isoline $q = 100\,\mathrm{kPa}$), the thermal

loads on structural components become excessive due to the increased gas residence time and convective heating. Conversely, at higher altitudes (dynamic-pressure isoline $q = 20\,\mathrm{kPa}$), combustion becomes more difficult to stabilise owing to the reduced air density and pressure, and plasma-assisted combustion is often required to ensure stable operation. In such conditions, the flame may struggle to remain attached to the flame-holder because of excessively lean or rich mixing, an insufficiently extended recirculation zone, or a combustion zone that is too strongly influenced by the main flow.

### 1.1.1 Thrust generation principle

Airbreathing engines generate thrust by ejecting mass at high velocity, according to the Newton's third law. The thrust $T$ produced by an airbreathing engine is given by

$$T = \dot{m}_{\mathrm{out}} u_{\mathrm{out}} - \dot{m}_{\mathrm{in}} u_{\mathrm{in}} + (p_{\mathrm{out}} - p_{\mathrm{in}})\,\mathrm{A}_{\mathrm{out}}, \tag{1.1}$$

where $\dot{m}$ is the mass-flow rate, $u$ the velocity, $p$ the static pressure, and A the cross-sectional area. Subscripts $(\,)_{\mathrm{in}}$ and $(\,)_{\mathrm{out}}$ denote the inlet and outlet conditions, respectively. A nomenclature is provided at the end of this manuscript, detailing all mathematical symbols and terms.

The mass flux passing through the nozzle corresponds to the mass of combustion products. Increasing it can enhance thrust; however, it also reduces the characteristic residence time in the combustion chamber, thereby limiting the total delivered specific impulse. Enhancing the exhaust velocity is often a more effective means of improving performance. Convergent–divergent (or de Laval) nozzles are specifically designed to maximise $u_{\mathrm{out}}$ by converting thermal energy into kinetic energy. In such nozzles, the convergent section accelerates the subsonic flow ($\mathrm{M} < 1$) to sonic speed at the throat ($\mathrm{M} = 1$), while the divergent section further accelerates it into the supersonic regime ($\mathrm{M} > 1$).

### 1.1.2 Ramjet technology

At higher flight speeds, conventional turbojet engines become inefficient, giving rise to propulsion systems that rely on aerodynamic compression rather than mechanical compressors: ramjets and scramjets.

#### Ramjet engine

Ramjets are subsonic-combustion propulsion systems that use atmospheric air as the oxidiser and enable sustained supersonic flight. Figure 1.2 illustrates the main components of a ramjet engine. The supersonic incoming air is first decelerated to a subsonic regime and compressed through the air intake and diffuser (1–2). The diffuser serves to limit the influence of the combustor on the upstream flow, particularly on the air intake. In the combustion chamber (3), the subsonic air is mixed with the injected fuel and subsequently burned. The resulting high-temperature gases are then expanded and accelerated through the convergent–divergent nozzle (4-5) to generate the thrust.

The main advantage of ramjets lies in their absence of moving parts: compression is achieved entirely by the air intake. Nonetheless, ramjets require a sufficiently high initial flight speed to operate and are therefore unable to sustain itself from take-off. Auxiliary propulsion systems, such as turbojets, solid rocket boosters, or even air-launch techniques involving vehicle release, are therefore required [33–35].

The high internal flow velocity in ramjets results in a short gas residence time within the combustion chamber, typically only a few milliseconds [9]. Hence, a major challenge for flame stabilisation appears, as the laminar flame speed is two to three orders of magnitude lower

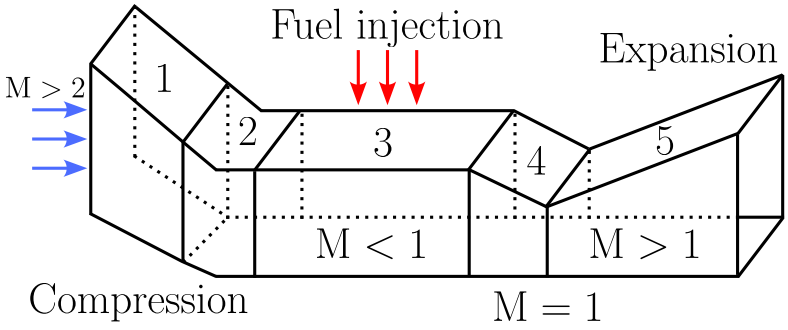


**Figure 1.2** Sketch of the components of a simplified ramjet engine, adapted from Bouchez [9].

than the flow velocity inside the chamber. Without specific flame stabilisation mechanisms, the flame would tend to detach, be blown off, or even extinguish, thereby compromising both ramjet operation and thrust generation.

To stabilise the flame in specific regions of the chamber, recirculation zones are typically created where the local flow velocity is sufficiently reduced to fall below the flame propagation speed [36]. This can be achieved by modifying the combustor geometry, for instance, in side-dump ramjet [37], where air is injected laterally into the chamber, producing recirculation zones on both sides of the fuel jet, as implemented in the *Statoréacteur de Recherche* at ONERA [38]. In other configurations, flame-holders [39, 40] or backward-facing steps [41, 42] are employed within the combustor; these act as aerodynamic obstacles that create low-velocity wake regions, enabling stable flame anchoring.

### Scramjet engine

As the flight Mach number increases beyond about 5, the inlet shock system (shock train) induces significant total-pressure losses, while chemical dissociation and recombination effects further reduce efficiency [43]. To mitigate these effects, the air intake geometry is modified to ensure that the flow entering the combustor remains supersonic, see (1) of Fig. 1.3. This design leads to the so-called supersonic-combustion ramjet, or scramjet, in which the flow velocity remains supersonic throughout the entire engine, including the combustion chamber. Downstream of the combustor (2), since the flow is already supersonic, only a divergent nozzle (3) is required for expansion and thrust generation.

In scramjets, the combustion and flow residence times are of comparable magnitude, creating severe challenges for flame stabilisation and efficient mixing. For instance, flame stabilisation can be assisted using plasma-based techniques [44].

### Dual-mode ramjet

To reach hypersonic regime, the airbreathing engine must operate as a scramjet. A ramjet can be used to accelerate the vehicle to such speeds. Combining these two propulsion concepts yields a dual-mode ramjet configuration, which extends the operational Mach number range. However, this type of engine introduces significant structural and aerodynamic challenges.

In the ramjet operating mode, where the flow within the combustion chamber is subsonic, a convergent–divergent nozzle is used to choke the flow, *i.e.*, to accelerate the flow downstream of the combustor to supersonic speeds. The flow becomes sonic at the minimum cross-sectional area, called "critical" throat. In contrast, during scramjet operation, when the flow remains supersonic throughout the combustor, such a geometric contraction instead decelerates the flow.

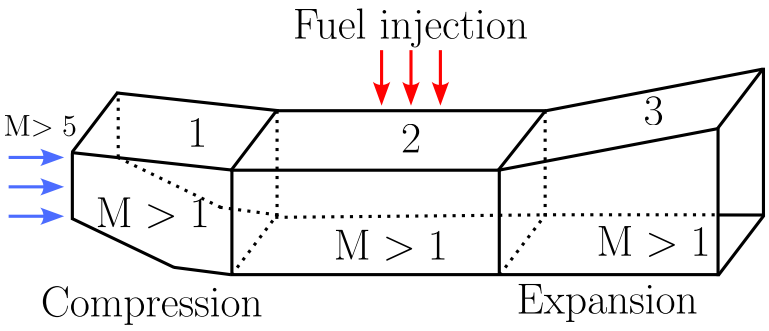


**Figure 1.3** Sketch of the components of a simplified scramjet engine, adapted from Sen *et al.* [45].

To address this issue, several solutions have been proposed [9], leading to three main design approaches:

- The first approach relies on in-flight variable-geometry nozzles to enable the transition between ramjet and scramjet operation. During the flight, the shape of the convergent–divergent nozzle can be modified by actuating watertight cylinders (see (1) in Fig. 1.4), thereby removing the geometric throat. Once the throat is opened, the flow remains supersonic throughout the combustor, allowing supersonic combustion to occur.
- A second approach restricts the geometric variation to a single degree of freedom, typically through translation along the longitudinal axis (see (2) in Fig. 1.4) or rotation [9], offering a compromise between mechanical complexity and aerodynamic performance.

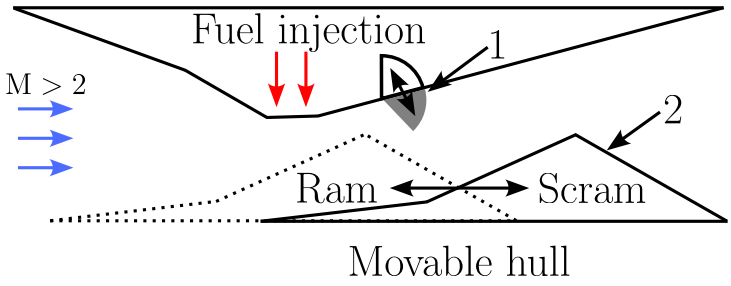


**Figure 1.4** Sketch of a simplified dual-mode ramjet engine incorporating a variable-geometry nozzle concept.

However, both variable-geometry concepts significantly increase overall system complexity by introducing additional mechanical components. To avoid modifying the engine geometry, a fixed-geometry design can be employed, requiring another choking mechanism: the thermal throat.

### 1.1.3 Thermal choking solution

In a non-uniform duct, the addition of energy through combustion[1] of a fuel–oxidiser mixture can increase the flow velocity. If this heat addition is properly adjusted, the flow can smoothly

[1] In this thesis, and within the context of ramjet-based engines, heat addition is assumed to result from combustion. Other authors have investigated thermal choking induced by gaseous phase change, such as evaporation or condensation [46, 47].

accelerate and become supersonic, as shown analytically by Heiser *et al.* [4] and Delale *et al.* [47]. The location where the flow reaches sonic conditions is referred to as the thermal throat, analogous to the geometric throat in a convergent–divergent nozzle.

Figure 1.5 illustrates an ideal dual-mode ramjet engine incorporating a thermal throat as the thermally choked-flow mechanism. This solution typically employs two combustors arranged in series, each with a different divergence angle. The first section acts as the combustor in scramjet mode and as a diffuser in ramjet mode, while the second section, with a larger divergence, serves to choke the flow at low Mach numbers and functions as the divergent nozzle in scramjet mode. This configuration requires two separate fuel-injection systems. In this design, the thermal choking mechanism is achieved through the formation of a thermal throat [5, 48–51].

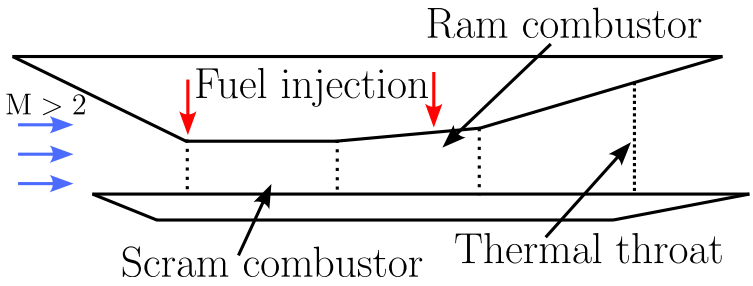


**Figure 1.5** Sketch of a simplified dual-mode ramjet incorporating a thermal throat, adapted from Falempin [52].

In ONERA/DLR program JAPHAR (Joint Airbreathing Propulsion for Hypersonic Aircraft Research), Dessornes and Scherrer [5] demonstrated the feasibility of a thermally choked-flow nozzle for an oxygen–hydrogen combustor (see Fig. 1.6). This program succeeded the PREPHA test campaign [52]. It showed the possibility of using a thermal throat in ramjet mode, without being geometrically constrained by the nozzle in scramjet mode. Three inlet Mach numbers were tested with several fuel-injection configurations. The campaign also demonstrated the capability to control the formation of the thermal throat in such a configuration by adjusting the fuel injection.

## 1.2 Combustion instabilities in airbreathing engines

As the combustion process is inherently sensitive to local thermodynamic and flow conditions, small fluctuations in these parameters can trigger instability mechanisms. In ramjet, scramjet, and dual-mode ramjet engines operating at high Reynolds numbers [7, 15], large-amplitude pressure and velocity oscillations may develop. When these fluctuations become excessive, they can disrupt the operating range of the engine, leading to flame flashback [38, 53, 54], combustion chamber extinction, or even severe mechanical damage [8, 41, 55, 56]. Such instabilities are further promoted by lean premixed pre-vaporised combustion techniques [57], as lean premixed and stratified flames are more prone to unsteady burning [58, 59].

### 1.2.1 Direct and indirect combustion noise

Combustion noise was first investigated in the context of combustion instabilities in rocket engines by Tsien [18], and later extended by Marble and Candel [16], who identified the fundamental mechanisms responsible for such pressure fluctuations generation by introducing the concept of wave propagation through accelerating subsonic and choked nozzles.

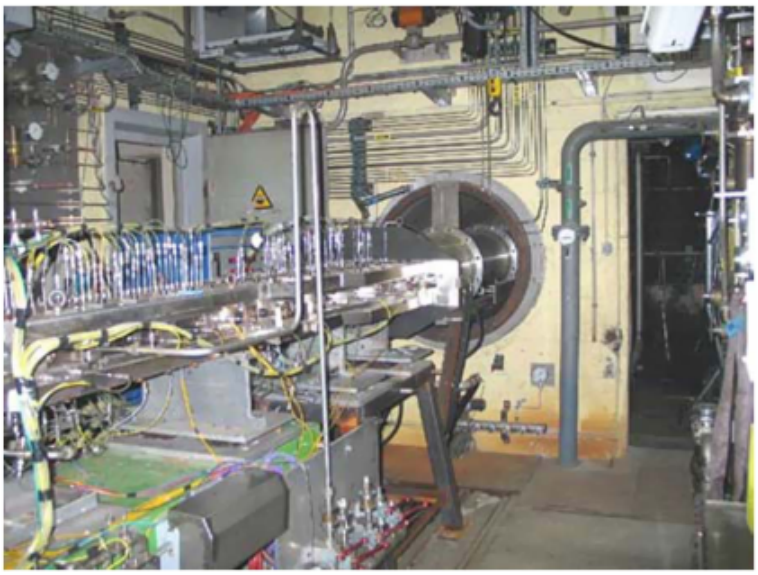

**Figure 1.6** Photograph of the JAPHAR [5] rig set-up.

In any combustion chamber, pressure fluctuations primarily originate from unsteady heat-release rate $\dot{\omega}'_T$, which itself results from the turbulent nature of the flow (see Fig. 1.7). The flame dynamics are inherently coupled with the turbulent flow-motion within the combustor [41, 42]: turbulence wrinkles the flame front, increases its surface area, and thereby enhances the overall heat-release rate. These unsteady heat-release processes are of particular importance, as they are expected to represent the dominant noise source in dual-mode ramjet engines. For a generic fluid, Kovásznay [60] showed that any perturbation can be expressed as the superposition of three fundamental fluctuations modes: acoustic, entropic, and vortical. The interactions among these modes were later investigated by Chu and Kovásznay [61], who demonstrated that they remain independent in uniform flows but become coupled to the first order[2] in the presence of mean-flow gradients, leading to the generation of noise. The acoustic mode satisfies hyperbolic equations, whereas the entropy and vorticity modes exhibit parabolic behaviour, consistent with the mathematical nature of their respective governing equations.

Two main mechanisms contribute to the generation of combustion noise. The first corresponds to the direct generation of acoustic waves $p'$, induced by fluctuations in the heat-release rate $\dot{\omega}'_T$. The second, referred to as indirect combustion noise, arises from the formation of flow inhomogeneities downstream of the flame, such as entropy $s'$, or vorticity fluctuations $V'$. These disturbances are convected by the mean flow and generate sound when accelerated through regions of non-uniform mean flow.

### Direct combustion noise

Unsteady heat-release rate fluctuations, such as those arising from transient combustion processes, lead to local unsteady volume expansion. This phenomenon acts as an acoustic monopole point source [62, 63], radiating pressure fluctuations both within the combustion chamber and

[2]According to the classical modal decomposition of Chu and Kovásznay [61], in which any quantity $\chi$ is expanded as a series $\chi = \chi^{(0)} + \chi^{(1)} + \cdots + \chi^{(n)}$, entropy and vorticity fluctuations cannot generate acoustic waves at first order unless a mean-flow gradient is present. At second order, however, the nonlinear interaction terms inherent to the Navier–Stokes equations always couple the acoustic, entropic, and vortical modes, so that entropy- and vorticity-induced noise can be generated even in a homogeneous medium.

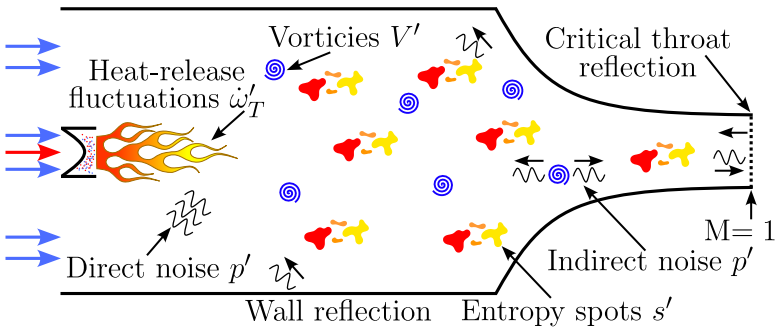


**Figure 1.7** Sketch of the flow couplings occurring in typical airbreathing engines, adapted from Dowling and Mahmoudi [62].

into the surrounding flow field. Several mechanisms can contribute to the generation of an acoustic field by heat-release rate fluctuations [64]. Among them, modulations of the flame surface area, fluctuations in the equivalence ratio, and coherent flow structures play a dominant role.

In premixed flames, modulations of the flame surface area $\delta A_f$, resulting from the interaction between acoustic or velocity waves and the flame front constitute one of the primary drivers of acoustic fluctuations [65]. For a steady flame, the propagation velocity of the flame front balances the component of the incoming flow velocity normal to the flame surface [66]. Acoustic oscillations disturb this equilibrium, and the resulting perturbations are convected along the flame surface toward the tip by the tangential flow, causing the flame to wrinkle. Consequently, the effective flame surface area [67], and thus the total heat-release rate, undergo periodic modulation. Because the heat released of a flame is proportional to its surface area, such modulations generate fluctuations in the heat-release rate according to Eq. (1.2).

$$\dot{\omega}'_T \propto \delta A_f \tag{1.2}$$

When these unsteady heat-release rate fluctuations couple constructively with the acoustic field of the combustor, acoustic energy is generated. Other mechanisms, such as equivalence-ratio fluctuations, can also generate acoustic waves within the flame region [64]. The resulting sound field may, in turn, interact with the flame, reinforcing or damping the pressure fluctuations. This feedback process is discussed in detail in Sec. 1.2.2.

### Indirect combustion noise

As detailed by Dowling and Mahmoudi [62], two main mechanisms can generate indirect combustion noise: vorticity and entropy.

The generation of sound by vorticity fluctuations has been extensively studied through the framework of acoustic analogies, which establish a mathematical connection between the flow field and the radiated acoustic field. In these formulations, the Navier–Stokes equations[3] are recast as an inhomogeneous wave equation for the pressure fluctuations, with the flow-induced terms acting as sources. This formulation provides a way to isolate specific noise-generation mechanisms in complex flows.

When the feedback of the acoustic field on the flow becomes significant, the concept of vortex sound is more appropriate than Lighthill's acoustic analogy [68]. Theoretical formulations of vortex sound were developed by Powell [69], Howe [70], and Möhring [71]. These models are particularly useful when the flow can be represented in terms of coherent vortex structures.

[3]The mathematical form of the Navier–Stokes equations is given in Sec. 2.2.

Initially formulated for free-field conditions, vortex-sound theory was later extended to confined flows, where the source term becomes spatially more localised due to concentrated vorticity distributions, in contrast to the distributed Reynolds-stress sources in Lighthill's formulation.

The acceleration of vorticity waves can generate sound, particularly in azimuthal modes. In combusting flows, however, this contribution is generally secondary for two reasons: (i) unsteady combustion produces large temperature fluctuations that give rise to dominant entropy-fluctuation structures, and (ii) viscosity increases sharply with temperature, dissipating large turbulent eddies downstream of the flame.

The role of entropy perturbations in sound generation was clarified by Tam and Parrish [72], who demonstrated that entropy-noise intensity increases with the mean velocity gradient, which acts as the driving mechanism for its generation. Their study, based on the convection of a positive density pulse through a nozzle, provided a physical interpretation of entropy–acoustic coupling. They showed that, in the presence of a positive velocity gradient, the leading edge of an entropy perturbation is accelerated first, stretching the entropy spot and inducing local expansion accompanied by a pressure drop. To restore pressure balance, compression waves are emitted downstream. Conversely, when an entropy perturbation is decelerated, compression waves are radiated upstream. Furthermore, the acceleration of fluid regions of different densities, as in a hot or cold gas non-uniformity, induces volume contraction, which acts as a dipole source of sound [73].

Experimental investigations by Bake *et al.* [74] and Knobloch *et al.* [75] confirmed these mechanisms. Using the DLR EWG and HAT facilities, they demonstrated that stronger temperature contrasts between the injected perturbations and the mean flow result in higher entropy-noise levels. Knobloch *et al.* [75] also found that increasing the mass-flow rate of the injected cold spots enhances noise emission, while Bake *et al.* [74] showed that the Mach-number dependence is non-monotonic: the entropy-noise amplitude increases up to about $M \approx 0.6$ at the throat, beyond which the pressure fluctuations amplitude reaches an asymptote. Numerical simulations revealed that the acoustic source strength continues to grow with Mach number, but destructive interference between oppositely phased waves limits the measured pressure fluctuations amplitude. The dominant source was found near the throat, with a downstream sink of similar magnitude, both intensifying with Mach number. Howe [76] later suggested that in cases of flow separation, correlations between vortex sound and entropy-noise could reduce the overall emitted noise, explaining the observed asymptote.

When entropy waves are accelerated through mean-flow gradients, the resulting entropy-noise splits into two components: an upstream-propagating acoustic wave that can interact with the flame and a downstream-propagating wave that contributes to the overall exhaust noise. The upstream component may close the feedback loop leading to thermoacoustic instabilities, as discussed in Sec. 1.2.2.

In addition, accelerated entropy waves can generate also vorticity fluctuations, which themselves act as secondary acoustic sources in the form of vortex sound [77, 78]. Hence, entropy–vorticity coupling plays a crucial role in the full description of indirect noise generation in non-isentropic, accelerated flows.

Analytical expressions for the sound generation by convected entropy and vorticity inhomogeneities in ducts with variable geometry have been formulated by Ffowcs Williams and Howe [79] and Howe [80], providing a rigorous theoretical framework for modelling indirect combustion noise in practical propulsion systems.

More recently, a third source of indirect combustion noise has been identified: compositional noise. This mechanism arises from the propagation of mixture inhomogeneities (a variation in chemical composition or species concentration) through accelerated flows.

Magri *et al.* [81] were the first to investigate the generation of acoustic waves caused by

such compositional inhomogeneities. Subsequent studies by Magri [82] and Ihme [83] analysed composition-to-acoustic transfer functions for various nozzle geometries under compact-nozzle assumptions, demonstrating that compositional perturbations can contribute significantly to the overall indirect noise. Later, the non-compact model of Duran and Moreau [22] was extended to multi-species gas flows by Magri [82] and Gentil *et al.* [84], revealing a strong frequency dependence of the composition-to-acoustic transfer functions.

### 1.2.2 Thermoacoustic coupling

Thermoacoustic instabilities are among the most critical phenomena in combustion systems [15, 85]. They arise from a constructive coupling between the unsteady heat-release rate of the flame $\dot{\omega}'_T$, and the acoustic field within the combustion chamber $p'$, as illustrated in Fig. 1.8. A perturbation in the flow field, such as in velocity, pressure, or another thermodynamic variable, induces a fluctuation of the flame front. This leads to oscillations in the heat-release rate $\dot{\omega}'_T$, which in turn generate pressure fluctuations, thus completing a feedback loop between acoustic and combustion.

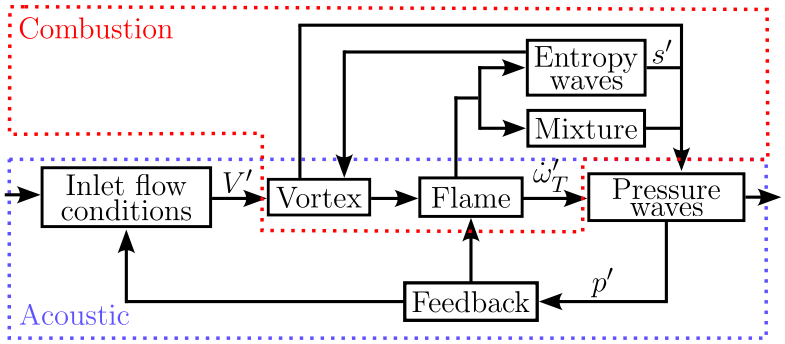


**Figure 1.8** Simplified Sketch representation of thermoacoustic coupling, adapted from Candel [86].

Thermoacoustic instabilities occur when the unsteady heat-release rate oscillations are in phase with the acoustic pressure fluctuations. This resonance amplifies pressure oscillations within the combustion chamber. If the energy supplied by the flame exceeds the acoustic losses of the system, the oscillations become self-sustained, leading to a limit-cycle instability. The underlying coupling mechanism was first identified by Lord Rayleigh, who showed that energy transfer occurs when pressure and heat-release rate oscillations are positively correlated. This principle was later formalised as the Rayleigh index [85, 87, 88], which characterises whether combustion acts as an energetic source:

$$R_I = \frac{1}{\tau}\int_\tau \int_V \left( \frac{(\bar{\gamma}-1)}{\bar{\gamma}\bar{p}} \dot{\omega}'_T \, p' \right) \mathrm{d}V \, \mathrm{d}t > \text{Acoustic losses} > 0, \tag{1.3}$$

where $R_I$ denotes the Rayleigh index, $\bar{\gamma}$ is the mean heat capacity ratio, $\bar{p}$ the mean pressure, and $\tau$ the total time of integration. A positive Rayleigh index indicates that the heat-release rate fluctuations amplify the acoustic field.

The accurate modelling of thermoacoustic dynamics thus depends on a faithful representation of both pressure and heat-release rate fluctuations, including their amplitudes, spatial distributions, and phase-angle. A realistic description must also account for non-linearities and multi-harmonic effects that often arise in practical combustors.

The acoustic field within airbreathing engines has been extensively studied in the literature, demonstrating that numerous physical phenomena influence the thermoacoustic behaviour of

such systems. Seminal works by Culick [15] and Yang and Culick [55] revealed that the dynamics predicted by low-order acoustic models are strongly affected by geometry, flow conditions, and the interaction between acoustic and hydrodynamic fields. These studies also emphasised the necessity of coupling the acoustic model with an accurate description of the unsteady flame response.

As first suggested by Crocco [17], the flame can be modelled as an acoustic element responding to local perturbations. In this framework, the fluctuating heat-release rate $\dot{\omega}'_T$, is linked to upstream acoustic disturbances such as velocity fluctuations $u'$, through a flame transfer function (FTF). Assuming small-amplitude oscillations, an FTF can be defined as:

$$\frac{\dot{\omega}'_T}{\bar{\dot{\omega}}_T} = \mathcal{F}(\omega)\,\frac{u'}{\bar{u}}, \tag{1.4}$$

where $\mathcal{F}(\omega)$ represents the complex gain and phase of the flame response at angular frequency $\omega = 2\pi f$.

While FTFs assume a linear dependence of heat-release rate fluctuations on the amplitude of the input disturbance, weakly non-linear effects can be captured using flame describing functions (FDFs) [65, 89–91]. FDFs account for the dependence of the gain and phase on the disturbance amplitude, which becomes important when the acoustic velocity fluctuations reach large values, as typically observed during instability. In such cases, the heat-release rate response becomes non-linear even though the acoustic field remains approximately linear.

The flame response model can be obtained from experiments [89], extracted from high-fidelity simulations such as large-eddy simulations (LES) [92], or analytically derived from a set of conservation equations [93]. At the flame location, appropriate jump conditions derived from the conservation equations must be applied for both mean and fluctuating quantities [62]. These conditions, combined with the flame model, provide closure for the inhomogeneous acoustic wave equation governing the coupled system.

Low-order models that incorporate analytical solutions for the acoustic field are particularly effective tools for investigating thermoacoustic behaviour. They enable rapid evaluation of the frequency response for given operating conditions and make parametric studies tractable, thereby helping to identify instability-prone frequency ranges. Despite their relative simplicity, such models provide valuable physical insight into complex systems.

### 1.2.3 Aeroacoustic response of a thermally choked-flow nozzle

The thermal throat, introduced in Sec. 1.1.3, acts as a natural acoustic boundary within the system, meaning that flow non-uniformities, particularly acoustic waves, can be reflected at this location, as already shown for geometric throat configurations [16, 22, 94]. Few studies have focused on the role of a thermal throat in potential thermoacoustic instabilities, and more particularly on acoustic reflection.

To the author's knowledge, Lin *et al.* [31] is among the few studies to treat the thermal throat as an acoustic boundary condition. The authors proposed an acoustic model to describe the pressure oscillations observed in an ethylene-fuelled scramjet combustor with a cavity flame-holder. The model identifies three feedback mechanisms: (i) a shock–flame acoustic loop, (ii) a shock–flame convective loop, and (iii) an injector–flame loop. Acoustic waves generated by unsteady heat-release rate (i) interact with the shock structure in the diffuser, while convected perturbations (ii) and injection fluctuations (iii) modulate the flame dynamics, closing the feed-back. A key feature of the model is the thermal throat, which acts as an acoustic boundary of the subsonic region. It defines the lower boundary of the subsonic cavity formed between the shock and the flame region. As the heat-release rate increases, the thermal throat moves upstream, shortening the cavity length and thereby increasing the oscillations frequency. Conversely, when

the throat moves downstream, the resonance weakens and the combustion stabilises. Thus, the thermal throat plays a central role in controlling both the acoustic feedback strength and the transition between ramjet and scramjet operating modes. However, in this model, the thermal throat and the flame location are assumed to coincide, so that the individual contributions of the flame and of the thermal throat cannot be distinguished. This assumption leads the authors to treat the thermal throat as a compact boundary condition associated with a localised heat source, *i.e.*, $L_{\text{flame}}/L_{\text{acoustic}} \ll 1$, which is completely opposite to the case of distributed heat release encountered in ramjet engines.

More generally, the aeroacoustic response of a non-uniform, transonic, and non-isentropic flow to imposed perturbations remains insufficiently understood. Previous studies have investigated related configurations, such as subsonic heated ducts [95] or geometrically-choked nozzles with heat addition [96], but not cases where heat addition itself constitutes the primary choking mechanism. The present thesis aims to address this gap.

### Chapter conclusion

This chapter introduced the fundamental principles governing airbreathing propulsion and established the physical context for the study of acoustic and thermoacoustic phenomena in dual-mode ramjet engines. The different operating regimes of airbreathing engines were first described, from subsonic turbojet operation to hypersonic scramjet propulsion. The analysis underlined the specific advantages of ramjet and scramjet configurations at high flight Mach numbers, as well as the challenges associated with their integration, efficiency, and stability.

Particular attention was devoted to the transition between the subsonic and supersonic combustion regimes and to the role of the thermal throat in enabling this transition. The concept of thermally choked flow was presented as a key feature of dual-mode ramjets, allowing a continuous increase of the internal flow without the need for geometrical modifications of the nozzle. This mechanism, while advantageous for operation, introduces additional complexity in the aeroacoustic behaviour of the system, as the critical throat becomes both a flow and acoustic boundary condition that depends on local thermodynamic and combustion conditions.

The chapter also reviewed the main instability mechanisms encountered in such engines. The distinction between direct and indirect combustion noise was clarified: the former is associated with unsteady heat release, while the latter results from the acceleration of entropy and vorticity perturbations through the nozzle. The notion of thermoacoustic coupling was introduced to describe the feedback loop between the flame dynamics and the acoustic field, which may lead to self-sustained oscillations and combustion instabilities. Finally, the influence of the thermal throat as an acoustic boundary was emphasised, showing its crucial role in modulating the reflection, transmission, and amplification of acoustic waves within the chamber.

In summary, this chapter has provided the theoretical and physical background necessary to analyse the complex interaction between heat release, entropy generation, and acoustic wave propagation in thermally choked configurations. It forms the foundation for the analytical developments and numerical investigations presented in the following chapters, which focus on the linear modelling and CFD-based assessment of the aeroacoustic response in such flows.

Chapter 2

# Methodology and tools

*Hollup...let him cook.*

**Woody**


## Abstract

This chapter presents the methodological framework and computational tools developed to investigate the aeroacoustic response of thermally choked flows in dual-mode ramjet nozzles. The modelling strategy is based on a low-order approach that isolates the dominant physical mechanisms while retaining sufficient generality to account for the essential coupling between flow, heat release, and acoustics. The flow is described by the Euler equations under the assumption of a mono-species, ideal-gas mixture with temperature-dependent thermodynamic properties. The heat-release source term, responsible for thermal choking, is introduced as a prescribed, steady volumetric power distribution, allowing the decoupling of steady and unsteady phenomena.
A simplified dual-mode ramjet geometry inspired by the ONERA–DLR JAPHAR program is detailed. The corresponding computational setup is described in detail, including the use of the ONERA CFD solver CEDRE, the numerical schemes, and the treatment of acoustic and entropy boundary conditions. A one-dimensional model is also developed to determine and tune the steady heat-release distribution required to generate a thermal throat at a desired location. Finally, a methodology is established to construct an equivalent geometric-throat nozzle with the same Mach-number distribution, providing a consistent reference configuration for comparison. These elements form the computational foundation for the subsequent analysis of acoustic-wave propagation and thermoacoustic coupling mechanisms.


## Contents


**2.1 Approach** . . . . . **20**
2.1.1 General assumptions . . . . . 20
**2.2 Governing flow-motion equations** . . . . . **22**
2.2.1 Euler equations with heat source . . . . . 22
2.2.2 Equation of state . . . . . 23
2.2.3 Gibbs relation . . . . . 23
2.2.4 Speed of sound . . . . . 23

2.2.5 Thermodynamic gas properties . . . 23
**2.3 Dual-mode ramjet geometry . . . 24**
2.3.1 Thermal-throat nozzle . . . 25
2.3.2 Inlet flow conditions . . . 25
**2.4 Numerical simulation tools . . . 26**
2.4.1 CFD code: CEDRE . . . 26
2.4.2 Boundary conditions of the system . . . 27
**2.5 Steady volumetric power distribution model . . . 28**
2.5.1 Instantaneous heat-release model . . . 29
2.5.2 Determination of the volumetric power profile . . . 30
2.5.3 Validation of the heat-release rate source term model . . . 32
**2.6 Equivalent geometric throat nozzle . . . 32**

## 2.1 Approach

To investigate the aeroacoustic response of a thermally-choked flow to perturbations (waves or more complex structures) and to compare it with analytical models, a modelling strategy based on several simplifications of the physics occurring in ramjet-based engines is proposed. This so-called low-order approach seeks to isolate and assess the influence of the main physical phenomena (flow, gas properties, turbulence, combustion, chemistry, geometry, *etc.*) on the acoustic behaviour of such a complex configuration, while deliberately neglecting certain aspects of physical complexity.

This approach contrasts with mid- to high-fidelity numerical simulations, such as RANS (Reynolds-Averaged Navier–Stokes), LES (Large-Eddy Simulation), or DNS (Direct Numerical Simulation). These methods enhance agreement with experimental data by modelling or resolving part of the turbulence scales[1]. However, they also introduce a larger number of modelling and numerical unknowns (mesh refinement, boundary-layer resolution, fuel injection, flame representation, turbulence scales, and computational cost, etc) making it difficult to clearly distinguish genuine physical effects from numerical artefacts. These types of numerical simulations are not the focus of this work; interested readers are referred to Roux *et al.* [38], Klein *et al.* [42], and Bekaert *et al.* [54] for LES-based simulations of ramjet engine configurations.

By contrast, low-order models provide an efficient framework in which all relevant phenomena are explicitly modelled, and complexity can be introduced progressively in order to study the coupling between individual mechanisms. Both approaches, low-order models and high-fidelity simulations, should therefore be regarded as complementary.

Building on this rationale, a set of general modelling assumptions is now introduced. These assumptions form the basis of the present low-order framework and provide the foundation for the subsequent refinements regarding gas properties and heat release.

### 2.1.1 General assumptions

To model the flow, the Euler flow framework is adopted. In this formulation, viscous and thermal losses, as well as molecular diffusion, are neglected, and no external forces such as gravity are considered. The inviscid assumption is widely employed in the literature on geometrical-throat

[1] In RANS-based simulations, all turbulence scales are modelled, whereas in LES simulations, the turbulence scales are resolved down to a cut-off frequency determined by Kolmogorov's energy cascade; below this scale, the turbulence is modelled. In DNS simulations, all turbulence scales are fully resolved.

nozzles [16, 22, 73, 84], since boundary layers are typically thin in ramjet configurations. Nevertheless, boundary layers can significantly affect the flow resolution, and inadequate resolution of the boundary layer may introduce discrepancies in experimental comparisons, particularly in the subsonic flow regime. However, as shown by Huet *et al.* [26], viscosity primarily influences the steady flow field by reducing the effective cross-sectional area through which the flow propagates. This effect remains minor compared with the influence of non-uniform flow properties. For the main flow, the inviscid flow model is therefore sufficient. The following sections refine the gas and heat-release rate assumptions.

Given the complexity of ramjet flows, the gas is modelled as an ideal gas with the thermodynamic properties of air. This gas model is rather restrictive, as it reduces the complex flow modifications occurring in ramjet-based engines to a single-gas approximation. In reality, the flow is considerably more complex, involving fresh air from the intake, biphasic mixtures with liquid fuel injected from the strut into the combustor, and combustion products in the form of burned gases downstream of the combustion chamber as shown by Roux *et al.* [38]. Under the present assumption, indirect noise generated by gas-mixture non-uniformities (see Sec. 1.2.1), as investigated by Gentil *et al.* [84, 97], is not accounted for. This simplification also motivates a similarly idealised treatment of heat-release rate, discussed in the following paragraph.

The volumetric power source term, which enforces thermal choking of the flow, is assumed to be non-uniform and steady, with fluctuations in heat-release rate neglected at this stage. This assumption omits an important aspect of the complex physics occurring in dual-mode ramjet combustors. In reality, the combustion of fresh gases with liquid fuel generates a chemical energy source $\dot{\omega}_T$, which is strongly dependent on the local thermochemical state and mixture ratio. Such complexity, however, lies beyond the scope of the present work. Instead, the focus here is on assessing the impact of heat-release rate on the acoustic field when heat addition is the choking mechanism.

To this end, the heat-release rate is modelled as a volumetric power source term $P_v$ added to the flow to mimic the effect of the flame on the fluid motion. This volumetric heat-release-rate term $P_v$ is introduced as a phenomenological source representing the net heat released by combustion in the combustor of a dual-mode ramjet engine. In a fully reacting-flow description, $P_v$ would be related to finite-rate chemical kinetics through $P_v = -\sum_k h_k \dot{\omega}_k$ [98], where $h_k$ denotes the specific enthalpy of species $k$ and $\dot{\omega}_k$ the corresponding reaction rate, typically modelled by Arrhenius-type laws. In this work, however, the detailed chemical-kinetic mechanism is not resolved. Instead, a spatially distributed heat-release-rate field is prescribed, chosen to be representative of ramjet operation and consistent with the quasi-one-dimensional assumptions, and the analysis focuses on its acoustic and thermoacoustic implications.

A numerical decoupling is also introduced between the steady-state component and the fluctuating quantities, thereby suppressing any feedback loop between heat-release rate and the flow field, following the approach adopted in previous studies [95, 99, 100]. Although Yeddula *et al.* [28] emphasised this limitation, it remains a useful first step before incorporating more complex thermoacoustic interactions.

Having established the flow and combustion modelling assumptions, attention is now turned to the nozzle configuration. The dual-mode ramjet nozzle is deliberately selected to be representative of experimental nozzles used to study thermal-throat configurations. However, only the combustion chamber and divergent duct are considered here. The shock train, which decelerates the upstream flow to a subsonic regime with the ram effect, is not included, as it would increase the complexity of the study [14, 101]. To enable comparison of the thermal-throat configuration with the more extensively studied geometric-throat configuration, a methodology is developed to construct an equivalent geometric-throat nozzle based on the Mach-number profile. The Mach number is chosen as the reference quantity because it directly characterises the conversion of

thermal energy into kinetic energy throughout the nozzle.

Computational fluid dynamics (CFD) simulations are then performed within the Euler framework. To enable comparison with analytical models, the simulations are carried out in a two-dimensional planar configuration, thereby avoiding complex geometric effects.

## 2.2 Governing flow-motion equations

For a homogeneous, multi-species Newtonian fluid, the conservation equations of mass, species, momentum (commonly referred to as the Navier–Stokes equations), and total energy for a continuous flow are expressed as [98]:

$$\begin{cases} \dfrac{\partial}{\partial t}\rho + \nabla \cdot (\rho \mathbf{u}) = 0 \\ \dfrac{\partial}{\partial t}(\rho Y_i) + \nabla \cdot (\rho Y_i \mathbf{u}) = -\nabla \cdot \boldsymbol{\phi}_i + \dot{q}_i, \\ \dfrac{\partial}{\partial t}(\rho \mathbf{u}) + \nabla \cdot (\rho \mathbf{u} \otimes \mathbf{u}) = -\nabla p + \nabla \cdot \bar{\bar{\tau}} + \rho \boldsymbol{f}, \\ \dfrac{\partial}{\partial t}(\rho e_0) + \nabla \cdot [(\rho e_0 + p)\,\mathbf{u}] = P_v + \nabla \cdot (\bar{\bar{\tau}} \cdot \mathbf{u}) - \nabla \cdot \boldsymbol{\phi}_e + \rho \boldsymbol{f} \cdot \mathbf{u}, \end{cases} \tag{2.1}$$

where $Y_i$ is the mass fraction, $\boldsymbol{\phi}_i$ the diffusion flux, and $\dot{q}_i$ the mass source term for species $i$. The tensor $\bar{\bar{\tau}}$ denotes the viscous stress tensor, $\boldsymbol{f}$ the external force field, $P_v$ the volumetric power source term, and $\boldsymbol{\phi}_e$ the heat flux due to thermal diffusion. Furthermore, $\mathbf{u} = (u, v, w)$ is the velocity vector, $\rho$ the mass density, $p$ the static pressure, and $e_0 = e + |\mathbf{u}|/2$ the total specific energy, with $e$ being the specific internal energy. The operator $\nabla$ denotes the Nabla operator, $t$ is time, and $\otimes$ represents the dyadic product.

According to Stokes' hypothesis, the viscous stress tensor $\bar{\bar{\tau}}$ is given by:

$$\bar{\bar{\tau}} = \mu \left( \nabla \mathbf{u} + \nabla \mathbf{u}^T \right) - \frac{2}{3} \mu \, (\nabla \cdot \mathbf{u}) \, \boldsymbol{I}_3, \tag{2.2}$$

where $\mu$ is the dynamic viscosity of the fluid, and $\boldsymbol{I}_3$ the three-dimensional identity tensor.

This general system of equations is subsequently simplified according to the modelling assumptions outlined in Sec. 2.1.

### 2.2.1 Euler equations with heat source

For a mono-species gas, neglecting viscosity, thermal diffusion, and external forces, the equations for mass, momentum, and total energy reduce to the conservative form:

$$\begin{cases} \dfrac{\partial \rho}{\partial t} + \nabla \cdot (\rho \mathbf{u}) = 0, \\ \dfrac{\partial}{\partial t}(\rho \mathbf{u}) + \nabla \cdot (\rho \mathbf{u} \otimes \mathbf{u}) + \nabla p = 0, \\ \dfrac{\partial}{\partial t}(\rho e_0) + \nabla \cdot [(\rho e_0 + p)\,\mathbf{u}] = P_v, \end{cases} \tag{2.3}$$

This system is hereafter referred to as the "Euler equations with heat source" and will hereafter be referred to as "the Euler equations", for simplicity.

### 2.2.2 Equation of state

To close the Euler equations (Eq. (2.3)), an equation of state is required. Assuming that gas molecules interact only through instantaneous collisions and that their size is negligible compared to the average intermolecular distance, the gas can be considered ideal. Under this approximation, the ideal gas law relates the static pressure $p$, density $\rho$, and static temperature $T$ as:

$$p = \rho r T, \tag{2.4}$$

where $r = \mathcal{R}/\mathcal{W}$ is the specific gas constant, with $\mathcal{R} = 8.3145\,\mathrm{J\,mol^{-1}\,K^{-1}}$ the universal gas constant, and $\mathcal{W}$ the molar mass of the gas. For an ideal gas, the specific gas constant $r$ satisfies $r = c_p - c_v$, where $c_p$ and $c_v$ denote the specific heat capacities at constant pressure and constant volume, respectively. This relation leads to the definition of the heat-capacity ratio $\gamma = c_p/c_v$. In this framework, the specific internal energy $e$ and the specific enthalpy $h$ depend only on temperature, and their differentials are given by

$$\mathrm{d}e = c_v\,\mathrm{d}T, \tag{2.5}$$
$$\mathrm{d}h = c_p\,\mathrm{d}T. \tag{2.6}$$

### 2.2.3 Gibbs relation

For a uniform mono-species gas and a reversible process, the Gibbs energy relation links the reversible entropy variation $\mathrm{d}s$, to that of the static temperature $\mathrm{d}T$, and static pressure $\mathrm{d}p$ [102]:

$$\frac{\mathrm{d}s}{c_p} = \frac{\mathrm{d}T}{T} - (\gamma - 1)\frac{\mathrm{d}p}{\gamma p}. \tag{2.7}$$

This relation remains valid for both calorically perfect gases, with constant $c_p$, and thermally perfect gases, with temperature-dependent $c_p(T)$, in mono-species mixtures [103, 104]. The interested reader is referred to Refs. [81, 105, 106] for extensions of this framework to multi-species gas flows.

### 2.2.4 Speed of sound

The isentropic speed of sound is defined as:

$$c^2 = \left.\frac{\partial p}{\partial \rho}\right|_s. \tag{2.8}$$

For an ideal gas, this reduces to $c^2 = \gamma r T$. The state equation (Eq. (2.4)) can then be rewritten as:

$$\gamma p = \rho c^2. \tag{2.9}$$

### 2.2.5 Thermodynamic gas properties

Due to the large temperature variations encountered in typical dual-mode ramjet flows, as shown by Bekaert [11] and Pelletier *et al.* [107], the specific heat at constant pressure $c_p$ cannot be assumed constant. Air is therefore modelled as an ideal gas with a temperature-dependent isobaric heat capacity $c_p(T)$, expressed as a seventh-order polynomial in $T$:

$$c_p(T) = \sum_{n=0}^{7} \frac{\alpha_n}{\mathcal{W}} \left(\frac{T}{T_{\mathrm{ref}}}\right)^n, \tag{2.10}$$

where $T_{\text{ref}} = 1000\,\text{K}$, and $\alpha_n$ are the heat capacity coefficients tabulated by Lemmon *et al.* [108] and reported in Tab. 2.1. The heat capacity ratio $\gamma$ of the flow is therefore also dependent on the local temperature $T$.

**Table 2.1** Air isobaric heat capacity coefficients $\alpha_n$ in $\text{J}\,\text{kg}^{-1}\,\text{K}^{-1}$ (rounded to $10^{-4}$).

| $\alpha_0$ | $\alpha_1$ | $\alpha_2$ | $\alpha_3$ | $\alpha_4$ | $\alpha_5$ | $\alpha_6$ | $\alpha_7$ |
|---|---|---|---|---|---|---|---|
| 30.6549 | -15.2304 | 43.9493 | -42.7479 | 21.6329 | -6.0749 | 0.8973 | -0.0544 |

## 2.3 Dual-mode ramjet geometry

To investigate the aeroacoustic response of a thermally choked nozzle, a dual-mode ramjet configuration is required. In the present work, the geometry is simplified so as to capture the dominant physical mechanisms while remaining representative of realistic engines. Several authors have experimentally and numerically investigated the flow behaviour of dual-mode ramjet engine configurations; see, *e.g.*, Refs. [109–113]. Although their designs differ in detail[2], these dual-mode ramjet nozzles share similar global features: an isolator followed by one or two diverging combustion chambers. The configuration adopted here is derived from the ATD 5 test facility at ONERA.

Within the framework of the bilateral ONERA–DLR research program JAPHAR [5], the ability of a thermal throat to choke a dual-mode ramjet engine was successfully demonstrated. In particular, the feasibility of a thermally-choked nozzle was experimentally validated for an air–hydrogen inflow at flight conditions up to Mach 8. The ATD 5 facility offers the following inlet capacities:

**Table 2.2** Maximum inlet capacities of the ATD 5 test cell, adapted from Dessornes and Scherrer [5].

| Total pressure | Total temperature | Air mass-flow | $O_2$ mass-flow | $H_2$ mass-flow |
|---|---|---|---|---|
| 40 bar | 2400 K | $8\,\text{kg}\,\text{s}^{-1}$ | $1.4\,\text{kg}\,\text{s}^{-1}$ | $0.3\,\text{kg}\,\text{s}^{-1}$ |

Figure 2.1 details the JAPHAR nozzle geometry used during the experimental campaign. It consists of a two-stage divergent nozzle with different divergence angles along its longitudinal axis. These angles could be adjusted during the experiments to increase or decrease the overall divergence. Two rows of injection struts were employed. The first stage is a slowly diverging section, designed for fully subsonic flow, and contains one injection strut together with three wall injectors. The second stage is more strongly diverging, with two struts and three additional injectors in total. This stage is designed to sustain transonic flow and to generate a thermal throat. The combustor inlet cross-section is $100 \times 100\ \text{mm}^2$, and the total length of the test bench is 2.3 m. The use of joints between the two stages allowed for modifications of the choking position.

Based on the JAPHAR experiments, a simplified nozzle geometry is defined hereafter. This configuration corresponds to the $C_4$ case of the JAPHAR project: only the two rows of injectors are retained with an injection level of 100 %, allowing for the generation of a thermal throat in the second divergent stage.

[2]The main differences arise from the length of the different components, the divergence angle, and potential aerodynamic obstacles, *i.e.*, backward-facing steps or flame-holders.

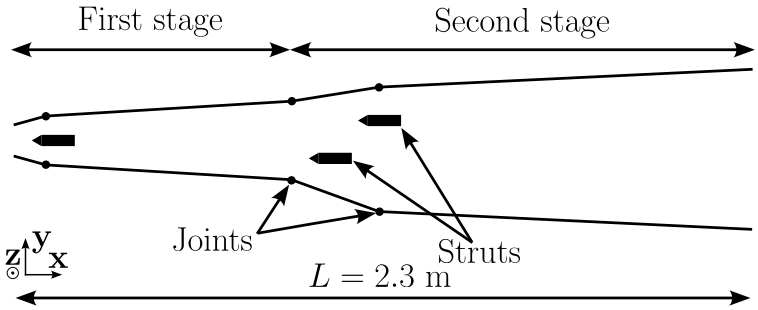


**Figure 2.1** Sketch of the JAPHAR nozzle geometry used for the experiments by Dessornes and Scherrer [5].

### 2.3.1 Thermal-throat nozzle

The dual-mode ramjet nozzle used to investigate the aeroacoustic response of a thermal throat is described below. It is based on the $C_4$ case of the JAPHAR configuration, subject to the following assumptions:

- the upstream section of the nozzle is a straight duct,
- only half of the geometry is considered, with a symmetry condition on the axis,
- the inlet Mach number is subsonic,
- the struts are not considered, as no combustion is performed (see Sec. 2.1).

The resulting geometry, shown in Fig. 2.2, consists of three main sections:

- a straight-duct upstream section ($0 \leq x/L < x_\mathrm{u}/L = 0.42$),
- a smooth transition section ($x_\mathrm{u}/L = 0.42 \leq x/L < x_\mathrm{d}/L = 0.58$) formed by a circular-arc wall with angle $\alpha = 3°$,
- a divergent duct with a constant divergence angle $\alpha = 3°$ ($x/L > x_\mathrm{d}/L = 0.58$).

The use of the transition section avoids a discontinuity between the straight- and divergent-ducts and prevents numerical issues related to mesh refinement.

The nozzle has a total length of $L = 2.4\,\mathrm{m}$ and an inlet height $y_\mathrm{in} = 25 \times 10^{-3}\,\mathrm{m}$. The transition region is defined by a circular-arc radius of $R_\mathrm{t}/y_\mathrm{in} = 305$.

Hereafter, the constant cross-section duct is referred to as the straight-duct, while the varying cross-section region (transition and divergent sections) is referred to as the divergent-duct.

### 2.3.2 Inlet flow conditions

The airflow at the inlet is subsonic, as detailed in Tab. 2.3, since the computational domain is assumed to begin just downstream of the engine intake. In reality, an unsteady shock-train structure (oblique shocks) is present at the intake, decelerating the flow until subsonic conditions are reached. In the present study, these structures are not taken into account, and steady inlet conditions are imposed in terms of Mach number, static pressure, and total temperature. The chosen inlet conditions are representative of typical dual-mode ramjet operation, as reported by Dessornes and Scherrer [5]. Interested readers are referred to Refs. [109–113] for similar inlet conditions.

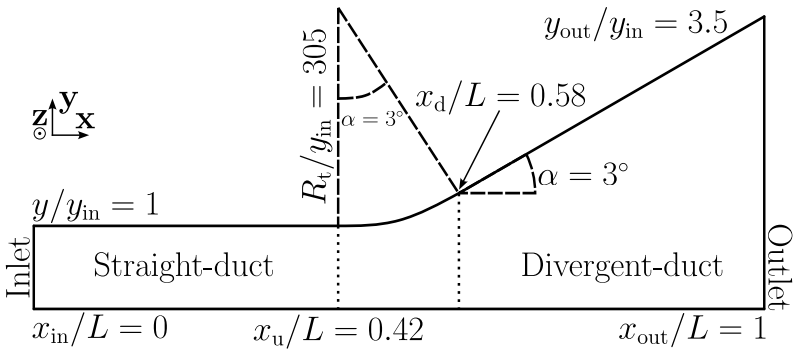


**Figure 2.2** Simplified two-dimensional planar sketch of a dual-mode ramjet geometry (not to scale).

**Table 2.3** Nozzle-inlet conditions corresponding to a flight Mach number of M = 3.

| Parameter | Value | Unit |
|---|---|---|
| Mach number ($M_{in}$) | 0.60 | – |
| Total temperature ($T_{0,in}$) | 600 | K |
| Static pressure ($p_{in}$) | 2.00 | bar |

## 2.4 Numerical simulation tools

### 2.4.1 CFD code: CEDRE

Computational fluid dynamics (CFD) simulations in this work are performed by solving the Euler equations with heat source presented in Eq. (2.3) using a finite-volume approach. Many CFD codes exist, ranging from open-source packages such as OpenFOAM to commercial software such as ANSYS Fluent. In this study, the ONERA CFD code CEDRE is employed. This highly scalable software suite includes several solvers that can be coupled either weakly or strongly, enabling multi-physics applications on unstructured grids [114–117]. Among these solvers, only one is relevant for the present work: CHARME, which is dedicated to the simulation of energetic gas flows. The interested reader is referred to Refloch *et al.* [118] and related documentation for further details.

In this work, CFD simulations are performed in a two-dimensional framework, primarily using the planar approximation. Owing to the simplicity of the nozzle geometry considered (see Sec. 2.3.1), a mesh (mainly structured) is generated with the open-source software GMSH, which allows the mesh size to be easily adjusted depending on the case studied. The spatial discretisation in CEDRE employs a second-order multi-slope MUSCL (Monotonic Upstream-centered Scheme for Conservation Laws) scheme, as described by Le Touze *et al.* [119], together with an HLLC (Harten-Lax-van Leer-Contact) flux scheme [120] and Van Leer as flux limiters. Other spatial discretisation schemes are available in the CEDRE CFD code, in particular a fourth-order scheme. However, for the configurations considered in this work, this higher-order scheme did not provide any significant improvement in accuracy.

Temporal integration is carried out using an implicit second-order Runge–Kutta (RKI2) scheme [121], with the implicit system solved via GMRES. This scheme provides the same level of accuracy as explicit time integration while allowing for a larger time step.

### 2.4.2 Boundary conditions of the system

To study the scattering of acoustic waves in a thermally-choked-flow nozzle, perturbations must be introduced into the computational domain (Sec. 2.3). In CEDRE this is achieved using the CILEPI tool, which enables spatial and temporal variations of boundary conditions. In this study, two types of inlet forcing are considered: downstream-propagating isentropic acoustic waves and entropy waves, as summarised in Tab. 2.4. These perturbations are prescribed based on the Gibbs energy equation (Eq. (2.7)), where $(\,)'$ denotes fluctuations and $\bar{(\,)}$ steady quantities:

$$\frac{s'}{\bar{c}_p} = \frac{T'}{\bar{T}} - (\bar{\gamma} - 1)\frac{p'}{\bar{\gamma}\bar{p}}. \tag{2.11}$$

Static pressure $p$ and static temperature $T$ are prescribed as inlet boundary conditions. These two quantities can be directly tuned to inject acoustic or entropy waves into the system, while the inlet flow velocity $u$ is left unchanged. For isentropic acoustic forcing, pressure fluctuations $p'_{\text{in}}$ are superimposed onto the inlet static pressure of the base flow $\bar{p}_{\text{in}}$, and the inlet temperature is chosen accordingly as defined in Tab. 2.4. The corresponding entropy fluctuation vanishes directly when applying Eq. (2.11). Conversely, for entropy forcing, the static pressure is prescribed as constant at the inlet, while the static temperature is modified by adding temperature fluctuations $T'_{\text{in}}$, to generate the desired entropy perturbation.

**Table 2.4** Inlet boundary conditions used to inject downstream-propagating waves.

| **Forcing type** | **Isentropic acoustic** | **Entropy** |
|---|---|---|
| Pressure | $p_{\text{in}} = \bar{p}_{\text{in}}\,(1 + p'_{\text{in}}/\bar{p}_{\text{in}})$ | $p_{\text{in}} = \bar{p}_{\text{in}}$ |
| Temperature | $T_{\text{in}} = \bar{T}_{\text{in}}\,(1 + \dfrac{\bar{\gamma}_{\text{in}} - 1}{\bar{\gamma}_{\text{in}}\bar{p}_{\text{in}}} p'_{\text{in}})$ | $T_{\text{in}} = \bar{T}_{\text{in}}(1 + T'_{\text{in}}/\bar{T}_{\text{in}})$ |

The inlet fluctuating quantities ($p'_{\text{in}} = p'(x_{\text{in}}, y, t)$ and $T'_{\text{in}} = T'(x_{\text{in}}, y, t)$) can be applied uniformly in the transverse direction, resulting in the injection of plane waves. This case is addressed in Chap. 3. In contrast, Chap. 6 considers a non-uniform transverse entropy injection, which generates two-dimensional structures.

All configurations studied in this work are choked nozzles, either through heat addition or geometric contraction. Figure 2.3 illustrates the application of the different boundary conditions in the computational domain. The inlet of the computational domain is subsonic with a non-reflective treatment (**- - -**) and the outlet boundary condition is supersonic (**- - -**), with no state imposed and all waves evacuated. To reduce computational cost, only upper half of the nozzle is simulated. CEDRE handles two-dimensional planar simulations by applying a symmetry axis along the main axis of the chosen configuration (**· · · ·**). For two-dimensional axisymmetric numerical simulations (see Appendix C), the rotation axis is applied instead. A solid-wall boundary condition is applied to the outer wall of the considered geometry (**——**). This wall is adiabatic and non-permeable. To remain consistent with the approach adopted in this thesis (see Sec. 2.1), the boundary-layer model is defined as slip, thereby avoiding any wall-friction effects.

#### Non-reflective boundary condition

Non-reflective boundary conditions are essential for the accurate simulation of aeroacoustic phenomena, and several formulations have been proposed in the literature. In CEDRE, the approach differs from classical methods: boundary conditions are implemented through direct relaxation of the variables at the computational domain boundaries, as described by Huet and Courbet [122].

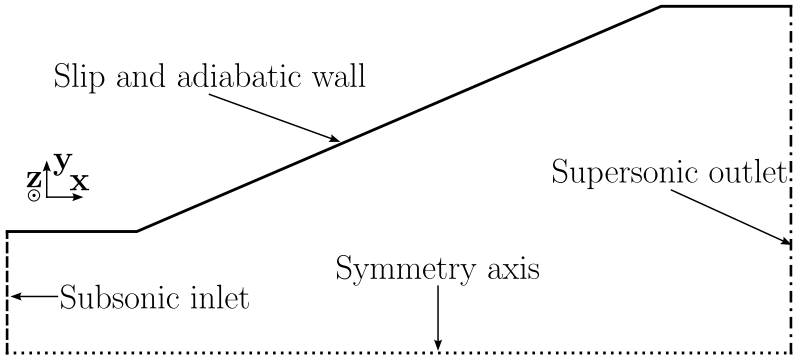


**Figure 2.3** Sketch of the boundary conditions applied in a typical thermally-choked computational domain. A similar approach can be applied to convergent–divergent nozzle geometries.

This relaxation is expressed as

$$\frac{\partial \chi_{\mathrm{b}}}{\partial t} = \tilde{f}\,(\chi_{\mathrm{m}} - \chi_{\mathrm{b}})\,, \tag{2.12}$$

where $\chi_{\mathrm{b}}$ is the variable at the boundary, $\chi_{\mathrm{m}}$ is the target value of this variable, and $\tilde{f}$ is the relaxation frequency. This relation is applied to each variable, which is either relaxed towards its prescribed boundary value or left to evolve as a function of the surrounding flow when it is not explicitly imposed. The condition of flux equality across the boundary is not inherently satisfied in this formulation, and an additional assumption on the flux is therefore required. In CEDRE, the same upwind flux model as that used at internal cell interfaces is applied by default. The principle of non-reflection holds whether boundary conditions are set to constant values or to time-dependent values prescribed with the CILEPI tool introduced in Sec. 2.4.2.

In practice, the degree of acoustic reflection at the boundary can be controlled in CEDRE through a parameter $\alpha = \tilde{f}\Delta t$, which governs the acoustic-reflection coefficient $R_a$ according to

$$|R_a|^2 = \frac{1}{1 + \left(\dfrac{4\pi f_c \Delta t}{\alpha}\right)^2} \quad ; \quad \arg[R_a] = -\tan\left(\frac{4\pi f_c \Delta t}{\alpha}\right) \tag{2.13}$$

where $f_c$ is the prescribed cut-off frequency and $\Delta t$ the time step. The parameter $\alpha$ thus acts as a first-order low-pass filter: frequencies $f \geq f_c$ are progressively damped. For sufficiently small $\alpha$, the boundary condition approaches non-reflective behaviour, enabling efficient evacuation of acoustic waves.

The non-reflective behaviour is therefore most effective at high frequencies. At the cut-off frequency $f = f_c$, the transfer-function amplitude is equal to $1/2$ for the inlet boundary. The quasi-non-reflective character of these boundary conditions has been numerically verified at ONERA in one- and two-dimensional configurations for planar acoustic and entropy waves by Huet and Courbet [122].

## 2.5 Steady volumetric power distribution model

To establish a thermal throat at a specified position within a divergent nozzle and thermally choke the flow, a one-dimensional volumetric power distribution $P_v(x)$, is required. As already discussed in Sec. 2.1, this heat addition mimics the role of a distributed flame in a dual-mode ramjet engine. The volumetric power source acts as a steady flame, supplying a fixed power per unit volume to the system. To correctly tune this source term, an analytical steady-state

quasi-one-dimensional model has been developed for a calorically semi-perfect ideal-gas flow. It is based on the instantaneous heat-release addition $q$, which, in the quasi-one-dimensional steady-state approximation, is related to the volumetric power by

$$P_v = \rho u \frac{\mathrm{d}q}{\mathrm{d}x}. \tag{2.14}$$

The principle of the model is as follows: for a prescribed steady-state thermal-throat position $x_*$ an initial guess of a dimensionless power number $\mathcal{P}_f$ is made. The Mach-number evolution $\mathrm{M}(x)$ is then computed from the sonic position up to the inlet. The resulting inlet Mach number is compared with the imposed boundary condition $\mathrm{M}_{\mathrm{in}}$. If the two values agree, the corresponding volumetric power distribution is determined and implemented in the CFD solver. Otherwise, a new value of $\mathcal{P}_f$ is selected and the procedure is repeated iteratively. Convergence towards the correct $\mathcal{P}_f$ is ensured using a Newton–Raphson method, with the initial guess typically chosen to be of order unity.

### 2.5.1 Instantaneous heat-release model

The profile of the heat-release model is based on the work of Wang *et al.* [123]:

$$q(x,\sigma) = \mathcal{P}_f h_{0,\mathrm{in}} \frac{1 - \exp\left(-\left(\dfrac{x - x_{\mathrm{u}}}{\sigma}\right)^2\right)}{1 - \exp\left(-\left(\dfrac{L - x_{\mathrm{u}}}{\sigma}\right)^2\right)}, \tag{2.15}$$

where $\mathcal{P}_f$ is the dimensionless flame power number, $h_{0,\mathrm{in}} = c_{p,\mathrm{in}} T_{0,\mathrm{in}}$ is the inlet total enthalpy, $x$ is the longitudinal position, $x_{\mathrm{u}}$ is the start of the divergent section, and, because of Eq. (2.15), the start of the heat-release region (see Sec. 2.3.1). $L$ is the total length of the nozzle, and $\sigma$ is the characteristic width of the heat-release region.

This model serves as the basis for the present non-uniform heat-release distribution, as it enables a smooth increase of the heat source, and, consequently the flow speed and the temperature, within a divergent nozzle. Moreover, by combining Eq. (2.14) with the flame model of Wang *et al.* [123], the resulting volumetric power distribution exhibits a log-normal profile. This configuration is reasonably consistent with the longitudinal and time-averaged heat-release rate $\bar{\dot{\omega}}_T$, obtained in numerical simulations of ramjet configurations, as shown by Roux *et al.* [10] and Gicquel and Roux [124]. However, in contrast to the dynamics of a real flame, the present model assumes the volumetric power source to be uniform in the transverse direction and steady in time, thereby applying the same amount of energy across the cross-section and remaining independent of unsteady flow properties. This approximation departs significantly from the physical complexity of actual flame–flow interactions. The reasons for these assumptions have been detailed in Sec. 2.1.

The normalised flame-power number, $\mathcal{P}_f = P_{\mathrm{tot}}/P_{\mathrm{conv}}$, is used in this work to quantify the ratio of the total added flame power $P_{\mathrm{tot}}$, to the inlet convective flux of heat $P_{\mathrm{conv}}$. For high dimensionless power numbers ($\mathcal{P}_f \gg 1$), a large amount of energy is required to thermally choke the flow, leading to a significant increase in the critical static temperature. Conversely, for low power numbers ($\mathcal{P}_f \ll 1$), the flow is nearly choked (for instance, if the inlet Mach number is already close to unity), and only a small amount of heat addition is needed to reach the thermally choked condition.

When the thermal throat is located deep within the divergent duct, a high dimensionless power number results in a thermal throat positioned near the onset of heat addition. In contrast,

a low dimensionless power number places the thermal throat farther downstream. This parameter is directly used to adjust the heat-release source term, as detailed in Sec. 2.5.2.

### 2.5.2 Determination of the volumetric power profile

To correctly tune the volumetric power source term $P_v$ through the instantaneous heat release $q$, it is necessary to compute the evolution of the Mach number M, and the static temperature $T$, in a quasi-one-dimensional steady ideal-gas flow. This ensures that the heat addition is consistent with both the prescribed thermal-throat position and the inlet conditions, detailed in Tab. 2.3. To this end, the following equations are employed, as reported by Shapiro [125]:

$$\frac{1}{\mathrm{M}}\frac{\mathrm{dM}}{\mathrm{d}x} = -\frac{1+\frac{\gamma-1}{2}\mathrm{M}^2}{1-\mathrm{M}^2}\frac{1}{\mathrm{A}}\frac{\mathrm{dA}}{\mathrm{d}x} + \frac{1+\gamma\mathrm{M}^2}{1-\mathrm{M}^2}\frac{1}{2c_pT}\frac{\mathrm{d}q}{\mathrm{d}x} - \frac{1}{2\gamma}\frac{\mathrm{d}\gamma}{\mathrm{d}x}, \tag{2.16}$$

$$\frac{1}{T}\frac{\mathrm{d}T}{\mathrm{d}x} = \frac{(\gamma-1)\mathrm{M}^2}{1-\mathrm{M}^2}\frac{1}{\mathrm{A}}\frac{\mathrm{dA}}{\mathrm{d}x} + \frac{1-\gamma\mathrm{M}^2}{1-\mathrm{M}^2}\frac{1}{c_pT}\frac{\mathrm{d}q}{\mathrm{d}x}. \tag{2.17}$$

These equations are derived from the Euler equations (Eq. (2.3)) under the quasi-one-dimensional steady-flow assumption. Further details on this approximation can be found in Sec. 4.2.

The width of the heat-release region $\sigma$ is directly related to the cross-sectional area A at the sonic location $x_*$, through the critical-throat relation of Heiser *et al.* [4]:

$$\left.\frac{1}{\mathrm{A}}\frac{\mathrm{dA}}{\mathrm{d}x}\right|_{x_*} = \left.\frac{1}{c_pT}\frac{\mathrm{d}q}{\mathrm{d}x}\right|_{x_*}, \tag{2.18}$$

This relation is obtained directly from the Mach-number equation Eq. (2.16) at the critical point. It shows that, in the geometric-throat case ($q = 0$), the critical throat must coincide with the location of minimum cross-sectional area, whereas for a thermally-choked flow ($q \neq 0$), the geometry and heat-release gradients are closely coupled.

To close the system, the static temperature at any position can be determined by solving the conservation equation for the total specific enthalpy $h_0$:

$$h_{0,\mathrm{in}} + q(x) = h(x) + \frac{\gamma(x)\, r\, T(x)\, \mathrm{M}^2(x)}{2}, \tag{2.19}$$

where the specific enthalpy $h(x)$, is given by

$$h(x) = \int_{T_{\mathrm{ref}}}^{T(x)} c_p(T)\,\mathrm{d}T, \tag{2.20}$$

with $T_{\mathrm{ref}} = 298.15\,\mathrm{K}$.

Direct integration of Eqs. (2.16) and (2.17), however, is hampered by the presence of the term $(1-\mathrm{M}^2)^{-1}$, which induces numerical instabilities near the sonic position. To circumvent this difficulty, an auxiliary function, $\Phi$, is introduced:

$$\Phi = -\frac{(1-\mathrm{M}^2)}{2} - \ln(\mathrm{M}). \tag{2.21}$$

Using Eqs. (2.16) and (2.17), the evolution of $\Phi$ can be expressed as

$$\begin{aligned}\frac{\mathrm{d}\Phi}{\mathrm{d}x} = &\left(1 + \frac{(\gamma-1)\mathrm{M}^2}{2} - (\gamma-1)^2\frac{\mathrm{M}^2T\kappa}{2}\right)\frac{1}{\mathrm{A}}\frac{\mathrm{dA}}{\mathrm{d}x} \\ &- \left(\frac{(1+\gamma\mathrm{M}^2)}{2} + (\gamma-1)\frac{(1-\gamma\mathrm{M}^2)T\kappa}{2}\right)\frac{1}{c_pT}\frac{\mathrm{d}q}{\mathrm{d}x},\end{aligned} \tag{2.22}$$

where $\kappa = (\mathrm{d}c_p/\mathrm{d}T)/c_p$ is obtained analytically from Eq. (2.10). The function $\Phi$ is always positive for any Mach number M, with its minimum at the sonic condition, $\mathrm{M} = \mathrm{M}_* = 1$, where $\Phi(\mathrm{M}_*) = 0$. Furthermore, $\mathrm{d}\Phi/\mathrm{d}x$ is negative in the subsonic region and positive in the supersonic region, ensuring a consistent description across the critical throat.

With these governing equations and closure relations established, the algorithm used to tune the volumetric power source term $P_v$ can be described, as presented in Fig. 2.4. As outlined earlier, the resolution proceeds in two steps: first, the subsonic region is solved for a prescribed steady-state position $x_*$, and then the supersonic region is computed using the flow states at the critical throat as boundary conditions. For all root-finding algorithms employed in this section, the relative error is constrained to $1 \times 10^{-12}$ to ensure sufficient accuracy. In what follows, the geometry $\mathrm{A}(x)$ is considered known.

### Subsonic region

For a given steady-state thermal-throat position $x_*$, and an initial guess of the dimensionless power number $\mathcal{P}_{f,g}$, the width $\sigma$ of the heat-release profile $q(x, \sigma)$, and the critical static temperature $T_*$ are implicitly determined from Eqs. (2.18) and (2.19). This is achieved using a bisection method. Once these quantities are known, the distribution $q(x)$ is specified throughout the domain, enabling the determination of the subsonic portion of the flow.

The Mach number $\mathrm{M}(x)$, and static temperature $T(x)$ profiles are then obtained iteratively in two steps. First, at any position $x_j$, knowing the Mach number $\mathrm{M}(x_{j+1})$, and static temperature $T(x_{j+1})$, Eq. (2.22) is used to compute the value $\Phi_j = \Phi(x_j)$ with a fourth-order backward differentiation formula (BDF4) scheme. To this end, the nozzle is discretised into $n$ cells of uniform width $\Delta x$, indexed by $j \in [\![0, \dots, l-1, l, l+1, \dots, n]\!]$, with $l$ denoting the index of the critical-throat position. In the subsonic region, and $j \leq l - 4$, the scheme reads:

$$\Phi_{j-4} = \frac{1}{3}\left(12\,\Delta x\, f(x_j) - 25\,\Phi_j + 48\,\Phi_{j-1} - 36\,\Phi_{j-2} + 16\,\Phi_{j-3}\right), \tag{2.23}$$

where $f(x_j)$ denotes the right-hand side of Eq. (2.22).

Next, using Eq. (2.21), the Mach number $\mathrm{M}(x_j)$ is computed, and the static temperature $T(x_j)$ is obtained from Eq. (2.19). At each spatial location $x_j$, the convergence of $\mathrm{M}(x_j)$ and $T(x_j)$ is ensured by a bisection method. Equation (2.10) is used to compute the isentropic heat capacity ratio $\gamma$ at each position $x_j$, given the static temperature $T(x_j)$. Close to the critical-throat position, *i.e.* for $[\![l - 3 \leq j \leq l]\!]$, the order of the BDF scheme is gradually increased from first order to fourth order backward in $j$. Further details on BDF numerical schemes and their stability criteria can be found in Chapter 12.12 of Süli and Mayers [126]. The choice of this numerical method ensures both stability and accuracy in the computation of M and $T$. In cases of strong heat addition ($\mathcal{P}_f \gg 1$), low-order BDF schemes proved inefficient for computing these quantities.

Once the subsonic Mach-number profile $\mathrm{M}(x)$ is obtained, the inlet value $\mathrm{M}(x_0)$ can be compared to the prescribed inlet boundary condition $\mathrm{M}_{\mathrm{in}}$ using a scalar root function $h(\mathcal{P}_{f,g})$. The inlet guess $\mathcal{P}_{f,g}$ is then updated with the Newton–Raphson method:

$$\mathcal{P}_{f,g+1} = \mathcal{P}_{f,g} - \frac{h(\mathcal{P}_{f,g})}{h'(\mathcal{P}_{f,g})}, \tag{2.24}$$

where the derivative $h'(\mathcal{P}_{f,g})$ is approximated using a first-order explicit finite-difference scheme.

The initial guess for the dimensionless power number $\mathcal{P}_{f,g}$ is set to an order of magnitude of 1. It has been verified that the initial guess does not influence the final value of $\mathcal{P}_f$.

**Supersonic region**

Once the subsonic region is solved, the supersonic domain can be determined, *i.e.*, $j \in [\![l, n]\!]$. The critical-throat conditions, $\mathrm{M}_* = 1$ and $T_*$, are imposed as boundary conditions at $j = l$, and a fourth-order Runge-Kutta (RK4) scheme is used to integrate Eq. (2.22) as follows:

$$\Phi_{j+1} = \Phi_j + \frac{\Delta x}{6}\left(k_1 + 2k_2 + 2k_3 + k_4\right), \tag{2.25}$$

with the intermediate slopes, for all $j \geq l$, defined as

$$k_1 = f(x_j)\,, \tag{2.26}$$
$$k_2 = f\big(x_j + \tfrac{\Delta x}{2}\, k_1\big)\,, \tag{2.27}$$
$$k_3 = f\big(x_j + \tfrac{\Delta x}{2}\, k_2\big)\,, \tag{2.28}$$
$$k_4 = f(x_j + \Delta x\, k_3)\,. \tag{2.29}$$

In this context, $f(x)$ denotes the right-hand side of Eq. (2.22). The intermediate slopes are computed using a downwind Euler scheme.

Based on the Mach number M, and static temperature $T$ profiles, the other quantities ($\rho$, $u$, $p$, *etc.*) are computed using the standard relations (see Sec. 2.2). At this stage, the volumetric power source term $P_v$ is directly calculated from Eq. (2.14) using the obtained $\mathcal{P}_f$.

### 2.5.3 Validation of the heat-release rate source term model

To validate the proposed methodology implemented to thermally choke a nozzle, a reference case is considered. The dual-mode ramjet nozzle geometry described in Sec. 2.3.1 is used, and the volumetric heat source term is tuned in order to place the thermal throat at the position $x_*/L = 0.8$. The resulting steady Mach number M, and static temperature $T$ fields are then obtained from the CFD solver Sec. 2.4 and compared with the corresponding values calculated from the algorithm of Fig. 2.4. Figure 2.5 presents the comparison between the steady CFD solution and the algorithm predictions for the same heat-release rate source term $P_v$. All quantities are extracted along the symmetry axis.

A good agreement is observed between the CFD and the algorithm. The maximum absolute relative deviation in the Mach-number profile is $5 \times 10^{-4}$.

## 2.6 Equivalent geometric throat nozzle

It is important to compare the acoustic behaviour of a thermally choked nozzle with geometrical-throat configurations, which are more commonly studied in the literature [16, 22]. This comparison will make it possible to better isolate the effect of thermal choking from that of cold-gas acceleration. For this purpose, nozzles with a geometric throat are considered. These are typically convergent–divergent nozzles, known as de Laval nozzles. To enable a consistent comparison between the two types of nozzles, the Mach-number profiles are matched. The Mach number is chosen as the reference parameter, as it is the fundamental quantity characterising nozzle behaviour. This approach ensures that both nozzles exhibit the same acceleration profile.

To construct an equivalent nozzle geometry ($(\,)_{\mathrm{is}}$) that reproduces the same Mach-number evolution $\mathrm{M}(x)$, the corresponding cross-sectional area $\mathrm{A}_{\mathrm{is}}(x)$ must be determined. Several assumptions are introduced to achieve this. First, the inlet conditions given in Tab. 2.3, as well as the inlet cross-sectional area, $\mathrm{A}_{\mathrm{in}}$, are kept identical. In a geometrically-choked flow without heat addition, the static temperature decreases while the velocity increases due to flow expansion.

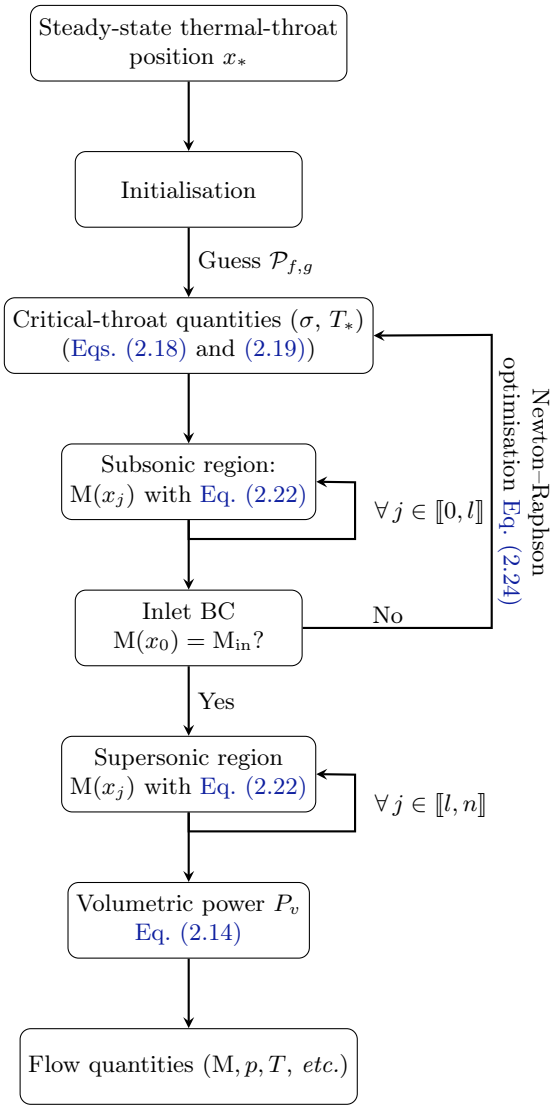


**Figure 2.4** Flowchart of the quasi-one-dimensional steady-state volumetric power algorithm used to position a thermal-throat within a divergent nozzle.

Under these conditions, the heat capacity $c_p$ does not vary significantly and can be considered nearly constant. Consequently, the heat capacity ratio $\gamma_{\mathrm{is}}$ is assumed constant in the equivalent nozzle.

Using Eq. (2.16), one obtains the relation between the thermally-choked flow and geometric-throat quantities:

$$\frac{1+\frac{\gamma_{\mathrm{is}}-1}{2}\mathrm{M}^2}{1-\mathrm{M}^2}\,\frac{1}{\mathrm{A_{is}}}\frac{\mathrm{dA_{is}}}{\mathrm{d}x} = \frac{1+\frac{\gamma-1}{2}\mathrm{M}^2}{1-\mathrm{M}^2}\,\frac{1}{\mathrm{A}}\frac{\mathrm{dA}}{\mathrm{d}x} - \frac{1+\gamma\mathrm{M}^2}{1-\mathrm{M}^2}\,\frac{1}{2c_pT}\frac{\mathrm{d}q}{\mathrm{d}x} + \frac{1}{2\gamma}\frac{\mathrm{d}\gamma}{\mathrm{d}x}. \tag{2.30}$$

For brevity, symbols without subscripts denote the thermally-choked case. By introducing the relation for the volumetric power source term,

$$\frac{\mathrm{d}q}{\mathrm{d}x} = \frac{\mathrm{A}}{\dot{m}}\,P_v, \tag{2.31}$$

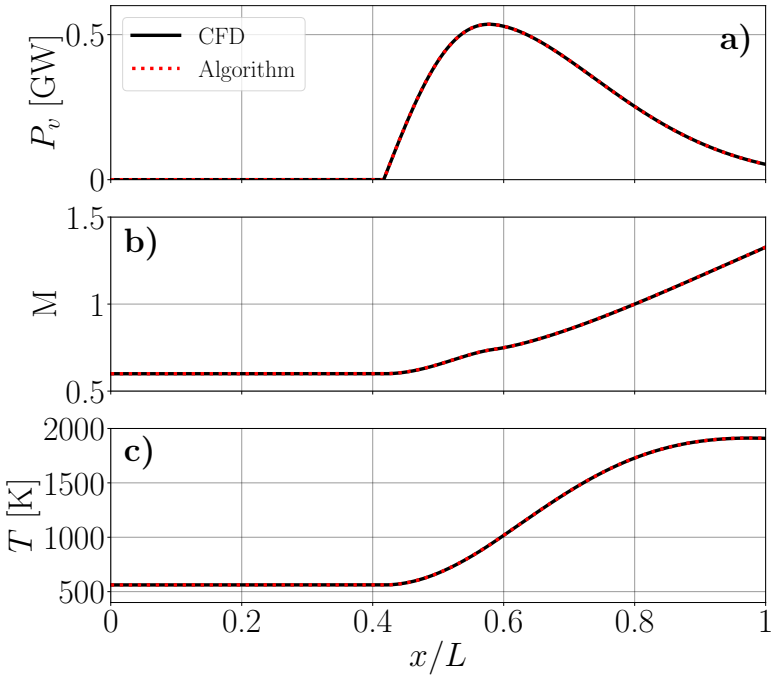


**Figure 2.5** (Colour) Comparison of results from CFD and the algorithm for the same volumetric power distribution: **(a)** Heat-release-rate source term $P_v$, **(b)** Mach number M, and **(c)** static temperature $T$.

one obtains:

$$\mathrm{A_{is}}(x) = \mathrm{A_{in}} \int_0^x \frac{2+(\gamma-1)\mathrm{M}^2}{2+(\gamma_{\mathrm{is}}-1)\mathrm{M}^2} \left[ \frac{1}{\mathrm{A}}\frac{\mathrm{dA}}{\mathrm{d}x} - \frac{\dfrac{\mathrm{A}P_v(1+\gamma\mathrm{M}^2)}{c_p T\dot{m}} - (1-\mathrm{M}^2)\,\dfrac{1}{\gamma}\dfrac{\mathrm{d}\gamma}{\mathrm{d}x}}{2+(\gamma-1)\mathrm{M}^2} \right] \mathrm{d}\xi \tag{2.32}$$

To validate the calculation of the equivalent nozzle geometry, a reference case is presented in Fig. 2.6.

The thermal-throat configuration used to generate the equivalent geometric-throat nozzle is the one described in Sec. 2.5.3. The critical-throat position (whether thermal or geometric) is set at a longitudinal location $x_*/L = 0.8$. The quantities required to construct the geometric-throat configuration are numerically extracted from the thermal-throat case along the symmetry axis. A maximum relative deviation of the Mach number obtained in the thermal and isentropic nozzles is found to be on the order of $5 \times 10^{-4}$, validating the proposed methodology. Due to the relatively high inlet Mach number, $\mathrm{M_{in}} = 0.6$, and the long subsonic section ($(x_\mathrm{u} - x_*)/L = 0.38$), the geometric contraction ratio required to choke the flow is relatively small: $y_*/y_{\mathrm{in}} = 0.84$, compared with $y_*/y_{\mathrm{in}} = 2.5$ for the thermally-choked-flow nozzle.

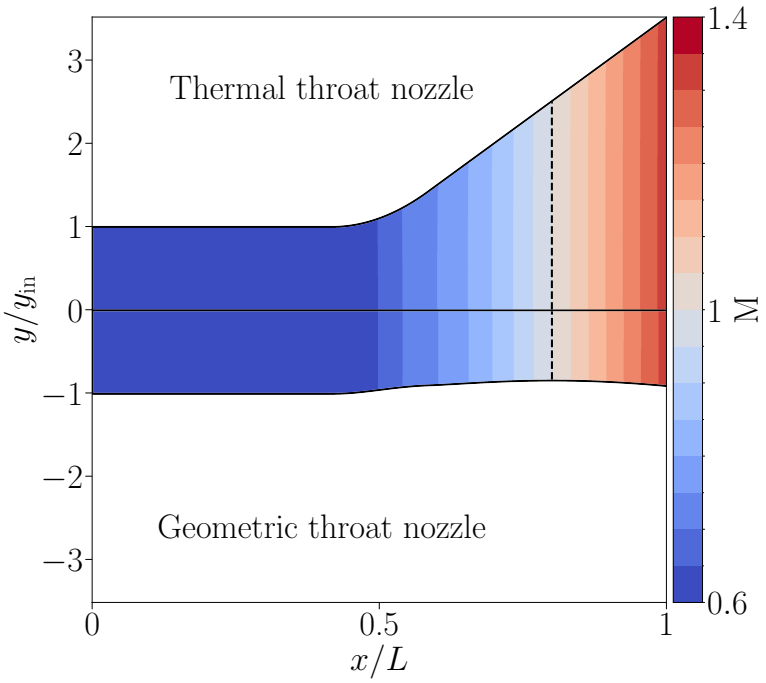


**Figure 2.6** (Colour) Two-dimensional steady-state Mach number field M for the thermal-throat (top) and geometric-throat (bottom) choking cases obtained with the CFD solver. The sonic line is indicated (**- - -**).

### Chapter conclusion

This chapter has established the methodological and numerical foundation of the present work. The modelling approach relies on a low-order framework designed to capture the key physical mechanisms governing the aeroacoustic response of thermally choked flows, while remaining computationally efficient and conceptually transparent.

The Euler equations were selected to describe the inviscid flow, neglecting viscous and diffusive effects that have a minor influence on the global acoustic behaviour. Air was modelled as an ideal gas with temperature-dependent specific heats, ensuring that thermodynamic variations induced by heat addition are accurately represented. A steady, spatially non-uniform volumetric power source was introduced to mimic the distributed heat release typical of dual-mode ramjet combustion, leading to the formation of a thermal throat.

A simplified dual-mode ramjet geometry derived from the JAPHAR experiments was implemented in the CFD solver CEDRE, together with a set of consistent boundary conditions enabling both acoustic and entropy forcing. The model describing the spatial distribution of the volumetric heat source was formulated and validated through a quasi-one-dimensional steady-state algorithm, demonstrating good agreement with numerical simulations. Furthermore, an equivalent geometric-throat nozzle was constructed based on the matching of Mach-number profiles, ensuring that the two choking mechanisms, thermal and geometric, could be directly compared under identical flow conditions.

In summary, this chapter provides the complete numerical and theoretical framework required to investigate the linear aeroacoustic response of thermally choked configurations. The next chapter builds upon this foundation to characterise the scattering of one-dimensional acoustic and entropy waves in both thermal- and geometric-throat nozzles, thereby quantifying the mechanisms that govern indirect combustion noise generation.

Chapter 3

# Linear aeroacoustic response of a thermally choked-flow nozzle to acoustic and entropy plane waves

*On a beau expliquer tout ce qu'on veut expliquer,*
*au bout d'un moment, pour savoir faire du cheval, il faut faire du cheval !*

**Genièvre [2]**


## Abstract

In this chapter, the linear aeroacoustic response of a thermally choked-flow nozzle representative of a dual-mode ramjet is numerically and analytically characterised. The study focuses on the reflection, transmission, and entropy–noise–production coefficients, as well as on the definition of an appropriate acoustic boundary condition at the thermal throat. Six different choking configurations are examined, combining geometric and thermal choking mechanisms with various heat-release distributions and lengths.

Results show that, at low frequencies, thermal choking substantially reduces the acoustic-reflection coefficient compared with an equivalent geometric throat. This attenuation originates from the conversion of acoustic fluctuations into entropy fluctuations within the heated region, governed by the static temperature gradient. The entropy–noise–production coefficient remains comparable to that of an isentropic nozzle, indicating that the steady acceleration of entropy perturbations dominates over heat addition effects. At high frequencies, all choking configurations asymptotically converge toward an isentropic simple-wave radiation regime.

Finally, the classical assumption of vanishing Mach-number fluctuations at the critical throat ($M'_* = 0$) is revisited and shown to hold only for isentropic nozzles. In thermally choked flows, finite Mach-number fluctuations persist, reflecting the complex coupling between acoustic and entropy waves at the thermal throat. These results provide a robust foundation for the development of a quasi-one-dimensional analytical model of thermoacoustic coupling in the next chapter.


This chapter is a truncation of the following publication, published during the PhD:

F. Olivon, A. Genot, J.-E. Durand, A. Hirschberg, and E. Piot. "On the linear aeroacoustic response of a thermally-choked-flow nozzle to acoustic and entropy plane waves". In: *Journal of Sound and Vibration* 626 (2026), 119619. ISSN: 0022-460X. DOI: 10.1016/j.jsv.2025.119619.

## Contents

**3.1 Objective** . . . . . **38**
**3.2 Methodology** . . . . . **39**
3.2.1 Presentation of choking configuration cases . . . . . 39
3.2.2 Steady-state volumetric power distribution . . . . . 39
3.2.3 Linear acoustics forcing at the inlet . . . . . 41
3.2.4 Computational setup . . . . . 42
**3.3 Aeroacoustic coefficients** . . . . . **43**
3.3.1 Quasi-steady limit model for reflection coefficients . . . . . 45
**3.4 Aeroacoustic response of a thermally-choked-flow nozzle** . . . . . **47**
3.4.1 Steady-state flow fields . . . . . 47
3.4.2 Acoustic-reflection coefficient . . . . . 49
3.4.3 Acoustic-transmission coefficients . . . . . 50
3.4.4 Effect of the heat-release length on the acoustic-reflection coefficient . 53
3.4.5 Entropy-noise coefficients . . . . . 54
**3.5 Critical-throat acoustic boundary condition** . . . . . **57**

## 3.1 Objective

Combustion instabilities, and in particular thermoacoustic instabilities in thermally-choked-flow nozzles, are directly linked to the propagation of acoustic and entropy waves under such complex flow conditions. Although several studies have examined the propagation of acoustic and entropy waves through heated media [28, 95, 96], none has specifically addressed heat addition as the primary choking mechanism.

To bridge this gap, it is essential to investigate the transfer functions governing wave propagation in these systems. The acoustic-reflection and entropy-noise-production coefficients, defined as the ratios of upstream to downstream-propagating acoustic waves, and of upstream acoustic to downstream-propagating entropy waves, respectively, together with the acoustic-transmission and entropy-noise-transmission coefficients, provide key metrics for characterising the system response. These coefficients are central to understanding and predicting thermoacoustic instabilities in propulsion systems featuring a thermal throat. In this study, the volumetric power is prescribed as steady, serving as a first step before introducing additional complexities to the flow.

The objective of this chapter is to numerically and analytically characterise the aeroacoustic response of a thermally-choked nozzle: to quantify the acoustic-reflection, acoustic-transmission, entropy-noise-production, and entropy-noise-transmission coefficients, and to identify the appropriate boundary condition at the thermal throat induced by steady volumetric power distribution in the linear acoustic regime.

## 3.2 Methodology

The simplified dual-mode ramjet nozzle geometry described in Sec. 2.3.1, together with the inlet conditions specified in Sec. 2.3.2, are used in this chapter.

### 3.2.1 Presentation of choking configuration cases

To investigate the impact of a thermal throat on the acoustic field, several choking configurations are tested, as summarised in Tab. 3.1. The acoustic response of these configurations, labelled $\mathrm{C}_i$ ($i = 1$–$6$), is evaluated by numerically solving the Euler equations (Eq. (2.3)). These configurations were selected to encompass a wide range of thermally-choked-flow conditions. Four of them ($\mathrm{C}_{1-4}$) share the same heat-release rate length, $\delta_* = 0.38$, but differ in nozzle geometry (constant or divergent duct) and in the heat-release rate distribution (uniform or non-uniform), resulting in distinct total heat addition required to choke the flow.

To isolate the effect of thermal choking on the acoustic response, an isentropic geometric-throat case $\mathrm{C}_2$ is also considered. This nozzle was designed to reproduce exactly the same Mach-number profile as the thermally choked case $\mathrm{C}_1$ (see Sec. 2.6). In addition, to assess the impact of the heat-release rate length, two further cases ($\mathrm{C}_{5,6}$) are included. These configurations have the same normalised flame-power number ($\mathcal{P}_f$, Eq. (3.1)) as $\mathrm{C}_1$ but differ in their heat-release rate length $\delta_*$.

To compare the choking configurations, the following normalised flame-power number $\mathcal{P}_f$ is used to characterise the flame power addition relative to the inlet convective flow of thermal energy:

$$\mathcal{P}_f = \frac{1}{c_{p,\mathrm{in}} T_{\mathrm{in}} \dot{m}_{\mathrm{in}}} \int_{x_\mathrm{u}}^{x_*} \mathrm{A}(\xi) P_v(\xi)\, \mathrm{d}\xi. \tag{3.1}$$

Here, $x_\mathrm{u}$ denotes the beginning of the heat-addition region $P_v$ and $x_*$ the sonic position, which defines the heat-release rate length, $\delta_* = x_* - x_\mathrm{u}$.

**Table 3.1** Presentation of the different choking configurations.

| Configuration | Duct | Heat-release profile | Heat-release length | Normalised power $\mathcal{P}_f$ |
|---|---|---|---|---|
| $\mathrm{C}_1$ (Sec. 3.2.2) | Divergent | Non-uniform | $\delta_*/L = 0.38$ | $\mathcal{P}_f = 2.8$ |
| $\mathrm{C}_2$ (Sec. 2.6) | Convergent–Divergent | Isentropic | same $\mathrm{M}(x)$ as $\mathrm{C}_1$ | $\mathcal{P}_f = 0$ |
| $\mathrm{C}_3$ (Sec. 3.2.2) | Divergent | Uniform | $\delta_*/L = 0.38$ | $\mathcal{P}_f = 2.53$ |
| $\mathrm{C}_4$ (Sec. 3.2.2) | Constant | Uniform | $\delta_*/L = 0.38$ | $\mathcal{P}_f = 0.25$ |
| $\mathrm{C}_5$ (Sec. 3.2.2) | Divergent | Non-uniform | $\delta_*/L = 0.32$ | $\mathcal{P}_f = 2.81$ |
| $\mathrm{C}_6$ (Sec. 3.2.2) | Divergent | Non-uniform | $\delta_*/L = 0.44$ | $\mathcal{P}_f = 2.79$ |

The procedure used to obtain the isentropic nozzle geometry with the same Mach-number profile has already been detailed in Sec. 2.6. This method is applied to the $\mathrm{C}_1$ configuration to derive the $\mathrm{C}_2$ choking case.

### 3.2.2 Steady-state volumetric power distribution

A steady-state quasi-one-dimensional volumetric power distribution $P_v(x)$ is prescribed to establish a thermal throat at a specified position within the nozzle. This heat-release rate profile

represents a steady flame, supplying a constant power per unit volume to the flow. To assess its impact on the acoustic behaviour of the nozzle, five steady configurations of the thermal throat are considered: two located deep within the divergent-duct section, three with non-uniform volumetric heat-release rate distribution (as introduced in Sec. 2.5) using different heat-release rate lengths, and one with a uniform power distribution. In addition, one configuration places the thermal throat in the transition section, just downstream of the constant cross-section duct (see Fig. 2.2), also with uniform volumetric power distribution. The corresponding three models for the volumetric power $P_v(x)$ are detailed below.

### $C_{1,5,6}$ - Non-uniform heat-release rate profile for a divergent-duct nozzle

The model used to thermally choke the flow in a divergent duct with non-uniform heat release, as proposed by Wang *et al.* [123], has already been described in Sec. 2.5. Here, only the parameters used to tune the volumetric power source term are detailed.

The spatial distribution of $P_v$ is divided into two regions. In the straight duct (Fig. 2.2), the flow is unheated and $P_v = 0$. In the divergent duct ($x > x_\mathrm{u}$), the volumetric power distribution $P_v$ follows a log-normal profile function in $x$, as proposed by Wang *et al.* [123] and explained in Sec. 3.2.2.

The model is adjusted so that the steady-state thermal throat forms at $x_*/L = 0.8$, corresponding to a flame length of $(x_* - x_\mathrm{u})/L = \delta_*/L = 0.38$. This position was chosen to match the mean spatial location of the thermal throat in *Case C4* of the JAPHAR study by Dessornes and Scherrer [5].

To obtain the two other thermal-throat configurations $C_5$ and $C_6$, the same model is used with the same dimensionless power number $\mathcal{P}_f$, but with a different heat-release rate width $\sigma$ (see Sec. 2.5). This ensures that the total power added to the subsonic region of the flow remains the same ($\mathcal{P}_f \approx 2.8$).

### $C_3$ - Uniform heat-release rate profile for a divergent-duct nozzle

For the $C_3$ configuration, using the critical-throat relation from Heiser *et al.* [4], and assuming a constant heat capacity ratio $\gamma$ together with a uniform volumetric power addition $P_v$ in the subsonic region, the following expression holds at the critical-throat position:

$$\frac{1}{\mathrm{A}_*^2}\left.\frac{\mathrm{dA}}{\mathrm{d}x}\right|_* = \frac{\gamma - 1}{\gamma r T_*}\frac{P_v}{\dot{m}}. \tag{3.2}$$

In addition, conservation of total enthalpy gives:

$$T_{0,*} - T_{0,\mathrm{in}} = \frac{P_v}{c_p \dot{m}} \int_{x_\mathrm{in}}^{x_*} \mathrm{A}(\xi)\,\mathrm{d}\xi. \tag{3.3}$$

Combining these two relations yields:

$$\frac{1}{\mathrm{A}_*^2}\left.\frac{\mathrm{dA}}{\mathrm{d}x}\right|_* \int_{x_\mathrm{in}}^{x_*} \mathrm{A}(\xi)\,\mathrm{d}\xi = \frac{\gamma + 1}{2}\frac{P_v}{P_v + \dot{m} c_p T_{0,\mathrm{in}}}. \tag{3.4}$$

Solving for $P_v$ leads to the final expression:

$$P_v = \frac{\dot{m} c_p T_{0,\mathrm{in}} \dfrac{1}{\mathrm{A}_*^2}\left.\dfrac{\mathrm{dA}}{\mathrm{d}x}\right|_*}{\dfrac{\gamma + 1}{2} - \dfrac{1}{\mathrm{A}_*^2}\left.\dfrac{\mathrm{dA}}{\mathrm{d}x}\right|_* \displaystyle\int_{x_\mathrm{u}}^{x_*} \mathrm{A}(\xi)\,\mathrm{d}\xi}. \tag{3.5}$$

In the supersonic region, $x > x_*$, the volumetric power $P_v$ is progressively decreased (*i.e.*, $P_v \propto 1/\mathrm{A}$), following an inverse proportionality to the cross-sectional area.

In the numerical simulations, the uniform heat-release rate $P_v$ was calculated using Eq. (3.5) with a non-dimensional flame length of $\delta_*/L = (x_* - x_\mathrm{u})/L = 0.38$, corresponding to the flame length, $\delta_* = x_* - x_\mathrm{u}$, upstream of the thermal throat in the Wang-flame model ($\mathrm{C}_1$). The uniform heat-release rate profile was applied downstream of $x_\mathrm{u}/L = 0.42$, yielding a thermal throat in the divergent section at $x_*/L = 0.8$.

#### $\mathrm{C}_4$ - Uniform heat-release rate profile for a straight-duct nozzle

For the $\mathrm{C}_4$ configuration, the integral total energy conservation law for a perfect gas, as detailed by Shapiro [125], yields:

$$T_* \left( \frac{\gamma + 1}{2} \right) = c_p T_\mathrm{in} \left( 1 + \frac{\gamma - 1}{2} \mathrm{M}_\mathrm{in}^2 \right) + q_*. \tag{3.6}$$

In the constant cross-section duct, the volumetric power is given by:

$$P_v = \frac{\dot{m}}{\mathrm{A}\delta_*} q_*, \tag{3.7}$$

which leads to the final expression for the uniform volumetric heat-release rate $P_v$ required to generate a thermal throat at the outlet of the straight duct:

$$P_v = \frac{\dot{m}}{\mathrm{A}\delta_*} c_p T_{0,\mathrm{in}} \left( \frac{1}{2(\gamma+1)\mathrm{M}_\mathrm{in}^2} \frac{(1 + \gamma \mathrm{M}_\mathrm{in}^2)^2}{1 + \dfrac{\gamma - 1}{2} \mathrm{M}_\mathrm{in}^2} - 1 \right). \tag{3.8}$$

Since the duct cross-sectional area A is constant, the volumetric heat addition is uniform within the straight section. For $x > x_*$, the volumetric power $P_v$ gradually decreases in the supersonic region as the duct area increases ($P_v \propto 1/\mathrm{A}$). In the numerical model, the uniform volumetric heat-release rate was calculated using Eq. (3.8) with a flame length $\delta_*/L = 0.38$, equal to the length, $\delta_* = x_* - x_\mathrm{u}$, in the Wang-flame model ($\mathrm{C}_1$). The uniform heat-release rate was applied for $x/L \geq 0.06$, and a thermal throat was obtained in the transition section at $x_*/L = 0.44$.

#### Resulting volumetric source terms

Figure 3.1 shows the steady-state volumetric power distribution $P_v$ added as a source term to the Euler equations (Eq. (2.3)) to thermally choke the different configurations. For the isentropic nozzle configuration $\mathrm{C}_2$, where choking is achieved through geometric contraction, no heat addition is required and therefore $P_v = 0$.

### 3.2.3 Linear acoustics forcing at the inlet

Once the steady-state flow field is established, perturbations are introduced into the system. To this end, a uniform mono-harmonic forcing of frequency $\omega = 2\pi f$ is applied at the inlet boundary ($x = 0$). The type of inlet forcing depends on whether the acoustic or entropy-noise coefficient is being evaluated, as previously described in Sec. 2.4.2. The corresponding fluctuation functions are defined below. For isentropic acoustic forcing:

$$p'_\mathrm{in}(t) = \eta \, \bar{p}_\mathrm{in} \sin(\omega t), \tag{3.9}$$

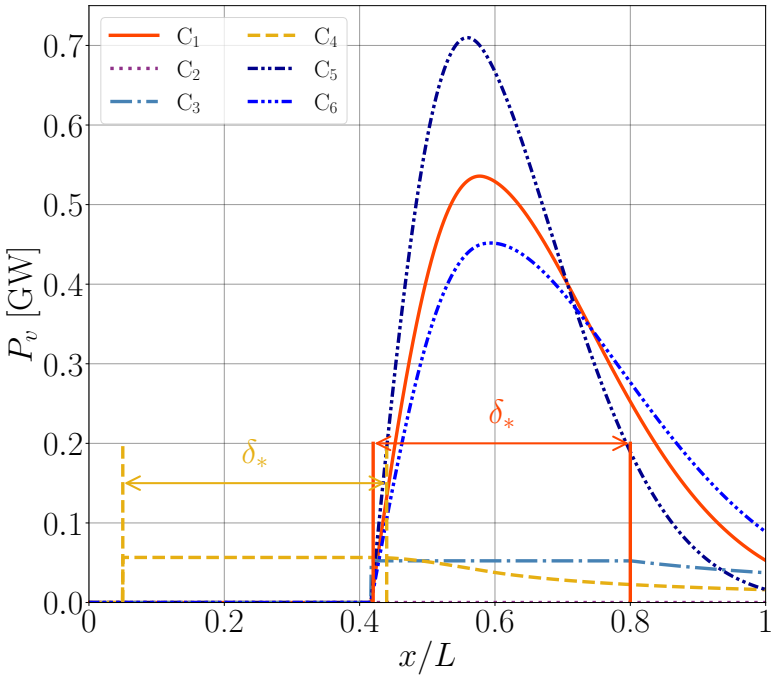


**Figure 3.1** (Colour) Volumetric power source term $P_v$ as a function of the longitudinal coordinate $x/L$ for the different choking configurations considered: $\mathrm{C}_{1-6}$.

and for entropy forcing:

$$T'_{\mathrm{in}}(t) = \eta\, \bar{T}_{\mathrm{in}} \sin(\omega t). \tag{3.10}$$

It is noteworthy that, by imposing constant pressure at the inlet, downstream-propagating acoustic waves are implicitly added to cancel the upstream-propagating waves generated by the passage of entropy fluctuations. As a result, the upstream acoustic field consists of a superposition of reflected downstream-propagating waves and additional waves generated by entropy–acoustic interactions within the nozzle. This effect is accounted for during post-processing when evaluating the entropy-noise-production coefficient $R_s$. For consistency, the forcing amplitude $\eta$ is selected such that $p'_{\mathrm{in}}/(\bar{\gamma}_{\mathrm{in}}\bar{p}_{\mathrm{in}}) = 1\,\%$, and $s'_{\mathrm{in}}/\bar{c}_{p,\mathrm{in}} = 1\,\%$.

In this study, a mono-harmonic forcing signal is used to facilitate the characterization of the acoustic response. However, other types of excitation could be employed, such as a multi-harmonic forcing, *i.e.*, a single temporal signal that excites a broad frequency spectrum. This approach was used by Olivon *et al.* [127], where a Ricker wavelet [128, 129] was employed to characterize the acoustic-reflection coefficient $R_a$ in a multi-harmonic manner. This signal has the advantage that its expressions in both the time and frequency domains are known analytically[1]. In practice, however, this multi-harmonic approach can be sensitive to numerical uncertainties, in particular those associated with the finite time window used in the simulations, which may affect the accurate characterization of the acoustic coefficients.

### 3.2.4 Computational setup

The numerical simulations are performed using the ONERA unstructured CFD code CEDRE (see Sec. 2.4), which solves the two-dimensional Euler equations (Eq. (2.3)). The numerical

[1] In the time domain, the Ricker wavelet [128] has the following expression: $p_{\mathrm{in}}(t) = \bar{p}_{\mathrm{in}} + \eta\,\bar{p}_{\mathrm{in}}(1 - \frac{\omega_m^2}{2}\,t^2)\exp(-\frac{\omega_m^2}{4}\,t^2)$.

schemes have already been described in Sec. 2.4.

The computational setup for the thermally-choked-flow nozzle ($C_{1,3-6}$) consists of a two-dimensional planar domain, as described in Sec. 2.3.1, discretized with 60 000 computational cells of size $\Delta x/L = 4 \times 10^{-4}$ (see Fig. 2.2). This resolution provides adequate spatial discretization of acoustic waves, ensuring at least 100 points per wavelength for frequencies up to $f = 6000\,\mathrm{Hz}$. Since the flow is primarily longitudinal, the same discretization ($\Delta x \simeq \Delta y$) is applied in both the longitudinal and transverse directions, resulting in 2400 points along the longitudinal axis and 25 points along the transverse axis.

Temporal integration is performed using a time step of $\Delta t = 1 \times 10^{-6}\,\mathrm{s}$, yielding a Courant-Friedrichs-Lewy (CFL) number of $(u_{\mathrm{in}} + c_{\mathrm{in}})\Delta t/\Delta x = 0.75$. The unsteady solutions corresponding to acoustic forcing, as described in Sec. 3.2.3, are obtained using a modulated post-processing time step based on the inlet forcing frequency. To ensure accurate spectral analysis, 75 periods are simulated, and 100 points per period are stored. A Fast Fourier Transform (FFT) is then applied to the last 35 periods to eliminate transient effects. For the geometric-throat configuration $C_2$ (see Sec. 2.6), the same numerical parameters are used, ensuring mesh and time-step independence.

The potential influence of computational resolution, both spatial and temporal, was assessed by varying the mesh size and the time step. The impact of these variations is evaluated using the normalised pressure fluctuations, which constitute the primary quantity of interest in this acoustic study:

$$\tilde{\varphi} = \frac{1}{V\tau} \int_{\tau} \int_{V} \left( \frac{p'}{\bar{\gamma}\bar{p}} \right) \mathrm{d}V\, \mathrm{d}\tau, \tag{3.11}$$

where $\tau$ is the total simulation time, and $V$ denotes the volume of the computational domain. A temporal and volumetric integration over the entire domain was performed at each time step to evaluate the normalised pressure fluctuations $p'/(\bar{\gamma}\bar{p})$.

Four computational grids and four time-step values were investigated. The mesh size $\Delta x$ was varied from 0.5 mm (235 000 grid points) to 4 mm (4000 grid points), while the time step $\Delta t$ ranged from $1 \times 10^{-7}\,\mathrm{s}$ to $5 \times 10^{-6}\,\mathrm{s}$.

The absolute relative error in the global normalised pressure fluctuations, defined as $|(\tilde{\varphi} - \tilde{\varphi}_{\mathrm{ref}})/\tilde{\varphi}_{\mathrm{ref}}|$ was evaluated for a forcing frequency of $f = 6000\,\mathrm{Hz}$, using the finest refinement $(\Delta x, \Delta t)_{\mathrm{ref}} = (0.5\,\mathrm{mm}, 1 \times 10^{-7}\,\mathrm{s})$ as the reference solution $\tilde{\varphi}_{\mathrm{ref}}$. The results, detailed Fig. 3.2, indicate that normalised pressure fluctuations become independent of spatial resolution for mesh sizes smaller than $\Delta x = 1\,\mathrm{mm}$.

Consequently, the mesh size and time step adopted for the present study, $(\Delta x, \Delta t) = (1\,\mathrm{mm}, 1 \times 10^{-6}\,\mathrm{s})$, corresponding to a CFL number of $(u_{\mathrm{in}} + c_{\mathrm{in}})\Delta t/\Delta x = 0.75$, represent the best compromise between numerical accuracy and computational cost. With this configuration, the absolute relative error remains below $1 \times 10^{-3}$ compared with the finest refinement.

To validate the linear acoustic response of the flow, simulations were performed with an acoustic forcing at the same frequency ($f = 6000\,\mathrm{Hz}$) and two forcing amplitudes of 1 % and 0.1 %. The resulting acoustic-reflection coefficients differed by less than $1 \times 10^{-3}$, thereby confirming the validity of the linear acoustics assumption.

## 3.3 Aeroacoustic coefficients

The acoustic and entropy-noise coefficients are determined in post-processing from the numerical simulations using the inlet boundary conditions described in Sec. 3.2.3. Figure 3.3 illustrates the wave decomposition in a thermally-choked-flow configuration, distinguishing downstream-propagating acoustic waves ($P^+$), upstream-propagating acoustic waves ($P^-$), and downstream-propagating entropy waves ($\sigma$). The same methodology is applicable to other choking config-

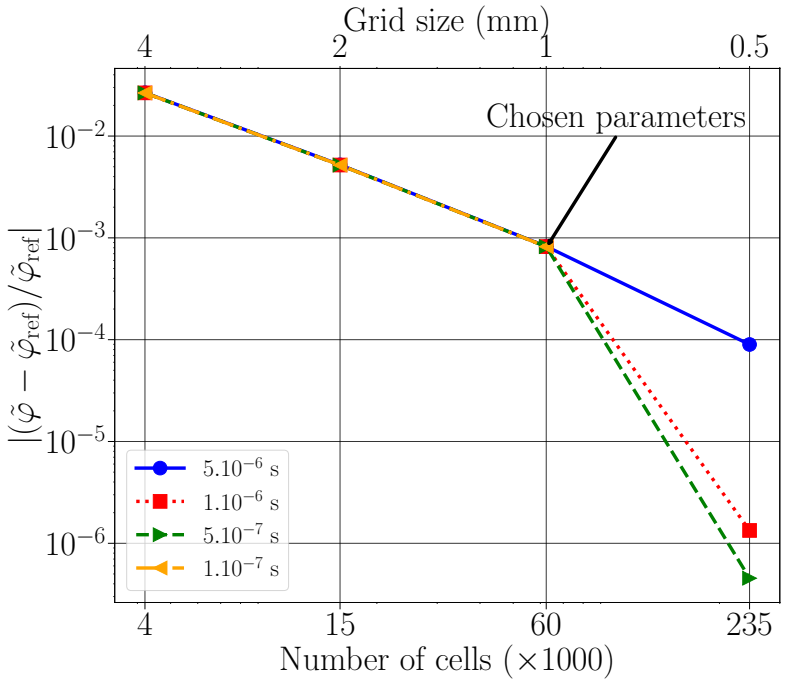


**Figure 3.2** (Colour) Absolute relative error of the global normalised pressure fluctuations $|(\tilde{\varphi} - \tilde{\varphi}_{\mathrm{ref}})/\tilde{\varphi}_{\mathrm{ref}}|$ as a function of mesh size and time-step refinement.

urations. All quantities are extracted along the nozzle symmetry axis at locations where the steady-state flow field is uniform, thereby ensuring the validity of the wave decomposition.

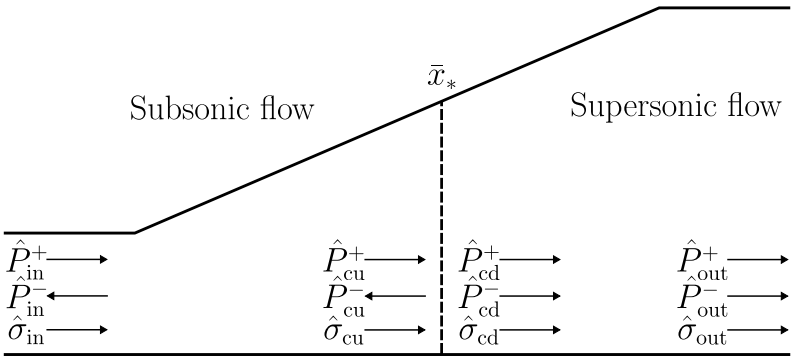


**Figure 3.3** Sketch of the decomposition of mono-harmonic downstream- and upstream-propagating acoustic waves and entropy waves in a thermally-choked-flow configuration. The subscripts $(_{\mathrm{cu}})$ and $(_{\mathrm{cd}})$ denote quantities evaluated immediately upstream and downstream of the critical throat position, respectively, where $\mathrm{M}(\bar{x}_*) = 1$.

In a uniform flow region, the acoustic pressure $P = p'/(\bar{\gamma}\bar{p})$, and velocity $U = u'/\bar{u}$ fields can be decomposed into downstream- $\hat{P}^+$ and upstream-propagating $\hat{P}^-$ wave components using the following relations:

$$\hat{P}^{\pm} = \frac{1}{2}\left(\hat{P} \pm \bar{\mathrm{M}}\,\hat{U}\right), \tag{3.12}$$

where $\bar{\mathrm{M}} = \bar{u}/\bar{c}$ is the steady Mach number, and $\hat{P}$ and $\hat{U}$ are the Fourier-transformed pressure and velocity fluctuations, respectively. It will be assumed that such a uniform region exists upstream and downstream of the nozzle (at the inlet and at the outlet). The algebra to obtain

such wave decomposition is detailed Appendix A.

Table 3.2 summarises the aeroacoustic coefficients used to characterise the acoustic behaviour of thermally-choked-flow nozzles. These coefficients can be separated into two categories depending on the nature of the inlet forcing.

When an isentropic acoustic forcing is applied, the acoustic-reflection coefficient $R_a$ quantifies the ratio of upstream- to downstream-propagating acoustic waves at the inlet, while the acoustic-transmission coefficient $T_a$ describes the ratio of downstream-propagating acoustic waves between the outlet and the inlet. As acoustic waves propagate through a heated medium, entropy waves may also be generated [95]; this effect is measured by the entropy-noise-production coefficient $G_s$ defined as the ratio of critical entropy waves to inlet downstream-propagating acoustic waves.

Conversely, when an entropy forcing is applied at the inlet, the entropy-noise-production coefficient $R_s$ characterises the ratio of the upstream-propagating acoustic wave to the inlet entropy wave, while the entropy-noise-transmission coefficient $T_s$ is defined as the ratio of the downstream-propagating acoustic wave at the outlet to the inlet entropy wave.

**Table 3.2** Presentation of the different aero-acoustic coefficients.

| Name of the coefficient | Coefficient | Relation |
|---|---|---|
| Acoustic-reflection | $R_a$ | $\hat{P}^-_{\text{in}}/\hat{P}^+_{\text{in}}$ |
| Acoustic-transmission | $T_a$ | $\hat{P}^+_{\text{out}}/\hat{P}^+_{\text{in}}$ |
| Critical-entropy-production | $G_s$ | $\hat{\sigma}_*/\hat{P}^+_{\text{in}}$ |
| Entropy-noise-production | $R_s$ | $(\hat{P}^-_{\text{in}} - R_a\hat{P}^+_{\text{in}})/\hat{\sigma}_{\text{in}}$ |
| Entropy-noise-transmission | $T_s$ | $\hat{P}^+_{\text{out}}/\hat{\sigma}_{\text{in}}$ |

For the entropy-noise-production coefficient $R_s$ the downstream-propagating acoustic component $\hat{P}^+$ must be considered owing to the entropy-forcing methodology (Sec. 3.2.3). Nevertheless, the amplitude of the injected acoustic wave $\hat{P}^+$ was found to be at least two orders of magnitude smaller than that of the downstream-propagating entropy wave $\hat{\sigma}$.

### 3.3.1 Quasi-steady limit model for reflection coefficients

The quasi-steady-state (QSS) limit of the reflection coefficients ($R_a$ and $R_s$) is of particular interest and can be determined analytically for a perfect-gas flow in a straight duct with a thermal throat located at the downstream end. This limit is reached when the forcing frequency $f$ tends to zero (*i.e.*, $f \to 0$). In this case, the formulation is equivalent to neglecting the temporal term (*i.e.*, $\partial/\partial t = 0$) in the Euler equations (Eq. (2.3)). A quasi-steady model for this configuration is proposed here.

The analytical formulation assumes ideal-gas behaviour, with constant specific heat at constant pressure $c_p$ and constant heat capacity ratio $\gamma$. A steady volumetric heat addition $P_v$ is imposed in a constant cross-sectional area duct, and only longitudinal quantities are considered. The steady-state integral form of the Euler equations between the inlet $(\,)_{\text{in}}$ and the steady critical-throat position $(\,)_*$ is given, following Anderson [130]:

$$\begin{cases} \rho_* u_* = \rho_{\text{in}} u_{\text{in}}, \\ p_* + \rho_* u_*^2 = p_{\text{in}} + \rho_{\text{in}} u_{\text{in}}^2, \\ c_p \left(T_{0,*} - T_{0,\text{in}}\right) = \dfrac{1}{\rho_{\text{in}} u_{\text{in}}} \displaystyle\int_{x_{\text{in}}}^{x_*} P_v(\xi)\, \mathrm{d}\xi, \end{cases} \tag{3.13}$$

where $\rho$ is the density, $u$ the longitudinal velocity, $p$ the static pressure, $T_0$ the total temperature, and $P_v$ the steady volumetric heat addition.

From these relations, the quasi-steady acoustic response at the thermal throat can be evaluated, allowing closed-form expressions of the reflection coefficients $R_a$ and $R_s$ to be derived.

Using the mass and momentum equations, the following relation between the sonic and inlet static temperatures is obtained:

$$\frac{T_*}{T_{\text{in}}} = \frac{1}{\mathrm{M}_{\text{in}}^2} \frac{\left(1+\gamma \mathrm{M}_{\text{in}}^2\right)^2}{(\gamma+1)^2}. \tag{3.14}$$

From the energy equation, one obtains:

$$\frac{T_*}{T_{\text{in}}} = \left( \frac{\displaystyle\int_{x_{\text{in}}}^{x_*} P_v(\xi)\,\mathrm{d}\xi}{c_p T_{\text{in}} \rho_{\text{in}} u_{\text{in}}} + 1 + \frac{\gamma-1}{2}\mathrm{M}_{\text{in}}^2 \right) \frac{2}{\gamma+1}. \tag{3.15}$$

Combining Eqs. (3.14) and (3.15) gives:

$$\mathcal{P}_f = \frac{1}{2\mathrm{M}_{\text{in}}^2} \frac{\left(1+\gamma \mathrm{M}_{\text{in}}^2\right)^2}{\gamma+1} - \left(1 + \frac{\gamma-1}{2}\mathrm{M}_{\text{in}}^2\right), \tag{3.16}$$

where $\mathcal{P}_f = \displaystyle\int_{x_{\text{in}}}^{x_*} P_v(\xi)\,\mathrm{d}\xi \,/\, (c_p T_{\text{in}} \rho_{\text{in}} u_{\text{in}})$ denotes the dimensionless power number[2], which quantifies the flame power added to the flow relative to the initial convective flux of heat.

Equation (3.16) highlights that the required energy addition to establish a thermal throat depends strongly on the inlet Mach number $\mathrm{M}_{\text{in}}$ and the heat capacity ratio $\gamma$. In particular, $\mathcal{P}_f$ decreases with increasing $\mathrm{M}_{\text{in}}$, indicating that higher inlet kinetic energies require proportionally less heat addition to achieve choking. Conversely, at low subsonic Mach numbers, the energy requirement becomes relatively significant. This relation therefore provides a compact criterion for predicting the thermal energy necessary to induce choking under given inlet conditions.

To determine the reflection coefficients, Eq. (3.16) is linearised following the convention $\chi = \bar{\chi} + \chi'$, where $(\,)'$ denotes a fluctuating quantity and $\bar{(\,)}$ denotes the corresponding steady-state value, with $\chi = [p_{\text{in}}, T_{\text{in}}, \rho_{\text{in}}, u_{\text{in}}, \mathrm{M}_{\text{in}}]$. It is further assumed that, in the quasi-steady limit, the Mach-number fluctuations at the critical throat (at the end of the tube) vanish, *i.e.*, $\mathrm{M}'_* = 0$. Neglecting second-order terms, the following relation is obtained:

$$\bar{\mathcal{P}}_f \left( \frac{p'_{\text{in}}}{\bar{p}_{\text{in}}} + \frac{u'_{\text{in}}}{\bar{u}_{\text{in}}} \right) = \frac{\mathrm{M}'_{\text{in}}}{\bar{\mathrm{M}}_{\text{in}}} \Gamma_{\text{in}}, \tag{3.17}$$

with $\Gamma_{\text{in}} = (1 - \bar{\mathrm{M}}_{\text{in}}^4)/(\bar{\mathrm{M}}_{\text{in}}^2(\gamma+1))$.

It is noteworthy that Eq. (3.17) explicitly shows that, even under quasi-steady conditions, Mach-number fluctuations may arise as a result of heat release. This constitutes a clear departure from the quasi-steady assumption of Marble and Candel [16], as later formalised by Duran and Moreau [22].

Rewriting the normalised Mach-number fluctuations $\mathrm{M}'_{\text{in}}/\bar{\mathrm{M}}_{\text{in}}$, in terms of the natural variables $p'_{\text{in}}/(\gamma \bar{p}_{\text{in}})$, $u'_{\text{in}}/\bar{u}_{\text{in}}$, and the normalised entropy fluctuation $\sigma_{\text{in}} = s'_{\text{in}}/c_p$, leads to

$$\frac{p'_{\text{in}}}{\gamma \bar{p}_{\text{in}}} \left( \frac{\gamma-1}{2} \bar{\mathrm{M}}_{\text{in}} \left( 1 + \frac{2\gamma}{\gamma-1} \frac{\bar{\mathcal{P}}_f}{\Gamma_{\text{in}}} \right) \right) - \bar{\mathrm{M}}_{\text{in}} \frac{u'_{\text{in}}}{\bar{u}_{\text{in}}} \left( 1 + \frac{\bar{\mathcal{P}}_f}{\Gamma_{\text{in}}} \right) + \frac{\bar{\mathrm{M}}_{\text{in}}}{2} \sigma_{\text{in}} = 0. \tag{3.18}$$

[2]This formulation is identical to that presented in Eq. (3.1) for a constant cross-section duct.

For the acoustic-reflection coefficient, $R_a = P^-_{\text{in}}/P^+_{\text{in}}$, Eq. (3.18) is solved using the wave decomposition

$$\frac{p'_{\text{in}}}{\gamma\bar{p}_{\text{in}}} = P^+_{\text{in}} + P^-_{\text{in}}, \quad \frac{u'_{\text{in}}}{\bar{u}_{\text{in}}} = \frac{P^+_{\text{in}} - P^-_{\text{in}}}{\bar{\text{M}}_{\text{in}}}, \quad \sigma_{\text{in}} = 0,$$

where $P^{\pm}_{\text{in}}$ denote the downstream- and upstream-propagating acoustic waves, respectively (see Appendix A for details on the decomposition). Substituting these relations into Eq. (3.18) yields

$$R_a = \frac{P^-_{\text{in}}}{P^+_{\text{in}}} = \frac{\left(1 - \dfrac{\gamma-1}{2}\bar{\text{M}}_{\text{in}}\right) - \dfrac{\bar{\mathcal{P}}_f}{\Gamma_{\text{in}}}\left(1 + \gamma\bar{\text{M}}_{\text{in}}\right)}{\left(1 + \dfrac{\gamma-1}{2}\bar{\text{M}}_{\text{in}}\right) - \dfrac{\bar{\mathcal{P}}_f}{\Gamma_{\text{in}}}\left(1 - \gamma\bar{\text{M}}_{\text{in}}\right)}. \tag{3.19}$$

Similarly, the entropy–sound coefficient, $R_s = P^-_{\text{in}}/\sigma_{\text{in}}$, is obtained by solving Eq. (3.18) with the decomposition

$$\frac{p'_{\text{in}}}{\gamma\bar{p}_{\text{in}}} = P^-_{\text{in}}, \quad \frac{u'_{\text{in}}}{\bar{u}_{\text{in}}} = -\frac{P^-_{\text{in}}}{\bar{\text{M}}_{\text{in}}}, \quad \sigma_{\text{in}} \neq 0,$$

which yields

$$R_s = \frac{P^-_{\text{in}}}{\sigma_{\text{in}}} = \frac{-\bar{\text{M}}_{\text{in}}/2}{\left(1 + \dfrac{\gamma-1}{2}\bar{\text{M}}_{\text{in}}\right) - \dfrac{\bar{\mathcal{P}}_f}{\Gamma_{\text{in}}}\left(1 - \gamma\bar{\text{M}}_{\text{in}}\right)}. \tag{3.20}$$

For the limiting case of an unheated, isentropic flow ($P_v = 0$), Eqs. (3.19) and (3.20) reduce to the classical quasi-steady results of Tsien [18] and Marble and Candel [16]. These isentropic quasi-steady results are hereafter denoted as $\text{QSS}_2$:

$$R_{a,\text{QSS}_2} = R_{a,\text{QSS}_1}(\bar{\mathcal{P}}_f = 0), \tag{3.21}$$

$$R_{s,\text{QSS}_2} = R_{s,\text{QSS}_1}(\bar{\mathcal{P}}_f = 0). \tag{3.22}$$

Table 3.3 provides a summary of the two quasi-steady-state models and the corresponding geometric configurations from which they are derived.

**Table 3.3** Presentation of the two quasi-steady-state analytical models for the acoustic coefficients.

| Model | Duct | Heat-release profile | Configuration |
|---|---|---|---|
| $\text{QSS}_1$ | Constant | Uniform | $\text{C}_4$ |
| $\text{QSS}_2$ [16] | Convergent–Divergent | Isentropic | $\text{C}_2$ |

In Appendix B, a quasi-steady model for the reflection coefficient, adapted to a thermal throat generated by a non-uniform heat release in a divergent duct, is also presented (Eqs. (B.12) and (B.13)). This model assumes that the critical Mach number does not vanish (*i.e.*, $\text{M}'_* \neq 0$) and accounts for a non-uniform heat capacity ratio along the nozzle. However, its application requires the normalised critical Mach-number fluctuations ($\text{M}'_*/\text{M}'_{\text{in}}$) to be numerically extracted. For this reason, the model is not employed in the present study.

## 3.4 Aeroacoustic response of a thermally-choked-flow nozzle

### 3.4.1 Steady-state flow fields

Once the steady state is reached, the flow fields for each configuration are obtained. Figure 3.4 presents the steady-state longitudinal profiles of the Mach number ($\bar{\text{M}}$), static pressure ($\bar{p}$),

and static temperature ($\bar{T}$). The vertical lines (- - - and —) indicate the subsonic heat-release length $\delta_*$. As discussed in Sec. 3.2.2, the steady-state thermal throat is located at $x_*/L = 0.80$ for configurations $C_1$ (—), $C_2$ (····), and $C_3$ (-·-). For the $C_4$ configuration (- - -), the sonic position is found at $x_*/L = 0.44$, which is very close to the outlet of the constant-area duct ($x_u/L = 0.42$). Owing to the very small transverse velocity obtained ($[\bar{v}/\bar{u}]_{max} \approx 1 \times 10^{-3}$), the quasi-one-dimensional assumption is validated (the transverse deviation of the Mach number, static pressure, and static temperature is below $5 \times 10^{-5}$), and only the longitudinal quantities along the symmetry axis are shown.

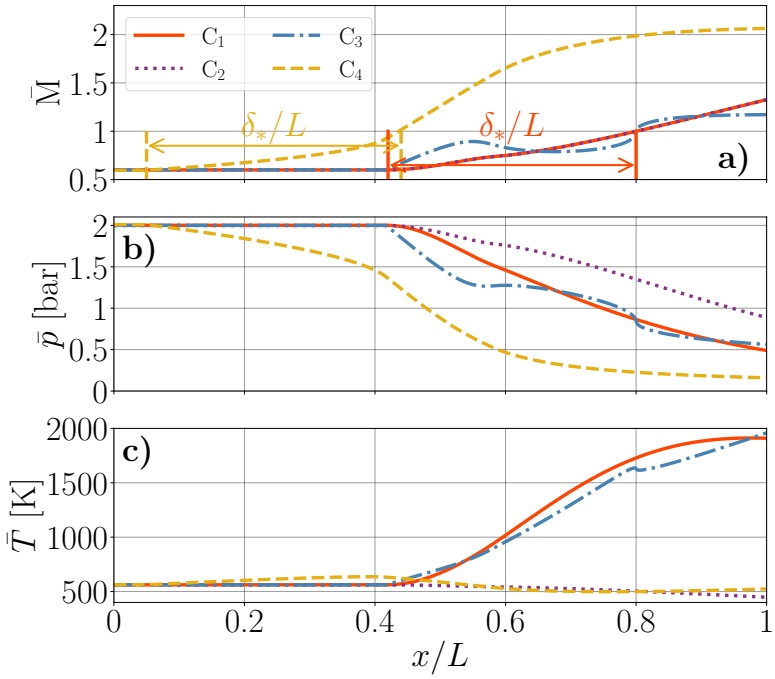


**Figure 3.4** (Colour) Steady-state flow fields as a function of the normalised longitudinal coordinate $x/L$ for the four choking configurations: $C_{1-4}$. **(a)** Mach number $\bar{M}$, **(b)** static pressure $\bar{p}$, and **(c)** static temperature $\bar{T}$. Vertical lines indicate the heat-release length $\delta_*/L = 0.38$, located upstream of the critical throat ($\bar{M} \leq 1$).

As expected, for all configurations the static pressure decreases as the local velocity increases. In contrast, the static temperature exhibits distinct behaviours depending on the configuration. For the $C_1$ and $C_3$ choking cases, a pronounced rise is observed, with $\bar{T}$ increasing from approximately 550 K to 2000 K. This substantial variation, caused by the imposed volumetric heat addition (see Sec. 3.2.2), highlights the necessity of accounting for a temperature-dependent heat capacity $c_p(\bar{T})$. In contrast, for the $C_2$ and $C_4$ configurations, the static temperature variation remains small, thus justifying the assumption of a constant isentropic ratio $\gamma$ adopted in the QSS analytical models (see Sec. 3.3.1). Finally, it is worth noting that the heat-release length $\delta_*$ is identical in the $C_4$ case to that in the three other configurations.

For clarity, the steady profiles (Mach number, static temperature, and static pressure) are not shown in Fig. 3.4 for configurations $C_5$ and $C_6$. These profiles are very similar to those of configuration $C_1$, exhibiting a slightly steeper gradient for $C_5$ and a slightly weaker one for $C_6$, as the thermal throat position is located somewhat closer to or farther from the inlet compared with $C_1$.

### 3.4.2 Acoustic-reflection coefficient

The acoustic-reflection coefficient, $R_a = \hat{P}^-/\hat{P}^+$, was numerically characterised over a wide range of frequencies using the forcing methodology described in Sec. 3.2.3 for each choking configuration. To enable direct comparison among the different configurations, a dimensionless frequency is defined through the Strouhal number, $S_t = f\delta_*/\bar{c}_*$, based on the heat-release length, $\delta_*$, and the steady critical speed of sound, $\bar{c}_*$. This formulation directly accounts for the heat-release length and incorporates the increase in static temperature through the local speed of sound, $\bar{c}_*$.

Figure 3.5 presents the modulus and phase-angle of the acoustic-reflection coefficient, $R_a = \hat{P}^-_{\text{in}}/\hat{P}^+_{\text{in}}$, as a function of the dimensionless frequency, $S_t = f\delta_*/\bar{c}_*$, for four choking configurations, $\text{C}_{1-4}$. The coefficient is evaluated at the beginning of the flame: $x/L = 0.42$ for configurations $\text{C}_1$, $\text{C}_2$, and $\text{C}_3$, and $x/L = 0.06$ for configuration $\text{C}_4$. This location corresponds to the point where the steady longitudinal Mach number begins to increase, either due to volumetric heat addition or to nozzle contraction. At this position, the flow is locally uniform, ensuring that the acoustic-wave decomposition introduced in Sec. 3.3 remains valid. Quasi-steady-state (QSS) analytical models for a perfect gas are also shown, corresponding either to the straight-duct configuration terminated by a thermal throat (Eq. (3.19), $\text{QSS}_1$) or to the geometric-throat case [16] ($\text{QSS}_2$).

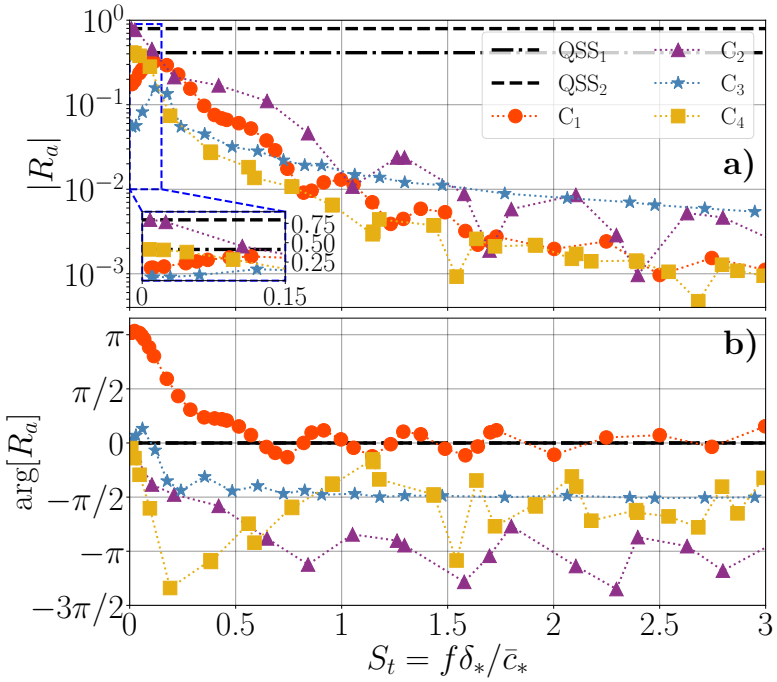


**Figure 3.5** (Colour) Acoustic-reflection coefficient, $R_a = \hat{P}^-_{\text{in}}/\hat{P}^+_{\text{in}}$: **(a)** modulus and **(b)** phase-angle, plotted as a function of the dimensionless frequency, $S_t = f\delta_*/\bar{c}_*$, for the different choking configurations, $\text{C}_{1-4}$, which share the same heat-release length, $\delta_*/L = 0.38$. Results from both numerical simulations (markers) and quasi-steady-state models ($\text{QSS}_{1-2}$, lines) are shown.

The modulus of the acoustic-reflection coefficient $R_a$ shows distinct behaviour, especially at very low frequencies $S_t \ll 1$, with a clear difference between the geometric-throat configuration ($\text{C}_2$) and the thermally choked-flow configurations ($\text{C}_1$, $\text{C}_3$, and $\text{C}_4$). For the geometric-throat nozzle (··▲··), the numerical acoustic-reflection coefficient tends to the analytical isentropic QSS

limit of Tsien [18] and Marble and Candel [16] (- - -):

$$R_{a,\mathrm{QSS}_2} = \frac{2 - (\bar{\gamma}_{\mathrm{in}} - 1)\bar{\mathrm{M}}_{\mathrm{in}}}{2 + (\bar{\gamma}_{\mathrm{in}} - 1)\bar{\mathrm{M}}_{\mathrm{in}}} = 0.795,$$

for $\bar{\mathrm{M}}_{\mathrm{in}} = 0.6$ and $\bar{\gamma}_{\mathrm{in}} = 1.379$. In contrast, the thermally choked configurations tend toward low-frequency limits of $|R_a| = 0.18$ for configuration $\mathrm{C}_1$ (·●·), $|R_a| = 0.05$ for configuration $\mathrm{C}_3$ (·★·), and $|R_a| = 0.41$ for configuration $\mathrm{C}_4$ (·■·). The analytical QSS model (Eq. (3.19)) for a uniform flame in a straight duct with a thermal throat at the outlet (- - -) also predicts well the zero-frequency limit for case $\mathrm{C}_4$:

$$R_{a,\mathrm{QSS}_1} = \frac{\left(1 - \dfrac{\bar{\gamma}_{\mathrm{in}} - 1}{2}\bar{\mathrm{M}}_{\mathrm{in}}\right) - \dfrac{\bar{\mathcal{P}}_f}{\Gamma_{\mathrm{in}}}\left(1 + \bar{\gamma}_{\mathrm{in}}\bar{\mathrm{M}}_{\mathrm{in}}\right)}{\left(1 + \dfrac{\bar{\gamma}_{\mathrm{in}} - 1}{2}\bar{\mathrm{M}}_{\mathrm{in}}\right) - \dfrac{\bar{\mathcal{P}}_f}{\Gamma_{\mathrm{in}}}\left(1 - \bar{\gamma}_{\mathrm{in}}\bar{\mathrm{M}}_{\mathrm{in}}\right)} = 0.407$$

(for $\bar{\mathrm{M}}_{\mathrm{in}} = 0.6$, $\bar{\gamma}_{\mathrm{in}} = 1.379$, and $\bar{\mathcal{P}}_f = 0.25$). In all cases with heat addition, $|R_a|$ is lower than the isentropic QSS value of $|R_a|_{\mathrm{C}_2} = 0.795$. This confirms that heat addition acts as an attenuating factor on acoustic waves, as described by Karimi *et al.* [95] and Lieuwen [131].

At low frequencies ($S_t = f\delta_*/\bar{c}_* < 0.1$), two distinct behaviours are observed. For choking configurations $\mathrm{C}_2$ and $\mathrm{C}_4$, the modulus of the acoustic-reflection coefficient decreases rapidly, by approximately one order of magnitude per frequency decade, relative to the QSS limit. In contrast, for configurations $\mathrm{C}_1$ and $\mathrm{C}_3$, where the thermal throat is located within the divergent nozzle, an initial increase in the acoustic-reflection coefficient is observed before it decreases at higher frequencies. Both configurations show a local maximum in $|R_a|$ around the same preferential frequency, $S_t = f\delta_*/\bar{c}_* = 0.12$.

A similar QSS trend is found for the phase-angle. For the $\mathrm{C}_2$ (·▲·), $\mathrm{C}_3$ (·★·), and $\mathrm{C}_4$ (·■·) choking configurations, the downstream and upstream acoustic waves are in phase at very low frequencies. Conversely, in the $\mathrm{C}_1$ configuration (·●·), the acoustic waves exhibit phase opposition, highlighting the strong influence of the volumetric heat-release distribution and geometry on the acoustic response. Once again, excellent agreement is observed between the CFD results and the analytical $\mathrm{QSS}_1$ and $\mathrm{QSS}_2$ models, corresponding respectively to the straight-duct thermal-throat ($\mathrm{C}_4$) and geometric-throat ($\mathrm{C}_2$) configurations.

The impact of the temperature-dependent heat capacity $c_p$ (presented Sec. 2.2.5) on the acoustic damping was assessed by imposing a constant heat capacity ratio $\gamma$ throughout the entire nozzle for the $\mathrm{C}_1$ choking configuration. Two cases were considered: one with $\gamma$ set to the inlet value ($\gamma_{\mathrm{in}} = 1.379$) and one with $\gamma$ set to the longitudinal spatial mean ($\gamma_{\mathrm{mean}} = 1.359$). A relative difference of up to 22 % in the modulus of the acoustic-reflection coefficient $R_a$ was observed for the spatial-mean $\gamma_{\mathrm{mean}}$ case, and 13 % for the inlet-value $\gamma_{\mathrm{in}}$ case, compared with the temperature-dependent reference. These results indicate that the dominant factors influencing the acoustic damping are the heat source $P_v$ and the geometry, rather than variations in heat capacity. Nevertheless, accounting for heat capacity variations remains necessary for accurate model predictions, as shown by Gentil *et al.* [106].

### 3.4.3 Acoustic-transmission coefficients

To better understand the acoustic-damping effect observed in the acoustic-reflection coefficient $R_a$, the entropy production at the critical throat position induced by the downstream-propagating acoustic forcing was evaluated. For this purpose, the critical entropy-production coefficient, $G_s = \hat{\sigma}_*/\hat{P}^+_{\mathrm{in}}$, was computed from quantities extracted along the symmetry axis. This coefficient

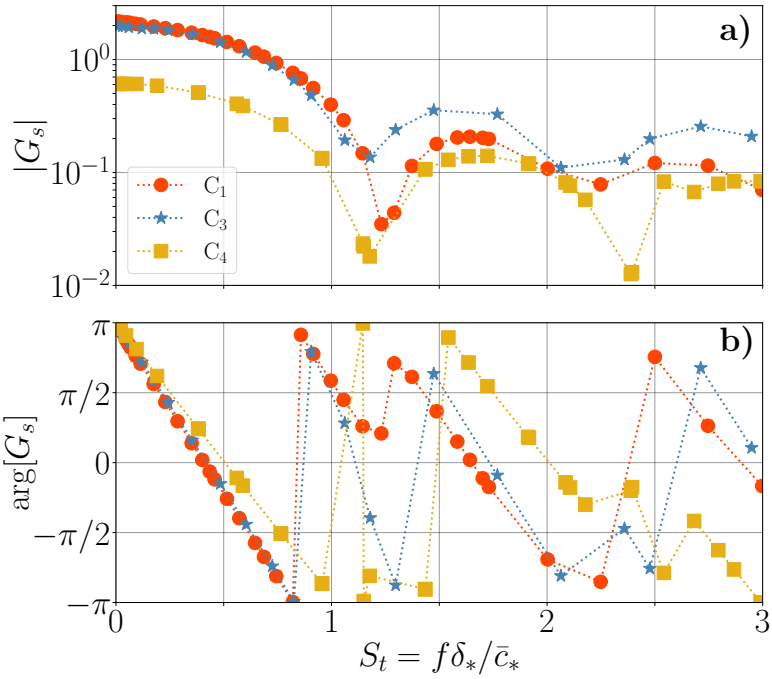


**Figure 3.6** (Colour) Critical entropy production, $G_s = \hat{\sigma}_*/\hat{P}^+_{\text{in}}$: **(a)** modulus and **(b)** phase-angle, plotted as a function of the dimensionless frequency, $S_t = f\delta_*/\bar{c}_*$, for different choking configurations. Results from numerical simulations (markers) are shown for three thermally choked-flow configurations, $C_1$, $C_2$, and $C_3$, which share the same heat-release length, $\delta_*/L = 0.38$.

is presented in Fig. 3.6, where it is plotted as a function of the dimensionless frequency, $S_t = f\delta_*/\bar{c}_*$, for each thermally choked-flow configuration.

As expected, entropy fluctuations are generated within the heated region by the acoustic forcing applied at the inlet. The geometric-throat configuration $C_2$ is not reported in the graph, as no entropy waves are produced in an isentropic flow under acoustic excitation. In contrast, the thermally choked-flow configurations exhibit significant entropy-wave generation at the outlet. Configurations $C_1$ (·●·) and $C_3$ (·★·) show, at very low frequencies, coefficient magnitudes of approximately $|G_s| = 2.1$ and 2.0, respectively. This results from the steep increase in steady temperature, $\bar{T}$, in the subsonic region (see Fig. 3.4). For configuration $C_4$ (·■·), the entropy generation is lower, with a coefficient of about $|G_s| = 0.6$, since the temperature rise is smaller than in the previous cases. The phase-angle between the outlet entropy waves and the inlet downstream-propagating acoustic waves exhibits similar behaviour across all configurations, indicating that the heat-release profile shape mainly affects the magnitude of entropy generation.

This generation of entropy explains the acoustic damping observed at very low frequencies in the acoustic-reflection coefficient $R_a$. As detailed by Karimi *et al.* [95] and Lieuwen [131], when acoustic waves are converted into entropy waves within the heated region, the amount of acoustic energy available for reflection is reduced. Moreover, although the entropy waves propagating downstream also produce acoustic waves propagating upstream, this contribution remains limited (see Sec. 3.4.5).

To highlight the conversion of acoustic waves into entropy waves, the acoustic-transmission coefficient, $T_a = \hat{P}^+_{\text{out}}/\hat{P}^+_{\text{in}}$, is shown in Fig. 3.7 as a function of the dimensionless frequency, $S_t = f\delta_*/\bar{c}_*$, for several choking configurations $C_{1-4}$, which share the same heat-release length, $\delta_*/L = 0.38$. The outlet quantities, $()_{\text{out}}$, are extracted at the outlet of the computational

domain along the symmetry axis. It is assumed that, at this location, the flow is sufficiently uniform to apply the acoustic-wave decomposition. In practice, small gradients remain in the steady fields, meaning that the outlet-wave amplitudes are not perfectly accurate. However, this does not affect the observed trends or the conclusions drawn.

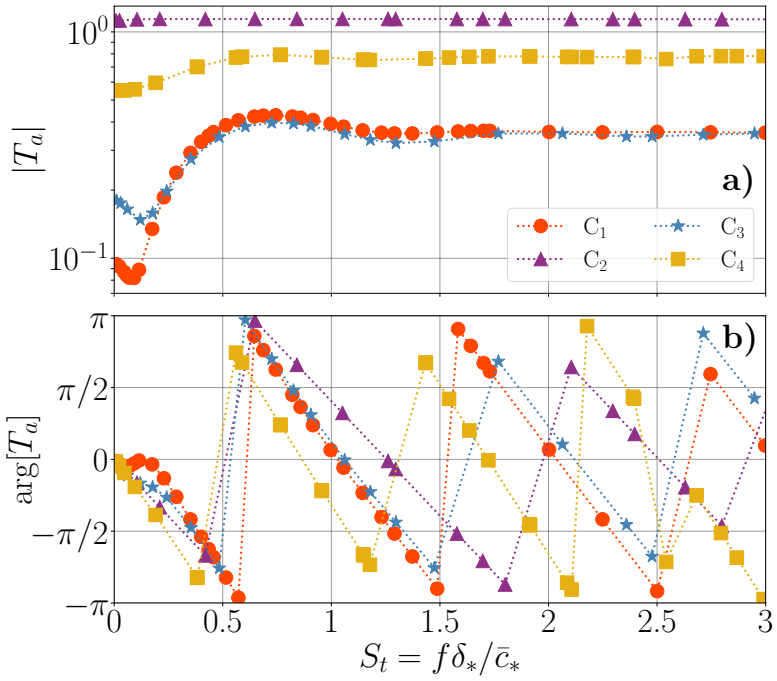


**Figure 3.7** (Colour) Acoustic-transmission coefficient, $T_a = \hat{P}^+_{\text{out}}/\hat{\sigma}_{\text{in}}$: **(a)** modulus and **(b)** phase-angle, plotted as a function of the dimensionless frequency, $S_t = f\delta_*/\bar{c}_*$, for the different choking configurations. Results from numerical simulations (markers) are shown for four thermally choked-flow configurations, $\text{C}_{1-4}$, which share the same heat-release length, $\delta_*/L = 0.38$.

Distinct behaviours are observed depending on the heat addition and the position of the thermal throat. For the geometric-throat configuration ($\text{C}_2$: ·▲·), the acoustic-transmission coefficient remains almost constant over the frequency range, with a value of $|T_a|_{\text{C}_2} = 1.12$ at low frequencies and $|T_a|_{\text{C}_2} = 1.14$ at very high frequencies. This indicates that, as the acoustic-reflection coefficient, $R_a$, decreases with frequency, the geometric throat tends toward a non-reflective behaviour and the acoustic waves are almost fully transmitted.

For the thermally choked-flow configurations ($\text{C}_{1,3,4}$), a similar trend is observed, but the underlying mechanism differs. In heated flows, entropy waves are generated, as shown in Fig. 3.6, particularly at low frequencies. This results in very low acoustic-transmission coefficients: $|T_a| = 0.09$ for $\text{C}_1$, $|T_a| = 0.18$ for $\text{C}_3$, and $|T_a| = 0.55$ for $\text{C}_4$. For configurations where the thermal throat is located deeper within the divergent duct ($\text{C}_1$: ·●· and $\text{C}_3$: ·★·), the same trend is maintained across all frequencies, indicating that geometric effects also play a role. At very low frequencies, the heat addition characterised by the dimensionless power number $\mathcal{P}_f$ primarily drives this shift. For the configuration with the thermal throat at the end of the straight duct ($\text{C}_4$: ·■·), the entropy generation is lower (see Fig. 3.6), which results in a higher acoustic-transmission coefficient.

In addition, for configuration $\text{C}_3$, the minimum of the acoustic-transmission coefficient $T_a$ coincides with the maximum of $R_a$, as expected. This behaviour is not exactly observed for configuration $\text{C}_1$, since a residual heat addition is still present at the outlet, which dampens the acoustic-wave decomposition, as shown by the model of Lieuwen [131].

The phase-angle measured for each configuration exhibits the same general trend but with a slight shift due to the heat addition: because the steady temperature fields differ, the local speed of sound also varies, and the acoustic waves therefore propagate at different velocities.

### 3.4.4 Effect of the heat-release length on the acoustic-reflection coefficient

In the previous section, the heat-release length $\delta_*$ was considered fixed and identical for all choking configurations. To assess its influence on the acoustic behaviour of a thermally choked nozzle, three non-uniform heat-release configurations are now examined: $C_5$ ($\delta_*/L = 0.32$), $C_1$ (0.38), and $C_6$ (0.44). All cases use the same normalised power number $\mathcal{P}_f$, while $\delta_*$ is varied to shift the steady position of the thermal throat (see Tab. 3.1). A relative deviation of $5 \times 10^{-3}$ is found in the normalised power number among the configurations, which does not affect the conclusions. The acoustic-reflection coefficient is considered, as it has been shown to be the most affected by heat addition, particularly at very low frequencies.

Figure 3.8 presents the acoustic reflection coefficient $R_a$ for the three configurations as a function of the dimensionless frequency, $S_t = f\delta_*/\bar{c}_*$. For $S_t \gtrsim 0.4$, all configurations exhibit the same trend in acoustic reflection: the influence of $\delta_*$ on $R_a$ remains limited. In contrast, increasing the heat-release length $\delta_*/L$ weakens entropy-wave generation and thus reduces acoustic damping, which at low frequencies ($S_t < 0.4$) leads to a higher reflection coefficient $R_a$. Configuration $C_6$ (▶, $|R_a| = 0.36$) exhibits a zero-frequency acoustic reflection coefficient larger than configurations $C_1$ (●, $|R_a| = 0.17$) and $C_5$ (◀, $|R_a| = 0.04$). For large $\delta_*/L$, the behaviour approaches that of the uniform heat-release configuration $C_4$, as the impact of the static temperature gradient becomes less significant.

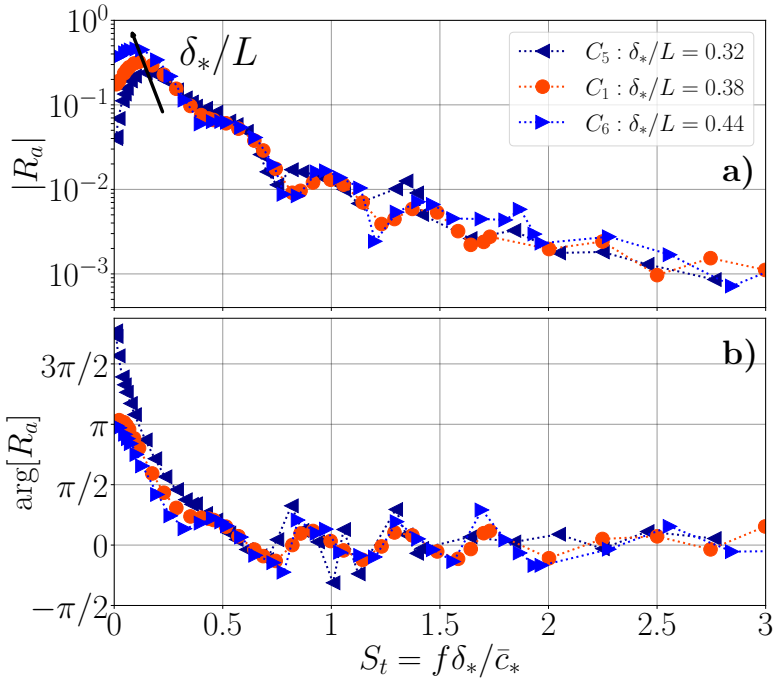


**Figure 3.8** (Colour) Acoustic-reflection coefficient, $R_a = \hat{P}^-_{\text{in}}/\hat{P}^+_{\text{in}}$: **(a)** modulus and **(b)** phase-angle, plotted as a function of the dimensionless frequency, $S_t = f\delta_*/\bar{c}_*$, for the different choking configurations, $C_{1,5,6}$, which share the same normalised power number, $\mathcal{P}_f = 2.80$. Results from numerical simulations (markers) are shown.

To highlight the entropy conversion, the entropy production at the critical throat induced

by an isentropic acoustic wave is examined. Figure 3.9 displays the corresponding entropy-production coefficient, $G_s = \hat{\sigma}_*/\hat{P}^{+}\text{in}$, as a function of $S_t$. As observed in Fig. 3.8, increasing $\delta_*/L$ decreases the entropy generation at the outlet, which corresponds to the higher values of $R_a$ observed at very low frequencies. The entropy-generation coefficient is approximately $|\hat{\sigma}_*/\hat{P}^{+}_{\text{in}}| = 2.5$ for $C_5$ (-◀-) and 2.2 for $C_6$ (-▶-). At low frequencies ($S_t < 0.5$), entropy generation is mainly driven by the local temperature gradient. Despite the small variation in $G_s$ between configurations ($C_5$: 2.3, $C_1$: 2.15, $C_6$: 2.05), a significant impact on the modulus of $R_a$ is observed.

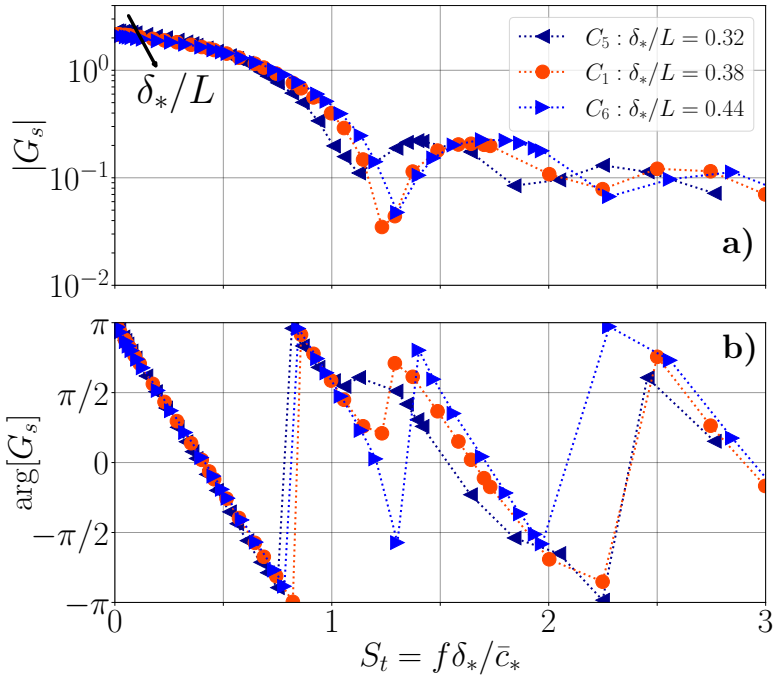


**Figure 3.9** (Colour) Critical entropy production, $G_s = \hat{\sigma}_*/\hat{P}^{+}_{\text{in}}$: **(a)** modulus and **(b)** phase-angle, plotted as a function of the dimensionless frequency, $S_t = f\delta_*/\bar{c}_*$, for different choking configurations, $C_{1,5,6}$, which share the same normalised power number, $\mathcal{P}_f = 2.80$. Results from numerical simulations (markers) are shown.

Finally, to isolate the effect of geometry, two additional cases (not shown here) were computed for a uniform heat-release profile in a straight duct, similar to configuration $C_4$. When varying $\delta_*$ at a constant normalised power number, no change in the low-frequency acoustic-reflection coefficient $R_a$ is observed at a dimensionless frequency of $S_t = 0.02$. The absolute relative difference between the cases remains below $1 \times 10^{-2}$. This behaviour is consistent with the predictions of the quasi-steady-state model $QSS_2$ (Eq. (3.19)), in which the cross-sectional area A has no influence.

### 3.4.5 Entropy-noise coefficients

The entropy-noise-production coefficient $R_s$ and the entropy-transmission coefficient $T_s$ are now numerically characterised over a wide range of frequencies to complement the previous analyses.

Figure 3.10 presents the amplitude and phase-angle of the entropy-noise-production coefficient, $R_s = (\hat{P}^{-}_{\text{in}} - R_a\hat{P}^{+}_{\text{in}})/\hat{\sigma}_{\text{in}}$, as a function of the dimensionless frequency, $S_t = f\delta_*/\bar{c}_*$, for four choking configurations, $C_{1\text{–}4}$, which share the same heat-release length $\delta_*$. The coefficients are evaluated at the beginning of the flame: $x/L = 0.42$ for cases $C_1$, $C_2$, and $C_3$, and $x/L = 0.06$

for case $C_4$.

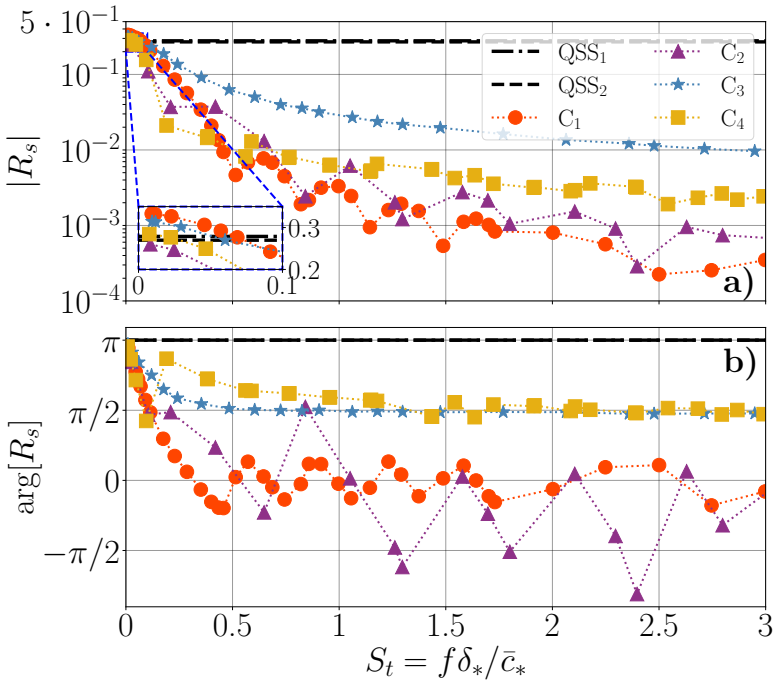


**Figure 3.10** (Colour) Entropy-noise-production coefficient, $R_s = (\hat{P}^-_{\text{in}} - R_a\hat{P}^+_{\text{in}})/\hat{\sigma}_{\text{in}}$: **(a)** modulus and **(b)** phase-angle, plotted as a function of the dimensionless frequency, $S_t = f\delta_*/\bar{c}_*$, for the different choking configurations, $C_{1\text{–}4}$, which share the same heat-release length, $\delta_*/L = 0.38$. Results from both numerical simulations (markers) and quasi-steady-state models ($QSS_{1\text{–}2}$, lines) are shown.

The entropy-noise-production coefficient exhibits similar behaviour across all choking configurations. At very low frequencies, for the geometric-throat nozzle $C_2$, both CFD results (-▲-) and the analytical $QSS_2$ model (- - -) are in agreement, yielding:

$$R_{s,\text{QSS}_2} = -\frac{\bar{\text{M}}_{\text{in}}}{2 + (\bar{\gamma}_{\text{in}} - 1)\bar{\text{M}}_{\text{in}}} = -0.269,$$

for $\bar{\text{M}}_{\text{in}} = 0.6$ and $\bar{\gamma}_{\text{in}} = 1.379$. The quasi-steady CFD limit for configuration $C_4$ (-■-) is also consistent with the analytical $QSS_1$ model (-·-) given by:

$$R_{s,\text{QSS}_1} = \frac{-\bar{\text{M}}_{\text{in}}/2}{\left(1 + \dfrac{\bar{\gamma}_{\text{in}} - 1}{2}\bar{\text{M}}_{\text{in}}\right) - \dfrac{\bar{\mathcal{P}}_f}{\bar{\Gamma}_{\text{in}}}\left(1 - \bar{\gamma}_{\text{in}}\bar{\text{M}}_{\text{in}}\right)} = -0.278 \tag{3.23}$$

(for $\bar{\text{M}}_{\text{in}} = 0.6$, $\bar{\gamma}_{\text{in}} = 1.379$, and $\bar{\mathcal{P}}_f = 0.25$). The asymptotic values for configurations $C_1$ and $C_3$ (-●- and -★-) are slightly higher, around $|R_s| = 0.33$ and $|R_s| = 0.30$, respectively.

This increase in the acoustic response for the thermally choked-flow configurations arises from the superposition of acoustic waves generated by two coupled mechanisms: (i) entropy waves are accelerated by the mean flow and generate acoustic waves, and (ii) these acoustic waves, in turn, produce entropy waves in the heated region, as discussed in Sec. 3.4.2, thereby reinforcing the overall upstream acoustic response. Nevertheless, this effect remains limited. This indicates that, for entropy-noise-production, both heat addition and nozzle geometry play a secondary role, while the response is primarily governed by the inlet Mach number $\bar{\text{M}}_{\text{in}}$ and by the acceleration of entropy waves.

Previously, the characteristic heat-release length $\delta_*$ was kept fixed and identical for all choking configurations. To assess its impact on indirect entropy noise and on the acoustic behaviour of a thermally choked nozzle, three non-uniform heat-release configurations are now examined: $C_5$ ($\delta_*/L = 0.32$), $C_1$ (0.38), and $C_6$ (0.44), as was already done in Sec. 3.4.4.

Figure 3.11 shows the entropy–noise–production coefficient $R_s$ as a function of the dimensionless frequency $S_t = f\delta_*/\bar{c}_*$ for three choking configurations: $C_5$ ($\delta_*/L = 0.32$), $C_1$ (0.38), and $C_6$ (0.44). In contrast to the acoustic-reflection coefficient $R_a$, which is strongly affected by the heat-release profile $P_v$, the indirect entropy noise is only weakly influenced. At low frequencies, $S_t \ll 1$, all configurations tend towards similar values, with a maximum deviation of about 15 % between cases $C_5$ and $C_6$. At higher frequencies, the amplitude of the acoustic response decreases with almost the same trend for all configurations. This result reinforces the finding that indirect entropy noise is mainly driven by the inlet Mach number $\bar{M}_{in}$, while the heat-release rate $P_v$ has only a minor impact.

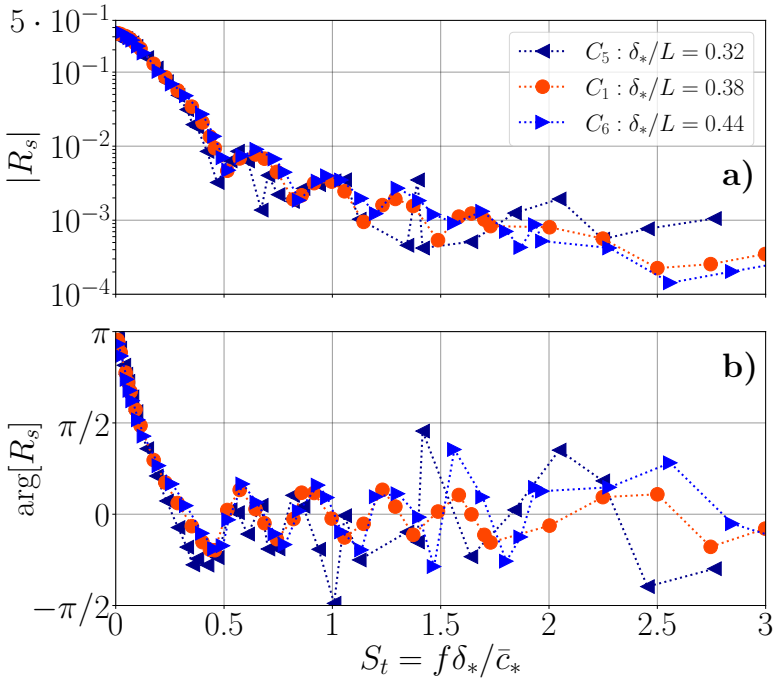


**Figure 3.11** (Colour) Entropy-noise-production coefficient, $R_s = (\hat{P}^-_{in} - R_a\hat{P}^+_{in})/\hat{\sigma}_{in}$: **(a)** modulus and **(b)** phase-angle, plotted as a function of the dimensionless frequency, $S_t = f\delta_*/\bar{c}_*$, for the different choking configurations, $C_{1,5,6}$, which share the same normalised power number, $\mathcal{P}_f = 2.80$. Results from numerical simulations (markers) are shown.

Finally, the influence of the temperature-dependent heat capacity $c_p$ has been reassessed. The same two cases tested previously (see Sec. 3.4.2) were considered. A relative difference of up to 3 % was observed for the $\gamma_{in}$ case in the modulus of the entropy-noise-production coefficient $R_s$, and up to 10 % for the $\gamma_{mean}$ case.

The generation of acoustic waves induced by the convection of entropy waves at the outlet of the nozzle is now characterised for the four choking configurations: $C_{1-4}$. Figure 3.12 details the entropy-transmission coefficient, $T_s = \hat{P}^+_{out}/\hat{\sigma}_{in}$, as a function of the dimensionless frequency $S_t = f\delta_*/\bar{c}_*$.

For all choking configurations, a similar trend is observed: $T_s$ decreases with increasing frequency, indicating that at very high frequencies ($S_t \gg 1$), the conversion of entropy waves into acoustic waves becomes strongly limited, and the flow tends toward a pure entropy-radiation

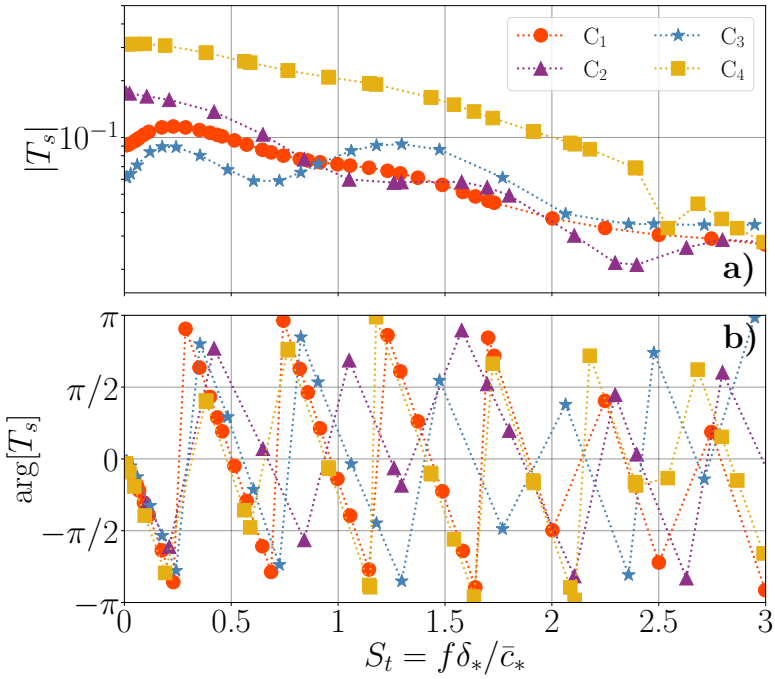


**Figure 3.12** (Colour) Entropy-noise-transmission coefficient $T_s = \hat{P}^+_{\text{out}}/\hat{\sigma}_{\text{in}}$ (**(a)**: modulus, **(b)**: phase-angle) plotted as a function of the dimensionless frequency, $S_t = f\delta_*/\bar{c}_*$, for different choking configurations, $\text{C}_{1-4}$, which share the same heat-release length, $\delta_*/L = 0.38$. Results from both numerical simulations (markers) and quasi-steady-state models ($\text{QSS}_{1-2}$, lines) are shown.

behaviour. Small discrepancies remain between the different configurations at low frequencies. For the geometric-throat configuration $\text{C}_2$ (··▲··) and for the thermal throat located at the outlet of a straight duct $\text{C}_4$ (··■··), the decrease in $T_s$ is monotonic with frequency. In contrast, for configurations $\text{C}_1$ (··●··) and $\text{C}_3$ (··★··), where the thermal throat is located deep within the divergent duct, a maximum in acoustic generation is observed at a common preferential frequency. This highlights a geometric effect associated with the heat-release length $\delta_*$, independent of the heat addition (*i.e.* independent of the normalised power number). Nevertheless, for the $\text{C}_3$ configuration, acoustic conversion remains significant at intermediate frequencies ($S_t = \mathcal{O}(1)$), underlining the influence of the heat-release profile on the generation mechanism.

## 3.5 Critical-throat acoustic boundary condition

To further analyse the previously obtained acoustic coefficients, it is useful to investigate the acoustic boundary condition at the critical throat. In the literature, it is often assumed that the fluctuations of the Mach number vanish at the throat, as detailed by Marble and Candel [16] and Duran and Morgans [132], *i.e.*, $\text{M}'_* = 0$. However, under acoustic or entropy forcing, Mach-number fluctuations may arise at the critical-throat position. These fluctuations can be observed either as a motion of the isoline $\text{M} = 1$ (for two-dimensional flow configurations) or as Mach-number fluctuations in a fixed reference frame associated with the steady Mach number $\bar{\text{M}}(\bar{x}_*) = 1$.

In what follows, the numerical Mach-number fluctuations $\hat{\text{M}}_*$, normalised by either static pressure fluctuations $\hat{P}_*$ or entropy fluctuations $\hat{\sigma}_*$ (depending on the forcing case), are measured at the steady-state critical-throat position $\bar{x}_*$ (*i.e.* $\bar{\text{M}}(\bar{x}_*) = 1$) along the axis, for each choking

configuration ($C_{1-6}$), and plotted as a function of the dimensionless frequencies, $S_t = f\delta_*/\bar{c}_*$.

Figure 3.13 presents the Mach-number fluctuations at the critical throat, normalised by the pressure fluctuations, $\hat{M}_*/\hat{P}_*$, as a function of the dimensionless frequency, $S_t = f\delta_*/\bar{c}_*$. It is first noted that the amplitude does not vanish ($M'_* \neq 0$), except for the geometric-throat configuration ($C_2$) at very low frequencies, corresponding to the QSS limit. Thermally choked-flow configurations exhibit a markedly different behaviour. For configuration $C_4$ (·■·), at low frequencies, the normalised Mach-number fluctuations, $\hat{M}_*/\hat{P}_*$, do not tend toward zero but instead reach a finite quasi-steady-state value. The same behaviour is observed for configurations where the thermal throat is located deep within the divergent duct, $C_1$ (·●·) and $C_3$ (·★·), although with different amplitudes. However, the overall trend in amplitude for configuration $C_4$ closely follows that of the geometric-throat case ($C_2$). In contrast, a local maximum in amplitude is found for the $C_1$ and $C_3$ configurations at specific frequencies, indicating a resonance mechanism induced by the geometry.

Regarding the phase, two distinct behaviours are observed. The thermally choked-flow configurations tend toward an in-phase relation between Mach number and pressure fluctuations at low frequencies, whereas for the geometric-throat configuration, a $\pi/2$ phase shift is obtained.

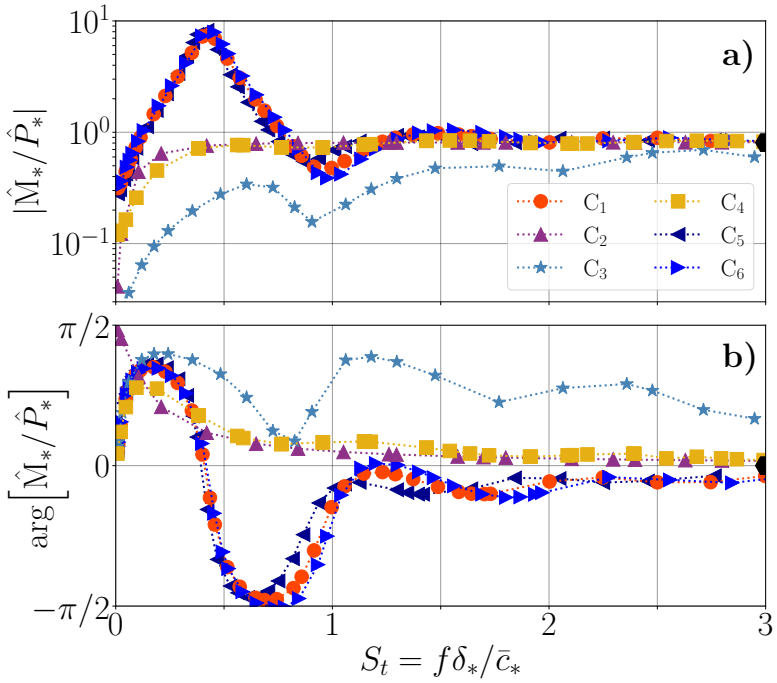


**Figure 3.13** (Colour) Mach-number fluctuations normalised by the static pressure fluctuations $\hat{M}_*/\hat{P}_*$: **(a)** modulus and **(b)** phase-angle at the steady critical-throat position, plotted as a function of the dimensionless frequency, $S_t = f\delta_*/\bar{c}_*$, for several choking configurations, $C_{1-6}$. The high-frequency asymptotic isentropic behaviour (●) is shown for the geometric-throat configuration.

At the thermal-throat position, the normalised power number $\mathcal{P}_f$ and the heat-release profile govern the normalised Mach-number fluctuations, as shown by configurations $C_1$ (·●·), $C_5$ (·◀·), and $C_6$ (·▶·). Geometric effects have no significant impact on this response.

At very high frequencies, all configurations converge toward a purely isentropic acoustic-radiation behaviour, characteristic of a uniform-duct response, governed by

$$\hat{p}_* = \bar{\rho}_* \bar{c}_* \hat{u}_*.$$

Under this assumption, the asymptotic value of the normalised Mach-number fluctuations can be directly obtained for isentropic flows as $\hat{\mathrm{M}}_*/\hat{P}_* = (3-\bar{\gamma}_*)/2$ (●). Since this asymptotic value depends on the local isentropic heat capacity ratio at the critical throat $\bar{\gamma}_*$ different values are expected for each choking configuration.

Moreover, it is noteworthy that in thermally choked-flow cases, even when the acoustic forcing is purely isentropic, entropy waves are generated as they propagate through the heated medium, as discussed in Sec. 3.4.3. Consequently, a superposition of acoustic and entropy waves reaches the throat, leading to two distinct noise sources. This behaviour has already been observed in other configurations, as reported in Karimi *et al.* [95, 133] and Nan *et al.* [134]. In contrast, for the geometric-throat configuration $\mathrm{C}_2$, such a superposition is impossible owing to the strictly isentropic nature of the flow throughout the entire nozzle.

Similarly, the Mach-number fluctuations normalised by entropy fluctuations $\hat{\mathrm{M}}_*/\hat{\sigma}_*$ are shown in Fig. 3.14 for different choking configurations. A strong similarity in the acoustic response to entropy perturbations is observed for $\mathrm{C}_1$ (·●·), $\mathrm{C}_2$ (·▲·) and $\mathrm{C}_4$ (·■·) choking configurations. The amplitude of Mach-number fluctuations is comparable for both geometric and thermal throat cases, tending toward zero at very low frequencies and converging to the pure acoustic radiation limit at very high frequencies. However, small discrepancies emerge between configurations around $S_t = f\delta_*/\bar{c}_* = \mathcal{O}(1)$ for $\mathrm{C}_1$ and $\mathrm{C}_2$. Large differences are found for $\mathrm{C}_3$ at $S_t = \mathcal{O}(1)$.

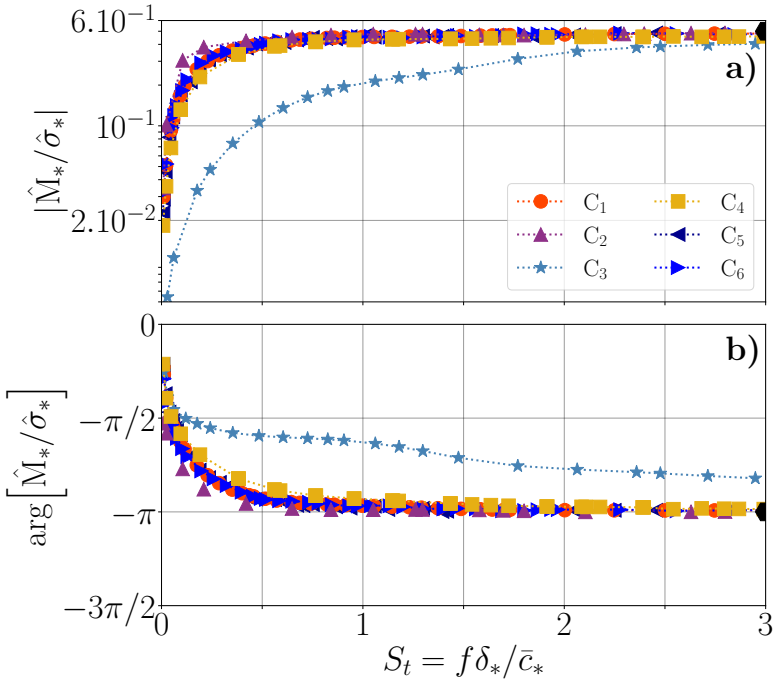


**Figure 3.14** (Colour) Mach-number fluctuations normalised by the entropy fluctuations $\hat{\mathrm{M}}_*/\hat{\sigma}_*$: **(a)** modulus and **(b)** phase-angle at the steady critical-throat position, plotted as a function of the dimensionless frequency, $S_t = f\delta_*/\bar{c}_*$, for several choking configurations, $\mathrm{C}_{1\text{–}6}$. The high-frequency asymptotic behaviour (●) is also shown.

The phase behaviour of the normalised Mach-number fluctuations differs depending on the choking mechanism. For the geometric-throat configuration $\mathrm{C}_2$ (·▲·), the phase tends toward $-\pi/2$. In contrast, for the thermal-throat configurations ($\mathrm{C}_1$: ·●·, $\mathrm{C}_3$: ·★·, and $\mathrm{C}_4$: ·■·), the phase approaches zero. This again highlights how heat addition fundamentally modifies the synchronicity of the acoustic response in the quasi-steady limit.

At very high frequencies, the normalised Mach-number fluctuations shown in Fig. 3.14 con-

verge to the asymptotic value $\hat{\mathrm{M}}_*/\hat{\sigma}_* = -1/2$ (●), which corresponds to a purely acoustic-radiation behaviour induced by entropy forcing, *i.e.*, $\hat{U}_* = -\hat{P}_*^- = 0$.

For the $\mathrm{C}_3$ choking configuration (·★·), a notably different behaviour is observed around the dimensionless frequency $S_t = f\delta_*/\bar{c}_* = \mathcal{O}(1)$, although the asymptotic value eventually converges to that of the other configurations. This indicates that the spatial distribution of $P_v$ strongly influences the Mach-number fluctuations. It is important to note that, in the vicinity of the critical-throat position, the steady Mach-number profile $\bar{\mathrm{M}}$ is very steep, which markedly differs from the other configurations.

## Chapter conclusion

This chapter has characterised the linear aeroacoustic behaviour of thermally choked flows through detailed numerical simulations and analytical modelling. By comparing thermal- and geometric-throat configurations, the main physical mechanisms governing the generation, reflection, and transmission of acoustic and entropy waves have been identified.

At very low frequencies, thermally choked nozzles exhibit strong attenuation of the acoustic-reflection coefficient compared with geometrically choked configurations. This damping arises from the conversion of acoustic to entropy fluctuations driven by the local temperature gradient within the heated region. The quasi-steady analytical model developed for a uniform duct with a thermal throat reproduces this behaviour with good accuracy, confirming that the low-frequency acoustic response is primarily controlled by the normalised flame power and the geometry of the heat-release region.

At high frequencies, all configurations converge to an isentropic radiation regime, revealing that the common assumption of a zero Mach-number fluctuation at the critical throat ($\mathrm{M}'_* = 0$) is not valid in thermally choked flows. Instead, finite Mach-number oscillations persist, highlighting the presence of coupled acoustic–entropy dynamics at the throat.

For entropy forcing, the acoustic response remains mainly governed by the steady flow acceleration, with heat addition acting as a secondary source that slightly amplifies the overall response. The study further demonstrates that geometric effects and heat-release distribution influence the location and amplitude of the resonance frequencies.

In conclusion, this chapter establishes the key physical trends and asymptotic behaviours governing acoustic and entropy wave propagation in thermally choked configurations. The findings form the foundation for the quasi-one-dimensional analytical model developed in the next chapter, which aims to provide a unified framework for predicting the aeroacoustic response and critical-throat boundary conditions of thermally choked dual-mode ramjet nozzles.

Chapter 4

# Development of a quasi-one-dimensional linear acoustic model for thermally choked nozzles with non-uniform flow

*Quand on veut être sûr de son coup, on plante des carottes.*

**Anna de Tintagel [2]**


## Abstract

This chapter presents the development and validation of a quasi-one-dimensional (Q1D) linear acoustic model designed to predict the propagation of acoustic and entropy waves in thermally choked nozzles representative of dual-mode ramjet engines. The model is derived from the quasi-one-dimensional Euler equations for a non-isentropic, heated flow, and extended to account for variable thermodynamic properties and distributed volumetric heat release.

A generalised critical-throat boundary condition (GEN) is proposed to replace the classical quasi-steady (QSS) Mach-number assumption, which fails in the presence of unsteady heat addition. The GEN formulation is obtained by enforcing the regularity of the acoustic solution at the critical throat and incorporates the influence of local temperature and density gradients, as well as of the unsteady heat source term. The model is solved numerically using a fourth-order Runge–Kutta scheme with Newton–Raphson iteration to ensure convergence at the critical throat. Validation against two-dimensional CFD simulations demonstrates that the GEN boundary condition accurately captures the reflection, transmission, and entropy–noise–production coefficients for both thermal- and geometric-throat configurations over a wide frequency range. At low frequencies, heat addition induces a strong coupling between acoustic and entropy modes, whereas at high frequencies, the system asymptotically recovers an isentropic, non-reflective behaviour.

The model is then used to assess in detail the impact of the inlet Mach number on the aeroacoustic response of a thermally choked-flow configuration, thereby completing the analysis in Chap. 3 on the effect of the steady thermal throat position. Finally, the validity range of the linear acoustic regime underlying the proposed model is evaluated using CFD simulations.

This chapter is a truncation of the following publication, published during the PhD:

F. Olivon, A. Genot, J.-E. Durand, A. Hirschberg, and E. Piot. "A quasi-one-dimensional critical-throat acoustic boundary condition for thermally choked dual-mode ramjet nozzles". In: *Acta Acustica* 9 (2025), 80. ISSN: 2681-4617. DOI: 10.1051/aacus/2025064.

## Contents


**4.1 Objective and state of the art . . . 62**
**4.2 Quasi-one-dimensional Euler equations . . . 64**
4.2.1 Quasi-one-dimensional approximation . . . 64
4.2.2 Continuity equation . . . 65
4.2.3 Momentum equation . . . 65
4.2.4 Total energy equation . . . 66
4.2.5 Quasi-one-dimensional Euler system . . . 67
**4.3 Linear acoustic model . . . 67**
4.3.1 Linearised Euler equations . . . 67
4.3.2 Fourier transform . . . 68
4.3.3 Matrix formulation . . . 69
**4.4 Boundary conditions . . . 70**
4.4.1 Inlet boundary conditions . . . 71
4.4.2 Critical-throat boundary condition . . . 71
**4.5 Resolution algorithm . . . 73**
**4.6 Validation of the linear acoustic model . . . 75**
4.6.1 Validation methodology . . . 75
4.6.2 Critical-throat boundary condition . . . 75
4.6.3 Aeroacoustic-reflection coefficients . . . 77
4.6.4 Aeroacoustic-transmission coefficients . . . 78
4.6.5 Impact of the critical-throat boundary condition on the aeroacoustic response . . . 80
**4.7 Impact of the inlet Mach number on the aeroacoustic response . . . 83**
**4.8 Limit of the linear acoustic regime . . . 87**


## 4.1 Objective and state of the art

Quasi-one-dimensional linear acoustic models are widely employed for analysing and designing the acoustic behaviour of combustion chambers, owing to their numerical efficiency. Whereas the unsteady simulations presented in Chap. 3 required several hours per frequency to resolve the flow field, a quasi-one-dimensional linear model requires only a steady-base flow to predict the acoustic response. A key element of such models, however, is the prescription of an appropriate acoustic boundary condition at the critical-throat location.

In this framework, the flow is treated as quasi-one-dimensional (Q1D), and only planar acoustic or entropy waves are considered. Accordingly, the Euler equations (Eq. (2.3)) must be reformulated under this assumption. The use of Euler equations to model thermally choked-flow nozzles has already been justified in Sec. 2.1.

Several modelling strategies have been developed to investigate thermoacoustic interactions and indirect combustion noise in airbreathing engines. Duran and Morgans [132] proposed a formulation based on the conservation of three flow invariants[1] across the nozzle. Using a Magnus expansion[2], they solved the resulting linearised Euler system of equations for arbitrary frequencies, provided that the perturbation wavelength exceeds the nozzle discretisation scale. This formulation was subsequently extended to non-isentropic flows by Yeddula *et al.* [27] and Yeddula and Morgans [135], and to configurations involving unsteady heat-release rate effects by Yeddula *et al.* [28]. More recently, the method was also extended to multi-species gases by Gentil *et al.* [84].

An alternative approach was proposed by Cummings [136], who solved the linearised Euler equations using the Wentzel-Kramers-Brillouin (WKB) approximation [137]. This method, was initially introduced for heated ducts with linear temperature gradients at very low Mach numbers, was later extended to arbitrary temperature gradients and moderate Mach numbers ($\mathrm{M} \approx 0.6$) by Li and Morgans [138]. The generalisation of Rani and Rani [99] allows treatment of arbitrary non-uniform mean flows. Nevertheless, WKB-based approaches remain restricted to high-frequency forcing and relatively low Mach numbers.

A third family of models, as developed by Emmanuelli *et al.* [25], Huet *et al.* [139], and Huet and Geiger [140], directly solves the linearised Euler equations, typically using implicit formulations. These methods impose no assumptions on the perturbation frequency or on the steady-flow profile, and are especially suited for configurations involving shocks, where numerical stability is critical. In the present work, thermally choked flows do not exhibit shock waves, and therefore an explicit resolution method is adopted.

In all previously developed acoustic models, boundary conditions are required to close the system. This is most commonly achieved by assuming that Mach-number fluctuations vanish at the critical-throat location [16, 21, 22, 82, 84, 139]. Physically, this assumption reflects the quasi-steady-flow limit: when the throat is choked, perturbations (acoustic or entropy waves) cannot induce Mach-number fluctuations upstream of the throat. For geometrically-choked flows, this follows directly from the dependence of the Mach number on the area ratio $\mathrm{A}_*/\mathrm{A}$, where $\mathrm{A}_*$ denotes the throat area, and A the local duct area. For a quasi-steady ideal gas with constant heat capacity ratio, $\gamma = c_p/c_v$, this relation is given by Shapiro [125]:

$$\frac{\mathrm{A}_*}{\mathrm{A}} = \mathrm{M}\left(\frac{\gamma+1}{2+(\gamma-1)\mathrm{M}^2}\right)^{\frac{\gamma+1}{2(\gamma-1)}}, \tag{4.1}$$

with the subscript $(\,)_*$ denoting critical-throat conditions ($\mathrm{M}_* = 1$).

Since the geometry does not fluctuate ($\mathrm{A}' = 0$), linearisation of Eq. (4.1) implies $\mathrm{M}' = 0$ everywhere upstream of the throat in the quasi-steady limit. This approximation was first introduced by Tsien [18] and formalised by Marble and Candel [16]. Stow *et al.* [19] further demonstrated that, to first order in frequency, the boundary condition $\mathrm{M}'_* = 0$ remains valid at the throat. Building on this, Duran and Moreau [22] argued that the narrow region surrounding the throat can always be treated as quasi-steady, since its length scale is small compared with the acoustic wavelength. Under this assumption, the condition $\mathrm{M}'_* = 0$ was extended to arbitrary frequencies.

In terms of normalised frequency-domain variables, this quasi-steady-state (QSS) boundary

[1] In their paper, Duran and Morgans [132] considered three flow invariants: the mass-flow rate $I_A = \dot{m}'/\bar{\dot{m}}$, the total temperature $I_B = T_0'/\bar{T}_0$, and the entropy $I_C = s'/\bar{c}_p$.

[2] The Magnus expansion consists in expanding the solution in powers of the dimensionless frequency $\Omega$. For any quantity $\chi$, the truncated series reads $\chi(x) = \chi^{(0)} + \Omega\,\chi^{(1)}(x) + \cdots + \Omega^n \chi^{(n)}(x)$, where only terms up to order $n$ are retained. The interested reader is referred to Duran and Morgans [132].

condition can be expressed as:

$$2\hat{U}_* = \gamma\hat{P}_* - \hat{D}_*, \tag{4.2}$$

where $\hat{P} = \hat{p}/(\gamma\bar{p})$, $\hat{U} = \hat{u}/\bar{u}$, and $\hat{D} = \hat{\rho}/\bar{\rho}$. Using the linearised Gibbs relation (Eq. (2.11)), the entropy-based form becomes:

$$2\hat{U}_* = (\gamma - 1)\hat{P}_* + \hat{\sigma}_*. \tag{4.3}$$

Although this closure remains widely used, its validity is restricted to isentropic, quasi-steady, geometrically-choked flows. As shown in Chap. 3, it breaks down under unsteady inlet conditions for both geometric and thermal throats. A more general boundary condition, based on enforcing regularity of the acoustic solution at the throat, is therefore required. This idea originates from Crocco in a footnote [18] and was first applied by Tsien [18], later by Marble and Candel [16] for specific geometries, and subsequently extended by Duran and Moreau [22]. A generalisation of this approach to thermally choked configurations is proposed in the present chapter.

The objective is thus to develop and validate a quasi-one-dimensional linear acoustic model and a boundary condition that captures the acoustic response of the critical throat subjected to both acoustic and entropy forcing in thermally choked configurations. The resulting quasi-one-dimensional model is systematically compared with two-dimensional Euler simulations to assess its accuracy.

## 4.2 Quasi-one-dimensional Euler equations

The three-dimensional Euler equations (Eq. (2.3)), introduced in Sec. 2.2.1, are now reformulated within a quasi-one-dimensional framework. For convenience in solving this system, the total energy equation is also rewritten in terms of natural variables (pressure, density, and velocity).

### 4.2.1 Quasi-one-dimensional approximation

In an orthogonal reference frame $(\mathbf{x}, \mathbf{y}, \mathbf{z})$, and assuming a quasi-one-dimensional flow, *i.e.*, $\mathbf{u} = (u(x,t), 0, 0)$, through a nozzle with cross-sectional area $\mathrm{A}(x)$, a control volume $V$ is defined, bounded by the surface $\Gamma$ with outward-pointing unit normal vector $\mathbf{n} = (n_x, n_y, n_z)$ (see Fig. 4.1). The control volume $V$ is enclosed by the inlet and outlet cross-sectional areas $\mathrm{A}(x)$ and $\mathrm{A}(x + \mathrm{d}x)$, together with the wall boundary $\mathrm{A}_w$.

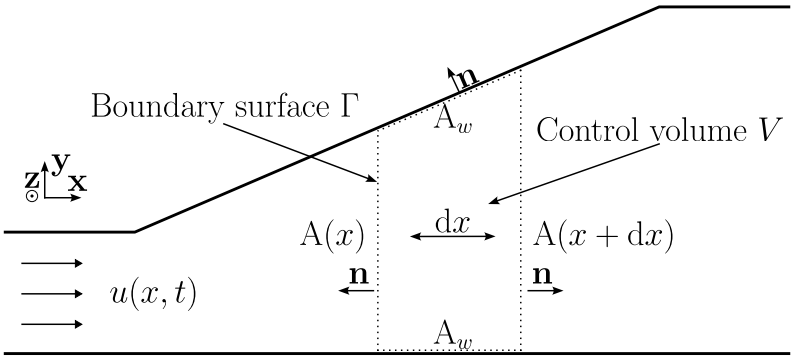


**Figure 4.1** Sketch of a simplified dual-mode ramjet nozzle, with control volume $V$ bounded by the surface $\Gamma$.

To first order, the control volume is approximated as $V = \mathrm{A}\,\mathrm{d}x$. For a scalar field, $f(x,t)$,

the integral approximation reads:

$$\int_V f \,\mathrm{d}V \;\simeq\; f(x,t)\,\mathrm{A}(x)\,\mathrm{d}x. \tag{4.4}$$

At this level of approximation, the gas state is assumed uniform across each cross-section, such that $p = p(x,t)$, $\rho = \rho(x,t)$, and $T = T(x,t)$.

**Divergence theorem** For a continuously differentiable vector field $\boldsymbol{f}$, over a control volume $V$ bounded by the surface $\partial V = \Gamma$, the divergence theorem states:

$$\int_V (\nabla \cdot \boldsymbol{f})\,\mathrm{d}V = \int_\Gamma (\boldsymbol{f}\cdot\mathbf{n})\,\mathrm{dA}. \tag{4.5}$$

Using a decomposition of the surface $\Gamma$, this boundary integral can be split into three contributions:

$$\begin{aligned}\int_\Gamma (\boldsymbol{f}\cdot\mathbf{n})\,\mathrm{dA} &= \int_{\mathrm{A}(x)} (\boldsymbol{f}\cdot\mathbf{n})\,\mathrm{dA} + \int_{\mathrm{A}(x+\mathrm{d}x)} (\boldsymbol{f}\cdot\mathbf{n})\,\mathrm{dA} + \int_{\mathrm{A}_w} (\boldsymbol{f}\cdot\mathbf{n})\,\mathrm{dA} \\ &\simeq \mathrm{A}\,(\boldsymbol{f}\cdot\mathbf{n})|_x + \mathrm{A}\,(\boldsymbol{f}\cdot\mathbf{n})|_{x+\mathrm{d}x} + \int_{\mathrm{A}_w} (\boldsymbol{f}\cdot\mathbf{n})\,\mathrm{dA}.\end{aligned} \tag{4.6}$$

### 4.2.2 Continuity equation

Integrating the continuity equation from Eq. (2.3) over a control volume $V$, and using the above notation, yields:

$$\int_V \left(\frac{\partial\rho}{\partial t} + \nabla\cdot(\rho\mathbf{u})\right)\mathrm{d}V = \int_V \frac{\partial\rho}{\partial t}\,\mathrm{d}V + \int_\Gamma (\rho\mathbf{u}\cdot\mathbf{n})\,\mathrm{dA} = 0. \tag{4.7}$$

This expression reduces to:

$$\mathrm{A}\frac{\partial\rho}{\partial t}\,\mathrm{d}x + \rho u\mathrm{A}|_{x+\mathrm{d}x} - \rho u\mathrm{A}|_x = 0, \tag{4.8}$$

since $(\rho\mathbf{u})\cdot\mathbf{n} = 0$ along the wall boundary, $\mathrm{A}_w$. To first order, this gives the quasi-one-dimensional convective form of the continuity equation:

$$\mathrm{A}\frac{\partial\rho}{\partial t} + \frac{\partial}{\partial x}(\rho u\mathrm{A}) = 0. \tag{4.9}$$

Introducing the material derivative, $\mathrm{D}/\mathrm{D}t = \partial/\partial t + u\,\partial/\partial x$, and the relative cross-sectional area variation, $\alpha = (\mathrm{dA}/\mathrm{d}x)/\mathrm{A}$, one obtains:

$$\frac{\mathrm{D}\rho}{\mathrm{D}t} + \rho\frac{\partial u}{\partial x} + \rho u\alpha = 0. \tag{4.10}$$

### 4.2.3 Momentum equation

Integrating the momentum conservation equation of Eq. (2.3) over a control volume $V$ gives:

$$\int_V \left(\frac{\partial}{\partial t}(\rho\mathbf{u}) + \nabla\cdot(\rho\mathbf{u}\otimes\mathbf{u}) + \nabla p\right)\mathrm{d}V = \int_V \frac{\partial}{\partial t}(\rho\mathbf{u})\,\mathrm{d}V + \int_\Gamma (\rho\mathbf{u}\otimes\mathbf{u}\cdot\mathbf{n})\,\mathrm{dA} + \int_\Gamma (p n_x)\,\mathrm{dA}. \tag{4.11}$$

This becomes:

$$\mathrm{A}\frac{\partial(\rho u)}{\partial t}\,\mathrm{d}x + \rho u^2\mathrm{A}\big|_{x+\mathrm{d}x} - \rho u^2\mathrm{A}\big|_x + p\mathrm{A}|_{x+\mathrm{d}x} - p\mathrm{A}|_x + \int_{\mathrm{A}_w}(pn_x)\,\mathrm{dA}. \tag{4.12}$$

The wall contribution does not vanish over $\mathrm{A}_w$ and can be approximated to first order as:

$$\int_{\mathrm{A}_w}(pn_x)\,\mathrm{dA} \simeq -\frac{p(x+\mathrm{d}x)+p(x)}{2}\,(\mathrm{A}(x+\mathrm{d}x)-\mathrm{A}(x)) = -p\frac{\mathrm{dA}}{\mathrm{d}x}\,\mathrm{d}x. \tag{4.13}$$

Hence, Eq. (4.12) reduces to:

$$\mathrm{A}\frac{\partial(\rho u)}{\partial t} + \frac{\partial}{\partial x}(\rho u^2\mathrm{A}) + \frac{\partial}{\partial x}(p\mathrm{A}) - p\frac{\mathrm{dA}}{\mathrm{d}x} = 0. \tag{4.14}$$

Finally, the quasi-one-dimensional momentum equation takes the form:

$$\mathrm{A}\frac{\partial(\rho u)}{\partial t} + \frac{\partial}{\partial x}(\rho u^2\mathrm{A}) + \mathrm{A}\frac{\partial p}{\partial x} = 0. \tag{4.15}$$

Expanding Eq. (4.15) and using the continuity equation Eq. (4.9) leads to:

$$\rho\frac{\mathrm{D}u}{\mathrm{D}t} + \frac{\partial p}{\partial x} = 0. \tag{4.16}$$

### 4.2.4 Total energy equation

Integrating the total energy equation over a control volume $V$ yields:

$$\mathrm{A}\frac{\partial}{\partial t}\left(\rho e_0\right)\mathrm{d}x + \int_\Gamma\left(\left(\rho e_0 + p\right)\mathbf{u}\cdot\mathbf{n}\right)\,\mathrm{dA} = \mathrm{A}P_v\,\mathrm{d}x. \tag{4.17}$$

The term $\left(\rho e_0 + p\right)\mathbf{u}\cdot\mathbf{n}$ vanishes all over the wall boundary $\mathrm{A}_w$, leading to:

$$\mathrm{A}\frac{\partial}{\partial t}\left(\rho e_0\right)\,\mathrm{d}x + \mathrm{A}\left(\rho e_0 + p\right)u|_{x+\mathrm{d}x} - \mathrm{A}\left(\rho e_0 + p\right)u|_x = \mathrm{A}P_v\,\mathrm{d}x. \tag{4.18}$$

To first order in the derivative, this gives:

$$\mathrm{A}\frac{\partial}{\partial t}\left(\rho e_0\right) + \frac{\partial}{\partial x}\left(\mathrm{A}\left(\rho e_0 + p\right)u\right) = \mathrm{A}P_v. \tag{4.19}$$

The specific energy is defined as $e = h - p/\rho + u^2/2$, with $h$ the specific enthalpy. Using this definition, Eq. (4.19) becomes:

$$\mathrm{A}\frac{\partial}{\partial t}\left(\rho h - p + \rho u^2/2\right) + \frac{\partial}{\partial x}\left(\mathrm{A}u\left(\rho h + \rho u^2/2\right)\right) = \mathrm{A}P_v. \tag{4.20}$$

By developing the above expression and applying both the continuity (Eq. (4.10)) and momentum equations (Eq. (4.16)), it comes:

$$\rho\frac{\mathrm{D}h}{\mathrm{D}t} - \frac{\mathrm{D}p}{\mathrm{D}t} = P_v. \tag{4.21}$$

Here, the gas must be single-species, or, in the case of a mixture, all species must share the same heat capacity, as discussed by Poinsot and Veynante [98]. The specific enthalpy is then defined for an ideal gas by

$$h = \int_{T_{\mathrm{ref}}}^{T} c_p(T)\,\mathrm{d}T, \tag{4.22}$$

leading to:

$$\rho c_p \frac{\mathrm{D}T}{\mathrm{D}t} - \frac{\mathrm{D}p}{\mathrm{D}t} = P_v. \tag{4.23}$$

Dividing Eq. (4.23) by $\rho c_p T$ gives:

$$\frac{1}{T}\frac{\mathrm{D}T}{\mathrm{D}t} - \frac{\gamma-1}{\gamma p}\frac{\mathrm{D}p}{\mathrm{D}t} = \frac{\gamma-1}{\gamma p}P_v. \tag{4.24}$$

Using the ideal gas law (Eq. (2.4)) in differential form yields:

$$\frac{1}{\gamma p}\frac{\mathrm{D}p}{\mathrm{D}t} - \frac{1}{\rho}\frac{\mathrm{D}\rho}{\mathrm{D}t} = \frac{\gamma-1}{\gamma p}P_v. \tag{4.25}$$

Finally, using the state equation (Eq. (2.9)), the total energy equation can be written as:

$$\frac{\mathrm{D}p}{\mathrm{D}t} - c^2\frac{\mathrm{D}\rho}{\mathrm{D}t} = (\gamma-1)P_v. \tag{4.26}$$

### 4.2.5 Quasi-one-dimensional Euler system

The resulting system of equations, referred to as the quasi-one-dimensional Euler equations, is:

$$\begin{cases} \dfrac{\mathrm{D}\rho}{\mathrm{D}t} + \rho\dfrac{\partial u}{\partial x} + \rho u\alpha = 0, \\ \dfrac{\mathrm{D}u}{\mathrm{D}t} + \dfrac{1}{\rho}\dfrac{\partial p}{\partial x} = 0, \\ \dfrac{\mathrm{D}p}{\mathrm{D}t} - c^2\dfrac{\mathrm{D}\rho}{\mathrm{D}t} = (\gamma-1)P_v. \end{cases} \tag{4.27}$$

## 4.3 Linear acoustic model

To develop a linear acoustic model, the quasi-one-dimensional Euler equations for a calorically semi-perfect ideal gas presented Eq. (4.27) are considered:

$$\begin{cases} \dfrac{\partial \rho}{\partial t} + u\dfrac{\partial \rho}{\partial x} + \rho\dfrac{\partial u}{\partial x} + \rho u\alpha = 0, \\ \dfrac{\partial u}{\partial t} + u\dfrac{\partial u}{\partial x} + \dfrac{1}{\rho}\dfrac{\partial p}{\partial x} = 0, \\ \dfrac{\partial p}{\partial t} + u\dfrac{\partial p}{\partial x} + c^2\left(\rho\dfrac{\partial u}{\partial x} + \rho u\alpha\right) = (\gamma-1)P_v. \end{cases} \tag{4.28}$$

### 4.3.1 Linearised Euler equations

The Euler equations (Eq. (4.28)) can be linearised by assuming that any quantity, $\chi(x,t)$, is the sum of a steady component, $\bar{\chi}(x)$, and a small fluctuating component, $\chi'(x,t)$, such that $\chi = \bar{\chi} + \chi'$ and $\chi' \ll \bar{\chi}$, where $\chi = [\rho, u, p, T, c, \gamma, P_v]$. By neglecting second-order terms (*i.e.*

$\chi'\chi' = 0$), the following linearised Euler equations are obtained:

$$\begin{cases} \dfrac{\partial \rho'}{\partial t} + \bar{u}\dfrac{\partial \rho'}{\partial x} + \bar{\rho}\dfrac{\partial u'}{\partial x} + \left(\dfrac{\mathrm{d}\bar{u}}{\mathrm{d}x} + \bar{u}\alpha\right)\rho' + \left(\dfrac{\mathrm{d}\bar{\rho}}{\mathrm{d}x} + \bar{\rho}\alpha\right)u' = 0, \\ \dfrac{\partial u'}{\partial t} + \bar{u}\dfrac{\partial u'}{\partial x} + \dfrac{1}{\bar{\rho}}\dfrac{\partial p'}{\partial x} + \dfrac{\mathrm{d}\bar{u}}{\mathrm{d}x}u' - \dfrac{1}{\bar{\rho}^2}\dfrac{\mathrm{d}\bar{p}}{\mathrm{d}x}\rho' = 0, \\ \dfrac{\partial p'}{\partial t} + \bar{u}\dfrac{\partial p'}{\partial x} + \dfrac{\mathrm{d}\bar{p}}{\mathrm{d}x}u' + 2\bar{c}^2\left(\bar{\rho}\dfrac{\mathrm{d}\bar{u}}{\mathrm{d}x} + \bar{\rho}\bar{u}\alpha\right)\left(\dfrac{c'}{\bar{c}}\right) + \bar{c}^2\left(\left(\dfrac{\mathrm{d}\bar{u}}{\mathrm{d}x} + \bar{u}\alpha\right)\rho' + \bar{\rho}\dfrac{\partial u'}{\partial x} + \bar{\rho}\alpha u'\right) \\ \qquad = \bar{\gamma}\bar{P}_v\left(\dfrac{\gamma'}{\bar{\gamma}}\right) + (\bar{\gamma}-1)\bar{P}_v\left(\dfrac{P_v'}{\bar{P}_v}\right). \end{cases} \tag{4.29}$$

To simplify the linearised Euler system, the following normalised variables are introduced:

$$D = \frac{\rho'}{\bar{\rho}}, \quad P = \frac{p'}{\bar{\gamma}\bar{p}}, \quad U = \frac{u'}{\bar{u}}. \tag{4.30}$$

The linearised state equation (Eq. (2.4)) becomes:

$$\frac{T'}{\bar{T}} = \bar{\gamma}P - D. \tag{4.31}$$

The heat capacity ratio $\gamma$, being a function of temperature only (see Sec. 2.2.5), has the following linearised form:

$$\frac{\gamma'}{\bar{\gamma}} = \bar{\kappa}\bar{T}\left(\frac{T'}{\bar{T}}\right) = \bar{\kappa}\bar{T}(\bar{\gamma}P - D), \tag{4.32}$$

where $\bar{\kappa} = \kappa(\bar{T}) = \dfrac{1}{\bar{\gamma}(\bar{T})}\dfrac{\mathrm{d}\gamma}{\mathrm{d}T}(\bar{T})$ is computed using Eq. (2.10).

The linearised expression for the sound-speed fluctuations is:

$$\frac{c'}{\bar{c}} = \frac{1}{2}\left(\frac{\gamma'}{\bar{\gamma}} + \frac{T'}{\bar{T}}\right) = \frac{(1+\bar{\kappa}\bar{T})}{2}(\bar{\gamma}P - D). \tag{4.33}$$

Substituting these relations into the linearised Euler system yields:

$$\begin{cases} \dfrac{\partial D}{\partial t} + \bar{u}\dfrac{\partial}{\partial x}(U + D) = 0, \\ \dfrac{\partial U}{\partial t} + \bar{u}\dfrac{\partial U}{\partial x} + \dfrac{\bar{c}^2}{\bar{u}}\dfrac{\partial P}{\partial x} + 2\dfrac{\mathrm{d}\bar{u}}{\mathrm{d}x}U + \left(\dfrac{\bar{\kappa}\bar{c}^2}{\bar{u}}\dfrac{\mathrm{d}\bar{T}}{\mathrm{d}x} - \bar{\gamma}\dfrac{\mathrm{d}\bar{u}}{\mathrm{d}x}\right)P + \dfrac{\mathrm{d}\bar{u}}{\mathrm{d}x}D = 0, \\ \dfrac{\partial P}{\partial t} + \bar{u}\dfrac{\partial}{\partial x}(U + P) + (\bar{\gamma}-1)\dfrac{\bar{P}_v}{\bar{\gamma}\bar{p}}U + \bar{\kappa}\bar{T}\left(\dfrac{\bar{P}_v}{\bar{p}} + \dfrac{\bar{u}}{\bar{\rho}}\dfrac{\mathrm{d}\bar{\rho}}{\mathrm{d}x}\right)D \\ \qquad + \left(\dfrac{\bar{P}_v}{\bar{p}}\left((\bar{\gamma}-1) - \bar{\kappa}\bar{\gamma}\bar{T}\right) + \bar{\kappa}\bar{u}\left(\dfrac{\mathrm{d}\bar{T}}{\mathrm{d}x} - \dfrac{\bar{\gamma}\bar{T}}{\bar{\rho}}\dfrac{\mathrm{d}\bar{\rho}}{\mathrm{d}x}\right)\right)P = \dfrac{(\bar{\gamma}-1)\bar{P}_v}{\bar{\gamma}\bar{p}}\left(\dfrac{P_v'}{\bar{P}_v}\right). \end{cases} \tag{4.34}$$

### 4.3.2 Fourier transform

The Fourier transform is applied to the linearised Euler system, adopting the convention

$$\chi'(x,t) = \hat{\chi}(x)\exp(+\mathrm{i}\omega t)\,, \tag{4.35}$$

where $\hat{\chi}(x)$ denotes the complex amplitude of the Fourier component of the variable $\chi$, $\omega = 2\pi f$ is the angular frequency corresponding to the frequency $f$, and $\mathrm{i} = \sqrt{-1}$ the imaginary unit. Applying this convention to Eq. (4.34) yields:

$$\begin{cases} \bar{u}\dfrac{\mathrm{d}\hat{U}}{\mathrm{d}x} + \bar{u}\dfrac{\mathrm{d}\hat{D}}{\mathrm{d}x} + \mathrm{i}\omega\hat{D} = 0, \\ \bar{u}\dfrac{\mathrm{d}\hat{U}}{\mathrm{d}x} + \dfrac{\bar{c}^2}{\bar{u}}\dfrac{\mathrm{d}\hat{P}}{\mathrm{d}x} + \left(2\dfrac{\mathrm{d}\bar{u}}{\mathrm{d}x} + \mathrm{i}\omega\right)\hat{U} + \left(\dfrac{\bar{\kappa}\bar{c}^2}{\bar{u}}\dfrac{\mathrm{d}\bar{T}}{\mathrm{d}x} - \bar{\gamma}\dfrac{\mathrm{d}\bar{u}}{\mathrm{d}x}\right)\hat{P} + \dfrac{\mathrm{d}\bar{u}}{\mathrm{d}x}\hat{D} = 0, \\ \bar{u}\dfrac{\mathrm{d}\hat{U}}{\mathrm{d}x} + \bar{u}\dfrac{\mathrm{d}\hat{P}}{\mathrm{d}x} + (\bar{\gamma}-1)\dfrac{\bar{P}_v}{\bar{\gamma}\bar{p}}\hat{U} + \left(\dfrac{\bar{P}_v}{\bar{p}}\left((\bar{\gamma}-1) - \bar{\kappa}\bar{\gamma}\bar{T}\right) + \bar{\kappa}\bar{u}\left(\dfrac{\mathrm{d}\bar{T}}{\mathrm{d}x} - \dfrac{\bar{\gamma}\bar{T}}{\bar{\rho}}\dfrac{\mathrm{d}\bar{\rho}}{\mathrm{d}x}\right) + \mathrm{i}\omega\right)\hat{P} \\ \qquad + \bar{\kappa}\bar{T}\left(\dfrac{\bar{P}_v}{\bar{p}} + \dfrac{\bar{u}}{\bar{\rho}}\dfrac{\mathrm{d}\bar{\rho}}{\mathrm{d}x}\right)\hat{D} = \dfrac{(\bar{\gamma}-1)\bar{P}_v}{\bar{\gamma}\bar{p}}\left(\dfrac{\hat{P}_v}{\bar{P}_v}\right). \end{cases} \tag{4.36}$$

### 4.3.3 Matrix formulation

To solve the linearised Euler equations, the unknown vector $\hat{X} = (\hat{U}, \hat{P}, \hat{D})^T$ is introduced. The system in Eq. (4.36) can then be recast as:

$$\bar{K}_1\frac{\mathrm{d}\hat{X}}{\mathrm{d}x} + \bar{K}_2\hat{X} = \bar{K}_3\begin{bmatrix} 0 \\ 0 \\ \left(\dfrac{\hat{P}_v}{\bar{P}_v}\right) \end{bmatrix}, \tag{4.37}$$

where

$$\bar{K}_1 = \begin{bmatrix} \bar{u} & 0 & \bar{u} \\ \bar{u} & \bar{c}^2/\bar{u} & 0 \\ \bar{u} & \bar{u} & 0 \end{bmatrix}, \quad \bar{K}_3 = (\bar{\gamma}-1)\bar{P}_v/(\bar{\gamma}\bar{p})$$

and

$$\bar{K}_2 = \begin{bmatrix} 0 & 0 & \mathrm{i}\omega \\ 2\dfrac{\mathrm{d}\bar{u}}{\mathrm{d}x} + \mathrm{i}\omega & \dfrac{\bar{\kappa}\bar{c}^2}{\bar{u}}\dfrac{\mathrm{d}\bar{T}}{\mathrm{d}x} - \bar{\gamma}\dfrac{\mathrm{d}\bar{u}}{\mathrm{d}x} & \dfrac{\mathrm{d}\bar{u}}{\mathrm{d}x} \\ \dfrac{(\bar{\gamma}-1)\bar{P}_v}{\bar{\gamma}\bar{p}} & \bar{K}_2^{32} & \bar{\kappa}\bar{T}\left(\dfrac{\bar{P}_v}{\bar{p}} + \dfrac{\bar{u}}{\bar{\rho}}\dfrac{\mathrm{d}\bar{\rho}}{\mathrm{d}x}\right) \end{bmatrix},$$

where the matrix coefficient $\bar{K}_2^{32}$ is given by:

$$\bar{K}_2^{32} = \frac{\bar{P}_v}{\bar{p}}\left((\bar{\gamma}-1) - \bar{\kappa}\bar{\gamma}\bar{T}\right) + \bar{\kappa}\bar{u}\left(\frac{\mathrm{d}\bar{T}}{\mathrm{d}x} - \frac{\bar{\gamma}\bar{T}}{\bar{\rho}}\frac{\mathrm{d}\bar{\rho}}{\mathrm{d}x}\right) + \mathrm{i}\omega. \tag{4.38}$$

To solve Eq. (4.37), the matrix $\bar{K}_1$ is inverted, yielding:

$$\frac{\mathrm{d}\hat{X}}{\mathrm{d}x} + \bar{K}_1^{-1}\bar{K}_2\hat{X} = \bar{K}_1^{-1}\bar{K}_3\begin{bmatrix} 0 \\ 0 \\ \left(\dfrac{\hat{P}_v}{\bar{P}_v}\right) \end{bmatrix} \tag{4.39}$$

with

$$\bar{K}_1^{-1} = \frac{1}{\bar{u}(1-\bar{\mathrm{M}}^2)}\begin{bmatrix} 0 & -\bar{\mathrm{M}}^2 & 1 \\ 0 & \bar{\mathrm{M}}^2 & -\bar{\mathrm{M}}^2 \\ 1-\bar{\mathrm{M}}^2 & \bar{\mathrm{M}}^2 & -1 \end{bmatrix},$$

where $\bar{\mathrm{M}} = \bar{u}/\bar{c}$ is the steady Mach number.

It is noteworthy that $\bar{K}_1$ is invertible if and only if $\bar{u} \neq 0$ and $\bar{\mathrm{M}} \neq 1$. This implies that the present acoustic model is not valid at the sonic (critical) throat or for a stagnant gas ($\bar{u} = 0$). For the choked configuration, $\bar{\mathrm{M}} = 1$, the singularity of the matrix $\bar{K}_1$ arises from the change in the propagation direction of the upstream-propagating acoustic wave. While this wave propagates toward the inlet in the subsonic region, it reverses direction and propagates toward the outlet in the supersonic region; the critical-throat position marks the location where this transition occurs. As detailed by Duran and Morgans [132], this sign change is equivalent to selecting the regular solution at the throat, as discussed by Stow *et al.* [19].

Assuming that the volumetric power fluctuations ($\hat{P}_v/\bar{P}_v$) can be expressed as a linear function $\boldsymbol{f}^{\perp} = (f_U, f_P, f_D)$ of the natural variables, one writes:

$$\frac{\hat{P}_v}{\bar{P}_v} = \boldsymbol{f}^{\perp}\,\hat{X}. \tag{4.40}$$

Here, $\boldsymbol{f}$ is a vector-valued function that describes the flame transfer function (FTF) of the flame. More details on the flame transfer functions can be found in Chap. 5.

Introducing the matrix

$$\bar{C} = -\bar{K}_1^{-1}\left(\bar{K}_2 - \bar{K}_3\boldsymbol{f}\right), \tag{4.41}$$

and discretising the nozzle into $j \in [\![0, \ldots, l-1, l, l+1, \ldots, n]\!]$ elements (with $l$ denoting the critical-throat position index), each of size $\Delta x$, and using an explicit fourth-order Runge–Kutta (RK4) scheme [126] for integration, the following recurrence relation is obtained:

$$\hat{X}_{j+1} = \hat{X}_j + \frac{\Delta x}{6}\left(k_1 + 2k_2 + 2k_3 + k_4\right), \tag{4.42}$$

with the intermediate slopes, for all $j \neq l$, defined as

$$\begin{aligned}
k_1 &= \bar{C}_j \hat{X}_j, \\
k_2 &= \frac{\bar{C}_j + \bar{C}_{j+1}}{2}\left(\hat{X}_j + \frac{\Delta x}{2}k_1\right), \\
k_3 &= \frac{\bar{C}_j + \bar{C}_{j+1}}{2}\left(\hat{X}_j + \frac{\Delta x}{2}k_2\right), \\
k_4 &= \bar{C}_{j+1}\left(\hat{X}_j + \Delta x\, k_3\right).
\end{aligned}$$

To ensure convergence of the solution, a Newton–Raphson root-finding method is employed to determine the appropriate boundary condition (see Sec. 4.5).

Among the several numerical schemes implemented to integrate Eq. (4.37) (upwind, centred, RK2, etc), the RK4 scheme was chosen as it provides the best trade-off between the number of cells, computation time, and solution accuracy.

## 4.4 Boundary conditions

To solve the quasi-one-dimensional linear acoustic model presented in Eq. (4.39), three boundary conditions must be specified at the system boundaries. Following the methodology of Duran and Moreau [22], the unknown vector $\hat{X}(x)$, is computed in two stages (see Fig. 4.2).

In the subsonic region, two boundary conditions (BC) are prescribed at the inlet ($x_{\mathrm{in}}$), while a third condition is imposed on the upstream side of the critical throat (denoted $\bar{x}_{\mathrm{cu}}$).

To ensure that the system Eq. (4.39) remains invertible ($\bar{\mathrm{M}} \neq 1$), the boundary conditions at the critical throat are not applied exactly at the sonic point but are instead shifted by an

infinitesimal distance $\epsilon$, as illustrated in Fig. 4.2. This leads to $\bar{x}_{\mathrm{cu}} = \bar{x}_* - \epsilon$ and $\bar{x}_{\mathrm{cd}} = \bar{x}_* + \epsilon$, where $\epsilon$ is taken equal to the spatial discretisation step $\Delta x$.

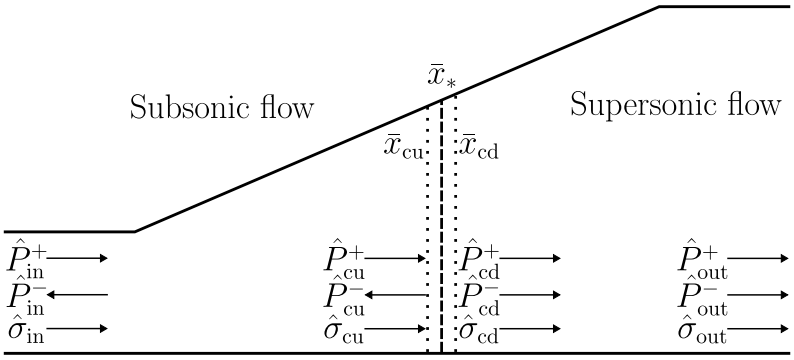


**Figure 4.2** Sketch representation of the boundary-condition treatment for a thermally choked-flow configuration. An analogous decomposition can be applied to a nozzle with a geometric throat.

### 4.4.1 Inlet boundary conditions

The boundary condition imposed at the nozzle inlet depends on the type of forcing considered. In all cases, however, it is expressed in terms of the propagation of either acoustic or entropy waves.

For an isentropic acoustic forcing of angular frequency $\omega = 2\pi f$, the inlet acoustic pressure fluctuations, $\hat{P}_{\mathrm{in}}$, is prescribed with amplitude $\eta$. Since the forcing is assumed to be perfectly isentropic, *i.e.*, $\hat{\sigma}_{\mathrm{in}} = \hat{P}_{\mathrm{in}} - \hat{D}_{\mathrm{in}} = 0$, the following inlet boundary conditions apply:

$$\begin{cases} \hat{P}_{\mathrm{in}} = \eta, \\ \hat{D}_{\mathrm{in}} = \hat{P}_{\mathrm{in}}. \end{cases} \tag{4.43}$$

For entropy forcing of angular frequency $\omega$, an entropy amplitude $\eta$ is imposed at the inlet, while the downstream-propagating acoustic wave is suppressed, *i.e.*, $\hat{P}^+_{\mathrm{in}} = \hat{P}_{\mathrm{in}} + \bar{\mathrm{M}}_{\mathrm{in}} \hat{U}_{\mathrm{in}} = 0$. This leads to the following inlet boundary conditions:

$$\begin{cases} \hat{D}_{\mathrm{in}} = \hat{P}_{\mathrm{in}} - \eta, \\ \hat{U}_{\mathrm{in}} = -\dfrac{\hat{P}_{\mathrm{in}}}{\bar{\mathrm{M}}_{\mathrm{in}}}. \end{cases} \tag{4.44}$$

It is worth noting that these boundary conditions are consistent with those employed in the numerical simulations presented in Sec. 3.2.3.

### 4.4.2 Critical-throat boundary condition

The objective here is to define an appropriate boundary condition at the critical-throat position of a thermally choked flow. In the literature, the most widely used approach is the quasi-steady critical Mach-number assumption, which states that Mach-number fluctuations vanish at the steady critical-throat location, *i.e.*, $\mathrm{M}'_* = 0$. This boundary condition can be reformulated in terms of the natural variables, as detailed in Eq. (4.2), and will hereafter be referred to as the QSS boundary condition. However, as shown in Sec. 3.5, the critical-throat position is not steady, and the quasi-steady assumption does not generally hold, even for isentropic nozzles, except in the very low-frequency limit.

To derive a quasi-one-dimensional critical-throat boundary condition for thermally choked nozzles, the linearised quasi-one-dimensional Euler equations for momentum and energy, given in Eq. (4.34), are recalled below:

$$\begin{cases} \dfrac{\partial U}{\partial t} + \bar{u}\dfrac{\partial U}{\partial x} + \dfrac{\bar{c}^2}{\bar{u}}\dfrac{\partial P}{\partial x} + 2\dfrac{\mathrm{d}\bar{u}}{\mathrm{d}x}U + \left(\dfrac{\bar{\kappa}\bar{c}^2}{\bar{u}}\dfrac{\mathrm{d}\bar{T}}{\mathrm{d}x} - \bar{\gamma}\dfrac{\mathrm{d}\bar{u}}{\mathrm{d}x}\right)P + \dfrac{\mathrm{d}\bar{u}}{\mathrm{d}x}D = 0, \\ \dfrac{\partial P}{\partial t} + \bar{u}\dfrac{\partial}{\partial x}(U+P) + (\bar{\gamma}-1)\dfrac{\bar{P}_v}{\bar{\gamma}\bar{p}}U + \bar{\kappa}\bar{T}\left(\dfrac{\bar{P}_v}{\bar{p}} + \dfrac{\bar{u}}{\bar{\rho}}\dfrac{\mathrm{d}\bar{\rho}}{\mathrm{d}x}\right)D \\ \quad + \left(\dfrac{\bar{P}_v}{\bar{p}}\left((\bar{\gamma}-1) - \bar{\kappa}\bar{\gamma}\bar{T}\right) + \bar{\kappa}\bar{u}\left(\dfrac{\mathrm{d}\bar{T}}{\mathrm{d}x} - \dfrac{\bar{\gamma}\bar{T}}{\bar{\rho}}\dfrac{\mathrm{d}\bar{\rho}}{\mathrm{d}x}\right)\right)P = \dfrac{(\bar{\gamma}-1)\bar{P}_v}{\bar{\gamma}\bar{p}}\left(\dfrac{P_v'}{\bar{P}_v}\right). \end{cases} \tag{4.45}$$

The steady velocity profile, $\bar{u}(x)$, is locally approximated near the throat as $\bar{u}(\tilde{x}) = (\mathrm{d}\bar{u}/\mathrm{d}x)_*\,\tilde{x}$, where $(\mathrm{d}\bar{u}/\mathrm{d}x)_*$ denotes the velocity gradient at the critical throat. The coordinate origin, $\tilde{x} = 0$, is chosen such that the extrapolated velocity profile vanishes, *i.e.*, $\bar{u}(0) = 0$. The throat position is therefore located at $\tilde{x}_* = \bar{c}_*/(\mathrm{d}\bar{u}/\mathrm{d}x)_*$. As performed by Marble and Candel [16], the following time–space transformation is introduced:

$$\tau = \frac{\bar{c}_*}{\tilde{x}_*}t, \qquad \xi = \left(\frac{\tilde{x}}{\tilde{x}_*}\right)^2.$$

With this change of variables, the linearised momentum and energy equations become:

$$\begin{cases} \dfrac{\partial U}{\partial \tau} + 2\xi\dfrac{\partial U}{\partial \xi} + 2\dfrac{\bar{c}^2}{\bar{c}_*^2}\dfrac{\partial P}{\partial \xi} + 2\,U + \left(\dfrac{2\bar{\kappa}\bar{c}^2}{\bar{c}_*^2}\dfrac{\mathrm{d}\bar{T}}{\mathrm{d}\xi} - \bar{\gamma}\right)P + D = 0, \\ \dfrac{\partial P}{\partial \tau} + 2\xi\dfrac{\partial}{\partial \xi}(U+P) + \dfrac{(\bar{\gamma}-1)}{(\mathrm{d}\bar{u}/\mathrm{d}x)_*}\dfrac{\bar{P}_v}{\bar{\gamma}\bar{p}}U + \bar{\kappa}\bar{T}\left(\dfrac{\bar{P}_v}{\bar{p}(\mathrm{d}\bar{u}/\mathrm{d}x)_*} + \dfrac{2\xi}{\bar{\rho}}\dfrac{\mathrm{d}\bar{\rho}}{\mathrm{d}\xi}\right)D \\ + \left(\dfrac{\bar{P}_v}{\bar{p}(\mathrm{d}\bar{u}/\mathrm{d}x)_*}((\bar{\gamma}-1) - \bar{\kappa}\bar{\gamma}\bar{T}) + 2\bar{\kappa}\xi\left(\dfrac{\mathrm{d}\bar{T}}{\mathrm{d}\xi} - \dfrac{\bar{\gamma}\bar{T}}{\bar{\rho}}\dfrac{\mathrm{d}\bar{\rho}}{\mathrm{d}\xi}\right)\right)P = \dfrac{(\bar{\gamma}-1)\bar{P}_v}{\bar{\gamma}\bar{p}(\mathrm{d}\bar{u}/\mathrm{d}x)_*}\left(\dfrac{P_v'}{\bar{P}_v}\right). \end{cases} \tag{4.46}$$

Introducing the dimensionless frequency $\Omega = 2\pi f/(\mathrm{d}\bar{u}/\mathrm{d}x)_*$, and applying a Fourier transform with the convention $\chi'(\xi,\tau) = \hat{\chi}(\xi)\exp(+\mathrm{i}\Omega\tau)$, the system becomes:

$$\begin{cases} 2\xi\dfrac{\mathrm{d}\hat{U}}{\mathrm{d}\xi} + 2\dfrac{\bar{c}^2}{\bar{c}_*^2}\dfrac{\mathrm{d}\hat{P}}{\mathrm{d}\xi} + (2+\mathrm{i}\Omega)\,\hat{U} + \left(\dfrac{2\bar{\kappa}\bar{c}^2}{\bar{c}_*^2}\dfrac{\mathrm{d}\bar{T}}{\mathrm{d}\xi} - \bar{\gamma}\right)\hat{P} + \hat{D} = 0, \\ 2\xi\dfrac{\mathrm{d}\hat{U}}{\mathrm{d}\xi} + 2\xi\dfrac{\mathrm{d}\hat{P}}{\mathrm{d}\xi} + \dfrac{(\bar{\gamma}-1)}{(\mathrm{d}\bar{u}/\mathrm{d}x)_*}\dfrac{\bar{P}_v}{\bar{\gamma}\bar{p}}\hat{U} + \bar{\kappa}\bar{T}\left(\dfrac{\bar{P}_v}{\bar{p}(\mathrm{d}\bar{u}/\mathrm{d}x)_*} + \dfrac{2\xi}{\bar{\rho}}\dfrac{\mathrm{d}\bar{\rho}}{\mathrm{d}\xi}\right)\hat{D} \\ + \left(\dfrac{\bar{P}_v}{\bar{p}(\mathrm{d}\bar{u}/\mathrm{d}x)_*}((\bar{\gamma}-1) - \bar{\kappa}\bar{\gamma}\bar{T}) + 2\bar{\kappa}\xi\left(\dfrac{\mathrm{d}\bar{T}}{\mathrm{d}\xi} - \dfrac{\bar{\gamma}\bar{T}}{\bar{\rho}}\dfrac{\mathrm{d}\bar{\rho}}{\mathrm{d}\xi}\right) + \mathrm{i}\Omega\right)\hat{P} \\ = \dfrac{(\bar{\gamma}-1)\bar{P}_v}{\bar{\gamma}\bar{p}(\mathrm{d}\bar{u}/\mathrm{d}x)_*}\left(\dfrac{\hat{P}_v}{\bar{P}_v}\right). \end{cases} \tag{4.47}$$

Subtracting the momentum equation from the energy equation yields:

$$\begin{aligned} &2\left(\xi - \frac{\bar{c}^2}{\bar{c}_*^2}\right)\frac{\mathrm{d}\hat{P}}{\mathrm{d}\xi} - \left(2 + \mathrm{i}\Omega - \frac{(\bar{\gamma}-1)}{(\mathrm{d}\bar{u}/\mathrm{d}x)_*}\frac{\bar{P}_v}{\bar{\gamma}\bar{p}}\right)\hat{U} \\ &+ \left(\bar{\gamma} + \mathrm{i}\Omega + \frac{\bar{P}_v}{\bar{p}(\mathrm{d}\bar{u}/\mathrm{d}x)_*}\left[(\bar{\gamma}-1) - \bar{\kappa}\bar{\gamma}\bar{T}\right] - \frac{2\bar{\kappa}\xi\bar{\gamma}\bar{T}}{\bar{\rho}}\frac{\mathrm{d}\bar{\rho}}{\mathrm{d}\xi} + 2\bar{\kappa}\left(\xi - \frac{\bar{c}^2}{\bar{c}_*^2}\right)\frac{\mathrm{d}\bar{T}}{\mathrm{d}\xi}\right)\hat{P} \\ &+ \left(\bar{\kappa}\bar{T}\left(\frac{\bar{P}_v}{\bar{p}(\mathrm{d}\bar{u}/\mathrm{d}x)_*} + \frac{2\xi}{\bar{\rho}}\frac{\mathrm{d}\bar{\rho}}{\mathrm{d}\xi}\right) - 1\right)\hat{D} = \frac{(\bar{\gamma}-1)\bar{P}_v}{\bar{\gamma}\bar{p}(\mathrm{d}\bar{u}/\mathrm{d}x)_*}\left(\frac{\hat{P}_v}{\bar{P}_v}\right). \end{aligned} \tag{4.48}$$

Assuming that the fluctuating volumetric power source term can be expressed as a linear function of the natural variables, *i.e.*, $(\hat{P}_v/\bar{P}_v) = f_U\,\hat{U} + f_P\,\hat{P} + f_D\,\hat{D}$ (flame transfer function, FTF), Eq. (4.48) can be evaluated at the steady critical throat. Following Crocco's assumption, as proposed by Tsien [18], the variables $\hat{U}$, $\hat{P}$, and $\hat{D}$, as well as their derivatives, are assumed continuous at the throat, and singular terms proportional to $1/(1-\xi)$ are excluded.

Under these assumptions, and since at the throat, $\xi = 1$ and $\bar{c}_* = \bar{c}$, the term proportional to $(\mathrm{d}\hat{P}/\mathrm{d}\xi)_*$ vanishes. The resulting generalised boundary condition (GEN) is:

$$\bar{g}_U \hat{U}_* = \bar{g}_P \hat{P}_* + \bar{g}_D \hat{D}_*, \tag{4.49}$$

where the coefficients are defined as:

$$\begin{cases} \bar{g}_U = 2 + \mathrm{i}\Omega - \dfrac{(\bar{\gamma}_* - 1)}{(\mathrm{d}\bar{u}/\mathrm{d}x)_*}\dfrac{\bar{P}_{v,*}}{\bar{\gamma}_*\bar{p}_*}\,(1 - f_{U,*})\,, \\ \bar{g}_P = \bar{\gamma}_* + \mathrm{i}\Omega + \dfrac{\bar{P}_{v,*}}{\bar{p}_*(\mathrm{d}\bar{u}/\mathrm{d}x)_*}\left[(\bar{\gamma}_* - 1) - \bar{\kappa}_*\bar{\gamma}_*\bar{T}_*\right] - \dfrac{2\bar{\kappa}_*\bar{\gamma}_*\bar{T}_*}{\bar{\rho}_*}\left.\dfrac{\mathrm{d}\bar{\rho}}{\mathrm{d}\xi}\right|_* \\ \qquad - \dfrac{(\bar{\gamma}_* - 1)\bar{P}_{v,*}}{\bar{\gamma}_*\bar{p}_*(\mathrm{d}\bar{u}/\mathrm{d}x)_*} f_{P,*}, \\ \bar{g}_D = \bar{\kappa}_*\bar{T}_*\left(\dfrac{\bar{P}_{v,*}}{\bar{p}_*(\mathrm{d}\bar{u}/\mathrm{d}x)_*} + \dfrac{2}{\bar{\rho}_*}\left.\dfrac{\mathrm{d}\bar{\rho}}{\mathrm{d}\xi}\right|_*\right) - \dfrac{(\bar{\gamma}_* - 1)\bar{P}_{v,*}}{\bar{\gamma}_*\bar{p}_*(\mathrm{d}\bar{u}/\mathrm{d}x)_*} f_{D,*} - 1. \end{cases} \tag{4.50}$$

This critical-throat boundary condition generalises the isentropic formulation derived in Appendix C to heated and non-calorically perfect gas flows.

At very high frequencies ($\Omega \gg 1$), the relation $\hat{U}_* \simeq \hat{P}_*$ emerges, showing that the generation of entropy by acoustic waves becomes negligible. In this regime, acoustic reflection at the throat vanishes, and the GEN boundary condition reduces to a non-reflective, isentropic form.

To summarise, depending on the chosen formulation, the critical-throat boundary condition reads:

$$\text{QSS:} \quad 2\hat{U}_* - \gamma\hat{P}_* + \hat{D}_* = 0, \tag{4.51}$$

$$\text{GEN:} \quad \bar{g}_U\hat{U}_* - \bar{g}_P\hat{P}_* - \bar{g}_D\hat{D}_* = 0. \tag{4.52}$$

## 4.5 Resolution algorithm

The algorithm used to compute the acoustic field in a thermally choked-flow nozzle is described below. A flowchart is provided in Fig. 4.3 to summarise the different steps.

### Subsonic flow field region

Since only two boundary conditions are imposed at the inlet of the subsonic region, a root-finding procedure is required to determine the third component of the inlet state vector $\hat{X}_{\mathrm{in}}$. Specifically, $\hat{P}_{\mathrm{in}}$ and $\hat{D}_{\mathrm{in}}$ are prescribed, while the velocity component $\hat{U}_{\mathrm{in}}$ is initially guessed, forming the inlet trial vector

$$\hat{X}_{\mathrm{in},g} = \left(\hat{U}_{\mathrm{guess}}, \hat{P}_{\mathrm{in}}, \hat{D}_{\mathrm{in}}\right)^T. \tag{4.53}$$

The linear acoustic model Eq. (4.39) is then integrated to obtain the subsonic spatial profiles $\hat{P}(x)$, $\hat{D}(x)$, and $\hat{U}(x)$. At the critical-throat position, $\bar{x}_{\mathrm{cu}}$, the selected boundary condition (see Sec. 4.4.2) is evaluated through a scalar root function, $h(\hat{X}_{\mathrm{in},g})$. The inlet guess vector is updated using the Newton–Raphson method,

$$\hat{X}_{\mathrm{in},g+1} = \hat{X}_{\mathrm{in},g} - \frac{h(\hat{X}_{\mathrm{in},g})}{h'(\hat{X}_{\mathrm{in},g})}, \tag{4.54}$$

where the derivative $h'(\hat{X}_{\text{in},g})$ is approximated using a first-order explicit finite-difference scheme.

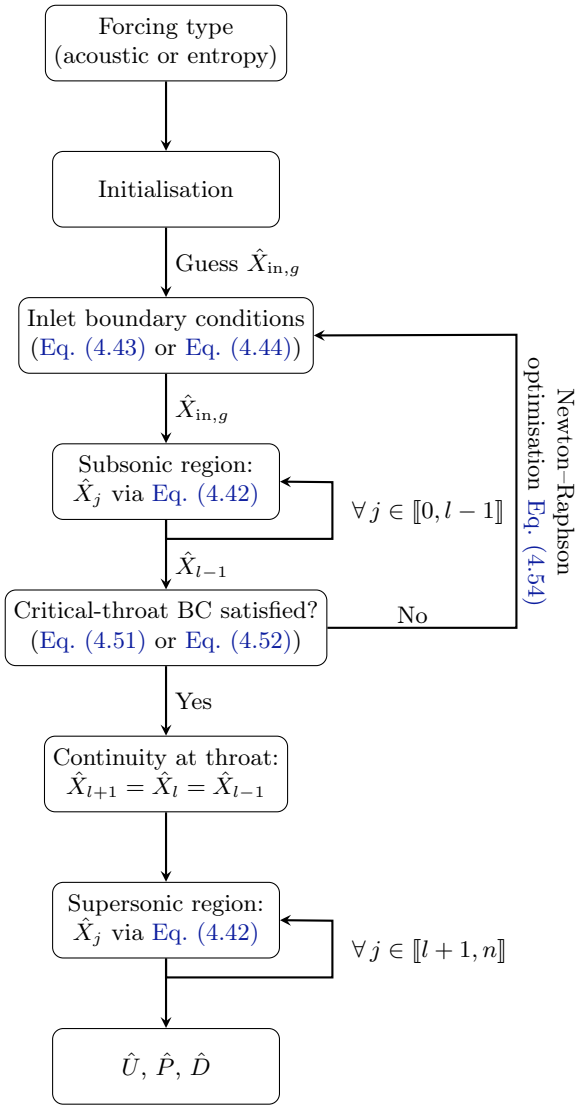


**Figure 4.3** Flowchart of the algorithm used to determine the acoustic field.

Convergence of the root-finding step is enforced by requiring a relative error of $1 \times 10^{-12}$ on the critical-throat boundary condition. The initial guess is taken as a downstream-propagating isentropic acoustic wave for acoustic forcing, and as a downstream-propagating entropy wave for entropy forcing. It has been verified that the initial guess does not affect the final value of $\hat{X}_{\text{in}}$.

### Supersonic flow field region

The supersonic region is then integrated by imposing three inlet boundary conditions immediately downstream of the critical-throat position, $\bar{x}_{\text{cd}}$, and no boundary condition at the outlet, $x_{\text{out}}$. The resulting solution satisfies the continuity constraint $\hat{X}(\bar{x}_{\text{cd}}) = \hat{X}(\bar{x}_*) = \hat{X}(\bar{x}_{\text{cu}})$.

## 4.6 Validation of the linear acoustic model

### 4.6.1 Validation methodology

The proposed GEN BC (Eq. (4.52)) is validated against both thermally and geometrically-choked-flow configurations. For this purpose, the Euler equations are solved using the quasi-one-dimensional linear acoustic model proposed Sec. 4.3 as well as the CFD solver described in Chap. 3. To emphasise the impact of the new formulation, results obtained with the commonly used QSS boundary condition are also reported for comparison.

The validation is carried out under the assumption of no fluctuations in the volumetric power source term, *i.e.*, $P_v'/\bar{P}_v = 0$. Two representative cases are considered: the thermally choked-flow nozzle (Case $C_1$, Sec. 3.2.2) and the equivalent geometric-throat nozzle (Case $C_2$, Sec. 3.2). Together, these two configurations span a broad range of choking mechanisms, thereby providing a comprehensive assessment of the proposed boundary condition.

### 4.6.2 Critical-throat boundary condition

Before validating the acoustic and entropy coefficients, the GEN boundary condition (Eq. (4.52)) is first compared against CFD results. Figure 4.4 shows the normalised critical-throat Mach-number fluctuations, $\hat{\mathrm{M}}_*/\hat{P}_*$, obtained under the isentropic acoustic forcing defined in Sec. 3.2.3, plotted as a function of the dimensionless frequency $\Omega = 2\pi f/(\mathrm{d}\bar{u}/\mathrm{d}x)_*$. Results are presented for the CFD solver: thermal throat (○) and geometric throat (□); and for the quasi-one-dimensional linear acoustic model using the GEN BC: thermal throat (- - -) and geometric throat (····).

From the GEN boundary condition detailed in Sec. 4.4.2, the analytical expression for the normalised critical-throat Mach-number fluctuations reads:

$$\frac{\hat{\mathrm{M}}_*}{\hat{P}_*} = \left[\frac{\bar{g}_P}{\bar{g}_U} - \bar{\gamma}_* \frac{(1+\bar{\kappa}_*\bar{T}_*)}{2}\right] + \left[\frac{\bar{g}_D}{\bar{g}_U} - \frac{(1+\bar{\kappa}_*\bar{T}_*)}{2}\right] \frac{\hat{D}_*}{\hat{P}_*}. \tag{4.55}$$

The relative deviation between the quasi-one-dimensional linear acoustic model (L) and CFD results is quantified as $|1 - (\hat{\mathrm{M}}_*/\hat{P}_*)^{\mathrm{L}}/(\hat{\mathrm{M}}_*/\hat{P}_*)^{\mathrm{CFD}}|$. The forcing amplitude is set to $|\hat{P}_{\mathrm{in}}| = \eta = 10^{-2}$, ensuring that non-linear effects remain negligible. To verify the linearity of the response, three frequencies $\Omega = [3, 8.5, 22]$ were tested with two isentropic forcing amplitudes ($|\hat{P}_{\mathrm{in}}| = 1\times10^{-2}$ and $1\times10^{-3}$). The relative deviations between the responses were on the order of $1\times10^{-3}$, confirming linear behaviour.

For the geometric-throat case, the GEN boundary condition (····) agrees closely with the CFD results (□), with a maximum deviation of about 1.5 % at very low frequencies, which decreases monotonically with increasing frequency.

In the thermally choked-configuration, the GEN boundary condition also performs well, with deviations of about 10 % for $\Omega < 7$ and below 0.1 % at higher frequencies, confirming the accuracy of the proposed model (- - -). At very low frequencies, however, a finite limit, $\lim_{\Omega\to0}|\hat{\mathrm{M}}_*/\hat{P}_*| \simeq 0.2$, is observed due to the volumetric power addition, $P_v$, contradicting the QSS assumption. Notably, applying the QSS condition, $\mathrm{M}_*' = 0$, produces a local singularity in the acoustic field at the critical throat, which is inconsistent with the physical assumption of a continuous and smooth solution.

Under the GEN boundary condition, a local maximum in the deviation is observed proximate to the frequency at which the normalised critical Mach-number fluctuations, $\hat{\mathrm{M}}_*/\hat{P}_*$, peaks. This maximum, occurring at $\Omega = 3.1$, is primarily attributed to the generation of entropy waves induced by the propagation of acoustic waves through a heated medium, as detailed in Sec. 3.4.3. For an unheated flow, *i.e.*, in the geometric-throat case, the density and pressure fluctuations satisfy $\hat{D}_*/\hat{P}_* = 1 - \hat{\sigma}_*/\hat{P}_* = 1$ across all frequencies, resulting in the absence

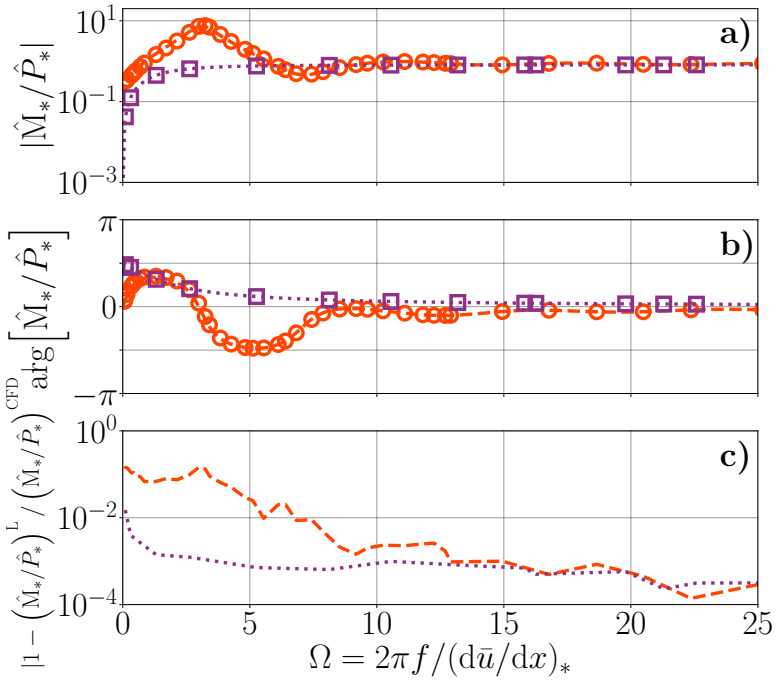


**Figure 4.4** (Colour) Modulus **(a)** and phase-angle **(b)** of the normalised critical Mach-number fluctuations due to isentropic acoustic forcing at the inlet, $\hat{\mathrm{M}}_*/\hat{P}_*$, as a function of the dimensionless frequency $\Omega = 2\pi f/(\mathrm{d}\bar{u}/\mathrm{d}x)_*$. Symbols: (○) and (□) denote CFD results for the thermal and geometric throats, respectively; (- - -) and (····) represent the corresponding results from the quasi-one-dimensional linear acoustic model (L) with the GEN boundary condition (Eq. (4.52)). Panel **(c)** shows the relative deviation between CFD and model predictions.

of a local maximum, as shown in Fig. 4.4. In contrast, for a heated flow, the ratio $\hat{\mathrm{M}}_*/\hat{P}_*$ becomes strongly dependent on the entropy generation term, $\hat{D}_*/\hat{P}_* = 1 - \hat{\sigma}_*/\hat{P}_*$, since the density fluctuations, $\hat{D}_*$, are directly linked to entropy fluctuations via Eq. (2.11). At low frequencies ($0 < \Omega < 3.1$), the entropy waves generated by the propagation of acoustic waves induce additional pressure fluctuations, thereby amplifying the Mach-number fluctuations at the critical throat. At moderate frequencies ($3.1 < \Omega < 10$), the generation of entropy waves induced by acoustic forcing decreases, leading to reduced Mach-number fluctuations at the throat. At high frequencies, $\Omega = \mathcal{O}(10)$, the ratio $\hat{D}_*/\hat{P}_*$ asymptotically approaches unity, indicating that acoustic wave propagation no longer generates significant entropy fluctuations. This completes the results presented in Sec. 3.4.

Figure 4.5 presents the response at the critical throat under entropy-wave forcing, as defined in Sec. 3.2.3, for both geometric-throat (····) and thermal-throat (- - -) configurations. The results are computed using the quasi-one-dimensional linear acoustic model with the GEN BC, and are compared with CFD predictions for the thermal-throat (○) and geometric-throat (□) cases. The normalised critical Mach-number fluctuations, $\hat{\mathrm{M}}_*/\hat{\sigma}_*$, are plotted as a function of the dimensionless frequency, $\Omega = 2\pi f/(\mathrm{d}\bar{u}/\mathrm{d}x)_*$.

The relative deviation between the quasi-one-dimensional linear acoustic model and CFD simulations is quantified as $|1 - (\hat{\mathrm{M}}_*/\hat{\sigma}_*)^{\mathrm{L}}/(\hat{\mathrm{M}}_*/\hat{\sigma}_*)^{\mathrm{CFD}}|$. The amplitude of the imposed entropy wave, $\hat{\sigma}_{\mathrm{in}}$, is set to $\eta = 10^{-2}$, ensuring negligible non-linear effects. For the geometric-throat case (····), the deviation between CFD and the linear model remains within a few percent at low frequencies and decreases rapidly with increasing frequency. In the thermally choked case (- - -), larger deviations are observed at very low frequencies, reaching up to 61 %, but the error falls

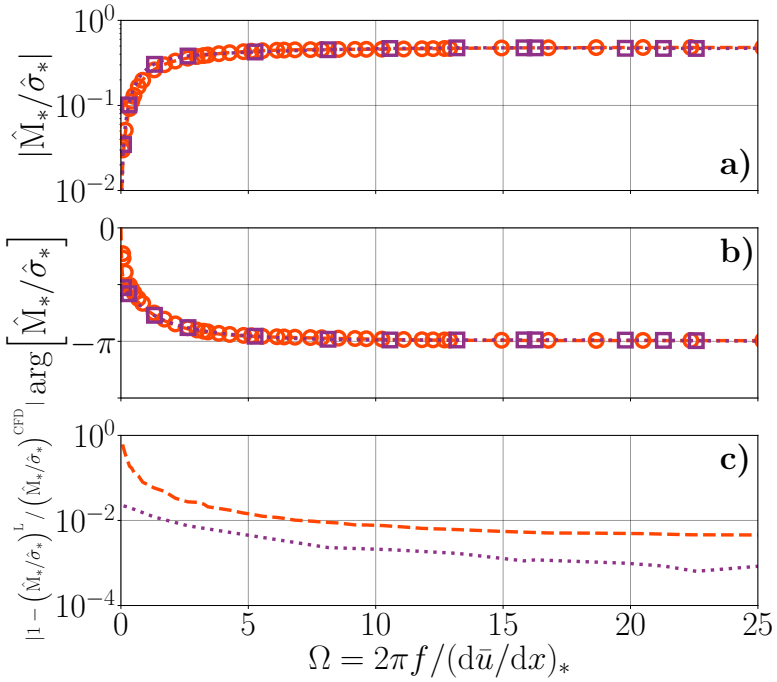


**Figure 4.5** (Colour) Modulus **(a)** and phase-angle **(b)** of the normalised critical Mach-number fluctuations, $\hat{M}_*/\hat{\sigma}_*$, due to entropy forcing at the inlet, as a function of the dimensionless frequency $\Omega = 2\pi f/(d\bar{u}/dx)_*$. Symbols: (○) and (□) denote CFD results for the thermal and geometric throats, respectively; (- - -) and (····) correspond to the quasi-one-dimensional linear acoustic model (L) with the GEN boundary condition (Eq. (4.52)) for the same configurations. Panel **(c)** shows the relative deviation between CFD and linear model predictions.

below 1 % for $\Omega > 5$. In both choking cases, the QSS boundary condition would yield a constant relative deviation of 100 %, due to the erroneous prescription of vanishing critical Mach-number fluctuations, $\hat{M}_* = 0$.

Overall, for both acoustic and entropy forcing, the GEN boundary condition provides a satisfactory prediction of Mach-number fluctuations at the critical throat in both geometrically and thermally choked configurations.

### 4.6.3 Aeroacoustic-reflection coefficients

Figure 4.6 presents the acoustic reflection coefficient, $R_a = \hat{P}^-_{\text{in}}/\hat{P}^+_{\text{in}}$, defined as the ratio of upstream to downstream-propagating acoustic waves at the inlet, for both geometric and thermal-throat configurations. Results from the quasi-one-dimensional linear acoustic model with the GEN boundary condition (lines) are compared with CFD simulations (markers) as a function of the dimensionless frequency, $\Omega = 2\pi f/(d\bar{u}/dx)_*$.

For both choking configurations, good agreement is obtained between the quasi-one-dimensional linear acoustic model (thermal throat: - - -, geometric throat: ····) and the CFD solver (thermal throat: ○, geometric throat: □). The relative deviation $|1 - R_a^{\text{L}}/R_a^{\text{CFD}}|$ remains within 1 % at low frequencies ($\Omega < 10$) when the GEN BC is applied. At higher frequencies ($\Omega > 15$), discrepancies in both modulus and phase become more pronounced, with deviations reaching up to 36 %. These discrepancies were verified to be independent of mesh resolution, time step, and forcing amplitude.

The entropy-noise-production coefficient, $R_s = \hat{P}^-_{\text{in}}/\hat{\sigma}_{\text{in}}$, representing the ratio of the upstream-

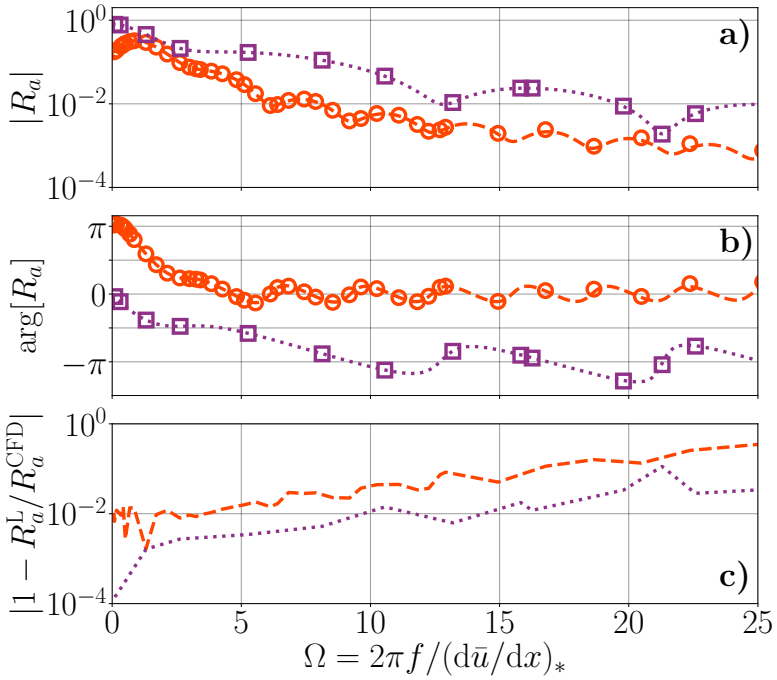


**Figure 4.6** (Colour) Modulus **(a)** and phase-angle **(b)** of the acoustic reflection coefficient, $R_a = \hat{P}^-_{\mathrm{in}}/\hat{P}^+_{\mathrm{in}}$, as a function of the dimensionless frequency, $\Omega = 2\pi f/(\mathrm{d}\bar{u}/\mathrm{d}x)_*$. Symbols: (○) and (□) denote CFD results for the thermal and geometric throats, respectively; (- - -) and (····) correspond to the quasi-one-dimensional linear acoustic model (L) with the GEN boundary condition (Eq. (4.52)) for the same configurations. Panel **(c)** shows the relative deviation between CFD and linear model results.

propagating acoustic wave to the incoming entropy wave, is shown in Fig. 4.7 as a function of $\Omega$.

Again, the GEN-based linear acoustic model (····, - - -) exhibits good agreement with CFD simulations (□, ○) for both nozzle configurations. The relative deviation $|1 - R_s^{\mathrm{L}}/R_s^{\mathrm{CFD}}|$ remains below 2 % for $\Omega < 5$, and within 25 % and 8 % for the thermal and geometric-throat configurations, respectively, across the full frequency range.

These results confirm that the newly proposed critical-throat boundary condition (Eq. (4.52)) provides a reliable closure for the quasi-one-dimensional linear acoustic model, yielding predictions consistent with two-dimensional CFD results.

### 4.6.4 Aeroacoustic-transmission coefficients

The transmission coefficient is now analysed for both geometric-throat and thermal-throat configurations. Figure 4.8 presents the transmission coefficient, $T_a = \hat{P}^+_{\mathrm{out}}/\hat{P}^+_{\mathrm{in}}$, plotted as a function of the dimensionless frequency $\Omega = 2\pi f/(\mathrm{d}\bar{u}/\mathrm{d}x)_*$ for both configurations, as defined in Fig. 4.2. Results are shown for the quasi-one-dimensional linear acoustic model with the GEN boundary condition (lines) and for the CFD solver (markers).

The quasi-one-dimensional linear acoustic model with the GEN boundary condition (thermal throat: - - -, geometric throat: ····) provides accurate predictions of the acoustic transmission coefficient $T_a$, closely matching the CFD results (thermal throat: ○, geometric throat: □) over the entire frequency range considered ($\Omega \leq 25$). The relative deviation, $|1 - T_a^{\mathrm{L}}/T_a^{\mathrm{CFD}}|$, quantifies the difference between the linear acoustic model and CFD. For both configurations, the deviation

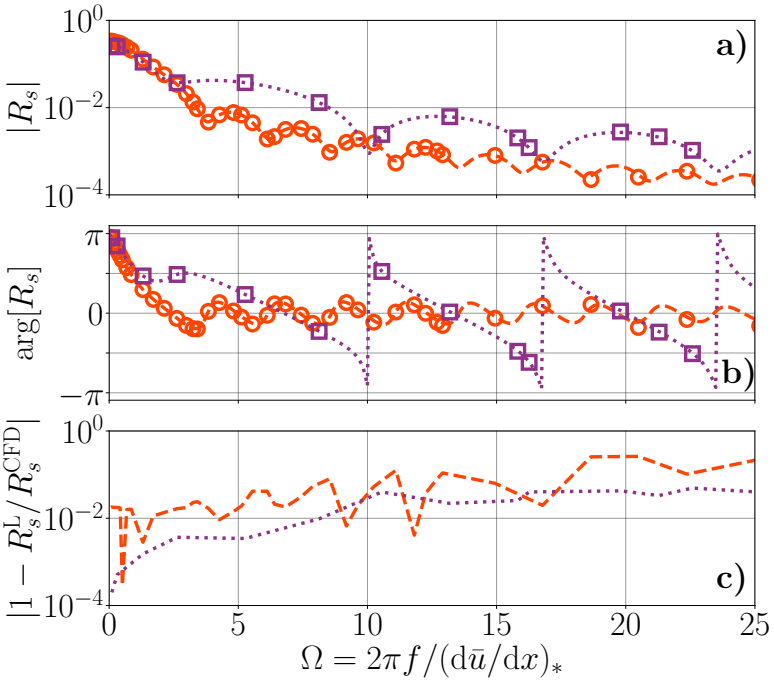


**Figure 4.7** (Colour) Modulus **(a)** and phase-angle **(b)** of the entropy-noise-production coefficient, $R_s = \hat{P}_{\mathrm{in}}^{-}/\hat{\sigma}_{\mathrm{in}}$, as a function of the dimensionless frequency, $\Omega = 2\pi f/(\mathrm{d}\bar{u}/\mathrm{d}x)_*$. Symbols: (○) and (□) denote CFD results for the thermal and geometric throats, respectively; (- - ·) and (····) correspond to the quasi-one-dimensional linear acoustic model (L) with the GEN boundary condition (Eq. (4.52)) for the same configurations. Panel **(c)** shows the relative deviation between CFD and linear model results.

remains below 2 % across all frequencies.

In contrast to the behaviour observed in the geometric-throat configuration, the acoustic transmission coefficient $T_a$ in the thermally choked flow remains below unity across all frequencies. This indicates that, at very low frequencies ($\Omega < 5$), a substantial fraction of the acoustic wave energy is converted into entropy waves. At higher frequencies ($\Omega > 10$), as the thermal throat approaches a purely isentropic acoustic radiation regime, the transmission coefficient converges toward an asymptotic value.

Figure 4.9 shows the entropy-noise-transmission coefficient, $T_s = \hat{P}_{\mathrm{out}}^{+}/\hat{\sigma}_{\mathrm{in}}$, as a function of the dimensionless frequency, $\Omega = 2\pi f/(\mathrm{d}\bar{u}/\mathrm{d}x)_*$, for both geometric and thermal-throat configurations. Results are provided from the quasi-one-dimensional linear acoustic model (lines) and the CFD solver (markers).

Fair agreement is obtained between the quasi-one-dimensional linear acoustic model using the GEN BC (L) and the CFD solver, with deviations of only a few percent at low frequencies for both choking configurations (- - · and ····). At very high frequencies, the deviation increases to approximately 5 %.

Overall, while the GEN boundary condition (Eq. (4.52)) has only a minor impact on the entropy-noise-transmission coefficient, $T_s$, in the geometric-throat configuration, it is essential for achieving accurate predictions in the thermally choked case.

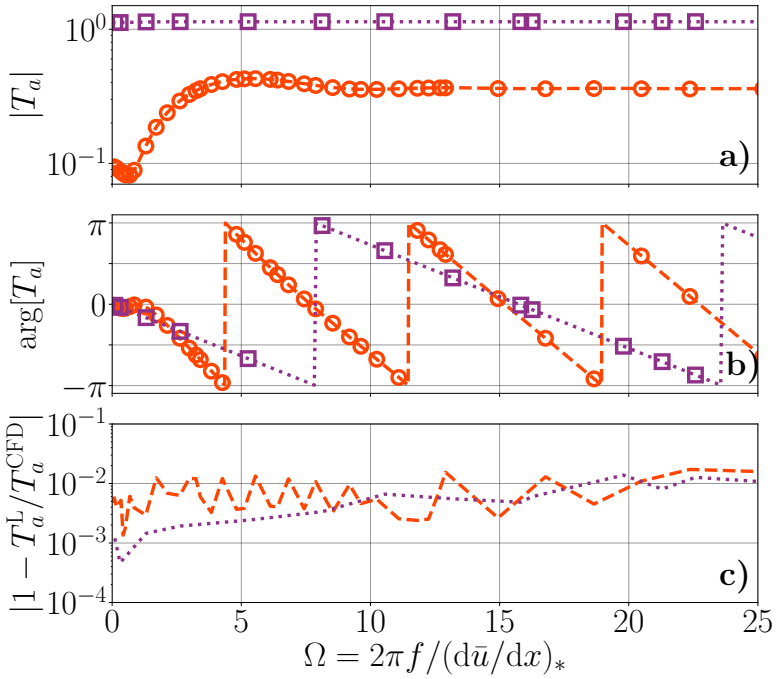


**Figure 4.8** (Colour) Modulus **(a)** and phase-angle **(b)** of the acoustic transmission coefficient, $T_a = \hat{P}^+_{\mathrm{out}}/\hat{P}^+_{\mathrm{in}}$, plotted as a function of the dimensionless frequency, $\Omega = 2\pi f/(\mathrm{d}\bar{u}/\mathrm{d}x)_*$. Symbols: (○) and (□) denote CFD results for the thermal and geometric throats, respectively; (- - ·) and (····) correspond to the quasi-one-dimensional linear acoustic model (L) with the GEN boundary condition (Eq. (4.52)) for the same configurations. Panel **(c)** shows the relative deviation between CFD and linear model results.

### 4.6.5 Impact of the critical-throat boundary condition on the aeroacoustic response

Finally, the impact of the generalised boundary condition (GEN, Eq. (4.52)) is assessed by comparison with the quasi-steady-state (QSS, Eq. (4.51)) boundary condition, which is widely used in the literature. To this end, the relative deviation between CFD results and the quasi-one-dimensional linear acoustic model employing either the GEN or QSS BC is evaluated.

Figure 4.10 presents the relative difference between CFD and linear acoustic model (L) predictions for the acoustic-reflection coefficient ($R_a$), entropy-noise-production coefficient ($R_s$), acoustic-transmission coefficient ($T_a$), and entropy-noise-transmission coefficient ($T_s$). The deviation is computed as $|1-\chi^{\mathrm{L}}/\chi^{\mathrm{CFD}}|$ for $\chi = [R_a, R_s, T_a, T_s]$, for both geometrically and thermally choked configurations, as a function of the dimensionless frequency, $\Omega = 2\pi f/(\mathrm{d}\bar{u}/\mathrm{d}x)_*$. For the thermal-throat configuration, results using the GEN or QSS BC are plotted as (- - ·) and (- - -), respectively; for the geometric-throat case, the GEN and QSS results are shown as (····) and (-··-).

For the geometric-throat configuration, the GEN boundary condition (····) provides a modest improvement over the QSS BC (-··-). The reflection coefficients ($R_a$ and $R_s$) are slightly better predicted, with relative differences of about 0.4 % for $R_a$ and a few percent for $R_s$, especially for frequencies below $\Omega < 10$. For the acoustic-transmission coefficient ($T_a$), the QSS assumption introduces only negligible errors (around 0.15 % at all frequencies). In contrast, for the entropy-noise-transmission coefficient ($T_s$), the GEN BC yields improved accuracy of a few percent across the entire frequency range. Overall, while the GEN boundary condition enhances predictions in

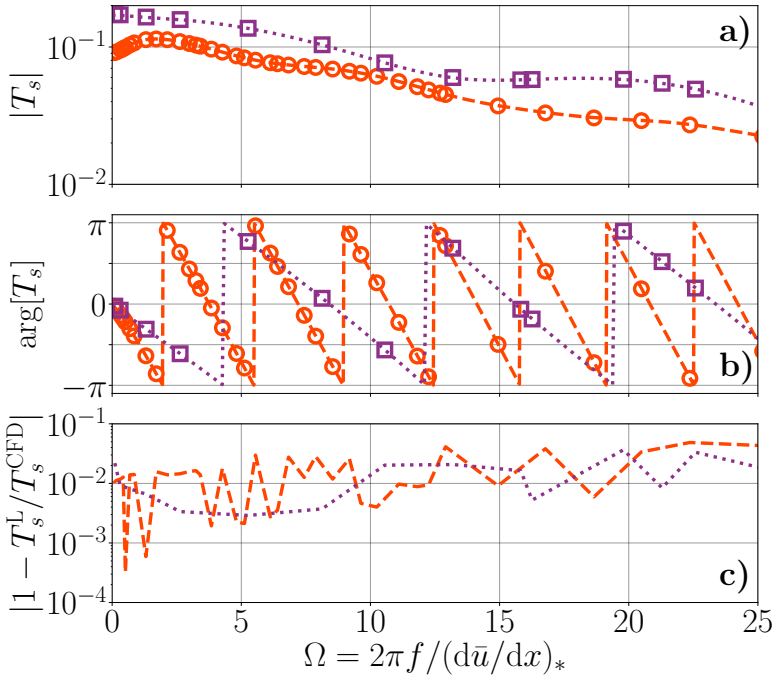


**Figure 4.9** (Colour) Modulus **(a)** and phase-angle **(b)** of the entropy-noise-transmission coefficient, $T_s = \hat{P}^+_{\mathrm{out}}/\hat{\sigma}_{\mathrm{in}}$, plotted as a function of the dimensionless frequency, $\Omega = 2\pi f/(\mathrm{d}\bar{u}/\mathrm{d}x)_*$. Symbols: (○) and (□) denote CFD results for the thermal and geometric throats, respectively; (- - ·) and (····) correspond to the quasi-one-dimensional linear acoustic model (L) with the GEN boundary condition (Eq. (4.52)) for the same configurations. Panel **(c)** shows the relative deviation between CFD and linear model results.

the geometric case, the QSS assumption remains reasonably accurate.

In the thermally choked configuration, the differences are much more pronounced between the GEN (- - ·) and QSS (- - -) boundary conditions. For both reflection coefficients ($R_a$ and $R_s$), errors introduced by the QSS BC range from 10 % to 30 % across most of the frequency range and can exceed 50 % at very low frequencies. The largest discrepancies arise for the transmission coefficients. For the acoustic-transmission coefficient ($T_a$), the QSS model fails to capture the throat behaviour, with errors reaching up to 140 % at very low frequencies and remaining around 10 % even at higher frequencies, where the throat response asymptotically approaches an isentropic acoustic condition. Similar behaviour is observed for the entropy-noise-transmission coefficient ($T_s$), where QSS-induced errors reach 40 % at low frequencies and remain near 20 % up to $\Omega = 25$.

At low frequencies ($\Omega < 10$), the QSS BC produces deviations of only a few percent in the geometric-throat case but up to 50 % in the thermal-throat configuration. This discrepancy is mainly due to the complex dynamics of the critical throat under acoustic forcing: while the QSS model enforces vanishing Mach-number fluctuations, the GEN formulation predicts a finite value, avoiding the unphysical divergence observed in the QSS case.

To further highlight the impact of the boundary condition on the aeroacoustic response in a thermally choked-flow configuration, the profile of the normalised pressure fluctuations $\hat{P}(x)$ for several acoustic forcing frequencies is plotted in Fig. 4.11. This quantity is obtained, at four forcing frequencies $\Omega = [0.09, 2.62, 6.12, 10.24]$, either from the CFD solver, or from the quasi-one-dimensional linear acoustic model incorporating either the proposed generalised boundary condition (GEN: Eq. (4.52)) or the usual quasi-steady boundary condition $\mathrm{M}'_* = 0$

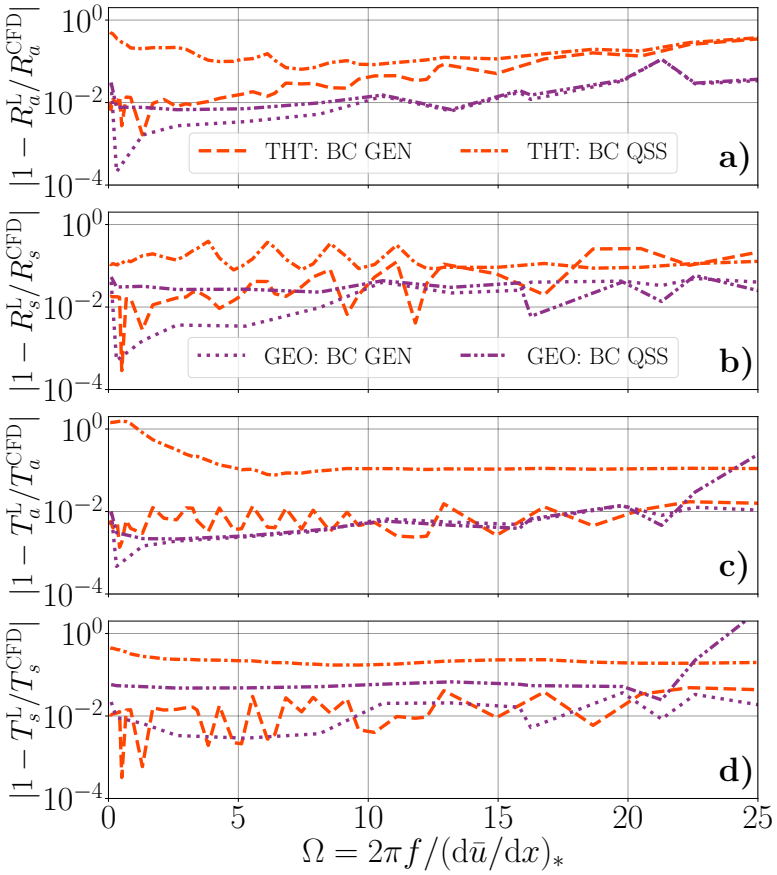


**Figure 4.10** (Colour) Relative deviation between CFD and two linear acoustic models employing different critical-throat boundary conditions. $\chi^{\mathrm{CFD}}$ denotes the CFD results, $\chi^{\mathrm{L}}$ the predictions obtained from the linear acoustic model using either the generalised boundary condition (Eq. (4.52)), or the quasi-steady-state (QSS) boundary condition (Eq. (4.51)). The acoustic quantities considered are $\chi = [R_a, R_s, T_a, T_s]$, shown as a function of the dimensionless frequency, $\Omega = 2\pi f/(\mathrm{d}\bar{u}/\mathrm{d}x)_*$ in panels **(a)**–**(d)**, respectively. Results are presented for both choking configurations: thermal throat (- - and - ·) and geometric throat (···· and - ··-).

(QSS: Eq. (4.51)).

A good level of agreement is obtained between the CFD results and the predictions of the linear acoustic model when the GEN boundary condition is used (Eq. (4.52)). This is particularly true at the critical throat, where the linear steady velocity profile assumption allows a smooth transition from the subsonic to the supersonic region for all forcing frequencies. This confirms that the proposed boundary condition correctly reproduces the physical behaviour of the thermal throat.

In contrast, using the QSS boundary condition (Eq. (4.51)) in the linear acoustic model introduces a singularity in the profile of the normalised pressure fluctuations $\hat{P}(x)$ at the critical throat. At low frequencies ($\Omega \leq 2.62$), this boundary condition generates a noticeable deviation in both the subsonic and supersonic pressure profiles. This deviation propagates to the other normalised quantities (velocity $\hat{U}$ and density $\hat{D}$, even if not shown here), which explains the discrepancies observed in the acoustic-reflection coefficient $R_a$ and the entropy–noise–production coefficient $R_s$ in Fig. 4.10.

For higher frequencies ($\Omega \geq 6.12$), although the behaviour at the critical throat is still not well captured by the QSS boundary condition, the pressure fluctuations in the subsonic part of

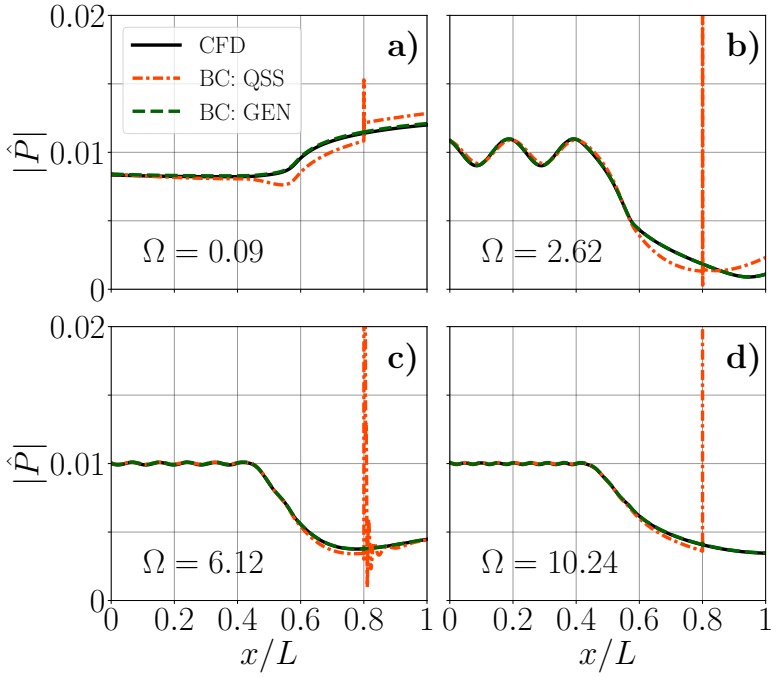


**Figure 4.11** (Colour) Modulus of the normalised pressure fluctuations $\hat{P}$ as a function of the longitudinal position $x/L$ for a thermally choked-flow configuration, at four acoustic forcing frequencies $\Omega = [0.09, 2.62, 6.12, 10.24]$, in panels **(a)**–**(d)**, respectively. The results are obtained either from the CFD solver (—) or from the linear acoustic model using two boundary conditions: GEN (Eq. (4.52), - - -) and QSS (Eq. (4.51), - - -).

the flow are fairly well reproduced. This leads to the moderate differences between the GEN and QSS boundary conditions previously observed in Fig. 4.10. This behaviour arises because, at high forcing frequencies, the characteristic time of the acoustic waves is much smaller than the characteristic time of the mean-flow adjustment, so that the influence of the latter on the acoustic field is reduced. At very high frequencies ($\Omega > 10$), however, the singularity induced by the QSS boundary condition causes the linear acoustic model to exhibit a large deviation in the supersonic part of the flow. As discussed in Sec. 4.6.2, the higher the forcing frequency, the larger the discrepancy becomes between the actual critical-throat behaviour and the quasi-steady assumption at the throat, which explains the growth of the singularity as the boundary condition becomes increasingly inaccurate.

In summary, the proposed GEN boundary condition is essential for accurately capturing the behaviour of thermally choked flows, where the QSS BC fails, and also provides moderate improvements in the geometric-throat case, particularly in the prediction of transmission coefficients over a wide frequency range.

## 4.7 Impact of the inlet Mach number on the aeroacoustic response

The proposed quasi-one-dimensional linear acoustic model is now used to assess the influence of the inlet Mach number on the aeroacoustic response, thereby completing the analysis previously performed in Chap. 3 on the effect of the steady thermal throat position. To isolate this effect, the thermal throat position is fixed at $\delta_*/L = 0.38$, and the volumetric power (see Sec. 2.5) is adjusted

to maintain this steady thermal throat while varying the inlet Mach number. The remaining inlet conditions, namely the total temperature and the static pressure, are kept identical for all cases, as specified in Tab. 3.1.

Figure 4.12 presents the steady fields of Mach number M, static pressure $p$, and static temperature $T$ as a function of the longitudinal coordinate $x/L$. Six inlet Mach numbers are considered, ranging from $\mathrm{M_{in}} = 0.5$ to 0.75, thereby covering a broad set of operational conditions. Owing to the very small transverse variations of these quantities, only the one-dimensional distributions are shown. All steady quantities are extracted along the symmetry axis, and it has been verified that the transverse position does not alter their values.

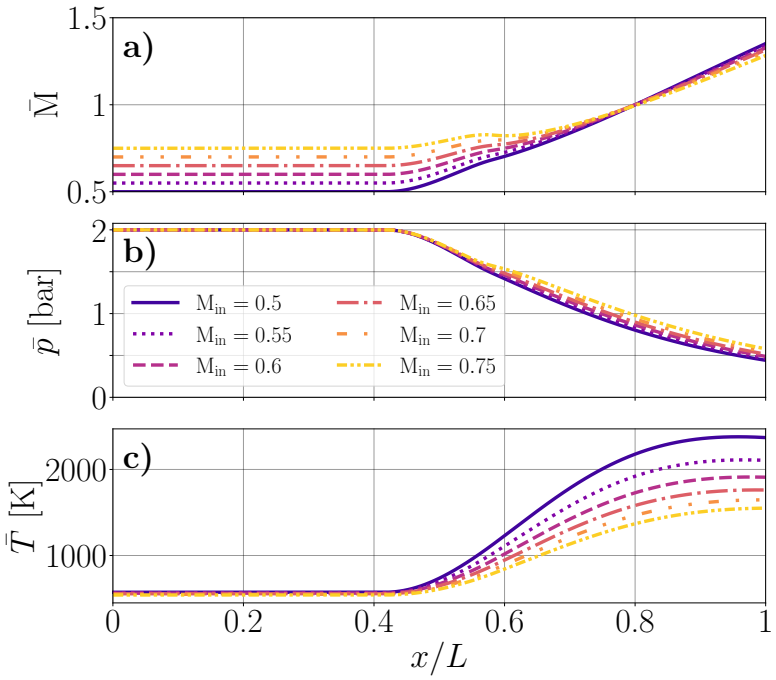


**Figure 4.12** (Colour) Steady Mach number $\bar{\mathrm{M}}(x)$, static pressure $\bar{p}(x)$, and static temperature $\bar{T}(x)$ as a function of $x/L$ for six different inlet Mach numbers: $\mathrm{M_{in}} = 0.5$ to 0.75.

As expected, the higher the inlet Mach number, the smaller the amount of energy required to choke the flow at a given position of $\delta_*/L = 0.38$. Consequently, the static-temperature rise is less pronounced for the higher–Mach-number cases, with a maximum value of $\bar{T}_{\mathrm{M_{in}}=0.75} = 1550\,\mathrm{K}$, compared with $\bar{T}_{\mathrm{M_{in}}=0.50} = 2380\,\mathrm{K}$. This weaker temperature increase leads to a smaller variation in the heat capacity ratio $\gamma$. This result highlights the necessity of accounting for the thermophysical dependence on static temperature (see Sec. 2.2.5), as this quantity can vary significantly depending on the operating condition. Moreover, since the inlet Mach number is varied while the inlet total temperature is kept constant, the inlet static temperature readjusts accordingly: it increases for lower inlet Mach numbers and decreases for higher inlet Mach numbers.

The resulting steady base flow is now used as input to the quasi-one-dimensional linear acoustic model presented in Sec. 4.3. Figure 4.13 displays the acoustic-reflection coefficient $R_a$, computed under an inlet acoustic forcing of normalised amplitude $p'_{\mathrm{in}}/(\bar{\gamma}_{\mathrm{in}}\bar{p}_{\mathrm{in}}) = \eta = 1\,\%$. The acoustic response is shown as a function of the dimensionless frequency $\Omega = 2\pi f/(\mathrm{d}\bar{u}/\mathrm{d}x)_*$.

The behaviour at very low frequencies ($\Omega < 0.2$) varies significantly with the inlet Mach number. For the lowest value, $\mathrm{M_{in}} = 0.5$ (—), the acoustic-reflection coefficient sharply decreases to $|R_a| \approx 3 \times 10^{-3}$. In contrast, for higher inlet Mach numbers, such as $\mathrm{M_{in}} = 0.75$ (-·-), the

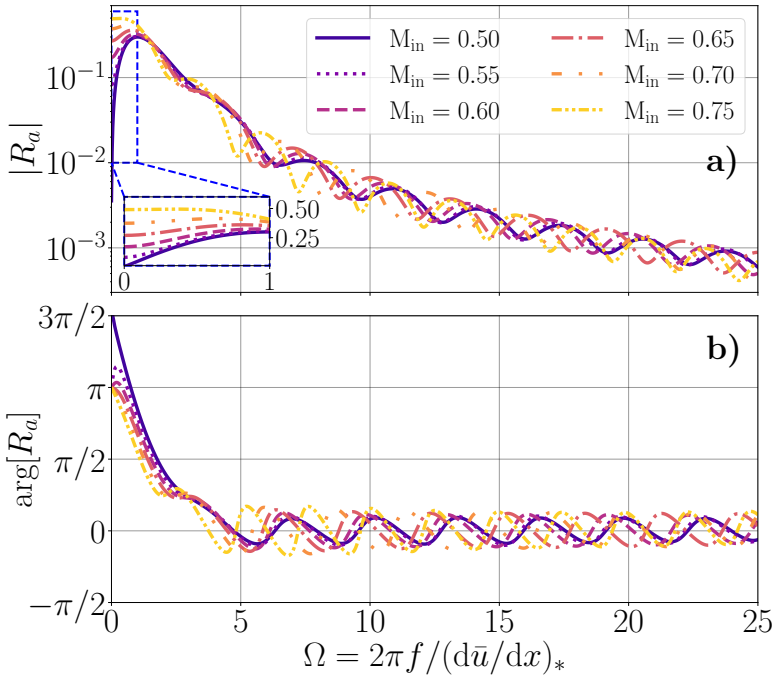


**Figure 4.13** (Colour) Modulus **(a)** and phase-angle **(b)** of the acoustic-reflection coefficient $R_a$ as a function of the dimensionless frequency $\Omega$ for six different inlet Mach numbers: $M_{in} = 0.5$ to 0.75.

damping is much less pronounced because the entropy conversion is weaker. In this case, the maximum acoustic response occurs in the zero-frequency limit (*i.e.*, as $\Omega \to 0$), where it reaches $|R_a| \approx 5 \times 10^{-1}$. The smaller static-temperature gradient associated with the higher inlet Mach number produces fewer entropy waves, explaining the weaker damping. In all cases, the quasi-steady limit predicted for an isentropic compact nozzle by Marble and Candel [16] is not recovered, owing to the presence of heat addition.

Despite these differences in the low-frequency regime, the frequency at which the maximum acoustic reflection occurs is nearly identical for all configurations, indicating that this peak is primarily governed by the fixed thermal-throat position. As discussed previously, the strong acoustic damping observed at low inlet Mach numbers results from the efficient conversion of the downstream-propagating acoustic wave into entropy waves, which drastically reduces the amplitude of the upstream-propagating acoustic component.

It can also be shown that the frequency at which the acoustic reflection reaches its maximum, corresponding to a change in the convexity of the curve, is close to $\Omega = 1$. This confirms that the dimensionless frequency $\Omega$ provides a physically meaningful scaling for interpreting the aeroacoustic response of thermally choked flows.

At high frequencies ($\Omega > 3$), the acoustic behaviour of all configurations becomes nearly identical, and local maxima appear in the modulus of the acoustic response. These preferential frequencies scale approximately as $\Delta f \approx 6/\tau$, where $\tau$ denotes the back and forth acoustic propagation time between the onset of the heated region and the steady thermal-throat position,

$$\tau = \int_{x_u}^{x_*} \left( \frac{1}{\bar{c}(\xi) + \bar{u}(\xi)} + \frac{1}{\bar{c}(\xi) - \bar{u}(\xi)} \right) \mathrm{d}\xi. \tag{4.56}$$

The physical interpretation of this scaling factor (6) is not yet fully understood.

The indirect entropy noise was then characterised for the same six thermally choked configurations using the entropy-noise-production coefficient $R_s$. Figure 4.14 shows $R_s$ as a function of the dimensionless frequency $\Omega$. A normalised entropy fluctuation of amplitude $\eta = s'/\bar{c}_p = 1\,\%$ was imposed at the inlet.

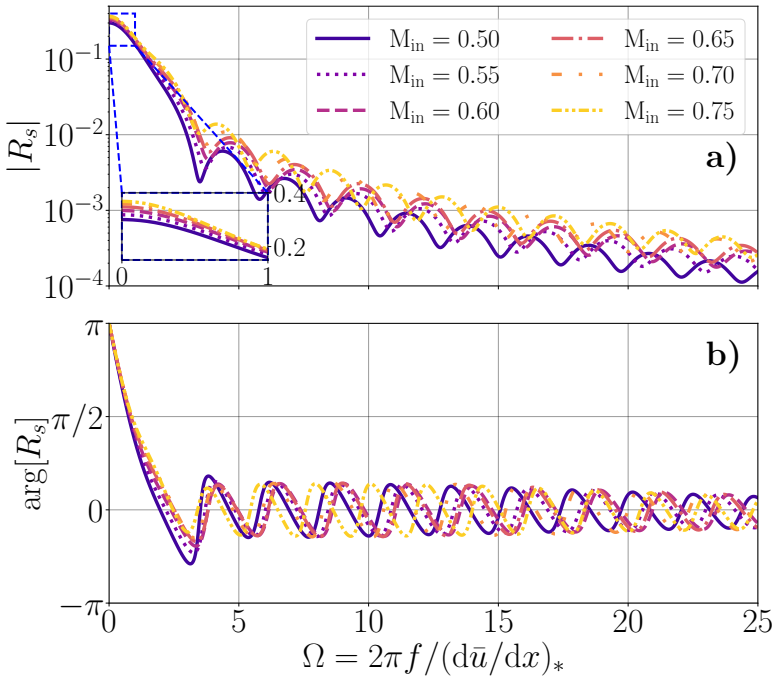


**Figure 4.14** (Colour) Modulus **(a)** and phase-angle **(b)** of the entropy-noise-production coefficient $R_s$ as a function of the dimensionless frequency $\Omega$ for six different inlet Mach numbers: $\mathrm{M_{in}} = 0.5$ to 0.75.

At low frequencies, the influence of the inlet Mach number on the entropy-induced acoustic response is significant. All configurations exhibit the same qualitative trend, but with different zero-frequency limits: $|R_s| \approx 0.30$ for the lowest inlet Mach number, $\mathrm{M_{in}} = 0.5$ (—), and $|R_s| \approx 0.36$ for the highest one, $\mathrm{M_{in}} = 0.75$ (-·-). This represents an increase of about 20 %.

Physically, at higher Mach numbers, the temperature gradient inside the nozzle is weaker, which reduces the acoustic damping normally associated with entropy forcing. As a result, a larger fraction of the imposed entropy fluctuations is able to generate acoustic waves. However, even under these favourable conditions, only about one third of the entropy disturbance is converted into acoustic energy, meaning that the indirect noise mechanism remains relatively inefficient compared with the entropy injected into the nozzle. Conversely, at lower Mach numbers, the stronger temperature gradient amplify the damping of acoustic waves, counteracting the stronger entropy generation. This balancing effect explains why the low-frequency entropy–acoustic response remains similar across configurations, despite the differences in Mach number.

At higher frequencies, all configurations exhibit similar behaviour, characterised by local maxima associated with the position of the steady thermal throat. Using the sum of the entropy- and acoustic-wave propagation times between the onset of the heat-release region and the steady thermal throat,

$$\tau = \int_{x_\mathrm{u}}^{x_*} \left( \frac{1}{\bar{u}(\xi)} + \frac{1}{\bar{c}(\xi) - \bar{u}(\xi)} \right) \mathrm{d}\xi, \tag{4.57}$$

where $\bar{u}$ and $\bar{c}$ denote the mean flow velocity and speed of sound, respectively, the frequency spacing of these maxima is found to scale approximately as $\Delta f \approx 5/\tau$. The origin of this scaling

factor remains to be explained.

To summarise, the base flow, whether through the steady thermal-throat position (see Sec. 3.4.4) or the inlet Mach number, has a significant impact on the aeroacoustic response, particularly at very low frequencies. The quasi-one-dimensional model provides a useful framework for examining in detail the role of each parameter.

## 4.8 Limit of the linear acoustic regime

Finally, to assess the limits of the proposed linear acoustic model, a sensitivity analysis of the aeroacoustic response coefficients, $R_a$ and $R_s$, with respect to the normalised forcing amplitude $\eta$ is carried out (see Sec. 3.2.3). A nonlinear acoustic response is expected for sufficiently large forcing amplitudes.

For each forcing type (isentropic acoustic and entropy), three normalised amplitudes are tested: $\eta = [1\,\%,\ 5\,\%,\ 10\,\%]$. At these levels of fluctuations, nonlinear effects are expected to occur. The configuration in which the thermal throat is located deep within the divergent nozzle, using the Wang flame model (see Sec. 2.5), is used to evaluate the validity of the linear acoustic model.

Figure 4.15 presents the acoustic-reflection coefficient, $R_a$, as a function of the dimensionless frequency, $\Omega$, for the thermally choked-flow configuration. Results from the linear acoustic model are shown alongside CFD data for the three forcing amplitudes.

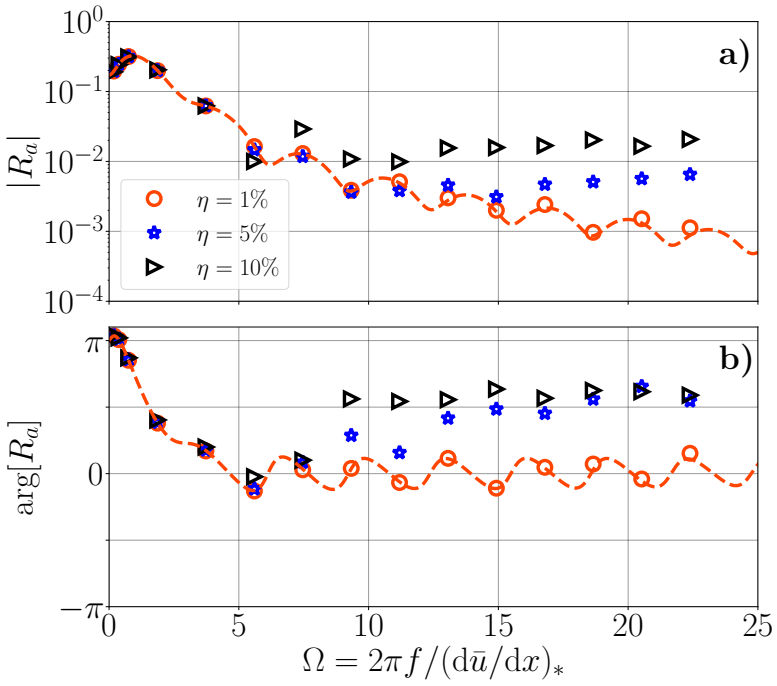


**Figure 4.15** (Colour) Modulus **(a)** and phase-angle **(b)** of the acoustic-reflection coefficient, $R_a$, as a function of the dimensionless frequency $\Omega = 2\pi f/(\mathrm{d}\bar{u}/\mathrm{d}x)_*$ for the thermal-throat configuration. Results from the linear acoustic model (- - -) are shown alongside CFD results for three distinct forcing amplitudes, $\eta$: 1 % (○), 5 % (☆), and 10 % (▷).

As expected, some discrepancies arise between the numerical results and the linear acoustic model. The frequency at which the deviation becomes significant is approximately $\Omega = 5$ for $\eta = 10\,\%$ and $\Omega = 7.5$ for $\eta = 5\,\%$, indicating that nonlinear effects depend on both frequency and forcing amplitude. It is noteworthy that a distinct difference appears between the linear

and nonlinear acoustic responses. The linear acoustic model predicts a decrease in the acoustic-reflection coefficient, $R_a$, which is consistent with the linear behaviour of the critical-throat boundary condition: at high frequencies, an isentropic acoustic radiation regime is expected. However, under nonlinear forcing, the acoustic-reflection coefficient does not decrease with frequency. This behaviour is unexpected, as in the nonlinear regime, part of the energy of the fundamental frequency is transferred to higher harmonics.

Figure 4.16 details the entropy-noise-production coefficient, $R_s$, for the thermally-choked-flow configuration as a function of the dimensionless frequency $\Omega$. The numerical results are shown for three amplitude forcing $\eta$: 1 % (○), 5 % (☆), and 10 % (▷) as well as the results from the linear acoustic model (- - -).

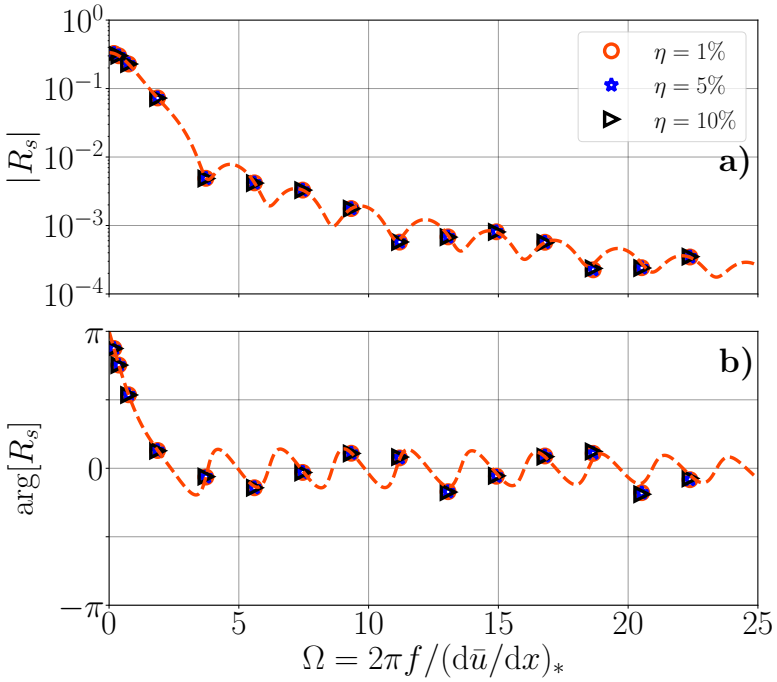


**Figure 4.16** (Colour) Modulus **(a)** and phase-angle **(b)** of the entropy-noise-production coefficient, $R_s$, as a function of the dimensionless frequency $\Omega = 2\pi f/(\mathrm{d}\bar{u}/\mathrm{d}x)_*$ for the thermal-throat configuration. Results from the linear acoustic model (- - -) are shown alongside CFD results for three distinct forcing amplitudes, $\eta$: 1 % (○), 5 % (☆), and 10 % (▷).

For all forcing amplitudes, the numerical results show good agreement with the linear acoustic model, even for large forcing amplitudes ($\eta = 10\,\%$). When entropy waves are introduced into the system, unlike acoustic waves, they are convected downstream with the mean flow and cannot propagate upstream. Consequently, the nonlinear terms, such as $s's'$, which become non-negligible compared with the steady component $\bar{s}$ at high forcing amplitudes, are also convected toward the nozzle outlet. The additional noise generated by these nonlinear contributions remains limited, as the conversion of entropy waves into acoustic waves is weak, as observed in Sec. 3.4.5.

To summarise, nonlinear behaviour of the acoustic response is observed for acoustic forcing, whereas the effect of large entropy forcing remains limited as the normalised forcing amplitude increases. Nevertheless, the linear acoustic model shows good agreement with the numerical results up to mid frequencies ($\Omega \approx 5$). Future work could extend the present model to larger forcing amplitudes by incorporating nonlinear effects into the formulation, *i.e.*, by retaining terms such that $\chi'\chi' \neq 0$. This is particularly relevant since thermoacoustic instabilities in dual-mode ramjet engines are known to occur over a wide range of frequencies, as demonstrated by Boulal

*et al.* [141].

### Chapter conclusion

In this chapter, a quasi-one-dimensional linear acoustic model has been developed to predict the aeroacoustic response of thermally choked nozzles with non-uniform flow. The model builds upon the theoretical framework introduced in the previous chapters and extends it by introducing a new critical-throat boundary condition (GEN) specifically adapted to heated, non-isentropic configurations.
Compared with the conventional quasi-steady-state assumption ($M'_* = 0$), the proposed GEN formulation captures the unsteady dynamics of the thermal throat more accurately. It ensures continuity of the acoustic solution and avoids the unphysical singularities produced by the QSS model at low frequencies. Validation against two-dimensional CFD simulations confirms the robustness of the model across both acoustic and entropy forcing.
The GEN boundary condition provides improved predictions for all aeroacoustic coefficients, with deviations from CFD results typically below $2-5$ % for most frequencies. It successfully reproduces the reduction in acoustic reflection and the enhanced entropy–acoustic coupling induced by the heated region, two key mechanisms governing the behaviour of thermally choked flows.
The model is then used to assess in detail the impact of the inlet Mach number on the aeroacoustic response of a thermally choked-flow configuration, thereby completing the analysis in Chap. 3 on the effect of the steady thermal throat position. The results show that, especially at low frequencies, a lower inlet Mach number leads to significant acoustic damping induced by the strong temperature gradient. As the inlet Mach number is increased, the static temperature gradient decreases, leading to a higher acoustic response at low frequencies. At high frequencies, the inlet Mach number has little impact on the acoustic response. Furthermore, a parametric analysis of the forcing amplitude demonstrates the range of validity of the linear regime. While the acoustic response exhibits nonlinear effects at high forcing levels, entropy forcing remains predominantly linear, validating the model assumptions for small-amplitude perturbations.
Overall, the proposed quasi-one-dimensional model offers a computationally efficient and physically consistent framework for analysing wave propagation in thermally choked configurations. It bridges the gap between CFD-based simulations and analytical stability studies. In the following chapter, this model is extended to include an unsteady flame-transfer function, enabling the investigation of thermoacoustic coupling mechanisms and instability development in dual-mode ramjet nozzles.

Chapter 5

# Influence of a thermoacoustic coupling on the aeroacoustic response of a thermally choked nozzle

*Après, moi, pour le détail, je sais pas...*

**Breccan [2]**


## Abstract

This chapter presents a systematic investigation of how unsteady volumetric heat release influences the aeroacoustic response of a thermally choked-flow nozzle. Building upon the quasi-one-dimensional linear acoustic model developed in Chap. 4, the study incorporates a simplified thermoacoustic coupling based on Dowling's kinematic premixed-flame model (*J. Fluid Mech.* 1999), enabling unsteady heat-release fluctuations to be introduced into the framework. Two flame parameters, the flame speed and the flame-holder ratio, are varied to characterise their influence on the coupled flame–acoustic dynamics. The analysis reveals that unsteady heat release can significantly amplify upstream-propagating acoustic waves, especially for fast flames and compact flame-holders. In contrast, entropy-induced noise remains only moderately affected by the coupling.

Finally, two indicators of thermoacoustic stability are evaluated: the amplification ratio of the acoustic response and the Rayleigh index. Both metrics show that configurations combining high flame speed, irrespective of the flame-holder ratios present the highest susceptibility to instability. The results demonstrate that even a simplified flame-transfer-function model can substantially alter the aeroacoustic behaviour of thermally choked flows and provides a first step toward understanding thermoacoustic coupling mechanisms in thermally choked dual-mode ramjet nozzles.



This chapter is a truncation of the following publication, submitted during the PhD:

F. Olivon, A. Genot, J.-E. Durand, and E. Piot. "Thermoacoustic instabilities linear study of a canonical thermally choked-flow nozzle". In: *Journal of Propulsion and Power* (2026). HAL: hal-05526862.

Contents

**5.1 Objective and literature review . . . . . 92**
**5.2 Model of the flame–acoustic response for a premixed ducted flame . 97**
5.2.1 Reformulation of the quasi-one-dimensional linear acoustic model . . . 98
5.2.2 Critical-throat boundary condition with FTF . . . . . 99
**5.3 Effects of a thermoacoustic model on the aeroacoustic response . . . 99**
5.3.1 Effect of the flame speed . . . . . 100
5.3.2 Effect of the flame-holder height . . . . . 103
5.3.3 Role of the non-dimensional flame frequency . . . . . 104
**5.4 Thermoacoustic stability study of a canonical thermally choked-flow nozzle . . . . . 107**
5.4.1 Amplification ratio of the aeroacoustic response . . . . . 107
5.4.2 Rayleigh index and potential instabilities . . . . . 108

## 5.1 Objective and literature review

In the preceding chapters, the volumetric power used to thermally choke the flow was kept constant; that is, flow perturbations did not modify the heat-release rate supplied to the mean flow. This setting enabled a systematic examination of how steady heat addition influences the scattering of acoustic and entropy waves across several thermally choked configurations (Chaps. 3 and 4). Building on these results, and in particular on the formulation of a new boundary condition at the critical throat, a quasi-one-dimensional linear acoustic model for non-uniformly heated flow was developed and validated (Chap. 4).

The present chapter employs this model to extend the analysis to a broader set of thermally choked-flow configurations, now considering unsteady volumetric power. The linear framework requires only the steady-state flow field to compute the frequency-domain acoustic response over a wide range of frequencies; each frequency evaluation is very cheap (a few seconds). In contrast, computational fluid dynamics (CFD) simulations demand orders of magnitude more computational time (hours per run), which underscores the efficiency and predictive capability of the linear approach for parametric studies.

Accordingly, this chapter bridges the gap between analyses with purely steady heat release and fully coupled thermoacoustic configurations (see Fig. 5.1). The quasi-one-dimensional linear acoustic model of Chap. 4 is used to investigate, within a small-perturbation framework, how the unsteady heat-release rate affects both acoustic and entropy waves. Two aspects are addressed: (i) the influence of the unsteady heat-release distribution on the upstream-propagating acoustic response across a wide range of inlet parameters; and (ii) the thermoacoustic stability of a thermally choked flow with a simplified flame–acoustic model.

Before introducing the thermoacoustic model adopted in this chapter, a brief review of the relevant literature is provided. The effects of steady and unsteady heat-release rates have largely been studied analytically in separate contexts, and the same separation is used here. The influence of a steady temperature gradient on the acoustic response is typically examined independently, as in Karimi *et al.* [95] and Yeddula *et al.* [96], which address subsonic or geometrically choked configurations. Conversely, the acoustic forcing of unsteady flames has been extensively investigated in laboratory-scale systems, notably by Bloxsidge *et al.* [142] and Schuller *et al.* [90]. In the context of geometrically choked configurations, Yeddula *et al.* [28] was among the first to couple a linear acoustic model with both a steady volumetric heat-release source term and a

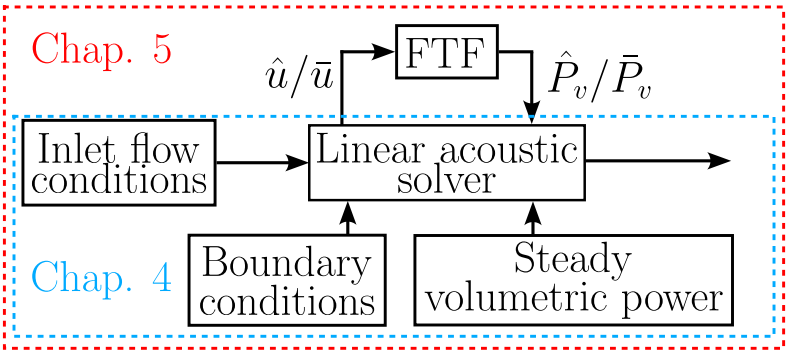


**Figure 5.1** (Colour) Sketch of the thermoacoustic coupling introduced in the quasi-one-dimensional linear acoustic model used in this chapter.

flame-response function. Whereas earlier studies typically focused on one mechanism at a time, Yeddula *et al.* [28] showed that including a fluctuating heat-release term via a flame-transfer function (FTF) introduces a low-frequency filtering effect.

For the latter class of models, the flame is generally assumed acoustically compact, meaning that its characteristic length (*e.g.*, the combustion zone) is much smaller than the acoustic wavelength of interest. Under this assumption, its influence on the mean flow and the acoustic field can be represented through jump conditions [98, 143]. However, in practical configurations, such as dual-mode ramjet combustors, both steady and unsteady heat-release rates are spatially distributed along the combustion chamber and the nozzle. To the best of the author's knowledge, no model currently captures, within a unified framework, the coupled effects of distributed steady and unsteady heat release on both the acoustic and entropy responses.

#### Flame structure in a dual-mode ramjet combustor

Before introducing the acoustic flame-response models proposed in the literature, the main flame types encountered in ramjet-based combustors are briefly reviewed. Owing to the complexity of reacting flows, the combustion community typically relies on canonical configurations to facilitate analysis. Following Poinsot and Veynante [98], flames are commonly classified into four categories according to the mixing process (fully premixed or non-premixed) and the flow regime (laminar or turbulent); see Fig. 5.2.

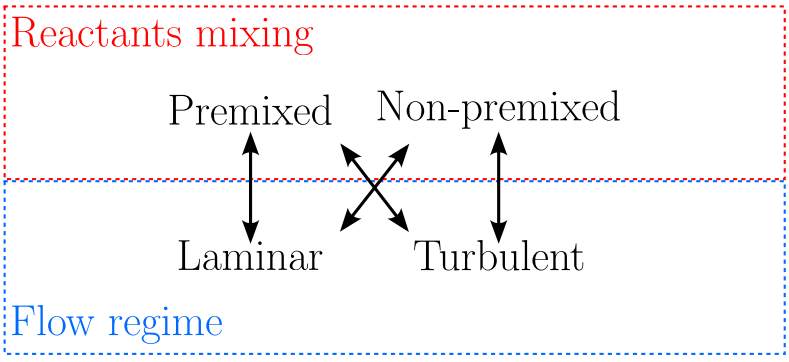


**Figure 5.2** (Colour) Sketch adapted from Veynante [144], showing the canonical flame configurations.

The first classification concerns the mixing of the reactants (fuel and oxidiser). If mixing takes place upstream of the high-temperature reaction zone, the flame is said to be premixed.

Conversely, if reactants mix predominantly within the reaction zone, the flame is referred to as non-premixed (or a diffusion flame). These two classes exhibit distinct physical and chemical behaviours.

A second classification concerns the flow regime. For low Reynolds numbers[1], the flow is laminar and the flame front remains smooth and stable. At high Reynolds numbers, the flow, and thus the flame, becomes turbulent: the front is wrinkled, unsteady, and highly convoluted. As combustion modelling is not the primary focus here, the reader is referred to Poinsot and Veynante [98] for an in-depth discussion of these regimes.

In dual-mode ramjet combustors, the flame structure is considerably more complex and cannot be reduced to a single, well-defined front. For example, Gicquel and Roux [124] reported, in ONERA's *Statoréacteur de Recherche*, the coexistence of regions exhibiting premixed behaviour with other regions governed by non-premixed (diffusion) combustion; see Fig. 5.3. The flame is highly turbulent and spatially distributed along the combustion chamber and into the nozzle [42], a feature that has direct implications for acoustic–flame coupling models introduced later in this chapter.

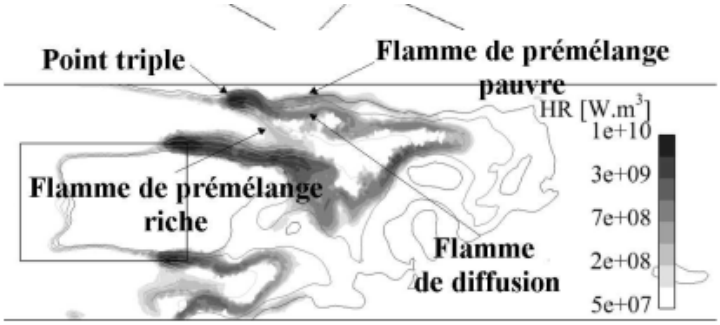


**Figure 5.3** Flame structure in the *Statoréacteur de Recherche*, visualised by the local heat-release rate (HR), reproduced from Roux [145]. Lean and rich premixed flames coexist with a diffusion flame.

Given the pronounced spatio–temporal variability and complexity of flame dynamics in ramjet-based combustors, the present study primarily considers premixed-flame configurations, which are deemed more representative of the operating conditions of interest. Nevertheless, the actual flame structure can be considerably more intricate, as shown by Bekaert *et al.* [101] and Roux [145].

### Flame–acoustic response models

The interaction between unsteady combustion and acoustics has been a central topic in the study of thermoacoustic instabilities for more than half a century. In premixed-flame systems, pressure fluctuations generate velocity perturbations at the flame base, modulating the flame surface area and, consequently, the heat-release rate. This unsteady heat release, in turn, produces acoustic waves that can either amplify or attenuate pressure oscillations depending on their phase relation with the acoustic field, as quantified by Rayleigh's index (see Sec. 1.2.2). Establishing quantitative models for this two-way coupling, referred to in this chapter as the flame response, remains one of the major challenges in thermoacoustic instability research.

A seminal contribution was made by Crocco and Cheng [146], who related fluctuations in the volumetric heat-release rate $P'_v$ to fluctuations in the velocity $u'$ through a simple time lag $\tau$ and

[1]The Reynolds number $R_e$ is the ratio of inertial to viscous forces. For predominantly one-dimensional flow, $R_e = \rho u L/\mu$, where $\rho$ is the density, $u$ the flow velocity, $L$ a characteristic length, and $\mu$ the dynamic viscosity.

a proportionality coefficient $n$:

$$P_v'(t) = n\,u'(t-\tau), \tag{5.1}$$

where the time lag $\tau$ represents the time required for the flame to respond to an incoming velocity perturbation (typically associated with the vortex convection time). Although simple, this model does not account for the low-pass filtering behaviour observed in laboratory flame experiments [147].

To extend such models, a framework for the description of such instabilities was developed by Bloxsidge *et al.* [142], who formulated a one-dimensional acoustic model for an afterburner-type configuration in which longitudinal acoustic modes couple with the unsteady combustion process. This early work provided the conceptual foundation for the modern view of the flame as an active acoustic boundary, capable of amplifying or attenuating the surrounding acoustic field.

To describe the flame-front dynamics, a widely adopted approach is based on the so-called $G$-equation, which tracks the propagation of a level set function $G(\mathbf{x},t) = 0$ representing the flame surface [98]. The equation

$$\frac{\partial G}{\partial t} + \mathbf{u}\cdot\nabla G = -\boldsymbol{S}_f|\nabla G|, \tag{5.2}$$

relates the local displacement of the flame front to the flow velocity $\mathbf{u}$ and the flame speed $\boldsymbol{S}_f$ (see Fig. 5.4).

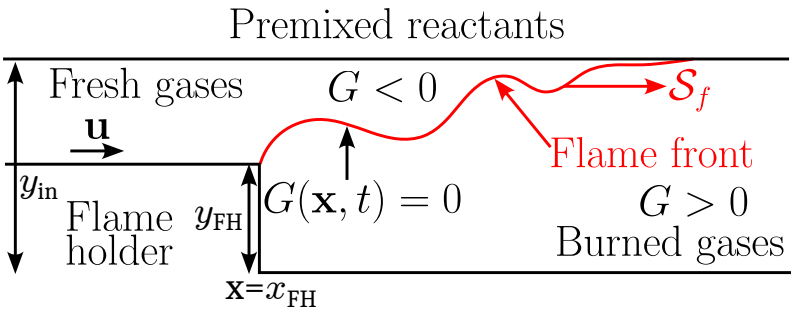


**Figure 5.4** (Colour) Sketch of principle of the $G$-equation (Eq. (5.2)), adapted from Dowling [67].

In the linear regime, small-amplitude perturbations of the velocity field induce proportional perturbations of the flame surface and, consequently, of the volumetric power distribution, such that

$$\frac{\hat{P}_v}{\bar{P}_v} = \mathcal{F}(\omega)\,\frac{\hat{u}}{\bar{u}}, \tag{5.3}$$

where $\mathcal{F}(\omega) = \mathcal{G}(\omega)\,\mathrm{e}^{\mathrm{i}\Phi(\omega)}$ denotes the complex flame transfer function (FTF) in the frequency domain.

This function encapsulates the frequency-dependent gain $\mathcal{G}(\omega)$ and phase lag $\Phi(\omega)$ between velocity and heat-release fluctuations, and represents the most widely used closure in low-order thermoacoustic modelling. Its accurate description, however, depends strongly on the underlying flame geometry, flow regime, and forcing amplitude.

The first systematic investigations of the FTF were primarily empirical. Controlled acoustic forcing was imposed on laboratory-scale premixed flames, and the resulting modulation of the global heat release was measured through chemiluminescence or pressure sensors [148–150]. These

experiments established the characteristic behaviour of premixed flames: a low-frequency regime where the flame responds quasi-steadily to flow perturbations, followed by a phase-lag increase and gain decay as the forcing frequency approaches the inverse convective time of the flame. Although extremely valuable for calibration, these empirical models are generally restricted to acoustically compact flames and cannot be directly extended to industrially relevant, spatially distributed systems.

To overcome these limitations, analytical kinematic models were developed to capture the spatio-temporal evolution of the flame front under flow perturbations. Dowling [67] proposed a model in which the unsteady displacement of a flame anchored in a duct is described using a linearised $G$-equation. This approach allowed the direct computation of the flame dynamic response as a function of the mean flame angle, flow velocity, and forcing frequency. It successfully reproduced the frequency shift and amplitude trends observed in the experiments of Bloxsidge *et al.* [142]. Subsequently, Schuller *et al.* [90] generalised this analysis by deriving analytical expressions of the transfer functions for both conical and V-shaped flames. Their work showed that the response depends primarily on two non-dimensional parameters: the reduced frequency $\omega R/(\mathcal{S}_L \cos\alpha)$, which represents the ratio of the acoustic wavelength to the flame length $R$, and the flame angle $\alpha$, which characterises the ratio of the laminar burning velocity $\mathcal{S}_L$ to the mean flow velocity. These analytical results provided a unifying framework for various flame configurations and clarified the physical role of convection in determining the phase lag between velocity and heat release rate fluctuations.

The growing recognition that flame dynamics are inherently nonlinear led to the extension of these ideas toward amplitude-dependent formulations. The so-called flame describing function (FDF) was introduced to generalise the linear FTF concept by incorporating the saturation effects of large-amplitude perturbations. The FDF framework, formalised by Noiray *et al.* [151] and further discussed by Lieuwen [91], assumes that the flame response can be described by a gain and phase that depend on both frequency and the amplitude of the imposed velocity oscillations, formalised in Eq. (5.4). This concept enabled a consistent description of nonlinear phenomena such as limit-cycle oscillations, hysteresis, and modal switching in practical combustors. It also provided a means to close low-order models that could predict self-sustained oscillations without resorting to fully time-resolved simulations.

$$\mathcal{F}(\omega, |u'(\omega)|) = \mathcal{G}(\omega,|u'(\omega)|)\mathrm{e}^{\mathrm{i}\Phi(\omega,|u'(\omega)|)} \tag{5.4}$$

Parallel to these theoretical efforts, numerical and experimental studies have progressively improved the quantitative characterisation of the FTF and FDF. Analytical studies [90, 91, 151] have provided simplified yet insightful descriptions, while detailed experiments have been performed on both laminar and turbulent flames to measure transfer functions under controlled forcing [148–150]. In parallel, computational methods based on unsteady Reynolds-averaged Navier–Stokes (URANS) and LES have been used to determine the nonlinear coupling between heat release and acoustics [10, 54]. LES in particular has proven capable of capturing self-excited oscillations, though at a considerable computational cost, while URANS remains the most common industrial tool for low-frequency, forced-response analyses. These combined efforts have considerably advanced the understanding of flame–acoustic coupling; yet, most available models remain tailored to compact, laboratory-scale flames and rely on simplified assumptions about geometry and mean flow.

For distributed or spatially extended flames, such as those encountered in ramjets, analytical models capable of representing both the steady and unsteady components of heat release are still lacking. In such configurations, the flame cannot be considered acoustically compact, and the volumetric distribution of the heat source plays a dominant role in the coupling dynamics. To the author's knowledge, no model presently captures both the distributed nature of the

flame and its frequency-dependent acoustic response within a tractable analytical framework. Therefore, the present work focuses on incorporating simplified flame response models into a quasi-one-dimensional acoustic formulation. The aim is twofold: (i) to integrate a term explicitly representing the flame response within the governing equations, and (ii) to assess how different flame response formulations affect the resulting aeroacoustic behaviour under various flow and heating configurations.

Accordingly, a single model is retained for comparison: the kinematic formulation of Dowling [67], which provides a physically grounded analytical expression for the flame response derived from the linearised $G$-equation. These approaches are complementary: the kinematic closure supplies the flame-response law, while its integration into the quasi-one-dimensional acoustic model enables a systematic assessment of how the chosen formulation influences the aeroacoustic behaviour and the potential stability of the nozzle.

## 5.2 Model of the flame–acoustic response for a premixed ducted flame

Dowling [67] developed a formulation to model the acoustic response of a premixed flame anchored in a ducted configuration. The approach relies on a kinematic description of the flame motion induced by velocity perturbations and by the propagation of vortex structures shed from the lips of the flame-holder (see Fig. 5.4). This model solely accounts for acoustic waves associated with velocity fluctuations and their interaction with the flame, and was developed under the assumptions of low-Mach-number flow and quasi-constant density across the flame front [67]. Two versions of the model were proposed to describe, respectively, the linear and nonlinear acoustic regimes. In the present study, only the linear formulation is retained.

Longitudinal harmonic fluctuations in the volumetric heat-release rate $\hat{P}_v/\bar{P}_v$ throughout the flame are assumed to originate solely from fluctuations in the velocity at the flame-holder location $\hat{U}(x_{\mathrm{FH}})$ which are convected downstream on the flame surface with a time delay $\tau(x)$ determined by the steady velocity field $\bar{u}(x)$. Accordingly, the local heat-release fluctuations are expressed in terms of the flame transfer function $\mathcal{F}$ as

$$\frac{\hat{P}_v(x)}{\bar{P}_v(x)} = \mathcal{F}(x, \Omega_{\mathcal{F}})\, \hat{U}(x_{\mathrm{FH}}), \tag{5.5}$$

where

$$\mathcal{F}(x, \Omega_{\mathcal{F}}) = \mathcal{G}(\Omega_{\mathcal{F}}) \exp(-\mathrm{i}\omega\tau(x))\,, \tag{5.6}$$

and the convective delay associated with the velocity fluctuations propagating along the flame surface is defined as

$$\tau(x) = \int_{x_{\mathrm{FH}}}^{x} \frac{\mathrm{d}\xi}{\bar{u}(\xi)}. \tag{5.7}$$

The gain function $\mathcal{G}(\Omega_{\mathcal{F}})$ depends on the dimensionless flame-related frequency $\Omega_{\mathcal{F}}$, which represents the ratio of the acoustic-forcing period to the convective time along the flame front, and on the flame-holder ratio $C_{\mathrm{FH}} = y_{\mathrm{FH}}/y_{\mathrm{in}}$:

$$\mathcal{G}(\Omega_{\mathcal{F}}) = \frac{2}{\mathrm{i}\Omega_{\mathcal{F}}(1 + C_{\mathrm{FH}})} \left[ C_{\mathrm{FH}} - \exp(-\mathrm{i}\Omega_{\mathcal{F}}) + \frac{1 - C_{\mathrm{FH}}}{\mathrm{i}\Omega_{\mathcal{F}}} \left(1 - \exp(-\mathrm{i}\Omega_{\mathcal{F}})\right) \right], \tag{5.8}$$

where the non-dimensional flame frequency is defined as

$$\Omega_{\mathcal{F}} = \frac{\omega\, y_{\mathrm{in}}\, (1 - C_{\mathrm{FH}})}{\mathcal{S}_f \sqrt{1 - (\mathcal{S}_f/\bar{u}(x_{\mathrm{FH}}))^2}}. \tag{5.9}$$

This model depends primarily on two geometric and physical parameters: the flame-holder ratio $C_{\mathrm{FH}}$ and the flame speed $\mathcal{S}_f$. These two quantities determine the characteristic length and time scales that govern how the flame responds to incoming velocity perturbations. The non-dimensional parameter $C_{\mathrm{FH}}$ directly controls the relative flame-holder height and therefore influences both the strength and the frequency dependence of the flame–acoustic coupling in the kinematic model.

At very low frequencies $\omega$, the dimensionless flame frequency $\Omega_{\mathcal{F}}$ tends to zero, which yields an indeterminate form for the flame function $\mathcal{G}(\Omega_{\mathcal{F}})$. To avoid numerical issues, a series expansion of $\mathcal{G}(\Omega_{\mathcal{F}})$ is performed for $\Omega_{\mathcal{F}} \to 0$. A first-order Taylor expansion gives

$$\mathcal{G}(\Omega_{\mathcal{F}}) \underset{\Omega_{\mathcal{F}}\to 0}{=} 1 \; - \; \mathrm{i}\,\frac{2 + C_{\mathrm{FH}}}{3\,(1 + C_{\mathrm{FH}})}\,\Omega_{\mathcal{F}} \; + \; \mathcal{O}\big(\Omega_{\mathcal{F}}^2\big)\,. \tag{5.10}$$

This expression shows that $\mathcal{G} \to 1$ as $\Omega_{\mathcal{F}} \to 0$, with a linear correction of slope $-\mathrm{i}\,(2 + C_{\mathrm{FH}})/\big[3\,(1 + C_{\mathrm{FH}})\big]$. In practice, this series expansion is used to regularise the evaluation at low frequency, and $\mathcal{G}(0) = 1$ is imposed for zero-frequency forcing. Physically, the limit $\mathcal{G} \to 1$ corresponds to the quasi-steady regime, in which the forcing period is much larger than the flame characteristic time, then the heat-release fluctuations follow the velocity perturbations without phase lag.

At very high frequencies, $\Omega_{\mathcal{F}} \to \infty$, the flame function satisfies $\mathcal{G}(\Omega_{\mathcal{F}}) \to 0$, indicating that the flame no longer influences the acoustic field. In this regime, the forcing period is much shorter than the characteristic flame time associated with the convection of velocity perturbations along the flame front. As a result, the flame cannot adjust its surface or heat-release rate in phase with the rapid acoustic oscillations, and its contribution to the acoustic field becomes negligible.

### 5.2.1 Reformulation of the quasi-one-dimensional linear acoustic model

The quasi-one-dimensional linear acoustic model introduced in Eq. (4.42) is reformulated to include the flame–transfer function (FTF) as

$$\frac{\mathrm{d}\hat{X}}{\mathrm{d}x} \; + \; \bar{K}_1^{-1}\bar{K}_2\,\hat{X} \; = \; \bar{L}(x), \tag{5.11}$$

where $\hat{X}(x)$ is the state vector, $\bar{C}(x) = -\bar{K}_1^{-1}\bar{K}_2$ is the coefficient matrix, and

$$\bar{L}(x) = \frac{(\bar{\gamma}-1)\bar{P}_v}{\bar{\gamma}\bar{p}}\frac{1}{\bar{u}(1-\bar{\mathrm{M}}^2)}\begin{bmatrix} 1 \\ -\bar{\mathrm{M}}^2 \\ -1 \end{bmatrix}\begin{pmatrix} \hat{P}_v \\ \bar{P}_v \end{pmatrix}, \tag{5.12}$$

The matrices $\bar{K}_1$ and $\bar{K}_2$ are defined in Sec. 4.3. The source term $\bar{L}(x)$ activates downstream of the flame-holder location $x_{\mathrm{FH}}$. Upstream of the flame-holder, $\hat{U}(x_{\mathrm{FH}})$ is set to zero in the evaluation of $\bar{L}$ so that the flame contribution is null before the injector.

Equation (5.11) is integrated along the discretised nozzle using a classical explicit fourth-order Runge–Kutta (RK4) scheme already presented in Chap. 4. The computational domain is divided into $n$ cells of uniform width $\Delta x$, indexed by $j \in [\![0, \ldots, l-1, l, l+1, \ldots, n]\!]$, with $j = l$ corresponding to the critical-throat location. The RK4 update reads

$$\hat{X}_{j+1} \; = \; \hat{X}_j \; + \; \frac{\Delta x}{6}\Big(k_1 + 2k_2 + 2k_3 + k_4\Big), \tag{5.13}$$

with intermediate slopes (for all $j \neq l$)

$$
\begin{aligned}
k_1 &= \bar{C}_j\,\hat{X}_j + \bar{L}_j,\\
k_2 &= \frac{\bar{C}_j + \bar{C}_{j+1}}{2}\left(\hat{X}_j + \frac{\Delta x}{2}\,k_1\right) + \frac{\bar{L}_j + \bar{L}_{j+1}}{2},\\
k_3 &= \frac{\bar{C}_j + \bar{C}_{j+1}}{2}\left(\hat{X}_j + \frac{\Delta x}{2}\,k_2\right) + \frac{\bar{L}_j + \bar{L}_{j+1}}{2},\\
k_4 &= \bar{C}_{j+1}\left(\hat{X}_j + \Delta x\,k_3\right) + \bar{L}_{j+1}.
\end{aligned}
$$

At $j = l$, the update is replaced by the critical-throat boundary condition below.

### 5.2.2 Critical-throat boundary condition with FTF

The boundary condition at the critical throat is modified to include the flame contribution:

$$
\bar{g}_U\,\hat{U}_* \;=\; \bar{g}_P\,\hat{P}_* \;+\; \bar{g}_D\,\hat{D}_* \;+\; \bar{g}_{\mathcal{F}}\frac{\hat{P}_{v,*}}{\bar{P}_{v,*}}, \tag{5.14}
$$

with coefficients

$$
\begin{cases}
\bar{g}_U = 2 + \mathrm{i}\Omega - \dfrac{(\bar{\gamma}_* - 1)}{(\mathrm{d}\bar{u}/\mathrm{d}x)_*}\dfrac{\bar{P}_{v,*}}{\bar{\gamma}_*\bar{p}_*},\\[2ex]
\bar{g}_P = \bar{\gamma}_* + \mathrm{i}\Omega + \dfrac{\bar{P}_{v,*}}{\bar{p}_*\,(\mathrm{d}\bar{u}/\mathrm{d}x)_*}\left[(\bar{\gamma}_* - 1) - \bar{\kappa}_*\bar{\gamma}_*\bar{T}_*\right] - \dfrac{2\,\bar{\kappa}_*\bar{\gamma}_*\bar{T}_*}{\bar{\rho}_*}\left.\dfrac{\mathrm{d}\bar{\rho}}{\mathrm{d}\xi}\right|_*,\\[2ex]
\bar{g}_D = \bar{\kappa}_*\bar{T}_*\left(\dfrac{\bar{P}_{v,*}}{\bar{p}_*\,(\mathrm{d}\bar{u}/\mathrm{d}x)_*} + \dfrac{2}{\bar{\rho}_*}\left.\dfrac{\mathrm{d}\bar{\rho}}{\mathrm{d}\xi}\right|_*\right) - 1,\\[2ex]
\bar{g}_{\mathcal{F}} = -\dfrac{(\bar{\gamma}_* - 1)\,\bar{P}_{v,*}}{\bar{\gamma}_*\,\bar{p}_*(\mathrm{d}\bar{u}/\mathrm{d}x)_*}.
\end{cases} \tag{5.15}
$$

The term $\bar{g}_{\mathcal{F}}$ embeds the local dimensionless flame response. More details on the derivation of this critical-throat boundary condition are given in Sec. 4.4.2. The complete numerical procedure is detailed in Sec. 4.5.

The asymptotic behaviour of this boundary condition is of particular interest. At very high frequencies ($\Omega \gg 1$), $\bar{g}_{\mathcal{F}}$ tends toward zero (see Eq. (5.5)), and the relation $\hat{U}_* = \hat{P}_*$ is recovered. This indicates that, in an unsteady heated medium, the entropy generated by propagating acoustic waves becomes negligible, since $\hat{D}_* = \hat{P}_* - \hat{\sigma}_*$ remains small compared with $\hat{P}_*$. Consequently, acoustic reflection at the critical throat vanishes, and the boundary condition asymptotically approaches an isentropic, non-reflective behaviour. Furthermore, the dimensionless flame frequency $\Omega_{\mathcal{F}}$ is linearly proportional, for a chosen parametric conditions, to the dimensionless acoustic frequency $\Omega$. Hence, one has $\Omega_{\mathcal{F}} \gg 1$ while $\Omega = \mathcal{O}(1)$, implying that flame–acoustics coupling effects are primarily significant at low frequencies.

## 5.3 Effects of a thermoacoustic model on the aeroacoustic response

The effects of introducing a thermoacoustic coupling into the quasi-one-dimensional linear acoustic model are now assessed over a wide range of conditions. The steady base flow corresponding to

a thermal-throat position of $\delta_*/L = 0.38$ and an inlet Mach number of $\mathrm{M_{in}} = 0.6$ is selected and used as input to the linear acoustic model. It is worth noting that the steady volumetric power distribution $P_v(x)$ remains unchanged, even when the FTF model parameters are modified. This is a limitation of the present study, as it would require recomputing the steady volumetric power profile as a function of the flame speed $\mathcal{S}_f$ and the flame-holder height $y_{\mathrm{in}}$. The acoustic–flame formulation (Eq. (5.8)) depends on two parameters: the flame speed $\mathcal{S}_f$ and the flame-holder ratio $C_{\mathrm{FH}}$. The ranges retained for these two parameters are justified below.

The flame speed $\mathcal{S}_f$ depends primarily on the fuel–air mixture, the local thermochemical state, and the flow regime. In laminar premixed flames, $\mathcal{S}_f$ increases with the equivalence ratio and with the reactants temperature, while in turbulent configurations, the effective flame speed is significantly enhanced through flame-surface wrinkling and stretch. Experimental and numerical studies conducted in the LAERTE facility at ONERA [41] indicate that, under typical ramjet operating conditions, effective flame speeds generally lie in the interval $\mathcal{S}_f \approx 0.5\,\mathrm{m\,s^{-1}}$ to $1\,\mathrm{m\,s^{-1}}$, and may reach up to $\mathcal{S}_f \approx 2\,\mathrm{m\,s^{-1}}$ when the flame is strongly turbulent.

Additional guidance comes from the work of Zettervall and Fureby [152], who analysed $H_2$–air combustion in a dual-mode ramjet configuration. Laminar flame speeds in the range $0.5\,\mathrm{m\,s^{-1}}$ to $0.9\,\mathrm{m\,s^{-1}}$ typically correspond to equivalence ratios $\phi \approx 0.5$–$0.9$, while richer mixtures can reach laminar flame speeds of up to $3\,\mathrm{m\,s^{-1}}$. These results illustrate the broad range of flame speeds encountered in dual-mode ramjet combustors. To cover a representative operating envelope while remaining consistent with the quasi-one-dimensional framework, the present study adopts the range $\mathcal{S}_f \in 0.4\,\mathrm{m\,s^{-1}}$ to $1.2\,\mathrm{m\,s^{-1}}$.

The flame-holder ratio $C_{\mathrm{FH}}$ represents the blockage induced by the stabilising mechanism and depends on flight Mach number, fuel, mission profile, and combustor design. In the SdR ramjet configuration studied by Boulal *et al.* [41], the flame-holder height corresponds to approximately 20 % to 30 % of the constant-duct height. Similar blockage levels are reported for cavity-based flame-holders in scramjet-type configurations [153, 154], typically ranging from 10 % to 25 %. Furthermore, the parametric study by Kummitha *et al.* [155] found that flame-holder blockage ratios in the range 5 % to 30 % are representative of realistic dual-mode combustor geometries. Based on these findings, the present analysis restricts the flame-holder ratio to values not exceeding 35 % of the constant-duct height, which adequately covers the range of practical designs.

It is important to emphasise that the present analysis does not include real combustion chemistry, turbulence, or the complex unsteady structures that appear in practical reacting flows (such as vortical flame wrinkling or local extinction/reignition). Consequently, the objective is not to reproduce a specific experimental configuration but rather to isolate and identify how a simplified thermoacoustic coupling modifies, or potentially destabilises, the aeroacoustic response of an otherwise canonical thermally choked nozzle.

### 5.3.1 Effect of the flame speed

The analysis begins by examining how the flame speed influences the aeroacoustic behaviour of a thermally choked flow. For this purpose, the flame-holder ratio is fixed at $C_{\mathrm{FH}} = 15\,\%$ so that only the flame dynamics are modified. To make the effect of the unsteady heat-release term explicit, the configuration without thermoacoustic coupling is also displayed (—), serving as a reference corresponding to the purely steady volumetric source term.

Figure 5.5 shows the acoustic-reflection coefficient $R_a$ as a function of the dimensionless frequency $\Omega = \omega/(\mathrm{d}\bar{u}/\mathrm{d}x)_*$, with both the modulus and phase-angle plotted. The influence of the FTF model is most apparent at low frequencies ($\Omega < 1$), where the flame has sufficient time to respond to acoustic perturbations and therefore strongly modifies the upstream-propagating acoustic waves. At higher frequencies, the flame cannot respond rapidly enough and the unsteady heat-release contribution becomes negligible, causing all curves to collapse onto the same

behaviour. For this reason, only the frequency range below $\Omega < 3$ is presented.

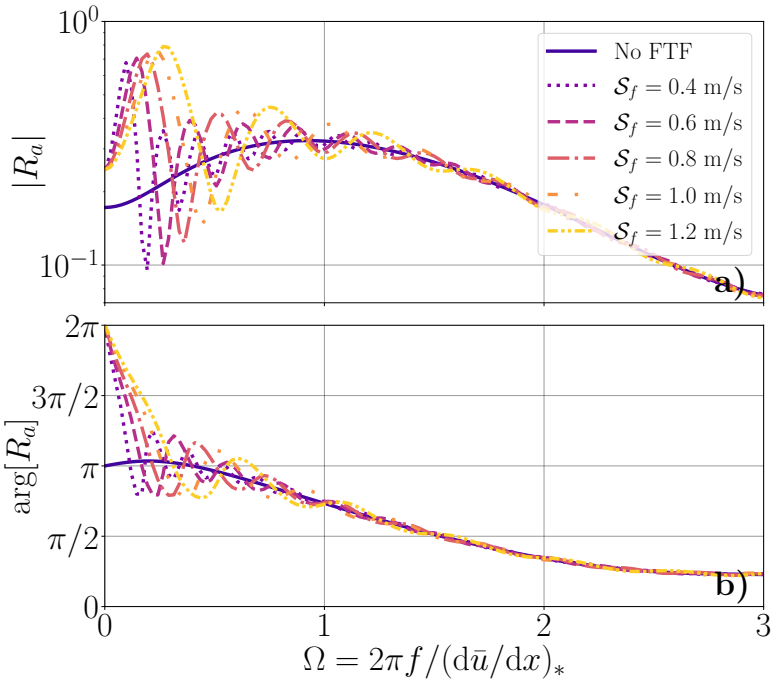


**Figure 5.5** (Colour) Modulus **(a)** and phase-angle **(b)** of the acoustic-reflection coefficient $R_a$ as a function of the dimensionless frequency $\Omega = \omega/(\mathrm{d}\bar{u}/\mathrm{d}x)_*$ for a flame-holder ratio $C_{\mathrm{FH}} = 0.15$ and five flame speeds $\mathcal{S}_f \in 0.4\,\mathrm{m\,s^{-1}}$ to $1.2\,\mathrm{m\,s^{-1}}$. The solid line (—) corresponds to the configuration in which the FTF model (Eq. (5.8)) is not activated.

As expected, taking into account the FTF model produces a substantial modification of the upstream-propagating acoustic response. A first noticeable effect appears in the quasi-steady limit: the value of the acoustic-reflection coefficient for $\Omega \to 0$ is no longer the same as in the case without FTF. When the FTF model is active, the modulus of the reflection coefficient systematically approaches $|R_a| \approx 0.24$, independently of the flame speed. This behaviour was already discussed in Sec. 5.2. It arises because, in the low-frequency limit, the flame-transfer function tends to $\mathcal{F} \to 1$, meaning that the unsteady heat-release fluctuations simply follow the velocity perturbation at the flame-holder point, $\hat{U}(x_{\mathrm{FH}})$. The flame therefore acts as a perfectly compact unsteady heat source, strengthening the coupling with the acoustic field.

For higher frequencies, up to $\Omega \lesssim 2$, the acoustic response becomes much more structured and exhibits clear oscillations. These oscillations depend strongly on the flame speed $\mathcal{S}_f$. A higher flame speed causes the heat-release perturbations to propagate more rapidly along the flame front, which enhances their ability to interact constructively with the acoustic waves. As a result, the amplitude of the upstream-propagating acoustic wave increases with $\mathcal{S}_f$.

In addition, increasing the flame speed shifts the frequency at which the maximum acoustic response occurs. Physically, faster flame fluctuations respond more rapidly to velocity perturbations, reducing the effective time delay in the heat-release process and thereby altering the resonance conditions of the coupled system. This is also reflected in the phase-angle evolution: a phase-angle change in slope appears around $\Omega \approx 0.5$, which marks the transition between regimes where the heat-release fluctuations are either in phase or out of phase with the acoustic field. This phase behaviour is characteristic of a resonance mechanism common to all configurations but modulated in intensity and frequency by the flame speed.

Figure 5.6 presents the entropy-noise-production coefficient $R_s$ as a function of the dimen-

sionless frequency $\Omega = \omega/(\mathrm{d}\bar{u}/\mathrm{d}x)_*$. Here again, the effects of the FTF model are concentrated at low frequencies ($\Omega < 1$), where entropy fluctuations have sufficient time to interact with the unsteady heat-release response.

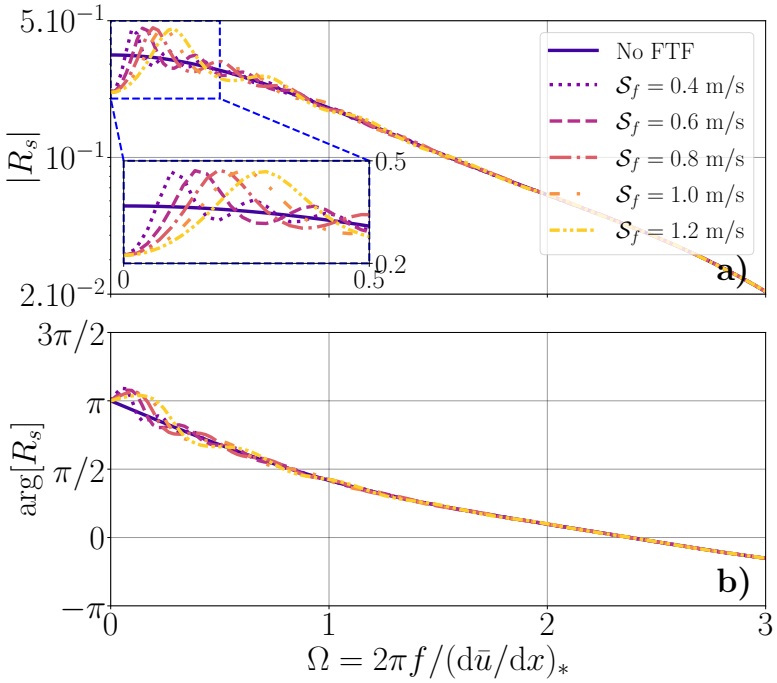


**Figure 5.6** (Colour) Modulus **(a)** and phase-angle **(b)** of the entropy-noise-production coefficient $R_s$ as a function of the dimensionless frequency $\Omega = \omega/(\mathrm{d}\bar{u}/\mathrm{d}x)_*$ for a flame-holder ratio $C_{\mathrm{FH}} = 0.15$ and five flame speeds $\mathcal{S}_f \in 0.4\,\mathrm{m\,s^{-1}}$ to $1.2\,\mathrm{m\,s^{-1}}$. The solid line (—) corresponds to the configuration in which the FTF model (Eq. (5.8)) is not activated.

The influence of the FTF model and the flame speed on the entropy-induced acoustic response is noticeably different from the behaviour observed under direct acoustic forcing. At very low frequencies, the entropy-noise-production coefficient $R_s$ approaches a value that is smaller than in the case without FTF. This decrease arises because, in this regime, the flame–acoustic interaction introduces an additional damping effect. Since the acoustic waves originate from the convection of entropy fluctuations, any unsteady heat-release response that opposes or delays this process reduces the efficiency of entropy–acoustic conversion, thereby lowering $R_s$.

As the frequency increases, the situation changes: a pronounced peak appears in the acoustic response. This peak can even exceed the maximum value obtained in the reference configuration without thermoacoustic coupling. Interestingly, the height of this peak is largely insensitive to the flame speed, with all cases reaching a similar maximum around $|R_s| \approx 0.45$. The flame speed mainly controls the position of this peak in frequency, reflecting the change in the effective time delay introduced by the flame dynamics.

For frequencies above $\Omega > 1$, the curves converge, indicating that the flame can no longer follow the rapid perturbations. In this regime, the thermoacoustic coupling becomes negligible, and the entropy–acoustic conversion reverts to its baseline, FTF-free behaviour. Consequently, the influence of the FTF model in entropy forcing is essentially confined to very low frequencies.

To summarise, increasing the flame speed strengthens the coupling between unsteady heat release and the acoustic field. This results in a larger peak amplitude of the acoustic-reflection coefficient and shifts the frequency at which this peak occurs toward higher values, since faster flames respond more rapidly to incoming perturbations.

For entropy forcing, the introduction of the FTF model likewise produces a distinct maximum in the acoustic response. However, in this case the peak amplitude is largely insensitive to the flame speed: varying $\mathcal{S}_f$ mainly shifts the position of the maximum in frequency rather than modifying its magnitude. This indicates that the entropy–acoustic conversion mechanism is less sensitive to the details of flame propagation than the direct acoustic forcing.

### 5.3.2 Effect of the flame-holder height

The impact of the flame-holder height was then assessed by varying the flame-holder ratio from $C_{\mathrm{FH}} = 0\,\%$ to $35\,\%$. The flame speed is kept constant at $\mathcal{S}_f = 0.75\,\mathrm{m\,s^{-1}}$ for all configurations. As before, to make the effect of the unsteady heat-release term explicit, the configuration without thermoacoustic coupling is also shown (—), serving as a reference corresponding to the purely steady volumetric source term.

Figure 5.7 shows the acoustic-reflection coefficient $R_a$ as a function of the dimensionless frequency $\Omega = \omega/(\mathrm{d}\bar{u}/\mathrm{d}x)_*$ for five distinct flame-holder ratios $C_{\mathrm{FH}} \in 0\,\%$ to $35\,\%$.

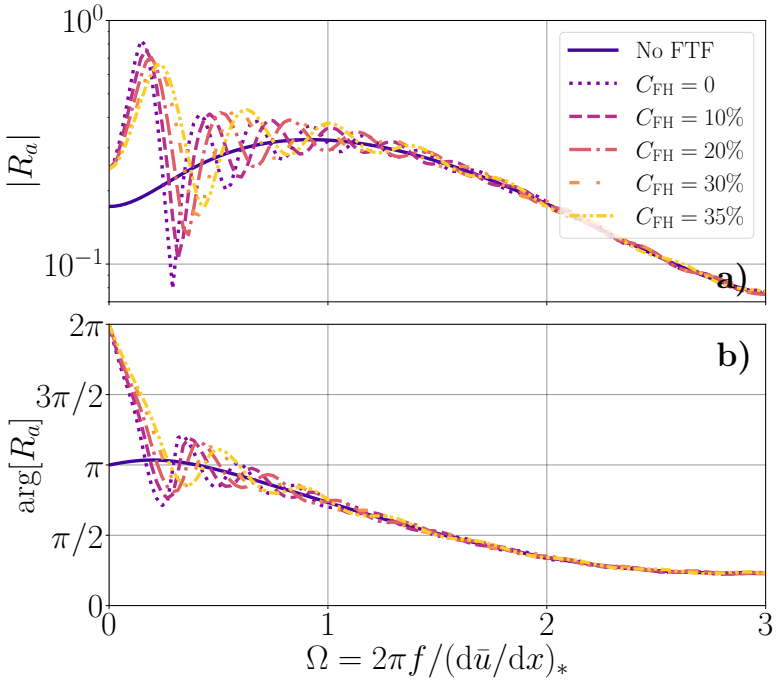


**Figure 5.7** (Colour) Modulus **(a)** and phase-angle **(b)** of the acoustic-reflection coefficient $R_a$ as a function of the dimensionless frequency $\Omega = \omega/(\mathrm{d}\bar{u}/\mathrm{d}x)_*$ for a flame speed $\mathcal{S}_f = 0.75\,\mathrm{m\,s^{-1}}$ and five flame-holder ratios $C_{\mathrm{FH}} \in 0\,\%$ to $35\,\%$. The solid line (—) corresponds to the configuration in which the FTF model (Eq. (5.8)) is not activated.

At very low frequencies, the behaviour remains similar to the flame-speed study (Sec. 5.3.1): all configurations converge toward the same quasi-steady value of $|R_a| = 0.24$. At higher frequencies, local maxima appear in the acoustic response, but their amplitude decreases as the flame-holder ratio increases. This occurs because a larger flame-holder height reduces the effectiveness of the flame-transfer function, whose magnitude tends toward zero when $C_{\mathrm{FH}}$ approaches unity (see Eq. (5.8)).

From a physical perspective, increasing the flame-holder height reduces the length of the attached flame front. With a shorter flame, the unsteady heat-release response becomes weaker, since a smaller portion of the flame is available to interact with acoustic perturbations. As

a result, the acoustic coupling strength decreases, leading to smaller maxima in the acoustic-reflection coefficient.

To complete this analysis, Fig. 5.8 presents the entropy-noise-production coefficient $R_s$ as a function of the dimensionless frequency $\Omega = \omega/(\mathrm{d}\bar{u}/\mathrm{d}x)_*$ for the five flame-holder ratios $C_{\mathrm{FH}} \in 0\,\%$ to $35\,\%$.

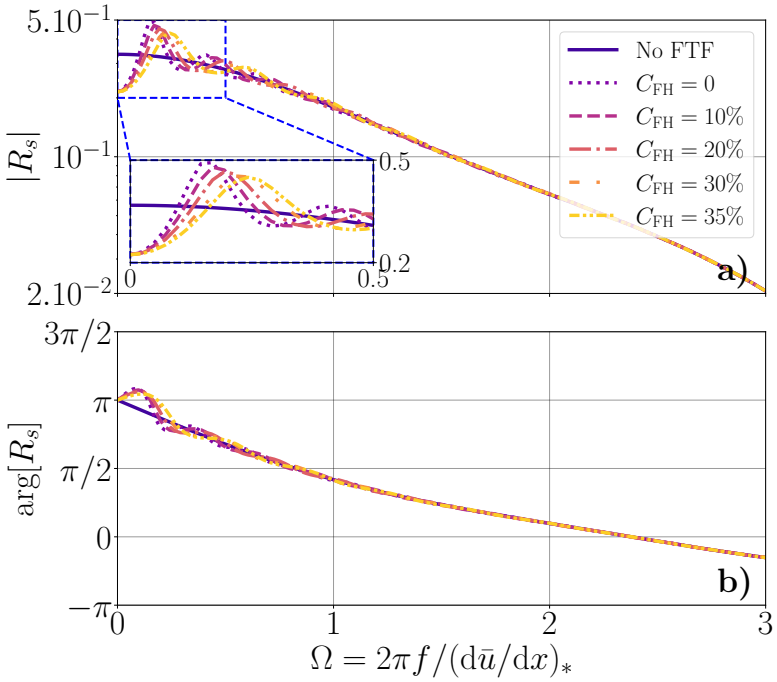


**Figure 5.8** (Colour) Modulus **(a)** and phase-angle **(b)** of the entropy-noise-production coefficient $R_s$ as a function of the dimensionless frequency $\Omega = \omega/(\mathrm{d}\bar{u}/\mathrm{d}x)_*$ for a flame speed $\mathcal{S}_f = 0.75\,\mathrm{m\,s^{-1}}$ and five flame-holder ratios $C_{\mathrm{FH}} \in 0\,\%$ to $35\,\%$. The solid line (—) corresponds to the configuration in which the FTF model (Eq. (5.8)) is not activated.

As observed in the flame-speed study (Sec. 5.3.1), the effect of the FTF model on entropy forcing is restricted to very low frequencies ($\Omega < 1$), where the flame has sufficient time to respond to the slowly varying perturbations. In this regime, the flame-holder ratio plays a key role in shaping the response: it alters both the height of the peak in $|R_s|$ and the frequency at which this peak occurs. Increasing $C_{\mathrm{FH}}$ reduces the length of the attached flame front, which weakens the unsteady heat-release response. As a consequence, the entropy–acoustic conversion becomes less efficient, and the peak in the entropy-noise-production coefficient becomes smaller and shifts to higher frequencies. This behaviour mirrors the trends observed for acoustic forcing and highlights the central role of the flame geometry in the low-frequency thermoacoustic coupling.

### 5.3.3 Role of the non-dimensional flame frequency

In the previous sections, the aeroacoustic response, resulting either from an imposed acoustic perturbation or from an entropy disturbance, was expressed as a function of the dimensionless frequency $\Omega = \omega/(\mathrm{d}\bar{u}/\mathrm{d}x)_*$. This choice made it straightforward to compare the behaviour of the system with and without thermoacoustic coupling, and it revealed that activating the FTF model can strongly modify the response. In particular, the flame–acoustic interaction was shown to enhance the maximum acoustic amplitude for both types of forcing.

To better isolate the influence of the flame parameters, the analysis is now recast in terms

of the dimensionless flame frequency $\Omega_{\mathcal{F}}$ defined in Eq. (5.9). Plotting only the modulus of the acoustic-reflection and entropy-noise-production coefficients as functions of $\Omega_{\mathcal{F}}$ highlights how the flame speed and flame-holder ratio shape the thermoacoustic response. This representation provides a clearer interpretation of the coupling mechanisms because it directly reflects the way the flame perceives and responds to unsteady perturbations.

Figure 5.9 presents the modulus of both the acoustic-reflection coefficient $R_a$ and the entropy-noise-production coefficient $R_s$ as a function of the flame dimensionless frequency $\Omega_{\mathcal{F}}$ (Eq. (5.9)), for a flame-holder ratio $C_{\mathrm{FH}} = 0.15$ and five flame speeds $\mathcal{S}_f \in 0.4\,\mathrm{m\,s^{-1}}$ to $1.2\,\mathrm{m\,s^{-1}}$. For reference, the acoustic dimensionless frequency $\Omega = 1$ is also plotted as coloured circle to facilitate comparison with the previous representations.

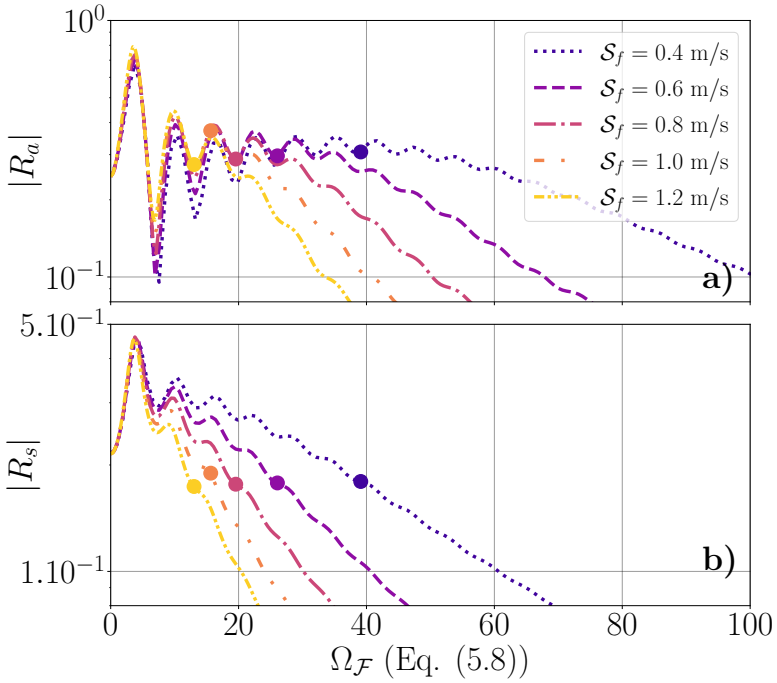


**Figure 5.9** (Colour) Modulus of the acoustic-reflection coefficient $R_a$ **(a)** and the entropy-noise-production coefficient $R_s$ **(b)** as a function of the dimensionless flame frequency $\Omega_{\mathcal{F}}$, for a flame-holder ratio $C_{\mathrm{FH}} = 0.15$ and five flame speeds $\mathcal{S}_f \in 0.4\,\mathrm{m\,s^{-1}}$ to $1.2\,\mathrm{m\,s^{-1}}$. The acoustic dimensionless frequency $\Omega = \omega/(\mathrm{d}\bar{u}/\mathrm{d}x)_* = 1$ is also plotted as a coloured circle for comparison.

When the acoustic response is viewed through the dimensionless flame frequency $\Omega_{\mathcal{F}}$, all configurations collapse onto similar trends at low frequency, which makes the role of the flame speed particularly clear. The acoustic-reflection coefficient shifts systematically with $\mathcal{S}_f$: a higher flame speed produces a stronger acoustic response along a narrower range of $\Omega_{\mathcal{F}}$. This is because faster flames respond more effectively to incoming perturbations and therefore inject more unsteady heat into the acoustic field. Interestingly, at low flame frequencies ($\Omega_{\mathcal{F}} < 20$ for acoustic forcing and $\Omega_{\mathcal{F}} < 10$ for entropy forcing), the curves collapse and the peak amplitude becomes nearly independent of $\mathcal{S}_f$.

As the flame frequency increases, the acoustic response begins to decay approximately as $1/\mathcal{S}_f$. This explains why high flame speeds produce a stronger acoustic amplification, and therefore a greater potential for thermoacoustic instability, while low flame speeds exert a weaker influence but remain active over a broader range of frequencies. In this regime, the flame behaves as a quasi-steady heat source, and the details of the flame dynamics play only a weak role.

A key insight from this representation is the large separation between the flame and flow time scales. Even for a relatively modest acoustic forcing of $\Omega = 1$, the corresponding reduced flame frequency reaches $\Omega_{\mathcal{F}} \approx 40$. This demonstrates that the flame typically operates in a regime where it reacts almost instantaneously to acoustic perturbations, behaving effectively as an unsteady heat source with negligible time lag.

Finally, Fig. 5.10 presents the modulus of both the acoustic-reflection coefficient $R_a$ and the entropy-noise-production coefficient $R_s$ as a function of the flame dimensionless frequency $\Omega_{\mathcal{F}}$ (Eq. (5.9)), for a flame speed $\mathcal{S}_f = 0.75\,\mathrm{m\,s^{-1}}$ and five flame-holder ratios $C_{\mathrm{FH}} \in 0\,\%$ to $35\,\%$.

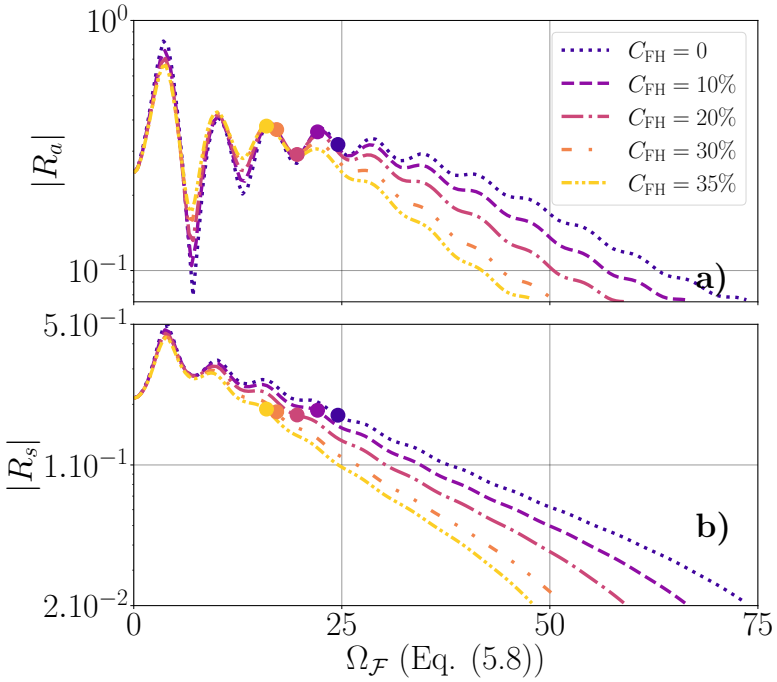


**Figure 5.10** (Colour) Modulus of the acoustic-reflection coefficient $R_a$ **(a)** and the entropy-noise-production coefficient $R_s$ **(b)** as a function of the dimensionless flame frequency $\Omega_{\mathcal{F}}$, for a flame speed $\mathcal{S}_f = 0.75\,\mathrm{m\,s^{-1}}$ and five flame-holder ratios $C_{\mathrm{FH}} \in 0\,\%$ to $35\,\%$. The acoustic dimensionless frequency $\Omega = \omega/(\mathrm{d}\bar{u}/\mathrm{d}x)_* = 1$ is also plotted as a coloured circle for comparison.

At high flame frequencies, beyond $\Omega_{\mathcal{F}} > 25$ for acoustic forcing and $\Omega_{\mathcal{F}} > 18$ for entropy forcing, the behaviour of all configurations becomes very similar. Because the flame speed is the same in each case ($\mathcal{S}_f = 0.75\,\mathrm{m\,s^{-1}}$), the decay of both $R_a$ and $R_s$ follows approximately the same slope, which scales as $1/\mathcal{S}_f$. In this regime, the flame can no longer respond to rapid perturbations, and the only remaining influence comes from the geometric differences: smaller flame-holder ratios allow the FTF effects to persist over a broader range of flame frequencies.

In contrast, at low flame frequencies, all curves collapse onto the same maximum value. As already noted, increasing the flame-holder ratio reduces the flame length and therefore weakens the no-lag heat-release contribution. This leads to a lower acoustic and entropy-induced response for larger $C_{\mathrm{FH}}$.

The influence of the flame-holder on the steady base flow $\bar{u}_{\mathrm{FH}}$ as a flow obstacle was assessed by incorporating the effect of the flame-holder ratio $C_{\mathrm{FH}}$ into the calculation of the local flow velocity at the flame-holder lips, and hence into the flame transfer function $\mathcal{G}(\Omega_{\mathcal{F}})$ (Eq. (5.8)) and the dimensionless flame frequency $\Omega_{\mathcal{F}}$ (Eq. (5.9)), using steady mass-flow-rate conservation:

$$\bar{u}_{\mathrm{FH}} = \bar{u}_{\mathrm{in}} \frac{1}{1 - C_{\mathrm{FH}}}. \tag{5.16}$$

It was found that this formulation has a very limited impact on the overall acoustic response, with a relative error on the order of $1 \times 10^{-4}$, since the base flow $\bar{u}$ is not affected in the constant-duct section or in the divergent part of the nozzle. This formulation therefore merely introduces a fictitious flow obstacle. Accounting for the actual geometric modification induced by the flame-holder would require simulating a more complex nozzle geometry, which would in turn challenge the quasi-one-dimensional approximation of the flow.

## 5.4 Thermoacoustic stability study of a canonical thermally choked-flow nozzle

In this final section, the objective is to assess the global stability of a canonical thermally choked configuration. The analysis focuses on two complementary indicators: the amplification of the acoustic response and the Rayleigh index. These quantities measure, respectively, the ratio between the maximal acoustic response with and without the FTF model, and the energy exchange between the unsteady heat release and the acoustic field. Both indicators are evaluated under acoustic and entropy forcing. The thermally choked configuration developed in the preceding section serves as the reference flow for this investigation.

### 5.4.1 Amplification ratio of the aeroacoustic response

To assess how the FTF model alters the acoustic behaviour of a thermally choked configuration, the amplification ratio is examined across a broad range of flame speeds $\mathcal{S}_f$ and flame-holder ratios $C_{\mathrm{FH}}$. This amplification ratio is defined as the maximum value of the acoustic reflection coefficient, $|R|_{\max}$, normalised by the maximum response obtained in the reference configuration without thermoacoustic coupling, $|R|_{\max,\mathrm{ref}}$. It is evaluated for both acoustic ($R = R_a$) and entropy forcing ($R = R_s$). This indicator provides a direct measure of the ability of the FTF model to amplify upstream-propagating acoustic waves for a given downstream-propagating acoustic or entropy wave, and thus to promote thermoacoustic instabilities in a thermally choked flow. In particular, if $|R|_{\max}/|R|_{\max,\mathrm{ref}} > 1$, the FTF increases the maximum upstream-propagating acoustic response compared with the maximum acoustic response obtained when the FTF is not activated. For the same downstream-propagating acoustic or entropy wave, the system then generates a larger upstream-propagating acoustic response. However, it should be noted that the frequency $\Omega$ at which the maximum acoustic or entropy reflection coefficient occurs is not the same when the FTF is activated as when it is not. This indicator characterises the overall behaviour of the system rather than its response at each individual frequency.

Figure 5.11 presents the acoustic amplification ratio $|R_a|_{\max}/|R_a|_{\max,\mathrm{ref}}$ as a function of the flame speed $\mathcal{S}_f$ and flame-holder ratio $C_{\mathrm{FH}}$.

The amplification of the acoustic response under acoustic forcing is substantial for all configurations considered. In nearly every case, the ratio $|R_a|_{\max}/|R_a|_{\max,\mathrm{ref}}$ exceeds 2, meaning that the presence of the FTF model more than doubles the maximum acoustic amplitude. The strongest amplification is observed for configurations with small flame-holder ratios and high flame speeds. This behaviour is fully consistent with the trends identified earlier: a shorter flame-holder and a faster flame both enhance the unsteady heat-release response, which in turn reinforces the upstream-propagating acoustic wave. As a result, these configurations are the most susceptible to thermoacoustic instability, although this condition is not sufficient on its own to guarantee the onset of an instability. A detailed analysis based on the Rayleigh index is presented in the next section.

From a practical perspective, however, although high flame speeds may occur in ramjet combustors, very small flame-holder ratios are unlikely in realistic designs, since the step is

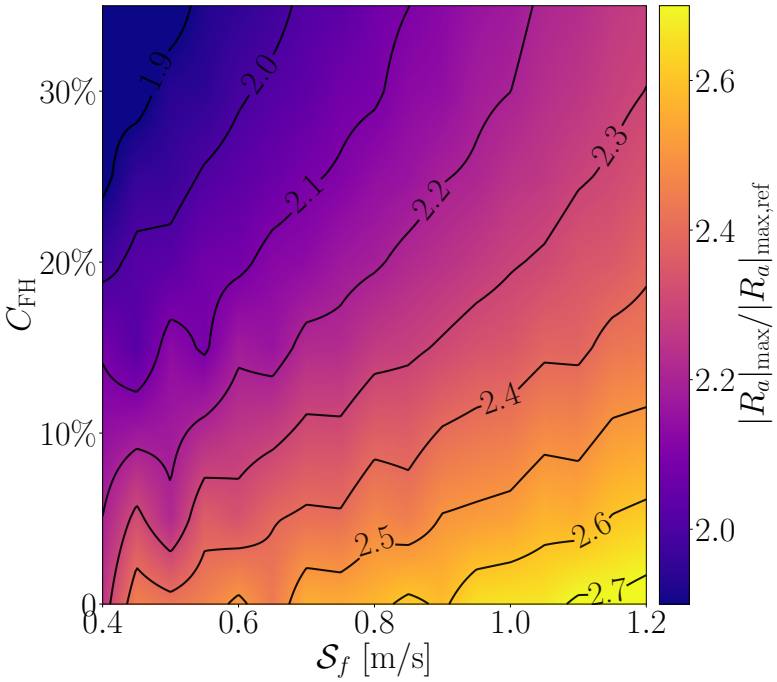


**Figure 5.11** (Colour) Normalised amplification ratio of the maximum acoustic response $|R_a|_{\max}/|R_a|_{\max,\mathrm{ref}}$ induced by an inlet acoustic forcing, for flame speeds $\mathcal{S}_f \in 0.4\,\mathrm{m\,s^{-1}}$ to $1.2\,\mathrm{m\,s^{-1}}$ and flame-holder ratios $C_{\mathrm{FH}} \in 0\,\%$ to $35\,\%$. The reference value corresponds to the configuration without the FTF model.

required to stabilise the flame and to generate a recirculation zone. This limits the occurrence of the most strongly amplified configurations in operational systems.

Figure 5.12 presents the entropy-noise amplification ratio $|R_s|_{\max}/|R_s|_{\max,\mathrm{ref}}$ as a function of the flame speed $\mathcal{S}_f$ and flame-holder ratio $C_{\mathrm{FH}}$.

Under entropy forcing, the amplification of the acoustic response remains modest, with amplification ratios of about $|R_s|_{\max}/|R_s|_{\max,\mathrm{ref}} = 1.4$ across all cases. This indicates that activating the FTF model only moderately alters the entropy-induced acoustic waves. Unlike the acoustic-forcing scenario, where both flame speed and flame-holder geometry play important roles, the amplification under entropy forcing is driven mainly by the flame-holder ratio: smaller $C_{\mathrm{FH}}$ values result in stronger entropy-to-acoustic conversion. However, as previously noted, such small flame-holder ratios are not typical in operational ramjet combustors, since they do not provide sufficient stabilisation or recirculation. As a result, the most amplified configurations are unlikely to occur in practice.

### 5.4.2 Rayleigh index and potential instabilities

Finally, the thermoacoustic stability of the thermally choked nozzle is assessed by employing the Rayleigh index [88, 156]. In a fully premixed combustion system, this index is written as:

$$R_I = \frac{\tau}{\pi} \int_\omega \int_V \left( \frac{\bar{\gamma} - 1}{\bar{\gamma}\,\bar{p}} \,\mathrm{Re}(\hat{p}^*\,\hat{P}_v) \right) \mathrm{d}V\,\mathrm{d}\omega, \tag{5.17}$$

which quantifies the energy exchange between pressure fluctuations $\hat{p}$ and unsteady heat-release fluctuations $\hat{P}_v$ in the subsonic heated region of the nozzle. Here, $\chi^*$ denotes the complex conjugate of the quantity $\chi$, and $\mathrm{Re}(\chi)$ is the real part of $\chi$. The total integration time is

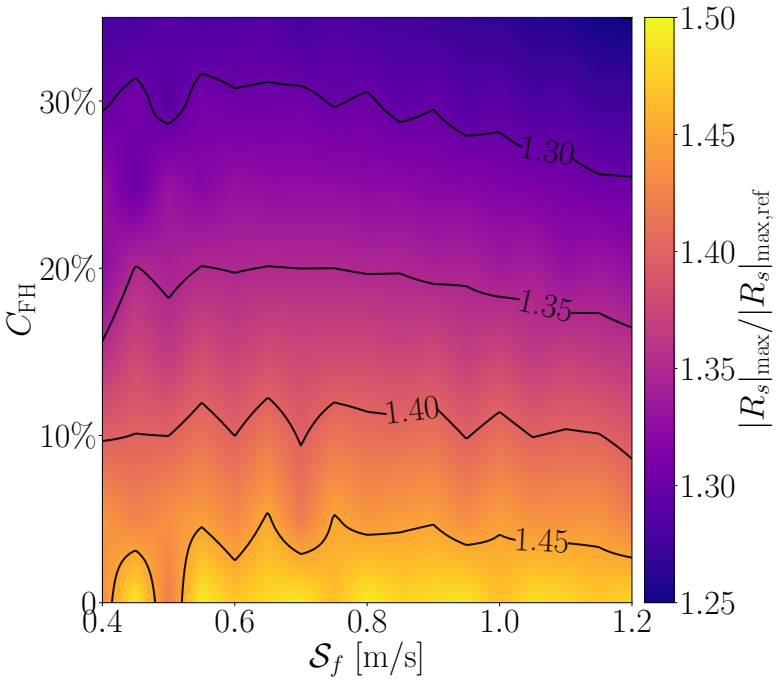


**Figure 5.12** (Colour) Normalised amplification ratio of the maximum acoustic response $|R_s|_{\max}/|R_s|_{\max,\mathrm{ref}}$ induced by an inlet entropy forcing, for flame speeds $\mathcal{S}_f \in 0.4\,\mathrm{m\,s^{-1}}$ to $1.2\,\mathrm{m\,s^{-1}}$ and flame-holder ratios $C_{\mathrm{FH}} \in 0\,\%$ to $35\,\%$. The reference value corresponds to the configuration without the FTF model.

arbitrarily set to $\tau = 1\,\mathrm{s}$, which is sufficiently long for the process to be considered statistically stationary in the framework of the quasi-one-dimensional model, as detailed in Schuermans *et al.* [88].

The Rayleigh index is computed by integrating the product of the unsteady heat-release perturbation and the pressure fluctuation over the entire subsonic heated region (from $x_{\mathrm{u}}$ to $x_*$). For each pair of parameters ($\mathcal{S}_f$, $C_{\mathrm{FH}}$), the index is integrated across the full frequency range $\omega$ and is retained as a measure of the overall thermoacoustic driving. Since the preceding analysis demonstrated that the strongest acoustic amplification occurs under isentropic acoustic forcing (the acoustic amplification is lower for entropy forcing), only this forcing condition is considered in the stability assessment.

Figure 5.13 presents the resulting Rayleigh index $R_I$ as a function of the flame speed $\mathcal{S}_f$ and the flame-holder ratio $C_{\mathrm{FH}}$.

The trends displayed in Fig. 5.13 exhibit noticeable differences from the amplification patterns discussed previously. The Rayleigh index reaches its highest values for configurations with fast flame speeds, irrespective of the flame-holder ratio. This behaviour is expected: when the flame responds rapidly to acoustic perturbations, the resulting heat-release fluctuations tend to remain closely in phase with the local pressure oscillations. Such phase alignment is the key ingredient for constructive thermoacoustic coupling, meaning that the flame effectively injects energy into the acoustic field rather than dissipating it. Consequently, the Rayleigh index increases.

Interestingly, increasing the flame-holder ratio does not suppress this mechanism. Even though larger flame-holders generally reduce the overall acoustic amplification, they still allow significant Rayleigh index values to develop. This indicates that the principal driver of thermoacoustic coupling in the present configuration is the flame response time, governed mainly by the flame speed, rather than geometrical effects alone.

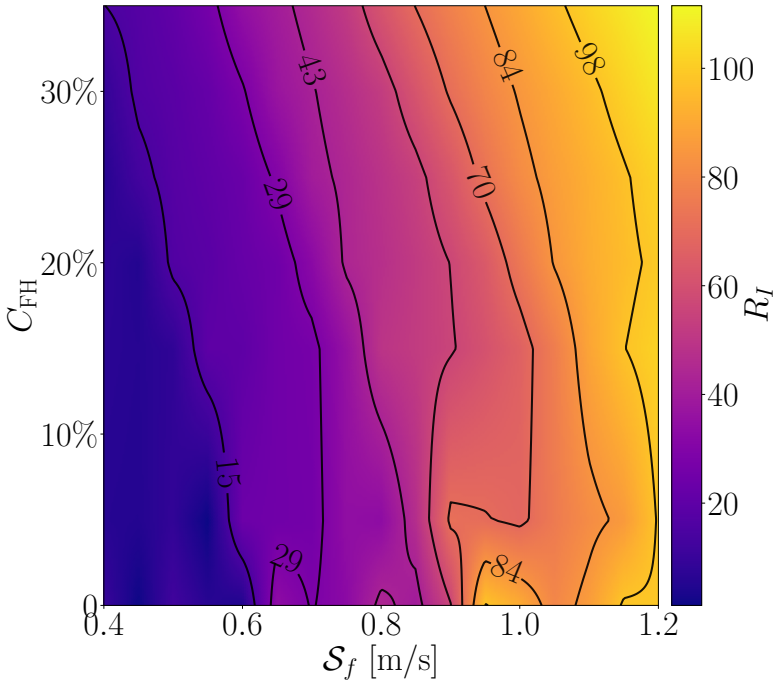


**Figure 5.13** (Colour) Rayleigh index $R_I$ (Eq. (5.17)) induced by an inlet acoustic forcing, for flame speeds $\mathcal{S}_f \in 0.4\,\mathrm{m\,s^{-1}}$ to $1.2\,\mathrm{m\,s^{-1}}$ and flame-holder ratios $C_{\mathrm{FH}} \in 0\,\%$ to $35\,\%$.

From these observations, it becomes clear that only configurations with sufficiently fast flame dynamics, capable of reacting promptly to the imposed acoustic field, are likely to generate Rayleigh index magnitudes large enough to destabilise the system. Slow flames, by contrast, fail to couple efficiently with acoustic oscillations and therefore remain largely stabilising or neutral.

However, an important point must be emphasised: a positive Rayleigh index $R_I$ does not automatically imply the onset of a thermoacoustic instability. The Rayleigh index quantifies the acoustic energy that unsteady heat release is able to supply to the acoustic field, but instability requires that this supplied energy exceeds all damping mechanisms acting within the system. These include, for instance, viscous losses, radiative damping at boundaries, and attenuation associated with entropy-acoustic conversion. Since such losses are not evaluated in the present study, the Rayleigh index alone cannot be used to determine whether self-sustained oscillations will actually develop. Moreover, the Rayleigh index only accounts for pressure and unsteady heat-release fluctuations. As shown in Chap. 3, entropy fluctuations arise even under isentropic acoustic forcing. To deepen the analysis, it would be interesting to consider a more general energetic criterion, such as the one proposed by Chu [157], which accounts for pressure, entropy, and heat-release fluctuations.

Figure 5.14 details the dimensionless frequency $\Omega_{\max}$ of each configuration where the maximum of the Rayleigh index is obtained, as a function of the flame speed $\mathcal{S}_f$ and flame-holder ratio $C_{\mathrm{FH}}$.

The frequency $\Omega$ at which the Rayleigh index reaches its maximum is governed jointly by the flame speed and the flame-holder ratio. Interestingly, this dependence differs markedly from the trends observed for the acoustic-reflection coefficient. In the case of the Rayleigh index, configurations with both a high flame speed and a large flame-holder ratio exhibit their maximum thermoacoustic driving at a relatively low acoustic frequency of $\Omega = 0.25$, whereas slow flames combined with small flame-holders produce their strongest coupling at lower values of $\Omega = 0.1$. Compared with the wide frequency range examined in Sec. 5.3 ($0 < \Omega < 100$), the frequency at

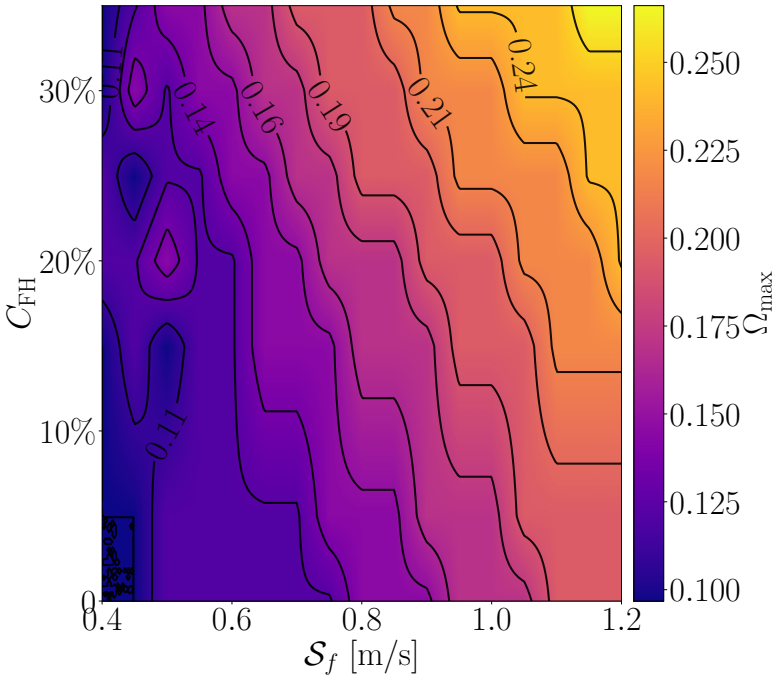


**Figure 5.14** (Colour) Non-dimensional flame frequency $\Omega_{\mathrm{max}}$ at which the maximum Rayleigh index occurs $R_I$ as a function of the flame speed $\mathcal{S}_f$ and the flame-holder ratio $C_{\mathrm{FH}}$.

which the Rayleigh index attains its maximum is always located in the very low-frequency regime. In practice, the corresponding normalised acoustic frequency remains of order $\Omega \sim \mathcal{O}(10^{-1})$.

This apparent inversion highlights the distinct physical mechanisms that control the Rayleigh index. While the acoustic-reflection coefficient is primarily influenced by the amplitude of the upstream-propagating acoustic wave, the Rayleigh index is governed by the phase alignment between unsteady heat release and pressure oscillations. A flame can provide energy to the acoustic field only when these two quantities are sufficiently in phase.

Fast flames respond rapidly to incoming perturbations; their short intrinsic timescales allow them to synchronise with the acoustic field only when the forcing frequency is high enough to match their rapid dynamics. In contrast, slow flames possess longer characteristic times and therefore achieve constructive pressure and heat-release coupling at lower frequencies.

Moreover, the frequency at which the Rayleigh index attains its maximum is not constant across configurations: the ratio between the lowest and highest peak frequencies can reach a factor of two when comparing slow flame speeds with small flame-holder ratios to fast flame speeds with large flame-holders. This substantial dispersion indicates that additional mechanisms, including convective delays, flame geometry, and local flow acceleration near the thermal throat, also contribute to determining the preferential frequencies associated with thermoacoustic driving, although their influence remains secondary.

These results underline the importance of analysing the Rayleigh index separately from the acoustic-amplification behaviour. The preferential coupling frequencies that maximise thermoacoustic driving are not necessarily the same as those associated with the steady heat-release distribution or the acoustic-reflection coefficient. Consequently, the stability of thermally choked configurations cannot be fully characterised without explicitly considering the frequency dependence of the Rayleigh index.

### Chapter conclusion

This chapter has assessed the influence of unsteady volumetric heat-release rates on the aeroacoustic behaviour of thermally choked nozzles by means of the quasi-one-dimensional linear acoustic model derived in Chap. 4. A simplified thermoacoustic coupling, based on Dowling's kinematic flame transfer-function model (*J. Fluid Mech.* 1999), was introduced to study the impact on the aeroacoustic response. By varying the flame speed and the flame-holder ratio, the study quantified how unsteady heat release modifies the acoustic and entropy–acoustic responses. The results revealed that the flame dynamics can significantly enhance the upstream-propagating acoustic waves, with the strongest amplification obtained for fast flames and small flame-holders. The representation in terms of the reduced flame frequency further clarified the separation of time scales between the flame and the nozzle and highlighted the regimes in which the flame acts quasi-steadily or becomes dynamically ineffective.

Finally, a global stability assessment based on two metrics, the amplification ratio of the acoustic response and the Rayleigh index, was conducted. Both indicators consistently demonstrated that the most unstable configurations correspond to high flame speeds, irrespective of the flame-holder configuration, for which unsteady heat-release fluctuations are strongly in phase with the acoustic pressure. From a practical perspective, the most unstable configurations remain unlikely in operational ramjet systems due to geometric constraints on flame-holder design.

Overall, this chapter highlights that even simplified models of unsteady heat release can profoundly alter the aeroacoustic response of thermally choked flows. The results provide physical insight into the mechanisms governing flame–acoustic coupling and establish the basis for the two-dimensional entropy-perturbation analysis performed in the next chapter.

Chapter 6

# Sound generation by two-dimensional entropy inhomogeneity in a thermally choked-flow nozzle

*Et ben, on est pas sortis du sable !*

**Guenièvre [2]**


## Abstract

This final chapter investigates the acoustic response induced by the convection of two-dimensional entropy perturbations, circular spots or rectangular slugs, through a thermally choked-flow nozzle. While previous analyses were limited to one-dimensional plane-wave entropy forcing, the present work extends the study to more realistic, spatially localised entropy structures. The objective is to elucidate the mechanisms governing indirect noise generation in thermally choked configurations and to assess the influence of entropy size, injection position, and steady-state flow parameters.

Two asymptotic acoustic regimes are identified and compared with predictions from one-dimensional linear models: the quasi-steady (QSS) and point-mass inertial (PM) regimes. The CFD simulations show good agreement with these models for large and small entropy structures, respectively, but also reveal significant deviations in intermediate regimes, where thermal and geometric effects strongly interact. The thermal-throat configuration systematically produces higher acoustic responses than the geometric throat in the quasi-steady regime, owing to additional wave coupling within the heated region. The effects of inlet Mach number, thermal-throat position, and transverse injection are also examined, highlighting the sensitivity of indirect noise to steady-flow gradients and two-dimensional flow features. These results demonstrate the necessity of considering multidimensional entropy structures to accurately predict indirect noise generation in ramjet-based propulsion systems.



This chapter is a truncation of the following publication, submitted during the PhD:

F. Olivon, A. Genot, A. Chédin, J.-E. Durand, L. Hirschberg, and E. Piot. "Two-dimensional indirect entropy noise in a thermally choked-flow nozzle". In: *Journal of Sound and Vibration* (2026). HAL: hal-05577111

Contents

**6.1 Objective** . . . . . **114**
**6.2 Methodology** . . . . . **115**
6.2.1 Entropy inhomogeneities injection . . . . . 115
6.2.2 Computational setup . . . . . 116
**6.3 One-dimensional entropy-noise response models** . . . . . **118**
6.3.1 Quasi-steady asymptotic limit model . . . . . 118
6.3.2 Point-mass inertial asymptotic limit model . . . . . 119
**6.4 Two-dimensional analysis of the acoustic response induced by entropy non-uniformities** . . . . . **119**
6.4.1 Phenomenological description of the acoustic response induced by a circular entropy perturbation . . . . . 120
6.4.2 Comparison of the linear acoustic response to two- and one-dimensional entropy forcing . . . . . 121
**6.5 One-dimensional entropy-noise generation mechanism** . . . . . **122**
6.5.1 Asymptotic scaling of the acoustic response with entropy-shape size . . 122
6.5.2 Two-dimensional base-flow effects and transverse injection . . . . . 125
6.5.3 Effect of the steady thermal-throat position . . . . . 126
6.5.4 Influence of the inlet Mach number . . . . . 127

## 6.1 Objective

In the previous chapters (Chaps. 3 to 5), the acoustic response induced by one-dimensional mono-harmonic entropy wave forcing was analysed. It was shown that the response is primarily governed by the steady flow field, while heat addition plays only a secondary role. Nevertheless, the overall acoustic response is slightly enhanced due to the secondary generation of acoustic waves within the heated region of the flow.

In a dual-mode ramjet, however, the generation of entropy inhomogeneities does not solely produce one-dimensional entropy waves. Large-eddy simulations (LES) or experimental campaigns [38, 141] have revealed the complex flame dynamics in ramjet-based engines, including detached flame structures and two-dimensional entropy patterns [10]. This multidimensional perspective was first introduced by Ffowcs Williams and Howe [79], whose modelling approach considered three-dimensional fluid patches, with a relative excess mass, convected by the mean flow.

Since the method of Ffowcs Williams and Howe [79] is not restricted to a single spatial dimension, it enables the study of the influence of entropy-patch size on sound generation. Ffowcs Williams and Howe [79] further investigated this effect by comparing the sound generation from a duct-sized entropy "slug" with that from a much smaller spherical "pellet" while they are convected through a duct contraction or a nozzle. It should be noted, however, that Ffowcs Williams and Howe [79] considered only low-Mach-number flows, *i.e.*, without choked conditions.

The present study aims to investigate the propagation of two-dimensional entropy inhomogeneities in order to analyse indirect combustion noise. Building on the works of Kowalski *et al.* [158] and Elbakly [159] on geometrically choked-nozzle configurations, two asymptotic regimes have been identified and are recalled in Sec. 6.3: a quasi-steady regime, associated with very large inhomogeneities, and an inertial regime, corresponding to very small ones. The objective here is

to highlight the influence of the thermal throat on acoustic-wave generation, in comparison with the geometric-throat configuration, for two-dimensional entropy structures.

It should be emphasised that the focus is on understanding the mechanisms governing sound generation by the convection of entropy patches. The asymptotic trends highlighted in this study are therefore primarily theoretical: for very small-scale entropy perturbations, turbulence in a real flow would likely mix the gas and attenuate or erase the inhomogeneities before they reach the nozzle.

## 6.2 Methodology

The simplified dual-mode ramjet nozzle geometry described in Sec. 2.3.1 is used in this chapter. The non-uniform volumetric power source term $P_v$ (see Sec. 2.5) is used to position a steady thermal throat at a chosen location.

### 6.2.1 Entropy inhomogeneities injection

The two-dimensional entropy injection in the numerical simulations is based on the linearised Gibbs equation (Eq. (2.11)). At the inlet, the static pressure $p_{\text{in}}$ is prescribed as constant ($p'_{\text{in}} = 0$). Consequently, a perturbation in the static temperature $T'$ directly generates an entropy fluctuation $s'$. The principle of the entropy injection is as follows: at each time step, the inlet temperature boundary condition is modified according to the instantaneous position of the entropy-perturbation centre, even when this position lies outside the computational domain.

The inlet boundary conditions for the injection of a circular entropy spot of radius $r_{\text{s}}$ are therefore defined as

$$\begin{cases} p_{\text{in}} = \bar{p}_{\text{in}}, \\ T_{\text{in}} = \bar{T}_{\text{in}} \left(1 + \eta \, \left(1 + \cos(\pi \, r(t,y)/r_{\text{s}})\right)/2\right), \end{cases}$$

where the instantaneous radius function $r(t,y)$ defines the spatial distribution of the injected entropy perturbation.

Figure 6.1 illustrates the methodology used to inject the entropy spot. At each time step $t_n \in [\![0, N_t]\!]$, the position of the perturbation centre, $x(t_n) = -x_0 + t_n \, \Delta x$, is computed from the initial perturbation location $x_0$, where $\Delta x$ denotes the longitudinal mesh size. The longitudinal and transverse mesh spacings are assumed identical, *i.e.*, $\Delta x = \Delta y$. For any transverse inlet position $y$, the instantaneous radius function is given by

$$r(t,y) = \sqrt{x(t)^2 + (y - y_0)^2}, \tag{6.1}$$

where $y_0$ denotes the initial transverse position of the spot centre. If the conditions $|x(t)| \leq r_{\text{s}}$ and $|y - y_0| \leq \sqrt{r_{\text{s}}^2 - x(t)^2}$ are not satisfied, meaning that the location lies outside the circular spot, then the inlet temperature is set to its mean value, *i.e.*, $T_{\text{in}}/\bar{T}_{\text{in}} = 1$.

For a slug perturbation (a rectangular entropy band), the transverse location $y$ is no more needed as the perturbation is assumed to be of the size of the inlet. Then, the instantaneous radius function simplifies to $r(t,y) = x(t)$.

Once the entropy perturbation is fully generated, the inlet boundary condition is switched to a non-reflective boundary condition, allowing the evacuation of upstream-propagating acoustic waves generated by the convection of the entropy spot (see Sec. 2.4.2). This boundary condition acts as a low-frequency filter and is parametrised to have an inlet acoustic reflection coefficient of $R_{a,\text{in}} = 1 \times 10^{-4}$ for frequencies above 4 Hz.

For this study, the entropy spot is introduced into the nozzle after a delay of $\delta t = 1 \times 10^{-4}$ s ($x_0 = r_{\text{s}} + \bar{u}_{\text{in}} \delta t$) to prevent any initial numerical disturbance of the steady flow field.

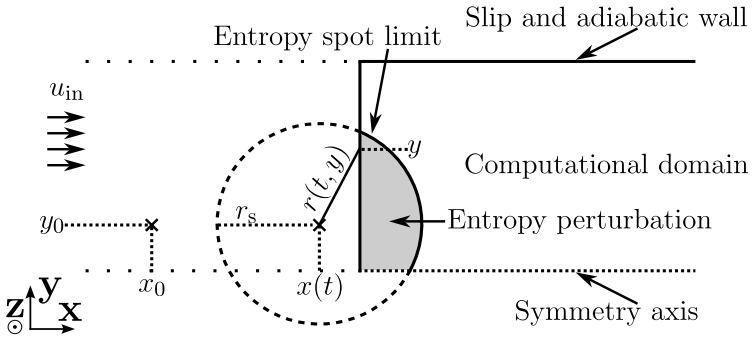


**Figure 6.1** Sketch of the entropy-spot injection methodology. A similar procedure is used for entropy-slug injection.

To ensure proper entropy injection, the time step must be adapted to the inlet flow velocity, $\bar{u}_{\text{in}}$, and the mesh discretisation, such that each inlet cell is updated sequentially according to

$$\Delta t = \frac{\Delta x}{\bar{u}_{\text{in}}}. \tag{6.2}$$

In this approach, the entropy perturbation is injected slice by slice. It is noteworthy that this condition is equivalent to setting the CFL number to unity, and the time step is therefore adjusted accordingly.

Figure 6.2 illustrates examples of an entropy spot and an entropy slug injected into a thermally choked nozzle.

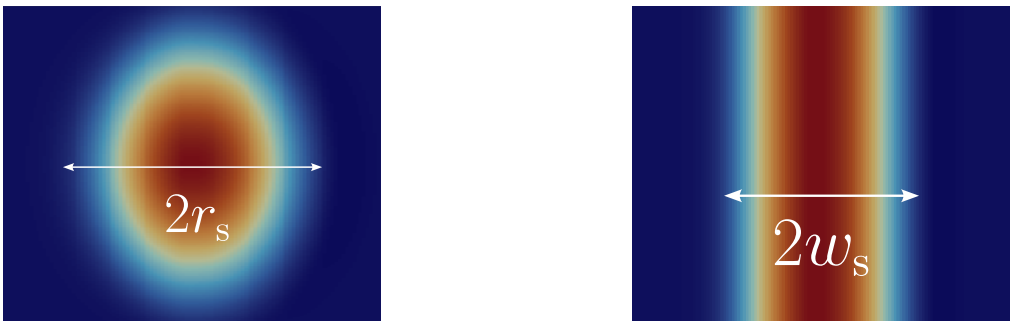


**(a)** Example of entropy spot of size $r_{\text{s}}/y_* = 0.2$. **(b)** Example of entropy slug of size $w_{\text{s}}/y_* = 0.2$.

**Figure 6.2** Example of entropy perturbations injection into a thermally choked-flow nozzle: **(a)**: Entropy spot of normalised sized $r_{\text{s}}/y_* = 0.2$ and **(b)** entropy slug of normalised sized $w_{\text{s}}/y_* = 0.2$. The injection centre is located at the centre of the inlet duct in the transverse direction, *i.e.*, $y_0 = y_{\text{in}}/2$.

### 6.2.2 Computational setup

The numerical simulations are performed using the CFD code CEDRE, presented in Sec. 2.4, which solves the Euler equations (Eq. (2.3)). The numerical schemes used for spatial discretisation and temporal integration are described in Sec. 2.4.

The computational setup consists of a two-dimensional planar domain, as detailed in Sec. 2.3.1, discretised with $3.8 \times 10^6$ computational cells of size $\Delta x/L = 5.2 \times 10^{-5}$. This resolution ensures adequate spatial discretisation of the entropy perturbations, providing at least 80 grid points

per spot radius for the smallest case considered ($r_s/y_* = 2 \times 10^{-1}$). Since the flow is primarily longitudinal, the same grid spacing ($\Delta x \simeq \Delta y$) is applied in both directions, resulting in approximately 19 000 points along the longitudinal axis and 200 points along the transverse axis.

Temporal integration is carried out using a time step $\Delta t = 2 \times 10^{-7}$ s, corresponding to a Courant-Friedrichs-Lewy (CFL) number of $\bar{u}_{\text{in}} \Delta t / \Delta x = 0.45$. The unsteady solutions described in Sec. 6.2.1 are post-processed using a total simulation time modulated according to the entropy perturbation characteristic size. To ensure the complete convection of a fully developed entropy spot through the nozzle and to capture the maximum acoustic response, the total simulation time is adjusted according to the size of the entropy perturbation $r_s$, and can reach up to $\tau_{\text{CFD}} = 50 L / \bar{u}_{\text{in}}$ for the largest cases. For adequate temporal resolution, 1000 time steps are recorded per run. The same numerical parameters are employed for the geometric throat configuration (see Sec. 2.6), ensuring both mesh and time-step independence.

The potential influence of numerical resolution, both spatial and temporal, is assessed by varying the mesh size and time step. The impact of these variations is evaluated on the maximum upstream-propagating acoustic response, using a circular entropy perturbation of size $r_s/y_* = 2 \times 10^{-1}$.

Four computational grids and four time-step values are examined. The mesh size $\Delta x$ is varied from 0.1 mm ($5.98 \times 10^6$ grid points) to 0.5 mm ($2.35 \times 10^5$ grid points), while the time step $\Delta t$ ranges from $1.5 \times 10^{-7}$ s to $3 \times 10^{-7}$ s.

The absolute relative error in the maximum upstream-propagating acoustic response for each case is compared with that obtained using the finest grid and smallest time step, $(\Delta x, \Delta t)_{\text{ref}} = (0.1\,\text{mm}, 1.5 \times 10^{-7}\,\text{s})$. The acoustic measurements are taken along the symmetry axis. The results shown in Fig. 6.3 indicate that the acoustic response becomes independent of spatial resolution for mesh sizes smaller than $\Delta x = 0.125$ mm, with an absolute relative error on the order of $1 \times 10^{-3}$.

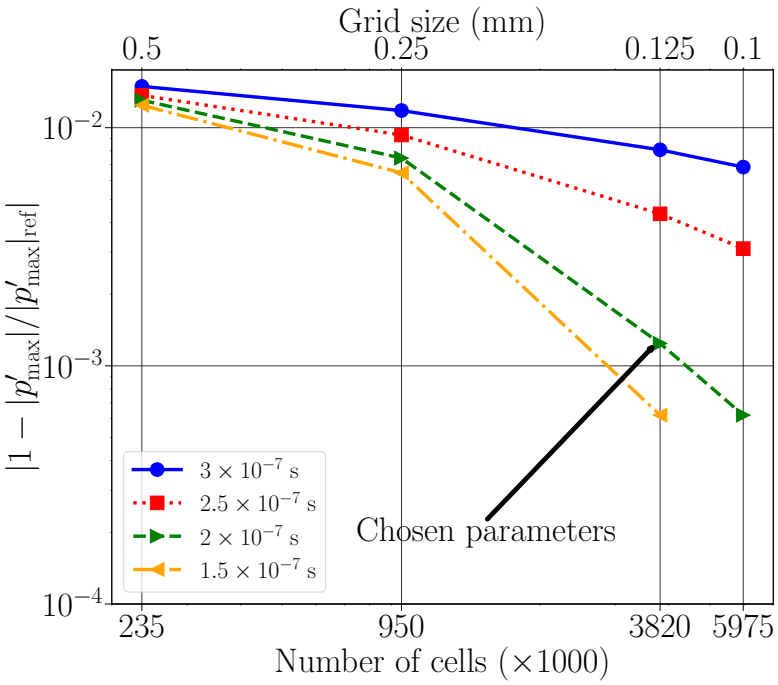


**Figure 6.3** (Colour) Absolute relative error of the maximum upstream-propagating acoustic response induced by the injection of a circular entropy perturbation of radius $r_s/y_* = 2 \times 10^{-1}$.

Consequently, the adopted numerical parameters, $(\Delta x, \Delta t) = (0.125\,\text{mm}, 2 \times 10^{-7}\,\text{s})$, rep-

resent an optimal compromise between numerical accuracy and computational cost. With this configuration, the absolute relative error remains on the order of $1 \times 10^{-3}$ compared with the finest refinement.

The acoustic response has been verified to be independent of both the transverse and longitudinal measurement positions within the constant-duct region.

## 6.3 One-dimensional entropy-noise response models

To assess the impact of the thermal throat on the generation of acoustic noise induced by the convection of entropy inhomogeneities, relative to a geometric-throat nozzle, two one-dimensional models are employed. These models, proposed by Marble and Candel [16] and Elbakly [159], determine whether the dominant sound-generation mechanism arises from the quasi-steady response of the nozzle (*i.e.*, variations in the critical mass-flow rate, as detailed by Hirschberg *et al.* [160]) or from inertial (acceleration) effects.

The framework of these models applies to isentropic geometric nozzles and characterises the asymptotic limits of entropy-perturbation size relative to the throat height, $r_\mathrm{s}/y_*$, where $r_\mathrm{s}$ denotes the characteristic size of the entropy perturbation and $y_*$ the throat height. For very large spots, the quasi-steady limit is approached, whereas for very small spots, the inertial limit is expected.

### 6.3.1 Quasi-steady asymptotic limit model

For a very large entropy spot, *i.e.*, $r_\mathrm{s}/y_* \gg 1$, the spot can be approximated as a one-dimensional entropy wave. Under this assumption, the quasi-steady (QSS) model of Marble and Candel [16] can be applied. This model relies on two key assumptions: (i) in the quasi-steady limit, the Mach-number fluctuations at the critical throat vanish under entropy-wave forcing, *i.e.*, $\mathrm{M}'_* = 0$; and (ii) the nozzle is assumed to be compact, meaning that the characteristic perturbation wavelength $\lambda$ is much larger than the nozzle length. Under this compact assumption, the condition $\mathrm{M}'_* = 0$ holds throughout the subsonic region and, in particular, at the inlet where $\mathrm{M}'_\mathrm{in} = 0$. More details are provided in Chap. 4.

Expressing the Mach-number fluctuations in terms of the natural variables, for a constant heat capacity ratio $\gamma$, yields:

$$\mathrm{M}'_\mathrm{in} = \frac{u'_\mathrm{in}}{\bar{u}_\mathrm{in}} - \frac{c'_\mathrm{in}}{\bar{c}_\mathrm{in}} = 0. \tag{6.3}$$

Using the linearised forms of Eqs. (2.7) and (2.8), one obtains:

$$\frac{u'_\mathrm{in}}{\bar{u}_\mathrm{in}} - \frac{c'_\mathrm{in}}{\bar{c}_\mathrm{in}} = \frac{u'_\mathrm{in}}{\bar{u}_\mathrm{in}} - \frac{(\gamma-1)}{2}\frac{p'_\mathrm{in}}{\gamma\bar{p}_\mathrm{in}} - \frac{1}{2}\frac{s'_\mathrm{in}}{c_p} = 0. \tag{6.4}$$

It is now assumed that the pressure $p'_\mathrm{in}$ and velocity $u'_\mathrm{in}$ fluctuations are solely induced by upstream-propagating acoustic waves $P^-$ (*i.e.*, $P^+ = 0$). Based on the uniform acoustic-wave decomposition (see Appendix A), one writes:

$$\begin{cases} \dfrac{p'_\mathrm{in}}{\gamma\bar{p}_\mathrm{in}} = P^+_\mathrm{in} + P^-_\mathrm{in} = P^-_\mathrm{in}, \\[2ex] \dfrac{u'_\mathrm{in}}{\bar{u}_\mathrm{in}} = \dfrac{P^+_\mathrm{in} - P^-_\mathrm{in}}{\bar{\mathrm{M}}_\mathrm{in}} = -\dfrac{P^-_\mathrm{in}}{\bar{\mathrm{M}}_\mathrm{in}}. \end{cases} \tag{6.5}$$

After some algebraic manipulations, the following relation is obtained:

$$|p'_\mathrm{in}| = \frac{\bar{\gamma}_\mathrm{in}\bar{p}_\mathrm{in}\bar{\mathrm{M}}_\mathrm{in}}{2 + (\bar{\gamma}_\mathrm{in} - 1)\bar{\mathrm{M}}_\mathrm{in}} \frac{|s'_\mathrm{in}|}{\bar{c}_{p,\mathrm{in}}}, \tag{6.6}$$

which gives the ratio between the maximum upstream-propagating acoustic-wave amplitude $|p'_{\text{in}}|$ and the maximum downstream-propagating entropy-wave amplitude $|s'_{\text{in}}|$.

As demonstrated in Chaps. 3 and 4, for a thermal-throat configuration, the quasi-steady condition $\text{M}'_* = 0$ at the critical throat is not strictly valid, since its value depends on the amount of added energy. Moreover, the compact assumption and constant heat capacity ratio assumption no longer apply because of the presence of heat addition. Nevertheless, this model is used here for comparison between both nozzle configurations and to identify the mechanism responsible for the acoustic response for very large entropy spots.

### 6.3.2 Point-mass inertial asymptotic limit model

For a very small entropy spot, *i.e.*, $r_{\text{s}}/y_* \ll 1$, the spot can be approximated as a point sound source with an excess mass density $m_e$, which generates an acoustic response at a given source position $x_{\text{s}}$. Following the work of Elbakly [159], the upstream acoustic response $|p'_{\text{in}}|$ due to a point excess mass density $m_e$ at position $x_{\text{s}}$, is given by:

$$|p'_{\text{in}}|(x_{\text{s}}) = \sqrt{\frac{\bar{\rho}_{\text{in}}\bar{c}_{\text{in}}}{\bar{\rho}(x_{\text{s}})\bar{c}(x_{\text{s}})}\frac{1}{\text{A}_{\text{in}}\text{A}(x_{\text{s}})}}\left(1+\bar{\text{M}}(x_{\text{s}})\right)\left(\frac{1-\bar{\text{M}}(x_{\text{s}})}{1-\bar{\text{M}}_{\text{in}}}\right)\bar{u}(x_{\text{s}})\left.\frac{\text{d}\bar{u}}{\text{d}x}\right|_{x_{\text{s}}}\frac{m_e}{2}. \tag{6.7}$$

The full derivation of the model proposed by Elbakly [159] is provided in Appendix D.

The point-mass (PM) model assumes that, for sufficiently small entropy spots, acoustic generation is solely due to inertial effects and that the acoustic response scales with the excess mass $m_e$ contained in the spot. Unlike the original model of Elbakly [159], the secondary acoustic response induced by the reflection of the acoustic waves on the critical throat is removed. Indeed, as observed in Chap. 3, at high frequencies, the thermal throat has a purely acoustic radiation behaviour, meaning that the reflection of acoustic waves is very low, especially compared with the QSS model of Marble and Candel [16].

To estimate the sound-source position, $x_{\text{s}}$, the methodology of Elbakly [159] is adopted. The position at which the quantity $|p'_{\text{in}}|(x)\text{A}_{\text{in}}^3/(m_e\bar{u}_{\text{in}}^2)$ reaches its maximum is taken as the location of the most intense sound generation.

The excess mass density $m_e$ is then numerically estimated by volumetric integration of the density fluctuations $\rho'_e = (\rho-\bar{\rho})/\bar{\rho}$ over the constant-duct region, such that

$$m_e = \int_V \rho'_e \,\text{d}V. \tag{6.8}$$

It should be noted that this model is derived for an isentropic nozzle, which is not strictly valid for the thermal-throat configuration. Nevertheless, it provides valuable insight into the sound-generation mechanisms in both choked configurations considered.

## 6.4 Two-dimensional analysis of the acoustic response induced by entropy non-uniformities

To provide the necessary background for understanding the mechanisms responsible for sound generation by the convection of two-dimensional entropy perturbations, a phenomenological description of the acoustic generation process in a thermally choked-flow nozzle is first presented. This preliminary analysis aims to clarify the main physical interactions between heat addition, flow acceleration, and entropy convection that govern the unsteady acoustic response of such configurations. In this section, the thermally choked-flow configuration defined in Sec. 2.3.1 is considered. The thermal throat is located at the steady position $\delta_*/L = 0.38$. Further details on the corresponding steady flow fields are provided in Sec. 3.4.1, for the $\text{C}_1$ case.

### 6.4.1 Phenomenological description of the acoustic response induced by a circular entropy perturbation

Figure 6.4 illustrates the propagation of a representative circular entropy spot of normalised size $r_s/y_* = 0.25$ at four different time instants. This spot size is selected to emphasize the strong change in scaling between the smallest entropy perturbations and the overall nozzle geometry. The upper field shows the normalised entropy fluctuations $s'/\bar{c}_p$, while the lower field displays the normalised pressure fluctuations $p'/(\bar{\gamma}\bar{p})$.

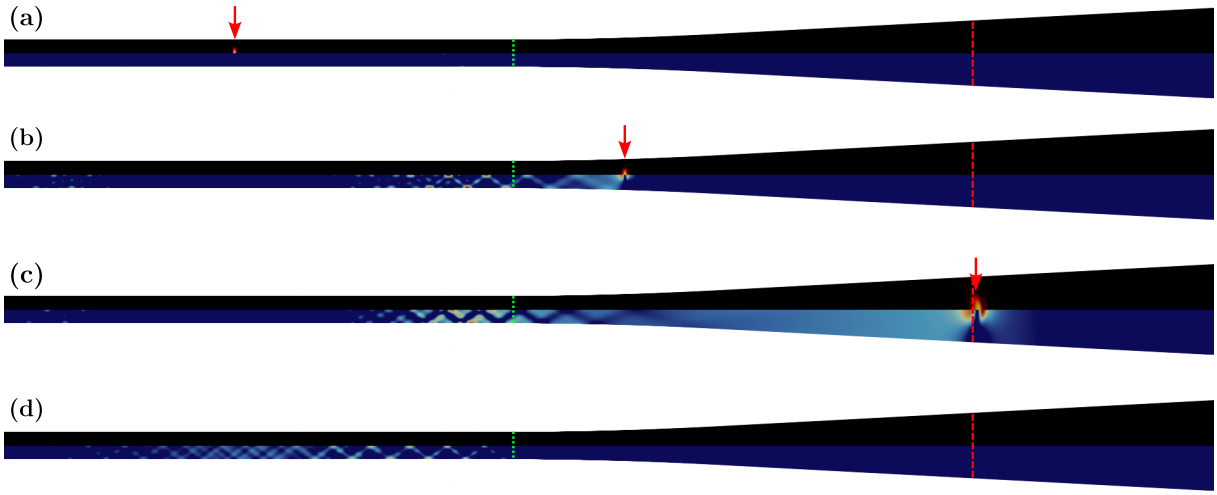


**Figure 6.4** Two-dimensional normalised fields of entropy (top) and pressure (bottom) fluctuations at four different time instants **(a)**–**(d)** in a thermally choked flow, for a normalised entropy-spot size of $r_s/y_* = 0.25$. The red arrow indicates the circular entropy spot. The green vertical dotted line indicates the onset of the divergent section (and of the heated region), while the red vertical dashed line indicates the steady thermal throat position.

At the first selected time instant, **(a)**, the small circular entropy spot is convected downstream by the mean flow $\bar{u}$. As the spot experiences acceleration at the onset of the volumetric heat-release region (around $x_u/L$), an acoustic response $p'$ is generated **(b)** and propagates both upstream and downstream, with the main pressure fluctuations occurring downstream. Two distinct acoustic fluctuation structures are observed: one longitudinal and one transverse, resulting in oblique acoustic-wave patterns. The transverse fluctuations arise because the entropy spot does not fill the entire nozzle height; small local variations in temperature along the transverse direction induce acoustic disturbances that are not purely longitudinal. For an entropy slug perturbation, or for large entropy spots, these transverse pressure fluctuations are no longer observed. At the subsequent time instant **(c)**, the entropy spot becomes deformed due to transverse acceleration effects. The downstream edge of the spot is accelerated more strongly than the upstream edge, leading to a distorted circular shape. Finally, when the spot exits the nozzle **(d)**, the acoustic response continues to propagate upstream at a velocity $\bar{c} - \bar{u}$, while residual transverse fluctuations remain visible.

The transverse pressure fluctuations ($p'_{\text{trans}}$) are found to oscillate at frequencies significantly higher than those of the longitudinal pressure fluctuations ($p'_{\text{long}}$) *i.e.*, $f_{\text{long}} \ll f_{\text{trans}}$. In the following analysis, these transverse components are therefore neglected.

### 6.4.2 Comparison of the linear acoustic response to two- and one-dimensional entropy forcing

To justify the use of two-dimensional entropy perturbations, a comparison of the acoustic response of a thermally choked nozzle to different types of entropy forcing is performed. Three kinds of perturbations are considered. The first corresponds to linear one-dimensional (1D) entropy plane waves, as introduced in Chap. 3. The second type is a two-dimensional (2D) circular entropy perturbation, referred to as a spot, while the third corresponds to a 2D rectangular entropy perturbation, referred to as a slug (see Fig. 6.1).

To enable a consistent comparison between the three responses, a Strouhal number $S_{t,\mathrm{eq}}$ is defined as the ratio between the characteristic frequency of the perturbation $f$, the length of the heat-release region $\delta_*$, and the speed of sound at the steady critical position $\bar{c}_*$:

$$S_{t,\mathrm{eq}} = f_{\mathrm{eq}} \frac{\delta_*}{\bar{c}_*}. \tag{6.9}$$

Additional details on this dimensionless number can be found in Chap. 3.

For the mono-harmonic entropy plane wave, the frequency $f$ is directly prescribed at the nozzle inlet, *i.e.*, $f_{\mathrm{eq}} = f$. However, for the spot and slug perturbations, an equivalent frequency $f_{\mathrm{eq}}$ must be defined. This is achieved by assuming that the characteristic convection speed of the perturbation is the inlet steady velocity $\bar{u}_{\mathrm{in}}$ and that its characteristic length $\lambda_{\mathrm{eq}}$ corresponds to the spot diameter, $D_{\mathrm{s}} = 2r_{\mathrm{s}}$, or to the slug width $2w_{\mathrm{s}}$. The equivalent frequency is therefore expressed as

$$f_{\mathrm{eq}} = \frac{\bar{u}_{\mathrm{in}}}{\lambda_{\mathrm{eq}}}. \tag{6.10}$$

The acoustic response for each configuration is quantified by the ratio between the maximum amplitude of the upstream-propagating acoustic wave $P^-_{\mathrm{max}}$, and the maximum amplitude of the entropy perturbation $\sigma_{\mathrm{max}}$, defined as

$$\frac{P^-_{\mathrm{max}}}{\sigma_{\mathrm{max}}} = \frac{\dfrac{p'_{\mathrm{max}}}{\bar{\gamma}\,\bar{p}} - \bar{\mathrm{M}}\,\dfrac{u'_{\mathrm{max}}}{\bar{u}}}{2\dfrac{s'_{\mathrm{max}}}{\bar{c}_p}}. \tag{6.11}$$

For the entropy spot configuration, only half of the spot is introduced in the computational domain. The acoustic response is measured along the symmetry axis at the inlet, and it has been verified that the transverse position does not affect the amplitude of the upstream-propagating acoustic wave.

Figure 6.5 shows the maximum normalised acoustic response induced by the three types of entropy perturbations (1D planar entropy wave, 2D entropy circular spot and 2D entropy rectangular slug), as a function of the equivalent Strouhal number $S_{t,\mathrm{eq}}$.

As expected, at very low Strouhal numbers ($S_{t,\mathrm{eq}} \ll 1 \times 10^{-1}$), all entropy perturbations tend toward the same quasi-steady acoustic-response regime. In this limit, the size of both the spot and the slug becomes large compared with the characteristic length of the nozzle, and the acoustic response is governed solely by variations in the mass-flow rate at the critical throat, as described by Hirschberg [94]. The specific shape of the perturbation therefore becomes negligible in this regime.

At higher Strouhal numbers ($S_{t,\mathrm{eq}} \gg 1 \times 10^{-1}$), significant differences arise between one-dimensional entropy waves and two-dimensional entropy structures (spots or slugs). For 1D waves, resonance behaviour appears for $S_{t,\mathrm{eq}} \gtrsim 5 \times 10^{-1}$, resulting from the continuous inlet forcing (see Sec. 3.2.3). In contrast, entropy spots and slugs exhibit similar responses, as their

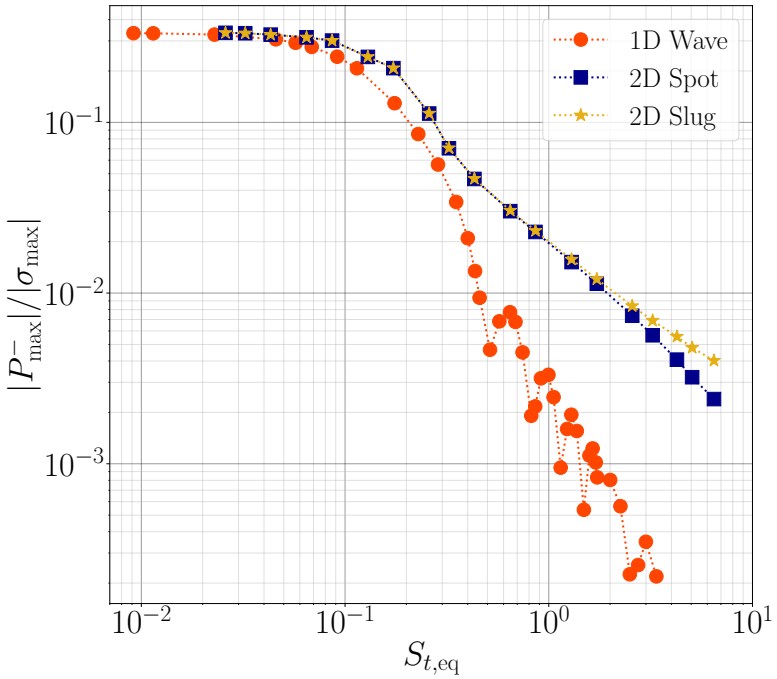


**Figure 6.5** (Colour) Maximum normalised acoustic response, $|P^-_{\max}/\sigma_{\max}|$, induced by three types of entropy forcing: a one-dimensional planar wave (-●-), a two-dimensional spot (-■-), and a two-dimensional slug (-★-), as a function of the equivalent Strouhal number $S_{t,\mathrm{eq}}$ in a thermally choked nozzle.

characteristic sizes are comparable. At very high Strouhal numbers ($S_{t,\mathrm{eq}} \gg 2$), however, differences emerge because the total entropy injected into the heated region is larger for the slug than for the spot.

These first results highlight the importance of considering two-dimensional entropy structures in the study of indirect entropy-noise.

## 6.5 One-dimensional entropy-noise generation mechanism

The mechanisms of acoustic noise generation induced by entropy spots and slugs of very small and very large sizes are numerically investigated by comparison with the one-dimensional linear model presented in Sec. 6.3. Several choking configurations, as well as different transverse injection positions, are examined. This approach provides a broad overview of the mechanisms responsible for sound generation in thermally choked flows.

### 6.5.1 Asymptotic scaling of the acoustic response with entropy-shape size

The mechanisms responsible for the acoustic noise generated by two-dimensional entropy structures of very small and very large sizes are now assessed in a thermally choked configuration and compared with an equivalent geometrically choked configuration. Two types of entropy perturbations are considered: circular spots and rectangular slugs. The thermal- and geometric-throat configurations correspond to those defined in Chap. 3, referred to as cases $C_1$ and $C_2$, respectively.

To examine the main mechanisms responsible for noise generation as a function of the entropy-perturbation size, the two one-dimensional linear models presented in Sec. 6.3 are considered and

used to normalise the numerical results obtained from the CFD simulations. The maximum value of the pressure fluctuations propagating upstream $p'_{\max}$ is considered and normalised either by the quasi-steady (QSS) model (Eq. (6.6)) or by the point-mass (PM) inertial model (Eq. (6.7)). To minimise strong two-dimensional steady flow effects, only half of the circular entropy spot is injected, with its centre coinciding with the symmetry axis. The effects of the transverse injection position and two-dimensional base-flow variations are assessed in Sec. 6.5.2.

Figure 6.6 presents the normalised maximum pressure fluctuations induced by a circular entropy spot for two choking configurations: a thermally choked flow (QSS: ·□·, PM: ·■·) and a geometrically choked flow (QSS: ·△·, PM: ·▲·). The results are shown as a function of the spot size normalised by the cross-section height at the critical-throat position, $r_s/y_*$.

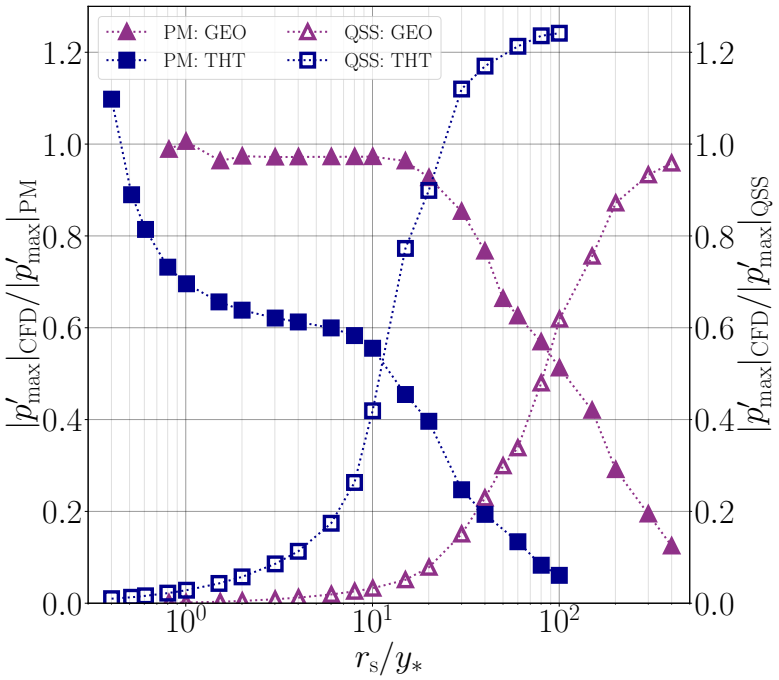


a

**Figure 6.6** (Colour) Acoustic response $|p'_{\max}|_{CFD}$ induced by a circular entropy spot of normalised size $r_s/y_*$. The response is normalised, on the left, by the point-mass model $|p'_{\max}|_{PM}$ (Eq. (6.7), filled markers) and, on the right, by the quasi-steady (QSS) model $|p'_{\max}|_{QSS}$ (Eq. (6.6), empty markers). Results are shown for the thermally choked configuration (PM: ·■·, QSS: ·□·) and the geometrically choked configuration (PM: ·▲·, QSS: ·△·).

For the geometric-throat configuration, as expected, a good agreement is observed between the linear models and the CFD results, as these models rely on an isentropic flow framework. Indeed for very small spot sizes, $r_s/y_* < 1 \times 10^1$ (·▲·), the normalised value $|p'_{\max}|_{CFD}/|p'_{\max}|_{PM}$ is close to 1, indicating that, in this asymptotic regime, the sound generation is mainly driven by the inertial acceleration of the entropy slug due to the local velocity gradient $(\mathrm{d}\bar{u}/\mathrm{d}x)_s$ at the source location. For very large entropy spots, $r_s/y_* > 5 \times 10^2$ (·△·), the quasi-steady regime is recovered as the normalised value approaches unity, *i.e.*, $|p'_{\max}|_{CFD}/|p'_{\max}|_{QSS} \approx 0.97$. In this limit, the acoustic response is governed by the readaptation of the mass-flow at the critical throat.

However, the transition spot size at which these asymptotic regimes are reached is significantly larger than that reported by Elbakly [159]. As demonstrated in Appendix D, this discrepancy is not related to the measurement methodology but rather to the nozzle geometry. The geometric throat considered here exhibits a smooth acceleration gradient, as the inlet Mach number is relatively high ($M_{in} = 0.6$). Consequently, the required geometric contraction to achieve choking

is moderate. This observation suggests that the dimensionless number $r_s/y_*$, as proposed by Elbakly [159], may not be sufficient to fully characterise both acoustic regimes in geometrically choked configurations.

In contrast, the thermally choked configuration exhibits distinct behaviour. For large entropy spots, $r_s/y_* > 1 \times 10^2$ (·□·), the quasi-steady regime is reached, but with a higher normalised value, $|p'_{max}|_{CFD}/|p'_{max}|_{QSS} \approx 1.2$. This increase is attributed to the presence of the heated region. As discussed in Chap. 3, within this region, entropy perturbations generate acoustic waves through flow acceleration; these waves, in turn, induce additional entropy perturbations, which produce a secondary acoustic response. The same mechanism is observed here. The quasi-steady value obtained is consistent with that reported in Sec. 3.4.5.

For small entropy spots, $r_s/y_* < 1 \times 10^1$ (·■·), the acoustic response differs markedly from the geometric-throat case. The normalised value $|p'_{max}|_{CFD}/|p'_{max}|_{PM}$ increases as the entropy spot size decreases. Below $r_s/y_* < 6$, the CFD results show that the acoustic response becomes independent of the spot size, reaching a minimum amplitude of $|p'_{max}| \approx 23\,\mathrm{Pa}$. Conversely, the point-mass model (Eq. (6.7)) predicts a linear scaling with the excess entropy mass injected into the system, a behaviour which is not observed in the simulations. This minimum acoustic response is likely associated with the heated region, which induces acoustic perturbations even for very small entropy disturbances. The physical mechanism underlying this minimal acoustic response is not yet fully understood.

This minimum in acoustic response is not observed for the geometric-throat configuration, in which the acoustic response scales approximately linearly with the excess entropy mass. In these cases, the acoustic amplitude can remain below $|p'_{max}| \approx 10\,\mathrm{Pa}$, making numerical issues unlikely.

Since both nozzle configurations exhibit similar one-dimensional Mach-number profiles, the normalised acoustic response for the thermally choked case is mainly shifted upward in the QSS regime due to the superposition of pressure waves, and downward in the PM regime.

Figure 6.7 presents the normalised maximum pressure fluctuations induced by a rectangular entropy slug for the two choking configurations: the thermally choked flow (QSS: ·☆·, PM: ·★·) and the geometrically choked flow (QSS: ·▽·, PM: ·▼·). The normalised acoustic response is plotted as a function of the dimensionless slug size $w_s/y_*$.

For the geometric-throat configuration, both asymptotic regimes are recovered at very small (PM: ·▼·) and very large (QSS: ·▽·) slug sizes. Only a slight difference is observed between the circular entropy spot and the rectangular entropy slug, with a relative deviation of about $1 \times 10^{-2}$ in the inertial regime. This similarity arises from the relatively large normalised slug size ($r_s/y_* \approx 10$), which already places the system near the quasi-steady regime. This observation reinforces the finding of Elbakly [159] that the dimensionless ratio $r_s/y_*$ alone is not sufficient to accurately characterise different entropy perturbations, and that geometric effects must be taken into account when analysing the acoustic response.

For the thermally choked configuration, a behaviour similar to that obtained with entropy spots is observed. For large slugs (·☆·), the quasi-steady regime is again reached, as expected. For very small slug sizes ($r_s/y_* < 10$, ·★·), the normalised acoustic response still tends to increase, though less sharply than for entropy spots. Unlike the spot case, a minimum acoustic level is not observed here, as the total entropy injected into the system is larger. This result suggests that the acoustic response scales with the total injected entropy mass $m_e$, although the relationship does not appear to be linear. Further analysis is required to clarify the underlying physical mechanisms governing this behaviour.

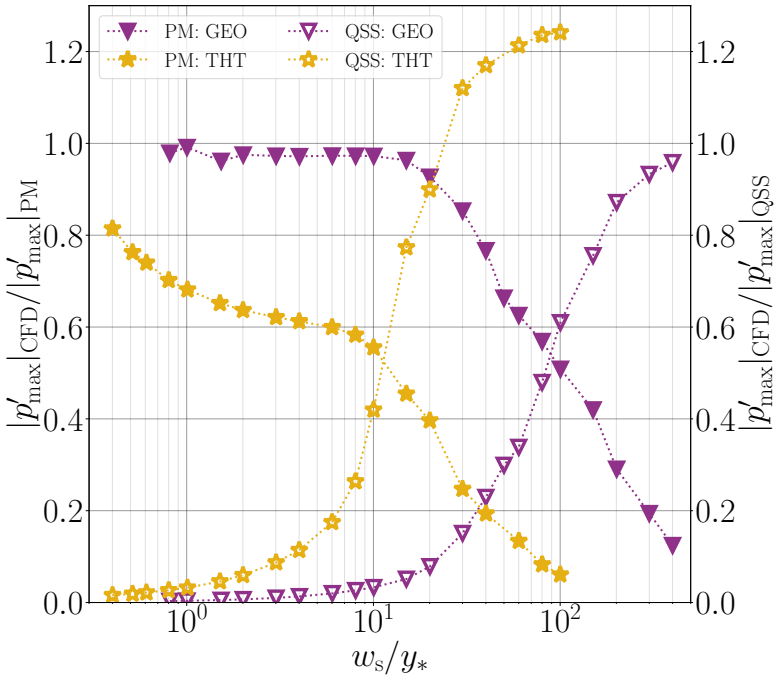


**Figure 6.7** (Colour) Acoustic response $|p'_{\max}|_{\mathrm{CFD}}$ induced by a rectangular entropy slug of normalised size $w_{\mathrm{s}}/y_*$. The response is normalised, on the left, by the point-mass model $|p'_{\max}|_{\mathrm{PM}}$ (Eq. (6.7), filled markers) and, on the right, by the quasi-steady (QSS) model $|p'_{\max}|_{\mathrm{QSS}}$ (Eq. (6.6), empty markers). Results are shown for the thermally choked configuration (PM: ★, QSS: ☆) and the geometrically choked configuration (PM: ▼, QSS: ▽).

### 6.5.2 Two-dimensional base-flow effects and transverse injection

In the previous section, the entropy spot was injected along the symmetry axis, with its centre located at a transverse position $y_0 = 0$. The influence of the transverse injection position and the resulting two-dimensional flow effects is assessed here. To this end, two additional injection positions are considered: $y_0 = y_{\mathrm{in}}/2$ and $y_0 = y_{\mathrm{in}}$.

Figure 6.8 presents the entropy-noise amplitude induced by a circular entropy spot, normalised using either the QSS model (Eq. (6.6)) or the PM model (Eq. (6.7)), as a function of the dimensionless entropy-spot size $r_{\mathrm{s}}/y_*$ for a thermally choked-flow configuration.

As expected, for very large entropy-spot sizes, the perturbation becomes much larger than the critical-throat height, and the influence of the transverse injection position becomes negligible. Consequently, all three configurations converge toward the quasi-steady-state regime. However, for very small entropy spots, distinct behaviours are observed. For the mid-plane injection position $y_0 = y_{\mathrm{in}}/2$, corresponding to the case where the full entropy spot is injected, the maximum normalised acoustic response is lower than that of the reference case $y_0 = 0$. This difference arises because the acoustic response, although larger in amplitude, does not scale linearly with the injected excess-entropy mass.

For the upper-wall injection case ($y_0 = y_{\mathrm{in}}$), the acoustic response becomes very weak for small spot sizes, with $|p'_{\max}| \approx 24\,\mathrm{Pa}$. Furthermore, near the slip wall, two-dimensional flow effects become more pronounced: the transverse velocity component $v$, although small compared with the longitudinal velocity $u$, is no longer negligible, leading to a strong deformation of the entropy spot. It is therefore assumed that these two-dimensional effects are responsible for the deviation from the inertial-model prediction.

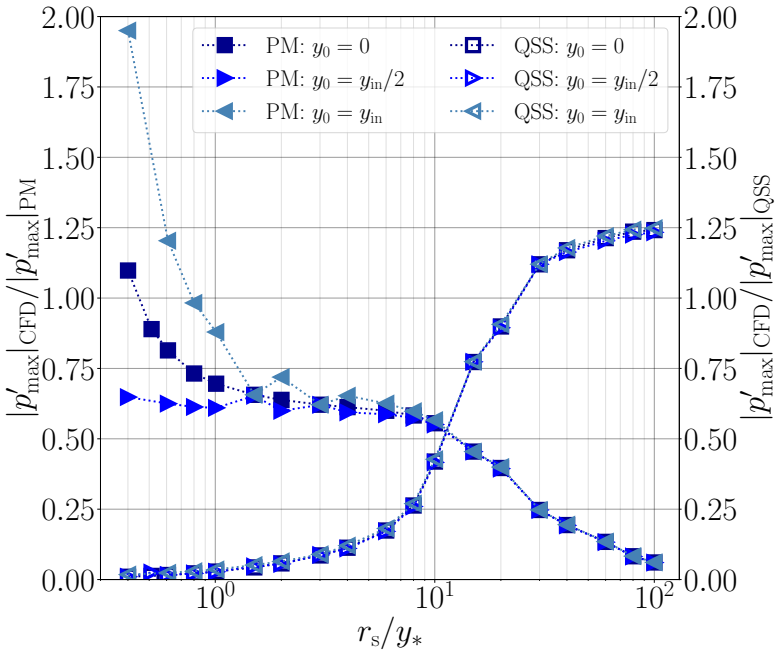


**Figure 6.8** (Colour) Acoustic response $|p'_{max}|_{CFD}$ induced by a circular entropy spot of normalised size $r_s/y_*$. The response is normalised, on the left, by the point-mass (PM) model $|p'_{max}|_{PM}$ (Eq. (6.7), filled markers) and, on the right, by the quasi-steady-state (QSS) model $|p'_{max}|_{QSS}$ (Eq. (6.6), empty markers). Results are shown for a thermally choked configuration at three transverse injection positions: $y_0 = 0$ (PM: ▪, QSS: ▫), $y_0 = y_{in}/2$ (PM: ▶, QSS: ▷), and $y_0 = y_{in}$ (PM: ◀, QSS: ◁).

### 6.5.3 Effect of the steady thermal-throat position

In the previous section, the steady thermal-throat position was considered fixed, *i.e.*, located at a reduced axial length of $\delta_*/L = 0.38$. The influence of this position on the acoustic response induced by a circular entropy spot is now investigated. As discussed in Sec. 3.4.4 and Chap. 5, variations in the steady position of the critical throat can lead to significant changes in the acoustic response. To this end, the thermal-throat location is varied while keeping the total heat addition constant. The methodology used to perform this adjustment is detailed in Sec. 3.2.1. In addition to the reference case ($\delta_*/L = 0.38$), two additional configurations are examined: one with the thermal throat positioned closer to the onset of the heat-release region ($\delta_*/L = 0.32$), and another located further downstream ($\delta_*/L = 0.44$).

Figure 6.9 presents, for the thermally choked flow, the normalised acoustic response $|p'_{max}|_{CFD}$, scaled either by the quasi-steady-state (QSS) model (Eq. (6.6)) or by the point-mass (PM) model (Eq. (6.7)). The acoustic response is plotted as a function of the dimensionless entropy spot size $r_s/y_*$ for the three steady thermal-throat positions $\delta_*/L = [0.32, 0.38, 0.44]$.

At very large entropy spot sizes, all configurations converge toward the quasi-steady regime, with slight deviations attributed to differences in the normalised size parameter $r_s/y_*$, which is not exactly identical across cases. An asymptotic value greater than unity is observed, indicating that geometric effects and steady-flow gradients continue to influence the acoustic response, even when the total heat addition remains constant, as already demonstrated for entropy plane waves in Chap. 3.

At very small spot sizes, however, distinct behaviours emerge, highlighting the complex mechanisms governing sound generation. The normalised acoustic response $p'_{max}|_{CFD}/|p'_{max}|_{PM}$ sig-

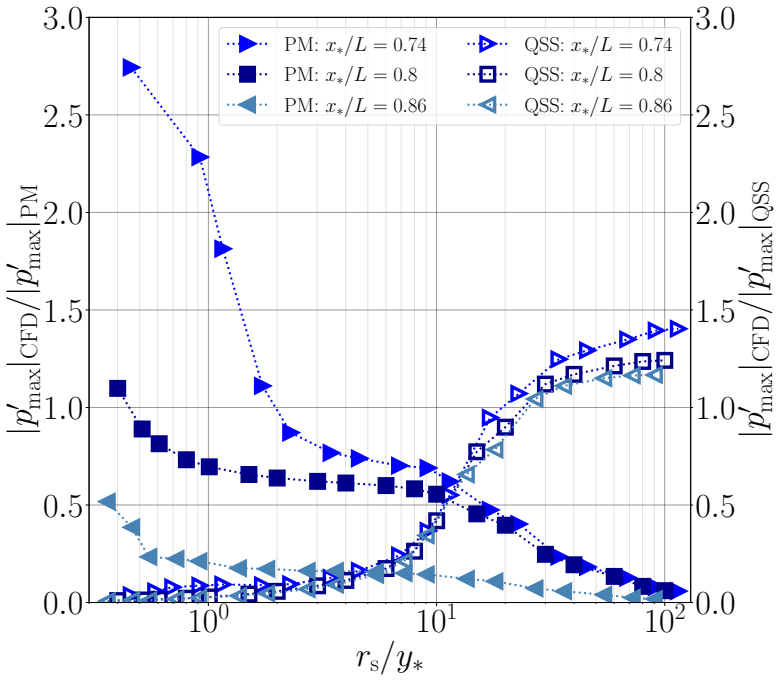


**Figure 6.9** (Colour) Acoustic response $|p'_{\max}|_{\mathrm{CFD}}$ induced by a circular entropy spot of normalised size $r_s/y_*$. The response is normalised, on the left, by the point-mass (PM) model $|p'_{\max}|_{\mathrm{PM}}$ (Eq. (6.7), filled markers) and, on the right, by the quasi-steady-state (QSS) model $|p'_{\max}|_{\mathrm{QSS}}$ (Eq. (6.6), empty markers). Results are shown for a thermally choked configuration at three steady thermal throat positions: $\delta_*/L = 0.32$ (PM: ·▶·, QSS: ·▷·), $\delta_*/L = 0.38$ (PM: ·■·, QSS: ·□·), and $\delta_*/L = 0.44$ (PM: ·◀·, QSS: ·◁·).

nificantly decreases for configurations in which the thermal throat is located further downstream ($p'_{\max}|_{\mathrm{CFD}}/|p'_{\max}|_{\mathrm{PM}} \approx 0.25$), while it becomes markedly stronger when the thermal throat is positioned upstream ($p'_{\max}|_{\mathrm{CFD}}/|p'_{\max}|_{\mathrm{PM}} \approx 2.75$). Since the steady velocity gradient varies with the thermal-throat location, it follows that, for a constant entropy injection, a wider (more downstream) thermal-throat configuration exhibits a lower velocity gradient and, consequently, a weaker acoustic response, a clear physical trend observed here.

Nevertheless, the large discrepancies between the different configurations suggest that additional factors, such as temperature gradients and geometric effects, also play a significant role in the sound-generation process. These physical mechanisms remain to be fully elucidated.

### 6.5.4 Influence of the inlet Mach number

Finally, the influence of the inlet Mach number, and consequently the effect of the mean velocity increase, is assessed. As demonstrated by Howe [70], entropy generation is primarily driven by steady pressure and velocity gradients. Therefore, by varying the inlet Mach number $\mathrm{M_{in}}$ while keeping the steady thermal-throat position constant at $\delta_*/L = 0.38$, variations in the acoustic response are expected. Specifically, for lower inlet Mach numbers, a stronger acoustic response is anticipated in both asymptotic size limits. The inlet Mach number was previously shown by Hirschberg [94] to play a dominant role in driving the acoustic response, and this behaviour is here examined for thermally choked configurations. In the reference case presented earlier, the inlet Mach number was set to $\mathrm{M_{in}} = 0.6$. Two additional cases are now considered, with $\mathrm{M_{in}} = 0.5$ and $\mathrm{M_{in}} = 0.7$.

Figure 6.10 presents the acoustic response induced by a circular entropy spot in a thermally choked-flow nozzle as a function of the dimensionless entropy-spot size for the three inlet Mach numbers $M_{in} = [0.5, 0.6, 0.7]$. The acoustic response is normalised using both the quasi-steady-state (QSS) model (Eq. (6.6)) and the point-mass (PM) model (Eq. (6.7)).

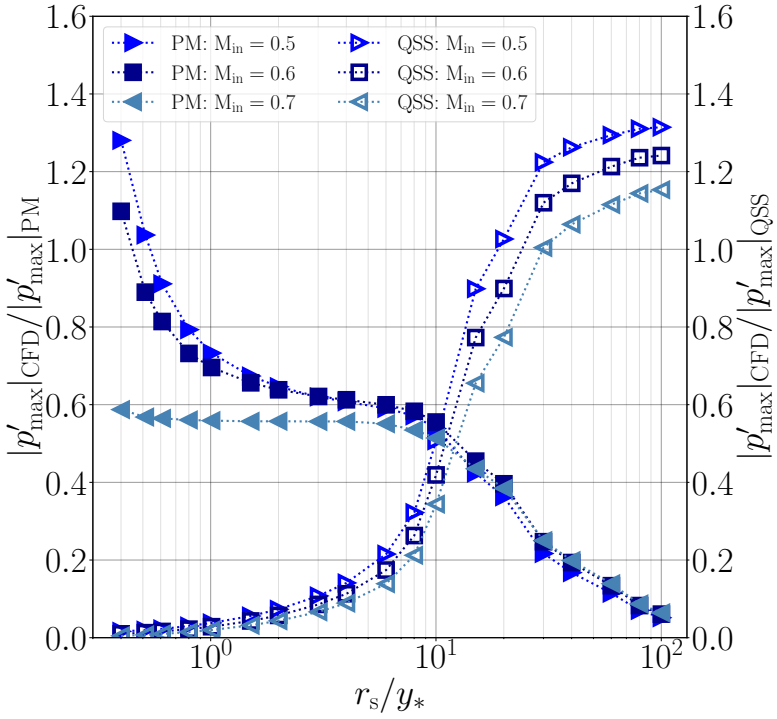


**Figure 6.10** (Colour) Acoustic response $|p'_{max}|_{CFD}$ induced by a circular entropy spot of normalised size $r_s/y_*$. The response is normalised, on the left, by the point-mass (PM) model $|p'_{max}|_{PM}$ (Eq. (6.7), filled markers) and, on the right, by the quasi-steady-state (QSS) model $|p'_{max}|_{QSS}$ (Eq. (6.6), empty markers). Results are shown for a thermally choked configuration at three inlet Mach numbers: $M_{in} = 0.5$ (PM: ▶, QSS: ▷), $M_{in} = 0.6$ (PM: ■, QSS: □), and $M_{in} = 0.7$ (PM: ◀, QSS: ◁).

All configurations tend toward the quasi-steady-state regime for very large entropy spot sizes, $r_s/y_* \gg 90$, as expected, although with different asymptotic values. The lower the inlet Mach number, the higher the measured acoustic response. This behaviour is consistent with the fact that, for a fixed thermal-throat position at $\delta_*/L = 0.38$, lower inlet Mach numbers are associated with stronger steady velocity gradients. The quasi-steady-state amplitude increases approximately linearly with the inlet Mach number, as previously observed by Hirschberg [94].

At very small entropy spot sizes, $r_s/y_* \ll 10$, the behaviour differs across cases. For inlet Mach numbers below $M_{in} = 0.6$, the previously observed minimum acoustic response is recovered. Since the point-mass (PM) model scales with the excess mass introduced by the entropy perturbation, the normalised value increases for very small spot sizes. However, for $M_{in} = 0.7$, the response appears to reach an inertial regime, with a normalised magnitude of approximately $p'_{max}|_{CFD}/|p'_{max}|_{PM} \approx 0.59$. For all configurations, the transition range of entropy spot sizes is nearly identical, indicating that the inlet Mach number has little influence at intermediate normalised values.

The underlying physical mechanism for this behaviour is not yet fully understood. It may result from the reduced heat addition required to choke the flow at higher inlet Mach numbers, where the flow tends toward an isentropic regime. Nevertheless, the asymptotic value remains

significantly below unity, suggesting that additional mechanisms, possibly related to geometric divergence, dampen the acoustic response in this regime.

### Chapter conclusion

This final chapter investigated the acoustic response induced by the interaction of two-dimensional entropy perturbations with a thermally choked-flow nozzle. Two distinct entropy perturbation shapes were examined: a circular "spot" and a rectangular "slug." Their acoustic responses were compared with one-dimensional models to identify the underlying asymptotic mechanisms and to highlight the differences between thermal and geometric choking configurations.

The study demonstrated that two-dimensional entropy perturbations generate an acoustic response that differs markedly from that predicted by one-dimensional plane-wave analyses. These differences arise primarily from the total entropy injected into the heated region. At very low frequencies, corresponding to large entropy structures, all configurations converge toward a quasi-steady regime, where the acoustic response becomes independent of the perturbation shape.

For both thermally and geometrically choked flows, the acoustic response approaches a quasi-steady limit as the perturbation size increases. However, in thermally choked configurations, the response amplitude is significantly higher owing to the additional acoustic generation induced by unsteady heat release. Conversely, at high frequencies, the geometric throat tends toward the inertial-response regime, while the thermal throat exhibits distinct behaviour: for slugs, the acoustic amplitude decreases, and for spots, a minimum perturbation size is found beyond which the response saturates and no longer scales with entropy amplitude.

Finally, the influence of the steady-state flow field was also assessed. It was shown that the inlet Mach number plays a dominant role in controlling the acoustic response by determining the acceleration of entropy perturbations, whereas the position of the thermal throat has a comparatively minor influence for a fixed total heat addition. These findings provide valuable insights into the mechanisms governing indirect noise generation in thermally choked configurations and lay the groundwork for future investigations.

# Conclusions and Perspectives

*Du passé faisons table en marbre.*

**Karadoc [2]**

## Conclusions

This thesis has investigated the aeroacoustic response of thermally choked nozzles, a flow configuration representative of dual-mode ramjet engines operating near the ram-to-scram transition. In such systems, distributed heat addition alone is capable of inducing choking, creating a thermal throat that acts simultaneously as a flow and acoustic boundary. While the aeroacoustics of geometrically choked nozzles have been widely studied for several decades, configurations in which choking emerges solely from heat release had received little attention prior to the present work. The primary objective of this thesis was therefore to characterise the acoustic and entropy-acoustic behaviour of thermally choked flows, to identify the physical mechanisms governing sound generation and reflection, and to develop accurate low-order models capable of predicting these mechanisms.

### Methodological framework

To achieve this objective, two complementary approaches were employed. First, numerical simulations were performed with the ONERA CFD solver CEDRE, using a simplified but representative dual-mode ramjet geometry and a calibrated model for the distributed volumetric heat release. These simulations provided detailed insight into the propagation, conversion, and reflection of acoustic and entropy disturbances. In parallel, a quasi-one-dimensional linear acoustic model was developed to isolate the key mechanisms responsible for the aeroacoustic behaviour of thermally choked flows. This model incorporates temperature-dependent thermodynamic properties, non-uniform mean flow, distributed heat addition, and an original critical-throat boundary condition tailored to heated configurations. It was validated extensively against the CFD results and subsequently used to explore a much broader parameter space.

### Acoustic response and damping mechanisms

A first major contribution of this thesis is the detailed characterisation of the acoustic response of thermally choked nozzles subjected to isentropic acoustic forcing. The results demonstrated that steady heat addition fundamentally modifies the low-frequency behaviour. In particular, a strong attenuation of the acoustic reflection coefficient was observed, driven by the conversion of acoustic waves into entropy fluctuations within the heated region. Consequently, the acoustic

behaviour at very low frequencies no longer converges to the classical predictions of Marble and Candel (*J. Sound Vib.* 1977) for isentropic nozzles. Two quasi-steady analytical models were proposed and validated to describe this regime. The first model considers a steady thermal throat generated by a uniform heat release at the end of a straight duct, whereas the second addresses a more general case in which an unsteady thermal throat, produced by a non-uniform heat release, is located deep within a divergent duct.

At high frequencies, all choking configurations, geometric or thermal, tended toward a similar isentropic radiation regime. However, the frequency at which this asymptotic behaviour was recovered was shown to depend strongly on the shape of the steady Mach-number profile. This dependence was later linked to the non-steady behaviour of the thermal throat and captured accurately by the newly proposed boundary condition.

### Entropy–acoustic conversion

The indirect noise generated by entropy perturbations convected through thermally choked flows was examined for both one-dimensional entropy waves and two-dimensional entropy inhomogeneities. For plane entropy waves, heat addition was shown to have a modest influence on the acoustic response, which remained primarily governed by the steady flow. At low frequencies, a quasi-steady regime was identified and modelled analytically. The dominant parameter was found to be the inlet Mach number.

Two-dimensional entropy perturbations, introduced in the final chapter, exhibited far richer and qualitatively different behaviours. For very small perturbations (high-frequency regime), the expected inertial asymptote of a geometric nozzle was not recovered; instead, a finite, non-zero acoustic response persisted. This minimum response, absent in isentropic nozzles, is a direct consequence of heat addition and depends on several parameters, including the injection position and thermal-throat location. For very large entropy structures, the quasi-steady regime was recovered, with higher acoustic amplitudes than in geometric nozzles due to additional acoustic coupling within the heated region.

### Development of a critical-throat boundary condition

The quasi-one-dimensional model required a new formulation of the acoustic boundary condition at the thermal throat. Classical approaches assume that Mach-number fluctuations vanish at the throat, an assumption that holds only for isentropic nozzles and only in the limit of very low frequencies. CFD simulations revealed that, in thermally choked flows, finite Mach-number fluctuations persist at the throat even in the low-frequency limit. A new boundary condition was therefore derived and implemented. It significantly improved the prediction of acoustic reflection, entropy-noise generation, and transmission in heated nozzles, while leaving geometric-throat predictions nearly unchanged. The development of this improved boundary condition is one of the main contributions of the thesis.

### Thermoacoustic coupling and stability

Finally, the influence of unsteady heat-release fluctuations was analysed using a simplified flame-transfer-function model inspired by Dowling's kinematic formulation (*J. Fluid. Mech.* 1999). This analysis demonstrated that unsteady heat release can significantly amplify the upstream-propagating acoustic wave, particularly for fast flames and compact flame holders. Two stability indicators, namely the amplification ratio of the acoustic response and the Rayleigh index, were computed over a wide parameter space. Both demonstrated that configurations combining fast

flame response, regardless of the flame-holder ratio, present the highest susceptibility to thermoacoustic instability. However, such configurations remain unlikely in practical ramjet combustors, where flame holders must be sufficiently large to generate a stable recirculation zone, and thus correspond to slow flame speeds.

### Overall assessment

Taken together, the results of this thesis demonstrate that thermally choked flows exhibit acoustic behaviours that differ fundamentally from those of geometrically choked configurations. Distributed heat addition modifies both steady and unsteady wave propagation, creating new mechanisms of acoustic damping, entropy–acoustic coupling, and thermally driven instability. The quasi-one-dimensional model developed here, together with the new thermal-throat boundary condition, provides a robust and computationally efficient framework for predicting these mechanisms over a wide range of operating conditions.

Beyond its contributions to fundamental aeroacoustics, this work provides physical insight and modelling tools relevant to the development of future dual-mode ramjet engines, in which stable operation requires a detailed understanding of the interplay between heat release, thermal throat, and acoustic feedback.

## Perspectives

To further advance the understanding of combustion instabilities in thermally choked-flow configurations, several research directions emerge naturally from the findings of this thesis. These perspectives aim to refine the physical modelling, extend the applicability of the developed tools, and strengthen the connection between simulations and experimental observations.

### Indirect noise and the role of vortical structures

A first line of investigation concerns the influence of two-dimensional and three-dimensional flow dynamics on indirect noise generation. In particular, the contribution of coherent vortical structures to the conversion of entropy and vorticity perturbations into acoustic waves remains largely unexplored [94]. Incorporating vortex–acoustic interactions would provide a more complete and physically realistic description of the mechanisms governing indirect noise in non-uniform, heated flows. In addition, analysing the response to pulsated or periodically injected entropy or vorticity two-dimensional disturbances would offer a more representative modelling of the unsteady conditions typically found in practical combustors.

### Improvements to the quasi-one-dimensional acoustic model

The quasi-one-dimensional linear acoustic model developed in this thesis can be enriched in several ways. Introducing multicomponent gas mixtures would enable the simulation of composition noise, which may play a significant role in reacting environments as shown by Gentil *et al.* [84]. Similarly, including simplified chemical kinetics would allow the model to capture the interaction between combustion chemistry and acoustics. Accounting for viscous and nonlinear effects, as performed by Huet and Giauque [23] and Huet *et al.* [26], would further extend its validity, particularly in regimes where the linear approximation becomes insufficient or where strong heat-release fluctuations are present.

### Towards realistic flame transfer functions and thermoacoustic coupling

A natural continuation of the present work consists in implementing more realistic steady volumetric power source term and flame transfer functions (FTFs) to describe the coupling between unsteady heat release and acoustic fluctuations. Experimentally validated or LES-derived FTFs would allow the framework to represent more accurately the frequency-dependent, nonlinear, and spatially distributed nature of flame dynamics. Such improvements would deepen the analysis of thermoacoustic instability mechanisms in thermally choked configurations and may reveal instability scenarios not captured by simplified formulations.

### Experimental validation and extension to realistic geometries

From an applied perspective, experimental validation of the mechanisms identified in this thesis is an essential next step. Comparing the predictions of the quasi-one-dimensional model with available measurements, such as those reported by Dessornes and Scherrer [5], would help quantify its accuracy and identify its limits. Furthermore, investigating the influence of nozzle geometry on the aeroacoustic and thermoacoustic responses could pave the way for shape-optimisation strategies aimed at mitigating instability risks in dual-mode ramjet engines. Extending the present analysis to more realistic three-dimensional geometries and complex heat-release distributions would bring the modelling framework closer to operational conditions.

# Appendices

Appendix A

# Acoustic-wave decomposition in a constant-cross-section isentropic-flow nozzle

*Not everything's a lesson. Sometimes you just fail.*
**Dwight Schrute [161]**


## Abstract

This appendix presents the theoretical decomposition of acoustic fluctuations into downstream and upstream-propagating wave components in a uniform, isentropic flow. Starting from the Euler conservation equations, the derivation systematically leads to the classical acoustic wave equation for a constant-area duct. The resulting formulation establishes the fundamental relations between pressure and velocity perturbations and defines the wave-number characteristics for both propagation directions. A non-dimensional form of the equations is also introduced, providing a consistent framework for the normalisation of acoustic variables used throughout this thesis. This decomposition serves as the analytical foundation for the acoustic-wave analysis and reflection-coefficient evaluations presented in subsequent chapters.


## Contents


**A.1 Formulation of the acoustic pressure wave equation . . . . . 138**

A.1.1 Flow governing equations and assumptions . . . . . 138

A.1.2 Acoustic pressure wave equation . . . . . 138

**A.2 Solution of the acoustic wave . . . . . 139**

A.2.1 Non-dimensional formulation . . . . . 140

## A.1 Formulation of the acoustic pressure wave equation

### A.1.1 Flow governing equations and assumptions

For a uniform flow in a duct of constant cross-sectional area, without any heat addition, the conservation equations of mass and momentum for an ideal gas can be expressed as:

$$\begin{cases} \dfrac{\mathrm{D}\rho}{\mathrm{D}t} + \rho\dfrac{\partial u}{\partial x} = 0, \\ \dfrac{\mathrm{D}u}{\mathrm{D}t} + \dfrac{1}{\rho}\dfrac{\partial p}{\partial x} = 0, \end{cases} \tag{A.1}$$

where $\rho$ denotes the density, $u$ the longitudinal velocity, $p$ the static pressure, and $t$ and $x$ the temporal and spatial coordinates, respectively. The ratio of specific heats, $\gamma = c_p/c_v$, with $c_p$ and $c_v$ the specific heats at constant pressure and constant volume, is assumed constant throughout the duct.

### A.1.2 Acoustic pressure wave equation

The one-dimensional Euler equations (Eq. (A.1)) are linearised by introducing the perturbation convention $\chi(x,t) = \bar{\chi}(x) + \chi'(x,t)$, where $\bar{\chi}$ denotes the steady component and $\chi'$ a small fluctuation of $\chi = [\rho, u, p]$, with $\chi' \ll \bar{\chi}$. For a uniform steady flow (*i.e.*, $\mathrm{d}\bar{\chi}/\mathrm{d}x = 0$) and neglecting second-order terms (*i.e.*, $\chi'\chi' = 0$), the governing equations reduce to

$$\frac{\partial \rho'}{\partial t} + \bar{u}\frac{\partial \rho'}{\partial x} + \bar{\rho}\frac{\partial u'}{\partial x} = 0, \tag{A.2}$$

$$\frac{\partial u'}{\partial t} + \bar{u}\frac{\partial u'}{\partial x} + \frac{1}{\bar{\rho}}\frac{\partial p'}{\partial x} = 0. \tag{A.3}$$

Assuming isentropic pressure fluctuations, *i.e.*, $p = p(\rho,s)$, the linearised relation between pressure and density is written as

$$p' = \bar{c}^2\rho', \tag{A.4}$$

where the sound speed $c$ for an ideal gas is defined by

$$c^2 = \left.\frac{\partial p}{\partial \rho}\right|_s = \gamma\frac{p}{\rho}. \tag{A.5}$$

The linearised Euler equations can thus be recast as

$$\frac{\partial p'}{\partial t} + \bar{u}\frac{\partial p'}{\partial x} + \gamma\bar{p}\frac{\partial u'}{\partial x} = 0, \tag{A.6}$$

$$\bar{\rho}\frac{\partial u'}{\partial t} + \bar{\rho}\bar{u}\frac{\partial u'}{\partial x} + \frac{\partial p'}{\partial x} = 0. \tag{A.7}$$

The velocity perturbation is eliminating by combining (A.6) and (A.7):

$$\frac{\partial}{\partial t}(\text{A.6}) - \bar{c}^2\frac{\partial}{\partial x}(\text{A.7}), \tag{A.8}$$

which yields:

$$\frac{\partial^2 p'}{\partial t^2} + \bar{u}\,\frac{\partial^2 p'}{\partial t \partial x} - \bar{c}^2\frac{\partial^2 p'}{\partial x^2} - \bar{\rho}\bar{c}^2\bar{u}\frac{\partial^2 u'}{\partial x^2} = 0. \tag{A.9}$$

Substituting the spatial derivative of Eq. (A.6) to eliminate $u'$, the acoustic pressure wave equation finally reads

$$\frac{\partial^2 p'}{\partial t^2} + 2\bar{u}\,\frac{\partial^2 p'}{\partial t \partial x} + \left(\bar{u}^2 - \bar{c}^2\right)\frac{\partial^2 p'}{\partial x^2} = 0. \tag{A.10}$$

This classical derivation establishes the governing relation for acoustic pressure fluctuations in a uniform-duct flow, providing the foundation for the developments presented in the subsequent sections.

## A.2 Solution of the acoustic wave

To solve the acoustic pressure wave equation, the Fourier transform is applied to the linearised quasi-one-dimensional Euler system using the convention

$$p'(x,t) = \hat{p}(x)\exp(+\mathrm{i}\omega t),$$

where $\hat{p}(x)$ denotes the complex amplitude of the pressure fluctuations and $\omega = 2\pi f$ is the angular frequency associated with the frequency $f$. Introducing the wave number, $k = \omega/\bar{c}$, and the steady Mach number, $\bar{\mathrm{M}} = \bar{u}/\bar{c}$, the acoustic pressure wave equation (Eq. (A.10)) in the frequency domain becomes

$$\frac{\mathrm{d}^2\hat{p}}{\mathrm{d}x^2} - \mathrm{i}\frac{2k\bar{\mathrm{M}}}{1-\bar{\mathrm{M}}^2}\frac{\mathrm{d}\hat{p}}{\mathrm{d}x} + \frac{k^2}{1-\bar{\mathrm{M}}^2}\hat{p} = 0. \tag{A.11}$$

The general solution of this second-order differential equation is

$$\hat{p}(x) = K_1\exp(-\mathrm{i}k^+x) + K_2\exp(\mathrm{i}k^-x), \tag{A.12}$$

$$= \hat{p}^+ + \hat{p}^-, \tag{A.13}$$

which corresponds to the superposition of two acoustic waves: one propagating downstream ($\hat{p}^+$) and one propagating upstream ($\hat{p}^-$), associated with the wave numbers $k^\pm = k/(1 \pm \bar{\mathrm{M}})$. The constants $K_1$ and $K_2$ are determined from the boundary conditions.

To obtain the profile of the velocity fluctuations $\hat{u}(x)$, the linearised mass conservation equation (Eq. (A.6)) is expressed in the Fourier domain, yielding

$$\frac{\mathrm{d}\hat{u}}{\mathrm{d}x} = -\frac{1}{\bar{\rho}\bar{c}}\left(\mathrm{i}k\hat{p} + \bar{\mathrm{M}}\,\frac{\mathrm{d}\hat{p}}{\mathrm{d}x}\right). \tag{A.14}$$

Substituting the solution of the pressure wave equation (Eq. (A.11)), one obtains

$$\frac{\mathrm{d}\hat{u}}{\mathrm{d}x} = \frac{1}{\bar{\rho}\bar{c}}\left(-\mathrm{i}k^+\hat{p}^+ - \mathrm{i}k^-\hat{p}^-\right), \tag{A.15}$$

which can be integrated over $x$, giving

$$\hat{u} = \frac{1}{\bar{\rho}\bar{c}}\left(\hat{p}^+ - \hat{p}^-\right). \tag{A.16}$$

It is noteworthy that the relations Eqs. (A.13) and (A.16) remain valid in the temporal domain, namely

$$p'(x,t) = p'^+ + p'^-, \tag{A.17}$$

$$u'(x,t) = \frac{1}{\bar{\rho}\bar{c}}\left(p'^+ - p'^-\right). \tag{A.18}$$

### A.2.1 Non-dimensional formulation

In aeroacoustic analysis, it is convenient to employ non-dimensional fluctuations, since these directly characterise the relative amplitude of perturbations propagating through the mean flow. Introducing the pressure and velocity fluctuations variables

$$P = \frac{p'}{\gamma \bar{p}}, \qquad U = \frac{u'}{\bar{u}},$$

the downstream and upstream-propagating acoustic waves are expressed as

$$P^{\pm} = \frac{p'^{\pm}}{\bar{\rho}\bar{c}^2} = \frac{1}{2}\left(P \pm \bar{\mathrm{M}}\, U\right). \tag{A.19}$$

Appendix B

# A quasi-steady-flow model for reflection coefficients in thermally choked-flow configurations

*Faut pas passer pour le mec qui comprend pas,*
*faut passer pour le mec qui est pas convaincu.*

**Pierre Bernigaud**


## Abstract

In this appendix, a quasi-steady analytical model is developed to estimate the acoustic-reflection and entropy–noise–production coefficients in thermally choked-flow nozzles. The formulation extends the quasi-one-dimensional steady Euler equations to include a distributed heat source and temperature-dependent thermodynamic properties. The pressure gradient is approximated as spatially linear, and a numerical correction term derived from CFD simulations is incorporated to account for unsteady effects at the critical throat. The resulting model generalises the model proposed in Chap. 3 with non-uniform heat addition and non-constant geometry. Validation against CFD simulations demonstrates fair agreement, particularly for thermal-throat configurations with non-uniform volumetric power distributions. The model highlights the influence of critical Mach-number fluctuations and nozzle contraction on the acoustic-reflection coefficient, while the entropy–noise–production coefficient remains less sensitive to these effects. The limitations and possible extensions of the model are also discussed.


## Contents


**B.1 Quasi-steady reflection coefficients model . . . . . 142**
B.1.1 Objective and motivations . . . . . 142
B.1.2 Flow governing equations and assumptions . . . . . 142
B.1.3 Quasi-steady formulation . . . . . 142
B.1.4 Linearised acoustic relation . . . . . 143
B.1.5 Reflection coefficients . . . . . 144

**B.2 Validation and limits of the present model . . . . . 144**
B.2.1 Results and validation . . . . . 144
B.2.2 Limits of the model . . . . . 146

## B.1 Quasi-steady reflection coefficients model

### B.1.1 Objective and motivations

In Chap. 3, a model was proposed to measure the acoustic-reflection $R_a$ and entropy-noise-production $R_s$ coefficients in the very-low-frequency limit, *i.e.*, under the quasi-steady assumption ($\partial/\partial t = 0$). This model was derived for a constant-area duct, with the thermal throat located at the downstream end of the duct. In this appendix, the objective is to extend this model to a general thermally choked-flow configuration, *e.g.*, when the cross-sectional area is not constant or the thermal throat is located further downstream within the divergent section.

### B.1.2 Flow governing equations and assumptions

The steady quasi-one-dimensional conservation equations of mass, momentum, and total specific enthalpy are considered and integrated between the inlet $(\,)_{\text{in}}$ and the critical-throat position $(\,)_*$, following the formulation of Anderson [130]:

$$\rho_{\text{in}} u_{\text{in}} \mathrm{A}_{\text{in}} = \rho_* u_* \mathrm{A}_*, \tag{B.1}$$

$$p_{\text{in}} \mathrm{A}_{\text{in}} + \rho_{\text{in}} u_{\text{in}}^2 \mathrm{A}_{\text{in}} + \int_{\mathrm{A}_{\text{in}}}^{\mathrm{A}_*} p(\mathrm{A})\,\mathrm{d}\mathrm{A} = p_* \mathrm{A}_* + \rho_* u_*^2 \mathrm{A}_*, \tag{B.2}$$

$$h_{0,*} - h_{0,\text{in}} = \frac{1}{\dot{m}} \int_{x_{\text{in}}}^{x_*} \mathrm{A}(\xi)\, P_v(\xi)\,\mathrm{d}\xi, \tag{B.3}$$

where $\rho$ denotes the density, $p$ the static pressure, $u$ the local velocity, A the cross-sectional area, $\dot{m} = \rho u \mathrm{A}$ the mass-flow rate, $h_0$ the total specific enthalpy, and $P_v$ the volumetric power source term. The algebraic derivation of the momentum equation in the quasi-steady framework is presented in Sec. 4.2.3.

The integral pressure-force term is approximated as spatially linear:

$$\int_{\mathrm{A}_{\text{in}}}^{\mathrm{A}_*} p(\mathrm{A})\,\mathrm{d}\mathrm{A} \simeq \frac{p_{\text{in}} + p_*}{2}\,(\mathrm{A}_* - \mathrm{A}_{\text{in}}). \tag{B.4}$$

The model developed hereafter relies on the following assumptions: (i) the heat capacity $c_p$ is temperature dependent, but its fluctuations are negligible, *i.e.*, $c_p(T') = 0$; (ii) the critical Mach-number fluctuations do not vanish, *i.e.*, $\mathrm{M}'_* \neq 0$, even though the steady critical Mach number equals unity.

### B.1.3 Quasi-steady formulation

Using the conservation of mass and momentum, the following relation between the critical throat and inlet static temperatures is obtained:

$$\frac{T_*}{T_{\text{in}}} = \frac{\mathrm{M}_*^2}{\mathrm{M}_{\text{in}}^2}\,\frac{\gamma_*}{\gamma_{\text{in}}}\,\frac{\left(1 + \gamma_{\text{in}}\mathrm{M}_{\text{in}}^2 + \Lambda C_r\right)^2}{\left(1 + \gamma_* \mathrm{M}_*^2 - C_r\right)^2}, \tag{B.5}$$

where $\Lambda = \mathrm{A}_*/\mathrm{A}_{\mathrm{in}}$ is the critical-to-inlet area ratio and $C_r = (1-1/\Lambda)/2$ is the contraction ratio. This latter quantity characterises the influence of the critical cross-sectional area on the static temperature. For a geometric-throat configuration, it is negative because the cross-sectional area $\mathrm{A}_*$ is smaller than the inlet area $\mathrm{A}_{\mathrm{in}}$, which implies a lower critical static temperature $T_*$ than in a constant-area duct to choke the flow. Conversely, $C_r$ is positive for a thermal-throat configuration, indicating that a higher critical temperature is required to choke the flow.

From total specific enthalpy conservation (Eq. (B.3)), one obtains

$$\frac{T_*}{T_{\mathrm{in}}} = \frac{c_{p,\mathrm{in}}/c_{p,*}}{1+\dfrac{\gamma_*-1}{2}\mathrm{M}_*^2}\left(\mathcal{P}_f + 1 + \frac{\gamma_{\mathrm{in}}-1}{2}\mathrm{M}_{\mathrm{in}}^2\right), \tag{B.6}$$

where the dimensionless flame-power number $\mathcal{P}_f$ is defined[1] as

$$\mathcal{P}_f = \frac{1}{\dot{m}_{\mathrm{in}} c_{p,\mathrm{in}} T_{\mathrm{in}}} \int_{x_{\mathrm{in}}}^{x_*} \mathrm{A}(\xi) P_v(\xi)\,\mathrm{d}\xi. \tag{B.7}$$

As described in Sec. 3.2, the normalised flame-power number $\mathcal{P}_f$ represents the ratio between the power added by the flame and the inlet convective flux of thermal energy.

Combining Eqs. (B.5) and (B.6), the ratio of energy addition to the initial flow energy required to choke the flow is obtained:

$$\mathcal{P}_f = \frac{c_{p,*}\gamma_*}{c_{p,\mathrm{in}}\gamma_{\mathrm{in}}}\frac{\mathrm{M}_*^2}{\mathrm{M}_{\mathrm{in}}^2}\left(1+\frac{\gamma_*-1}{2}\mathrm{M}_*^2\right)\frac{\left(1+\gamma_{\mathrm{in}}\mathrm{M}_{\mathrm{in}}^2+\Lambda C_r\right)^2}{\left(1+\gamma_*\mathrm{M}_*^2-C_r\right)^2} - \left(1+\frac{\gamma_{\mathrm{in}}-1}{2}\mathrm{M}_{\mathrm{in}}^2\right). \tag{B.8}$$

### B.1.4 Linearised acoustic relation

To derive the reflection coefficients, Eq. (B.8) is linearised using $\chi = \bar{\chi} + \chi'$, where $\bar{\chi}$ and $\chi'$ denote steady and fluctuating components, respectively, with $\chi' \ll \bar{\chi}$. Neglecting second-order terms, *i.e.*, $\chi'\chi' = 0$, yields

$$\bar{\mathcal{P}}_f\left(\gamma_{\mathrm{in}} P_{\mathrm{in}} - U_{\mathrm{in}}\right) = \Gamma\frac{\mathrm{M}'_{\mathrm{in}}}{\bar{\mathrm{M}}_{\mathrm{in}}}, \tag{B.9}$$

where the geometric coefficient $\Gamma$ is defined as

$$\Gamma = \frac{c_{p,*}}{c_{p,\mathrm{in}}}\frac{\gamma_*}{\gamma_{\mathrm{in}}}\left(\frac{\dfrac{c_{p,\mathrm{in}}\gamma_{\mathrm{in}}}{c_{p,*}\gamma_*}(\gamma_{\mathrm{in}}-1)\,\bar{\mathrm{M}}_{\mathrm{in}}^4\,(1+\gamma_*-C_r)^2 + (\gamma_*+1)\left((1+\Lambda C_r)^2-\gamma_{\mathrm{in}}^2\bar{\mathrm{M}}_{\mathrm{in}}^4\right)}{\bar{\mathrm{M}}_{\mathrm{in}}^2\,(1+\gamma_*-C_r)^2}\right.$$
$$\left. + \frac{2\,\gamma_* C_r}{\bar{\mathrm{M}}_{\mathrm{in}}}\frac{\left(1+\gamma_{\mathrm{in}}\bar{\mathrm{M}}_{\mathrm{in}}^2+\Lambda C_r\right)^2}{(1+\gamma_*-C_r)^3}\frac{\mathrm{M}'_*}{\mathrm{M}'_{\mathrm{in}}}\right), \tag{B.10}$$

and the normalised pressure and velocity fluctuations are defined as $P_{\mathrm{in}} = p'_{\mathrm{in}}/(\bar{\gamma}_{\mathrm{in}}\bar{p}_{\mathrm{in}})$ and $U_{\mathrm{in}} = u'_{\mathrm{in}}/\bar{u}_{\mathrm{in}}$, respectively.

Equation (B.9) shows that, even under quasi-steady conditions, Mach-number fluctuations may persist in the presence of heat-release rate. This constitutes a key departure from the quasi-steady assumption of Marble and Candel [16] and Tsien [18], as further emphasised by Duran and Moreau [22]. Moreover, Eq. (B.10) indicates that critical Mach-number fluctuations $\mathrm{M}'_*$ influence the acoustic coefficients whenever the duct geometry is not constant ($C_r \neq 0$).

The model requires $\gamma_*$ and $\mathrm{M}'_*/\mathrm{M}'_{\mathrm{in}}$ as inputs in order to evaluate $\Gamma$. These are determined from numerical simulations under quasi-steady inlet forcing conditions (*i.e.*, very low frequency acoustic or entropy perturbations), from which the required quantities are extracted. For a calorically perfect gas (*i.e.*, $c_p$ constant) and in a constant-area duct ($C_r = 0$), the formulation reduces to the classical definition given in Sec. 3.3.1.

[1] This formulation is identical to the one proposed in Eq. (3.1).

### B.1.5 Reflection coefficients

Rewriting the normalised Mach-number fluctuations $\mathrm{M}'_{\mathrm{in}}/\bar{\mathrm{M}}_{\mathrm{in}}$ in terms of the variables $P_{\mathrm{in}}$, $U_{\mathrm{in}}$, and $\sigma_{\mathrm{in}} = s'_{\mathrm{in}}/c_{p,\mathrm{in}}$ gives

$$P_{\mathrm{in}}\left(\frac{\gamma_{\mathrm{in}}-1}{2}\bar{\mathrm{M}}_{\mathrm{in}}\left(1+\frac{2\gamma_{\mathrm{in}}}{\gamma_{\mathrm{in}}-1}\frac{\bar{\mathcal{P}}_f}{\Gamma}\right)\right)-\bar{\mathrm{M}}_{\mathrm{in}}U_{\mathrm{in}}\left(1+\frac{\bar{\mathcal{P}}_f}{\Gamma}\right)+\frac{\bar{\mathrm{M}}_{\mathrm{in}}}{2}\sigma_{\mathrm{in}}=0. \tag{B.11}$$

For the acoustic-reflection coefficient $R_a$, Eq. (B.11) is solved with

$$P_{\mathrm{in}}=P^{+}_{\mathrm{in}}+P^{-}_{\mathrm{in}},\quad U_{\mathrm{in}}=\frac{P^{+}_{\mathrm{in}}-P^{-}_{\mathrm{in}}}{\bar{\mathrm{M}}_{\mathrm{in}}},\quad \sigma_{\mathrm{in}}=0,$$

where $P^{\pm}_{\mathrm{in}}$ denote the downstream and upstream-propagating acoustic waves at the inlet (see Appendix A). This yields

$$R_a=\frac{P^{-}_{\mathrm{in}}}{P^{+}_{\mathrm{in}}}=\frac{\left(1-\frac{\gamma_{\mathrm{in}}-1}{2}\bar{\mathrm{M}}_{\mathrm{in}}\right)-\frac{\bar{\mathcal{P}}_f}{\Gamma}\left(1+\gamma_{\mathrm{in}}\bar{\mathrm{M}}_{\mathrm{in}}\right)}{\left(1+\frac{\gamma_{\mathrm{in}}-1}{2}\bar{\mathrm{M}}_{\mathrm{in}}\right)-\frac{\bar{\mathcal{P}}_f}{\Gamma}\left(1-\gamma_{\mathrm{in}}\bar{\mathrm{M}}_{\mathrm{in}}\right)}. \tag{B.12}$$

Similarly, the entropy-noise-production coefficient $R_s$ is obtained by solving Eq. (B.11) with

$$P_{\mathrm{in}}=P^{-}_{\mathrm{in}},\quad U_{\mathrm{in}}=-\frac{P^{-}_{\mathrm{in}}}{\bar{\mathrm{M}}_{\mathrm{in}}},\quad \sigma_{\mathrm{in}}\neq 0,$$

which gives

$$R_s=\frac{P^{-}_{\mathrm{in}}}{\sigma_{\mathrm{in}}}=\frac{-\bar{\mathrm{M}}_{\mathrm{in}}/2}{\left(1+\frac{\gamma_{\mathrm{in}}-1}{2}\bar{\mathrm{M}}_{\mathrm{in}}\right)-\frac{\bar{\mathcal{P}}_f}{\Gamma}\left(1-\gamma_{\mathrm{in}}\bar{\mathrm{M}}_{\mathrm{in}}\right)}. \tag{B.13}$$

## B.2 Validation and limits of the present model

### B.2.1 Results and validation

To validate the proposed quasi-steady model (Eq. (B.9)), the three configurations considered in Chap. 3 are recalled:

- **THT**: a thermal throat located deep within a divergent nozzle with a non-uniform volumetric power distribution;
- **UNI**: a thermal throat positioned at the beginning of a divergent duct with a uniform volumetric power distribution;
- **GEO**: a geometric throat producing the same Mach-number profile as the THT configuration.

The comparison focuses on the acoustic-reflection coefficient $R_a$ and the entropy-noise-production coefficient $R_s$, as defined in Sec. 3.3. Results from CFD simulations $(\,)_{\mathrm{CFD}}$ (Secs. 3.4.2 and 3.4.5) are compared against three models: the model of Marble and Candel [16] $(\,)_{\mathrm{MC}}$, the quasi-steady model for a critical throat at the end of a constant duct (Eqs. (3.19) and (3.20)) $(\,)_{\mathrm{UNI}}$, and the proposed quasi-steady generalised formulation (Eqs. (B.12) and (B.13)) $(\,)_{\mathrm{GEN}}$.

The critical Mach-number fluctuations ratio $\mathrm{M}'_*/\mathrm{M}'_{\mathrm{in}}$ is extracted numerically from the CFD data, with measurements performed along the symmetry axis.

Table B.1 summarises the quasi-steady acoustic-reflection coefficient $R_a$ obtained from CFD simulations and from the quasi-steady models ($R_{a,\mathrm{MC}}$, Marble and Candel [16]; $R_{a,\mathrm{UNI}}$, Eq. (3.19); $R_{a,\mathrm{GEN}}$, Eq. (B.12)) for the three choking configurations: a geometric-throat configuration GEO, a constant-area duct with a thermal throat at its downstream end UNI, and a divergent duct with an internal thermal throat THT. The values in parentheses indicate the absolute relative error (in %).

**Table B.1** Quasi-steady acoustic-reflection coefficient $R_a$ for three choking configurations (GEO, UNI, THT). Results are reported from CFD simulations ($R_{a,\mathrm{CFD}}$) and from quasi-steady models ($R_{a,\mathrm{MC}}$: Marble and Candel [16]; $R_{a,\mathrm{UNI}}$: Eq. (3.19); $R_{a,\mathrm{GEN}}$: Eq. (B.12)). Values in parentheses indicate the absolute relative error (in %) with respect to the CFD predictions.

| | $R_{a,\mathrm{CFD}}$ | $R_{a,\mathrm{MC}}$ | $R_{a,\mathrm{UNI}}$ | $R_{a,\mathrm{GEN}}$ |
|---|---|---|---|---|
| GEO | 0.7976 | 0.7953 (12 %) | 0.7953 (12 %) | 0.7953 (12 %) |
| UNI | 0.4139 | 0.7953 (97 %) | 0.4129 (15 %) | 0.4109 (15 %) |
| THT | −0.1754 | 0.7953 (553 %) | −6.4104 (3555 %) | −0.1533 (14 %) |

For the geometric-throat configuration (GEO), good agreement is observed between all models and the CFD results, with a relative error below 12 %. This outcome is expected since both the uniform-power model (Eq. (3.19)) and the non-uniform-power model (Eq. (B.12)) are derived from the formulation of Marble and Candel [16].

For the thermal-throat configuration located at the beginning of the divergent duct with a uniform volumetric power distribution (UNI), good agreement is also obtained between the uniform- and non-uniform-power models and the CFD results, with a relative error below 15 %. In contrast, the model of Marble and Candel [16] shows large discrepancies because it does not account for the energy addition to the flow, quantified by $\bar{\mathcal{P}}_f$.

For the thermally choked configuration with a non-uniform volumetric power distribution (THT), good agreement is achieved between the non-uniform-power model and the CFD results, with a relative error below 14 %. The uniform-power model performs poorly, as it overestimates the influence of the heat-source term on the acoustic response and neglects geometric effects. Incorporating the critical Mach-number fluctuation ratio $\mathrm{M}'_*/\mathrm{M}'_{\mathrm{in}}$ improves the prediction accuracy by about 30 %. In contrast, assuming $\mathrm{M}'_*/\mathrm{M}'_{\mathrm{in}} = 1$ yields a relative error exceeding 70 %, and imposing $\mathrm{M}'_*/\mathrm{M}'_{\mathrm{in}} = 0$ (no thermal-throat fluctuations) leads to deviations of up to 152 % between the CFD results and the GEN model in the THT configuration.

Table B.2 summarises the quasi-steady entropy-noise-production coefficient $R_s$ obtained from CFD simulations and from the quasi-steady models ($R_{s,\mathrm{MC}}$: Marble and Candel [16]; $R_{s,\mathrm{UNI}}$: Eq. (3.20); $R_{s,\mathrm{GEN}}$: Eq. (B.13)) for the three configurations (GEO, UNI, THT).

**Table B.2** Quasi-steady entropy-noise-production coefficient $R_s$ for three choking configurations (GEO, UNI, THT). Results are obtained from CFD simulations ($R_{s,\mathrm{CFD}}$) and from quasi-steady models ($R_{s,\mathrm{MC}}$: Marble and Candel [16]; $R_{s,\mathrm{UNI}}$: Eq. (3.20); $R_{s,\mathrm{GEN}}$: Eq. (B.13)). Values in parentheses indicate the absolute relative error (in %) with respect to the CFD results.

| | $R_{s,\mathrm{CFD}}$ | $R_{s,\mathrm{MC}}$ | $R_{s,\mathrm{UNI}}$ | $R_{s,\mathrm{GEN}}$ |
|---|---|---|---|---|
| GEO | −0.2600 | −0.2698 (12 %) | −0.2698 (12 %) | −0.2698 (12 %) |
| UNI | −0.2844 | −0.2698 (15 %) | −0.2798 (14 %) | −0.2786 (14 %) |
| THT | −0.3330 | −0.2698 (23 %) | −0.4677 (44 %) | −0.2953 (17 %) |

For the geometric-throat configuration (GEO), good agreement is observed between the CFD results and all quasi-steady models. For the thermal throat with a uniform power distribution (UNI), both the uniform-power model ($R_{s,\mathrm{UNI}}$) and the non-uniform-power model ($R_{s,\mathrm{GEN}}$) show good agreement with the CFD results, with deviations below 14 %. A similar level of deviation is also observed between the model of Marble and Candel [16] and the CFD results. Finally, for the thermal throat with a non-uniform volumetric power distribution (THT), satisfactory agreement is obtained between the CFD data and the non-uniform-power model, with a deviation of 17 %. The influence of critical Mach-number fluctuations on the entropy-noise-production coefficient is found to be minimal, with a deviation of only 1 %.

Overall, these results confirm the relevance of the proposed model for studying the propagation of acoustic and entropy waves in thermally choked-flow nozzles. They highlight the importance of properly accounting for the heat-source term, the nozzle geometry, and critical Mach-number fluctuations when predicting reflection coefficients.

### B.2.2 Limits of the model

The first limitation of the proposed model (Eq. (B.9)) is its reliance on the normalised critical-throat Mach-number fluctuations $\mathrm{M}'_*/\mathrm{M}'_{\mathrm{in}}$. In this study, this quantity is extracted from numerical simulations. Although this coefficient significantly improves prediction accuracy, especially for the acoustic-reflection coefficient, an analytical relation would be highly desirable to clarify the influence of inlet Mach-number fluctuations $\mathrm{M}'_{\mathrm{in}}$ on the critical-throat fluctuations $\mathrm{M}'_*$.

A second limitation arises from the approximation of the integrated pressure forces, evaluated here using a spatially linear approximation. For the non-uniform thermally choked-flow case (THT), this approximation introduces an error of approximately 8 %. For the uniform thermal-throat case (UNI), the error increases to nearly 31 %, highlighting the limits of this approach.

Further investigation is required to fully characterise the interplay between heat-release rate and nozzle geometry in determining the reflection coefficients in thermally choked-flow configurations.

#### Chapter conclusion

This appendix introduced a quasi-steady model for predicting the acoustic-reflection and entropy–noise–production coefficients in thermally choked nozzles. The formulation improves upon the model proposed in Chap. 3 by incorporating the effects of distributed heat release, nozzle geometry, and critical Mach-number fluctuations. Comparison with CFD simulations confirms the relevance of the proposed approach, especially for configurations with a non-uniform heat-source distribution, where deviations remain below 15 %.

The model reveals that the inclusion of critical Mach-number fluctuations is essential to accurately capture the acoustic-reflection behaviour, while the entropy–noise–production coefficient is only weakly affected. Despite its effectiveness, the method relies on empirical quantities extracted from CFD results and on simplified integration of the pressure forces, which introduces some uncertainty.

Nevertheless, this quasi-steady formulation provides valuable insight into the coupling between thermal and geometric effects in thermally choked flows, forming a practical analytical basis for interpreting and predicting reflection mechanisms in dual-mode ramjet configurations.

Appendix C

# A quasi-one-dimensional critical-throat acoustic boundary condition for isentropic nozzles

*Ouais, ben si vous vouliez du captivant...*

**Père Blaise [2]**


## Abstract

In this appendix, a supporting analysis of the critical-throat acoustic boundary condition for isentropic nozzle geometries is presented. This condition, representing a simplified form of the model introduced in Chap. 4, is validated with canonical geometries commonly found in the literature. Particular attention is given to the limitations of this boundary condition, which are intrinsically linked to the evolution of the nozzle geometry. The proposed boundary condition, implemented in a quasi-one-dimensional linear acoustic model, is validated with numerical simulations. Good agreement is observed between the analytical model and CFD results when the nozzle geometry does not exhibit a discontinuity at the throat. The impact of the proposed boundary condition is also compared with the commonly used quasi-steady-state (QSS) boundary condition in terms of the predicted reflection and transmission coefficients. It is found that the proposed formulation does not significantly improve the accuracy of the predicted coefficients. However, unlike the QSS boundary condition, it eliminates the singularity in the acoustic pressure profile at the throat.



This appendix is a truncation of the following publication, published during the PhD:

F. Olivon, A. Genot, L. Hirschberg, S. Moreau, and A. Hirschberg. "On the critical-throat boundary condition in quasi-one-dimensional linearized-Euler equation models". In: *Journal of Fluid Mechanics* 1019 (2025), A4. ISSN: 0022-1120. DOI: 10.1017/jfm.2025.10568.


## Contents


C.1 Objective . . . . . 148

**C.2 Critical-throat boundary condition for isentropic nozzle . . . . . 149**
C.2.1 Limit of the proposed boundary condition . . . . . 150
**C.3 Validation methodology . . . . . 150**
C.3.1 Presentation of the isentropic nozzle geometries . . . . . 150
C.3.2 Numerical set-up . . . . . 153
**C.4 Discussion and results . . . . . 154**
C.4.1 Validation and limits of the quasi-one-dimensional model . . . . . 154
C.4.2 Influence of the boundary condition on the acoustic-pressure distribution 155
C.4.3 Acoustic reflection and transmission coefficients . . . . . 156
C.4.4 Comparison with experimental measurements . . . . . 159

## C.1 Objective

To integrate the quasi-one-dimensional linear acoustic model, appropriate boundary conditions must be prescribed at the system boundaries. In the case of an isentropic choked-flow nozzle, conditions are typically imposed at the inlet and at the throat.

At the quasi-steady-flow limit, the nozzle throat remains choked when subjected to perturbations (acoustic or entropy waves), and the Mach-number fluctuations $\mathrm{M}'$ vanish at any position upstream of the throat. This arises from the fact that, for an isentropic quasi-one-dimensional flow, the Mach number depends solely on the ratio $\mathrm{A}_*/\mathrm{A}$, where $\mathrm{A}_*$ and A denote the throat and local cross-sectional areas, respectively. For an ideal gas with constant heat capacity ratio, $\gamma = c_p/c_v$, this ratio is given by Shapiro [125]:

$$\frac{\mathrm{A}_*}{\mathrm{A}} = \mathrm{M}\left(\frac{\gamma+1}{2+(\gamma-1)\mathrm{M}^2}\right)^{\frac{\gamma+1}{2(\gamma-1)}}, \tag{C.1}$$

where the subscript $(\,)_*$ refers to conditions at the choked-nozzle throat ($\mathrm{M}_* = 1$).

Since there are no fluctuations in the geometry ($\mathrm{A}' = 0$), the linearisation of this relation implies $\mathrm{M}' = 0$ at any position upstream of the critical throat in the quasi-steady limit. This low-frequency approximation was originally introduced by Tsien [18] and Marble and Candel [16].

The analysis of Stow *et al.* [19] suggests that, to first order in frequency, the quasi-steady condition, $\mathrm{M}'_* = 0$, remains valid at the throat. Building on this, Duran and Moreau [22] assumed that a narrow region surrounding the critical throat can always be treated as quasi-steady, since its characteristic length is small compared with the perturbation wavelength. Under this assumption, the condition $\mathrm{M}'_* = 0$ would remain valid at any frequency. In terms of natural variables, this condition can be rewritten as

$$2\hat{U}_* = \gamma\hat{P}_* - \hat{D}_*, \tag{C.2}$$

where $\hat{P} = \hat{p}/(\gamma\bar{p})$, $\hat{U} = \hat{u}/\bar{u}$, and $\hat{D} = \hat{\rho}/\bar{\rho}$ are the normalised frequency-domain variables evaluated at the critical throat.

Using the linearised Gibbs relation (2.7), the entropy-based form of this condition, as given by Marble and Candel [16] and Duran and Moreau [22], becomes

$$2\hat{U}_* = (\gamma-1)\hat{P}_* + \hat{\sigma}_*. \tag{C.3}$$

Equation (C.3) will hereafter be referred to as the QSS (quasi-steady-state) boundary condition. It has been widely employed in the literature [22, 28, 82, 84, 97, 139, 162]. However, as demonstrated in Chap. 3, this assumption does not generally hold.

In the following, a corrected formulation of the upstream boundary condition at the critical throat is proposed for isentropic nozzle geometries. In addition, the limitations of the quasi-one-dimensional theory are examined, with particular emphasis on isentropic acoustic forcing.

## C.2 Critical-throat boundary condition for isentropic nozzle

Considering an isentropic flow ($P_v = 0$) with constant heat capacity ratio $\gamma$, the simplification of Eq. (4.49) yields

$$(2 + \mathrm{i}\Omega)\ \hat{U}_* = (\gamma + \mathrm{i}\Omega)\ \hat{P}_* - \hat{D}_*, \tag{C.4}$$

where $\mathrm{i} = \sqrt{-1}$ is the imaginary unit and $\Omega = 2\pi f/(\mathrm{d}\bar{u}/\mathrm{d}x)_*$ is the dimensionless frequency.

The entropy-based form of the boundary condition is expressed as

$$(2 + \mathrm{i}\Omega)\ \hat{U}_* = (\gamma - 1 + \mathrm{i}\Omega)\ \hat{P}_* + \hat{\sigma}_*. \tag{C.5}$$

Equation (C.5) will hereafter be referred to as the IS (isentropic) boundary condition. This formulation exhibits meaningful asymptotic behaviour in both the low- and high-frequency limits[1]. At low frequencies, $\Omega \ll 1$, expansion of Eq. (C.5) yields

$$\hat{U}_* = \left(\frac{\gamma - 1}{2} + \mathrm{i}\Omega\frac{3 - \gamma}{4}\right)\ \hat{P}_* + \left(1 - \mathrm{i}\frac{\Omega}{2}\right)\frac{\hat{\sigma}_*}{2} + O(\Omega^2), \tag{C.6}$$

which corresponds to the first-order correction to the QSS condition $\hat{\mathrm{M}}_* = 0$ (Eq. (C.3)).

At high frequencies, $\Omega \gg 1$, one obtains

$$\hat{U}_* = \left(1 - \mathrm{i}\frac{\gamma - 3}{\Omega}\right)\ \hat{P}_* - \mathrm{i}\frac{\hat{\sigma}_*}{\Omega} + O(\Omega^{-2}), \tag{C.7}$$

which constitutes a first-order correction to the simple-wave downstream radiation condition in a tube of uniform cross-section, $p'_* = \bar{\rho}_*\bar{c}_*u'_*$. At the throat, $(\mathrm{dA}/\mathrm{d}x)_* = 0$. It is noteworthy that the influence of entropy fluctuations on the boundary condition at the critical throat becomes negligible in the high-frequency limit.

In addition, for isentropic acoustic forcing, the normalised Mach-number fluctuations $\hat{\mathrm{M}}_*/\hat{P}_*$ at the throat can be directly expressed from Eq. (C.5) as

$$\hat{\mathrm{M}}_* = \left(\frac{\gamma - 1 + \mathrm{i}\Omega}{2 + \mathrm{i}\Omega} - \frac{\gamma - 1}{2}\right)\hat{P}_*. \tag{C.8}$$

Here, since the steady base flow is not heated, the propagation of isentropic acoustic waves does not generate entropy waves, as also observed in Chap. 3.

[1] In the original paper by Olivon *et al.*, "On critical-throat boundary conditions in quasi-one-dimensional linearized Euler equation models", *Journal of Fluid Mechanics* (2025) an error is present in the low and high-frequency series expansions at first order. The correct form is provided here.

### C.2.1 Limit of the proposed boundary condition

For a given cross-sectional area $\mathrm{A}(x)$, assuming a quasi-one-dimensional isentropic steady reference flow with constant $\gamma$, and applying L'Hôpital's rule to determine the critical flow behaviour (Section 8.10 of Shapiro [125]), one obtains

$$\left(\frac{\mathrm{d}\bar{u}}{\mathrm{d}x}\right)_* = c_* \sqrt{\frac{1}{(\gamma+1)\mathrm{A}_*}\left(\frac{\mathrm{d}^2\mathrm{A}}{\mathrm{d}x^2}\right)_*}. \tag{C.9}$$

Hence, as long as the second derivative $\mathrm{d}^2\mathrm{A}/\mathrm{d}x^2$ exists at the critical throat, characterised by $(\mathrm{dA}/\mathrm{d}x)_* = 0$, the IS boundary condition (Eq. (C.5)) can be applied. When $(\mathrm{dA}/\mathrm{d}x)_*$ is discontinuous, the boundary condition should instead be applied in the limit approaching the throat from the upstream (subsonic) side.

## C.3 Validation methodology

To validate the IS boundary condition (Eq. (C.5)), three isentropic nozzle geometries are considered, as detailed below. Results from both CFD simulations and the quasi-one-dimensional linear acoustic model using the IS boundary condition are presented to assess its validity. The quasi-one-dimensional linear acoustic model employed for this validation is described in detail in Chap. 4. A comparison with the commonly used QSS boundary condition is also carried out to evaluate the impact of the boundary condition on the prediction of acoustic coefficients.

### C.3.1 Presentation of the isentropic nozzle geometries

#### Two-dimensional discontinuous nozzle geometry

The two-dimensional planar nozzle geometry studied by Goh and Morgans [20] is defined as follows:

$$\frac{\mathrm{A}(\xi)}{\mathrm{A}_*} = \begin{cases} \dfrac{1}{2}\left(\dfrac{\mathrm{A}_{\mathrm{in}}}{\mathrm{A}_*} - 1\right)\left(\cos\left(\pi\dfrac{\xi}{\xi_*}\right) + 1\right), & \xi \in [0, \xi_*], \\ 1 + \left(\dfrac{\mathrm{A}_{\mathrm{out}}}{\mathrm{A}_*} - 1\right)\dfrac{\xi - \xi_*}{1 - \xi_*}, & \xi \in [\xi_*, 1], \end{cases} \tag{C.10}$$

where $\mathrm{A}(\xi)$ is the nozzle cross-sectional area at position $\xi = x/L$.

This geometry is fully defined by the normalised inlet and outlet sections, $\mathrm{A}_{\mathrm{in}}/\mathrm{A}_*$ and $\mathrm{A}_{\mathrm{out}}/\mathrm{A}_*$, as well as the normalised critical-throat position, $\xi_* = x_*/L = 0.15$. In this study, the inlet and outlet Mach numbers are prescribed as $\mathrm{M}_{\mathrm{in}} = 0.29$ and $\mathrm{M}_{\mathrm{out}} = 1.5$, respectively. The corresponding normalised inlet and outlet areas, $\mathrm{A}_{\mathrm{in}}/\mathrm{A}_*$ and $\mathrm{A}_{\mathrm{out}}/\mathrm{A}_*$, are obtained using the isentropic area–Mach-number relation in Eq. (C.1). This nozzle geometry will hereafter be referred to as the original geometry of Goh and Morgans [20].

Figure C.1 shows the normalised cross-sectional area ratio $\mathrm{A}/\mathrm{A}_*$ and Mach number M, as a function of the dimensionless length, $\xi = x/L$, for the original geometry of Goh and Morgans [20] (- - -). The critical position $\xi_*$ is also displayed. At this location, the critical Mach number, $\mathrm{M}_* = 1$, exhibits a sharp transition due to the discontinuous rate of change in the geometry $\mathrm{dA}/\mathrm{d}x$. As discussed in Sec. C.2.1, discrepancies are expected between the IS boundary condition Eq. (C.5) and CFD simulations for the normalised critical quantity $\hat{\mathrm{M}}_*/\hat{P}_*$.

To avoid such discontinuous behaviour in the Mach-number evolution, a smoothed version of this geometry is constructed by mirroring the subsonic profile with respect to the throat. The same subsonic length $x_*$ as in the original geometry is retained. The supersonic section of the smoothed geometry is shortened relative to the original in order to limit the outlet Mach number

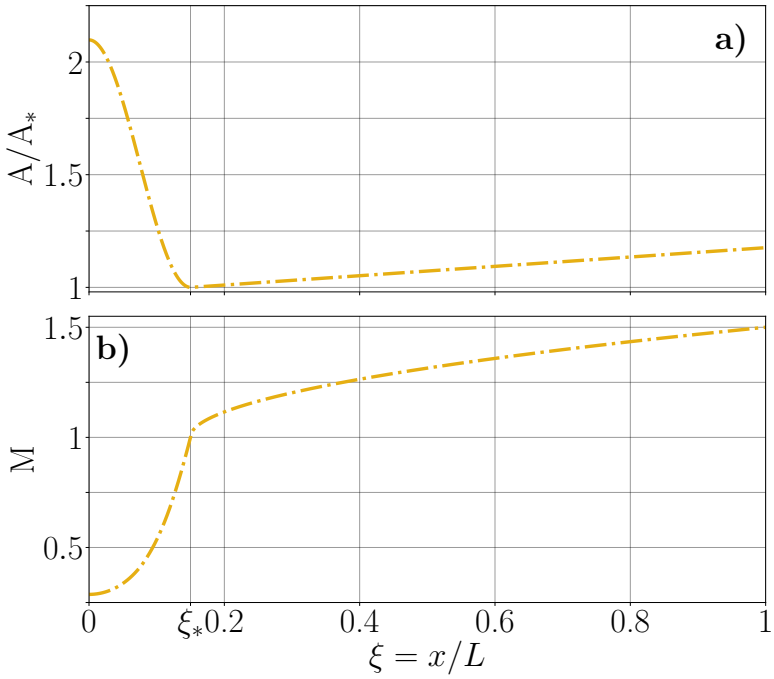


**Figure C.1** (Colour) Normalised cross-sectional area $A/A_*$ **(a)** and Mach number M **(b)** of the original nozzle geometry from Goh and Morgans [20] (-·-), plotted against the normalised longitudinal coordinate, $\xi = x/L$. The critical choked-throat position $\xi_*$ is also indicated.

and reduce computational cost. The total length of the smoothed geometry is set to $L = 0.2\,\mathrm{m}$, placing the throat at $\xi_* = x_*/L = 0.75$. This version of the geometry of Goh and Morgans [20] will hereafter be referred to as the smoothed nozzle geometry.

Figure C.2 shows the normalised cross-sectional area $A/A_*$ and Mach number M profiles along the smoothed nozzle geometry of Goh and Morgans [20] (····). As expected, the Mach-number variation is now continuous and monotonic across the domain, with no discontinuity at the throat location $\xi_*$. For this version of the geometry, the proposed IS boundary condition Eq. (C.5) is expected to closely match the CFD simulations.

### Experimental nozzle geometry

To assess the validity of the IS boundary condition in a more realistic nozzle configuration, the nozzle geometry proposed by Bell *et al.* [163] is employed. This nozzle was designed to evaluate the limitations of the quasi-one-dimensional isentropic framework, particularly regarding assumptions such as negligible boundary-layer effects and simplified flow behaviour within the nozzle. These assumptions can only be rigorously tested by comparison with either high-fidelity three-dimensional turbulent numerical simulations, which resolve all relevant flow scales, or experimental data obtained under realistic conditions. To this end, Bell *et al.* [163] and Zinn *et al.* [164] conducted experiments to measure the acoustic admittance of various rocket nozzle geometries, demonstrating the influence of nozzle shape on the admittance at finite frequencies. The axisymmetric nozzle profiles investigated in Bell *et al.* [163] are illustrated in Fig. C.3, where the radial contour $r(x)$ is plotted.

These nozzle geometries consist of three segments: an initial circular arc of radius $r_{\mathrm{cc}}$, originating at the inlet and turned through an angle $\theta$; followed by a conical section of the same angle $\theta$; and finally, a second circular arc of radius $r_{\mathrm{cc}}$ turned through angle $\theta$. Given that all

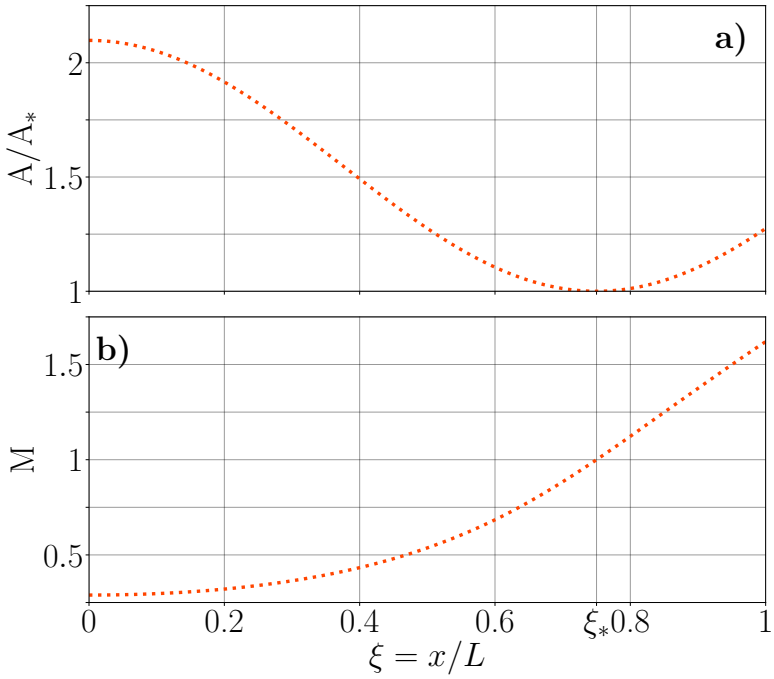


**Figure C.2** (Colour) Normalised cross-sectional area, $A/A_*$ **(a)**, and Mach number, M **(b)**, of the smoothed nozzle geometry from Goh and Morgans [20] (····), plotted against the normalised longitudinal coordinate, $\xi = x/L$. The critical-throat position $\xi_*$ is also indicated.

nozzles operate under choked conditions, the geometry of the converging section is fully defined by the inlet Mach number, $M_{in}$, and two geometric parameters: the angle $\theta$ and the curvature ratio $r_{cc}/r_c$, where $r_c$ is the nozzle inlet radius. The supersonic section is obtained by mirroring the third segment about the critical-throat location.

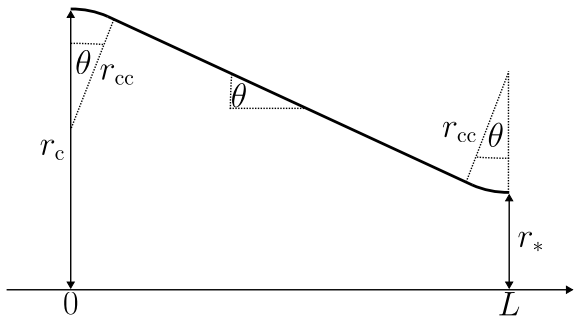


**Figure C.3** Sketch of the generic axisymmetric nozzle geometry proposed by Bell *et al.* [163].

For this study, the inlet Mach number is fixed at $M_{in} = 0.08$, the arc angle at $\theta = 15°$, and the arc curvature ratio at $r_{cc}/r_c = 0.44$. These coefficients are chosen to be consistent with the nozzle used in the experiments of Bell *et al.* [163]. The area ratio, $A/A_* = (r/r_*)^2$, is used to compute the Mach number via Eq. (C.1). Based on the nozzle description in Bell *et al.* [163],

the following piecewise function defines the nozzle profile:

$$r(x) = \begin{cases} r_\mathrm{c} - r_\mathrm{cc}\left[1 - \cos\left(\arcsin\left(\dfrac{x}{r_\mathrm{cc}}\right)\right)\right], & x \in [0, x_1], \\ r(x_1) - (x - x_1)\tan\theta, & x \in [x_1, x_2], \\ r_* + r_\mathrm{cc}\left[1 - \cos\left(\arcsin\left(\dfrac{x - x_3}{r_\mathrm{cc}}\right)\right)\right], & x \in [x_2, x_3], \end{cases} \tag{C.11}$$

where the positions $x_1$, $x_2$, and $x_3$ are defined as

$$x_1 = r_\mathrm{cc}\sin\theta, \qquad x_2 = x_1 + \frac{r_\mathrm{c} - 2r_\mathrm{cc}(1 - \cos\theta) - r_*}{\tan\theta}, \qquad x_3 = x_2 + x_1.$$

Figure C.4 shows the normalised cross-sectional area $\mathrm{A/A_*}$ and Mach number M profiles along the nozzle geometry from Bell *et al.* [163] (—). As the Mach number M varies smoothly, the IS boundary condition Eq. (C.5) is expected to perform well.

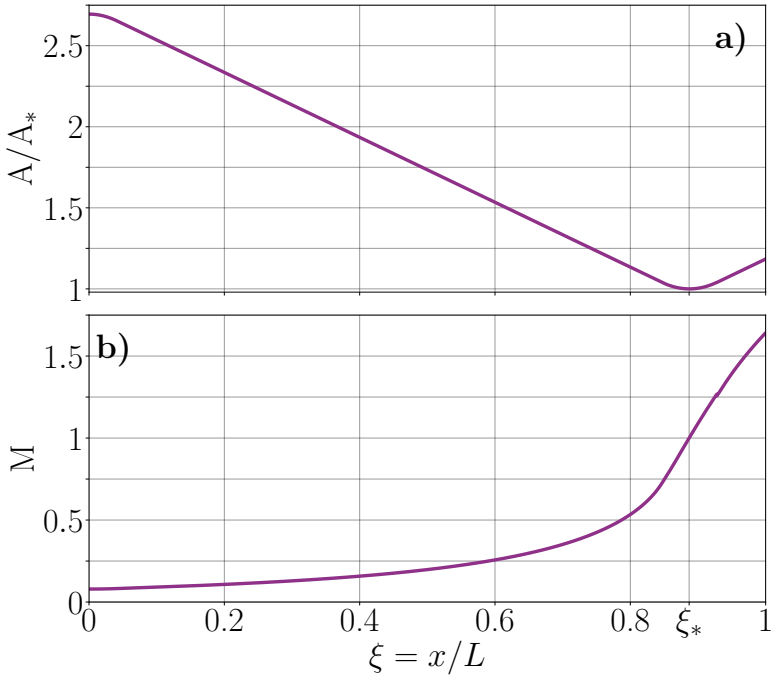


**Figure C.4** (Colour) Normalised cross-sectional area $\mathrm{A/A_*}$ **(a)** and Mach number M **(b)** of the nozzle geometry from Bell *et al.* [163] (—), plotted against the normalised longitudinal coordinate, $\xi = x/L$. The critical-throat position $\xi_*$ is also indicated.

### C.3.2 Numerical set-up

The numerical simulations are performed using the CFD code CEDRE, introduced in Sec. 2.4.

The computational set-up consists of a two-dimensional structured domain discretised with $\Delta x/L = 5 \times 10^{-5}$ for each geometry. This resolution ensures adequate spatial discretisation of acoustic waves, providing at least 50 points per wavelength for frequencies below $\Omega = 2\pi f/(\mathrm{d}\bar{u}/\mathrm{d}x)_* = 10$.

Since the flow is assumed to be purely longitudinal, only one cell is used to discretise the transverse direction. This single lateral mesh is computationally efficient, though it may not

represent the most efficient use of the code. A time step of $\Delta t = 5 \times 10^{-7}\,\mathrm{s}$ is used, ensuring a maximum CFL number of $(\bar{u}_{\mathrm{in}} + \bar{c}_{\mathrm{in}})\,\Delta t/\Delta x = 0.45$, where $\bar{u}_{\mathrm{in}}$ and $\bar{c}_{\mathrm{in}}$ denote the inlet steady velocity and sound speed, respectively. The spatial and temporal numerical schemes have already been described in Sec. 2.4.

The steady base flow is established by imposing an inlet static temperature of $T_{\mathrm{in}} = 300\,\mathrm{K}$, corresponding to a heat capacity ratio of $\gamma = 1.4$. This latter value is numerically prescribed constant throughout the entire nozzle for each geometry.

Unsteady solutions corresponding to acoustic forcing are obtained using a modulated post-processing time step based on the inlet forcing frequency. To ensure sufficient temporal resolution, 50 periods are simulated, with 100 points per period stored for post-processing. Spectral analysis (Fast Fourier Transform) is performed on the last 35 periods to exclude transient effects. This procedure ensures statistically converged spectra for the quantities of interest.

The mono-harmonic isentropic acoustic forcing has already been detailed in Sec. 2.4.2.

Simulations with four levels of grid refinement ($\Delta x/L = 5 \times 10^{-4}$, $1 \times 10^{-4}$, $5 \times 10^{-5}$, and $1\times10^{-5}$, where $L$ is the nozzle length) and three time steps ($\Delta t = 1\times10^{-6}$, $5\times10^{-7}$, and $1\times10^{-7}$) confirm that the results are grid and time-step-independent, indicating that discretisation errors in the presented simulations are negligible. Mesh independence is assessed by comparing the steady velocity gradient $(\mathrm{d}\bar{u}/\mathrm{d}x)_*$ at the critical throat. A maximum relative deviation of $9\times10^{-3}$ is observed between the value computed using CFD and the one-dimensional analytical solution Eq. (C.9) for the original nozzle geometry of Goh and Morgans [20]. Lower deviations are found for the other two nozzle geometries.

Time-step independence is validated by comparing the normalised pressure fluctuations $p'/(\gamma\bar{p})$ for each nozzle geometry under acoustic forcing at $\Omega = 10$. A maximum relative deviation of $6 \times 10^{-4}$ is found.

The influence of non-linear effects is assessed by performing numerical simulations with varying input amplitudes ($|p'_{\mathrm{in}}|/(\gamma\bar{p}_{\mathrm{in}}) = 0.1\,\%$ to $2\,\%$). The results indicate that non-linearities contribute less than $1 \times 10^{-3}$ to the overall deviation.

## C.4 Discussion and results

### C.4.1 Validation and limits of the quasi-one-dimensional model

Figure C.5 shows the evolution of the normalised Mach-number fluctuations $\hat{\mathrm{M}}_*/\hat{P}_*$ at the critical throat as a function of the dimensionless frequency, $\Omega = 2\pi f/(\mathrm{d}\bar{u}/\mathrm{d}x)_*$, comparing the analytical model Eq. (C.8) ($(\ )^{\mathrm{IS}}$) and the CFD results ($(\ )^{\mathrm{CFD}}$).

Good agreement is observed (within $1 \times 10^{-2}$) between the CFD data (markers) and the quasi-one-dimensional linear acoustic model (solid lines) for the nozzle geometry of Bell *et al.* [163] (●), and an order-of-magnitude better agreement is found for the smoothed nozzle of Goh and Morgans [20] (★). Both geometries feature a well-defined throat curvature, *i.e.*, $(\mathrm{d}^2\mathrm{A}/\mathrm{d}x^2)_*$. While deviations on the order of $1\times10^{-2}$ remain for the nozzle of Bell *et al.* [163], the IS boundary condition Eq. (C.5) provides a significantly better prediction of the critical-throat behaviour than the QSS assumption, $\hat{\mathrm{M}}_* = 0$.

The original nozzle geometry of Goh and Morgans [20], which features a discontinuity in $(\mathrm{dA}/\mathrm{d}x)$ at the throat, is also considered (■). The definition of $\Omega$ and the boundary condition Eq. (C.5) are assumed to remain valid as long as $(\mathrm{d}\bar{u}/\mathrm{d}x)_*$ has a well-defined, finite value; specifically, when the throat is approached from the subsonic side ($\mathrm{M} \leq 1$). The limit $(\mathrm{d}^2\mathrm{A}/\mathrm{d}x^2)_* = \lim_{x\uparrow x_*}(\mathrm{d}^2\mathrm{A}/\mathrm{d}x^2)$ on the subsonic side is used to compute $(\mathrm{d}\bar{u}/\mathrm{d}x)_*$. In Fig. C.5, a larger deviation is observed for the original geometry of Goh and Morgans [20] (■) compared with the smoothed version (★), with a maximum relative deviation of $4 \times 10^{-2}$.

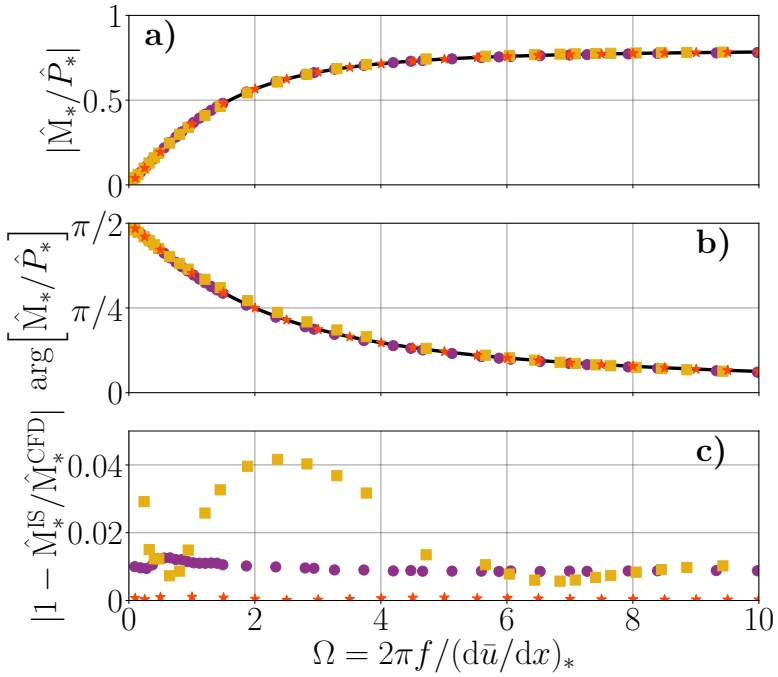


**Figure C.5** (Colour) Modulus $|\hat{M}_*/\hat{P}_*|$ **(a)**, phase-angle $\arg[\hat{M}_*/\hat{P}_*]$ **(b)**, and relative deviation $|1-\hat{M}_*^{IS}/\hat{M}_*^{CFD}|$ **(c)** of the normalised critical Mach-number fluctuations, comparing numerical results $\hat{M}_*^{CFD}$ (markers) and analytical results $\hat{M}_*^{IS}$ (—, Eq. (C.8)), as a function of the dimensionless frequency, $\Omega = 2\pi f/(d\bar{u}/dx)_*$. Results are shown for three nozzle geometries: Bell *et al.* [163] (●), the original geometry of Goh and Morgans [20] (■), and the smoothed version of Goh and Morgans [20] (★).

This discrepancy is at least partially attributed to limitations in the CFD numerical set-up (employing a single lateral mesh) for flows exhibiting a discontinuity in $(dA/dx)$ at the throat. A significant difference is found between the analytical value of $(d\bar{u}/dx)_*$, given by Eq. (C.9), and the value computed numerically. For the considered geometries, this relative difference is estimated to be approximately $1\times10^{-2}$, thereby introducing a systematic error in the calculation of $\Omega = 2\pi f/(d\bar{u}/dx)_*$.

### C.4.2 Influence of the boundary condition on the acoustic-pressure distribution

The influence of the IS boundary condition on the longitudinal distribution of pressure fluctuations is now examined. The quasi-one-dimensional linear acoustic model (presented in Chap. 4) is used with either the IS boundary condition Eq. (C.5) or the QSS boundary condition Eq. (C.3) imposed at the throat. Two representative frequencies are investigated: an order-unity case, $\Omega = 1$, and a higher-frequency case, $\Omega = 6$. For simplicity, the comparison is detailed only for the nozzle geometry of Bell *et al.* [163].

Figure C.6 shows, for $\Omega = 1$ and $\Omega = 6$, the normalised acoustic-pressure fluctuations $\hat{p}(x)/\hat{p}_{in}$ and the relative deviation $|1-\hat{p}^{QSS}/\hat{p}^{IS}|$ along the streamwise coordinate, $\xi = x/L$.

At $\Omega = 1$, except at the choked throat, the IS boundary condition (- - -) does not significantly alter the pressure-fluctuations field **(a)** in either the subsonic or supersonic regions when compared with the QSS solution (····). The relative deviation **(b)** remains within $1\times10^{-4}$ throughout. However, the singularity at the throat is eliminated, yielding a more physically

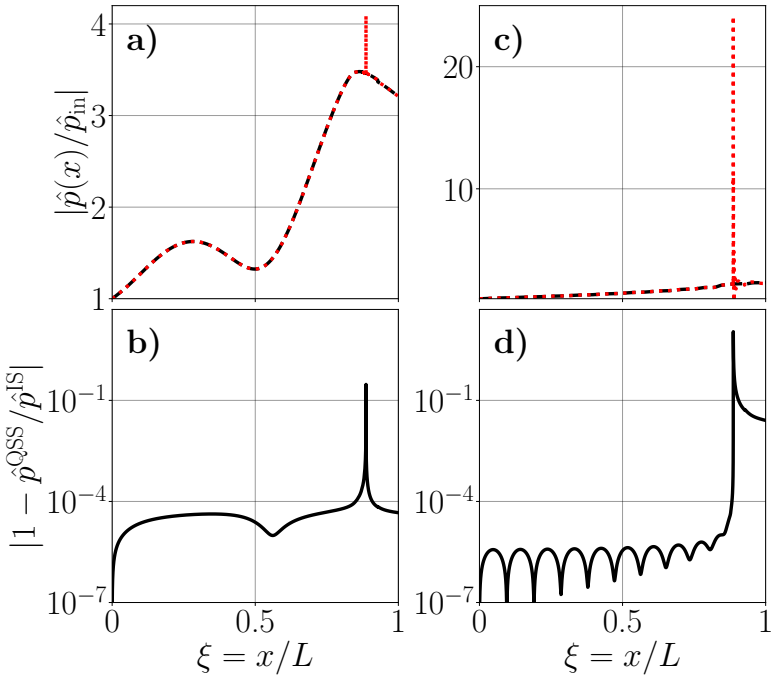


**Figure C.6** (Colour) Modulus of the acoustic pressure fluctuations, $|\hat{p}(x)/\hat{p}_{\text{in}}|$ (**(a)** and **(c)**), as a function of the streamwise position, $\xi = x/L$, for two distinct frequencies, $\Omega = 1$ and $\Omega = 6$. The solution is obtained from the quasi-one-dimensional linear acoustic model (Chap. 4) using either the IS (Eq. (C.5), **- - ·**) or QSS (Eq. (C.3), **····**) boundary condition. The relative deviation, $|1 - \hat{p}^{\text{QSS}}/\hat{p}^{\text{IS}}|$ (**(b)** and **(d)**, **—**), between the two boundary-condition solutions is also shown.

consistent solution.

At the higher frequency, $\Omega = 6$, a more pronounced discrepancy is observed **(c)**. As suggested by Eq. (C.5), the higher the frequency, the closer the boundary condition approaches a pure acoustic-radiation condition, thus rendering the QSS assumption increasingly inaccurate. In the subsonic region, the relative deviation **(d)** between the two boundary-condition solutions remains very small (approximately $1 \times 10^{-5}$). Downstream of the throat, however, the deviation increases, reaching up to $2.5 \times 10^{-2}$.

These observations motivate a more careful examination of the boundary condition at the choked throat. In both frequency cases, the discontinuity is eliminated when the IS boundary condition Eq. (C.5) is applied.

### C.4.3 Acoustic reflection and transmission coefficients

The aim of the quasi-one-dimensional linear acoustic models is to estimate the acoustic coefficients, such as the acoustic-reflection coefficient $R_a$ and the acoustic-transmission coefficient $T_a$ with high fidelity. These coefficients have already been introduced in Sec. 3.3 and are recalled below:

$$R_a = \frac{(\hat{P} - \bar{\mathrm{M}}\,\hat{U})_{\text{in}}}{(\hat{P} + \bar{\mathrm{M}}\,\hat{U})_{\text{in}}}, \tag{C.12}$$

$$T_a = \frac{(\hat{P} + \bar{\mathrm{M}}\,\hat{U})_{\text{out}}}{(\hat{P} + \bar{\mathrm{M}}\,\hat{U})_{\text{in}}}, \tag{C.13}$$

where $\hat{P} = \hat{p}/(\gamma\bar{p})$ and $\hat{U} = \hat{u}/\bar{u}$ are evaluated either at the inlet $(\,)_{\text{in}}$ or at the outlet $(\,)_{\text{out}}$.

These coefficients are computed using the acoustic-wave decomposition detailed in Appendix A. A uniform mean flow is assumed at both the inlet and outlet of each nozzle geometry.

Figure C.7 shows the acoustic-reflection coefficient $R_a$ (Eq. (C.12)) as a function of the dimensionless frequency, $\Omega = 2\pi f/(\mathrm{d}\bar{u}/\mathrm{d}x)_*$. Results are obtained using both CFD (markers) and the quasi-one-dimensional linear acoustic model closed with the IS boundary condition (C.5) (lines). Three nozzle geometries are considered: Bell *et al.* [163] (●, —), the original geometry of Goh and Morgans [20] (■, - - -), and the smoothed version of Goh and Morgans [20] (★, ····).

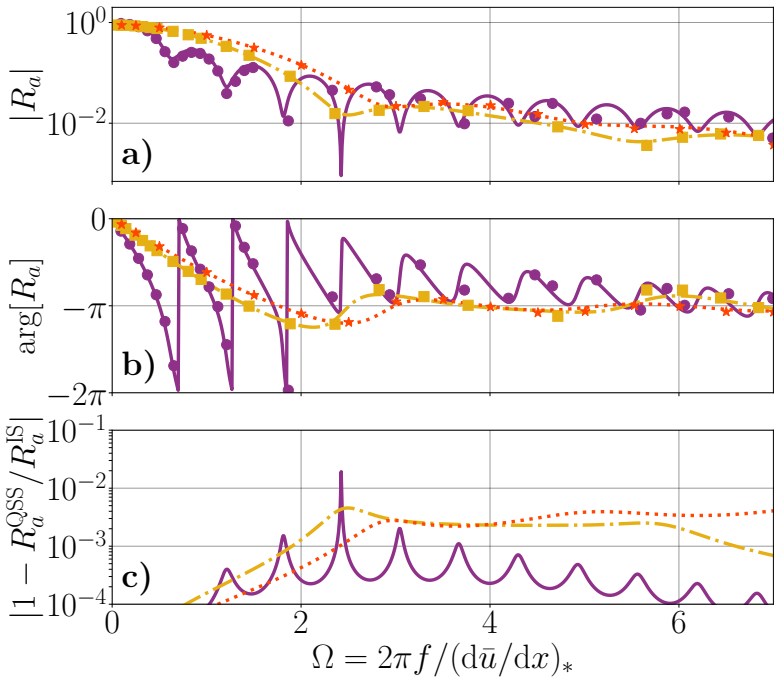


**Figure C.7** (Colour) Modulus $|R_a|$ **(a)** and phase-angle $\arg[R_a]$ **(b)** of the acoustic-reflection coefficient $R_a$, plotted as a function of the dimensionless frequency, $\Omega = 2\pi f/(\mathrm{d}\bar{u}/\mathrm{d}x)_*$. Results from CFD (markers) and the quasi-one-dimensional linear acoustic model using the IS boundary condition (lines) are shown for each nozzle geometry: Bell *et al.* [163] (●, —), the original geometry of Goh and Morgans [20] (■, - - -), and the smoothed version of Goh and Morgans [20] (★, ····). Subfigure **(c)** shows the relative deviation between the quasi-one-dimensional linear acoustic model using the IS boundary condition (Eq. (C.5)) and that using the QSS boundary condition (Eq. (C.3)).

For all three nozzle geometries, excellent agreement is observed between the linear acoustic model and the CFD simulation results. Some discrepancies appear for the original geometry of Goh and Morgans [20] at higher frequencies ($\Omega > 5.5$). As noted earlier, computing the velocity gradient $(\mathrm{d}\bar{u}/\mathrm{d}x)_*$ numerically is challenging in this case.

To assess the impact of the IS boundary condition relative to the commonly used QSS condition, $\mathrm{M}'_* = 0$, the relative difference in the linear-model results $|1 - R_a^{\mathrm{QSS}}/R_a^{\mathrm{IS}}|$ is evaluated using the two critical boundary conditions: IS (corresponding to $(\hat{\mathrm{M}}_*)_{\mathrm{IS}}$, Eq. (C.5)) and QSS (with $\mathrm{M}'_* = 0$). This relative difference is shown in subfigure **(c)**. As expected, at low frequencies the difference is minimal, since both conditions approach quasi-steady behaviour. The discrepancy increases with frequency, reaching $2\times10^{-2}$ for the geometry of Bell *et al.* [163] (—), and $3\times10^{-3}$ for both geometries of Goh and Morgans [20] (- - - and ····).

Figure C.8 shows the acoustic-transmission coefficient, $T_a$, as a function of $\Omega = 2\pi f/(\mathrm{d}\bar{u}/\mathrm{d}x)_*$ for the three nozzle geometries. The results are obtained using either CFD (markers) or the

quasi-one-dimensional linear acoustic model incorporating the IS boundary condition (lines).

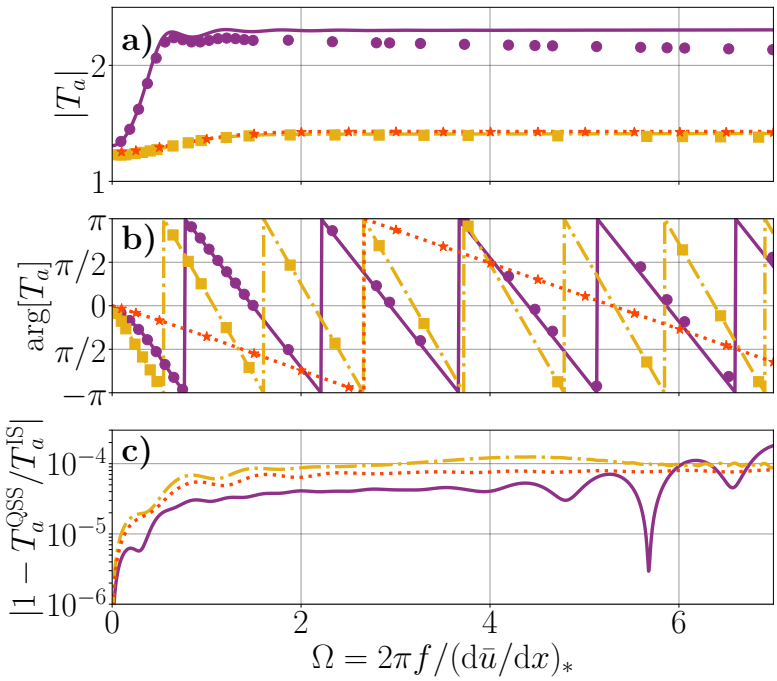


**Figure C.8** (Colour) Modulus $|T_a|$ **(a)** and phase-angle $\arg[T_a]$ **(b)** of the acoustic-transmission coefficient, $T_a$, plotted as a function of the dimensionless frequency, $\Omega = 2\pi f/(\mathrm{d}\bar{u}/\mathrm{d}x)_*$. Results from CFD simulations (markers) and the quasi-one-dimensional linear acoustic model using the IS boundary condition (lines) are shown for each nozzle geometry: Bell *et al.* [163] (●, —), the original geometry of Goh and Morgans [20] (■, - - -), and the smoothed version of Goh and Morgans [20] (★, ····). Subfigure **(c)** shows the relative deviation between the quasi-one-dimensional linear acoustic model using the IS boundary condition (Eq. (C.5)) and that using the QSS boundary condition (Eq. (C.3)).

A fair agreement is observed between the linear acoustic model and the CFD simulation results for both the original (■, - - -) and smoothed (★, ····) nozzle geometries of Goh and Morgans [20]. For the nozzle of Bell *et al.* [163], a maximum deviation of $3 \times 10^{-1}$ between CFD and model results is observed at very high frequencies, whereas at low frequencies ($\Omega < 1$) a fair agreement is maintained.

To evaluate the impact of the proposed IS boundary condition (Eq. (C.5)) compared with the quasi-steady critical Mach-number condition, $\mathrm{M}'_* = 0$ (Eq. (C.3)), the relative difference in the predicted $T_a$ is computed as $|1 - T_a^{\mathrm{QSS}}/T_a^{\mathrm{IS}}|$ **(c)**. As expected, the difference is negligible at low frequencies (below $1 \times 10^{-5}$). It increases with frequency, reaching $1 \times 10^{-4}$ for the two geometries of Goh and Morgans [20] (- - - and ····); a similar behaviour is observed for the nozzle of Bell *et al.* [163] (—), with a maximum deviation of $2 \times 10^{-4}$.

Since the errors introduced in the predicted acoustic-reflection ($R_a$) and transmission ($T_a$) coefficients by employing the quasi-steady boundary condition, $\mathrm{M}'_* = 0$, are relatively small, the overall conclusions drawn by Duran and Moreau [22] remain valid. Although, under the isentropic flow conditions considered here, only minor discrepancies are observed in the reflection and transmission coefficients, the presence of a singularity at the throat renders the solution physically inconsistent.

Moreover, as discussed in Chaps. 3 and 4, for thermally-choked nozzles the choice of boundary condition at the critical throat has a significantly larger impact on the predicted transmission

coefficient and on the overall acoustic response.

### C.4.4 Comparison with experimental measurements

The experimental geometries of Bell *et al.* [163] were designed to characterise a wide range of isentropic rocket-nozzle geometries. The comparison between nozzles was performed using the acoustic admittance $Y$, defined as the inverse of the impedance $Z$:

$$Y = \frac{1}{Z} = \bar{\rho}\,\bar{c}\,\left.\frac{\hat{u}}{\hat{p}}\right|_{\text{in}} = \bar{\mathrm{M}}\,\left.\frac{\hat{U}}{\hat{P}}\right|_{\text{in}} = \frac{1-R_a}{1+R_a}. \tag{C.14}$$

The comparison is carried out over a range of dimensionless frequencies $S = 1$ to 5, defined as $S = 2\pi f\, r_{\text{c}}/\bar{c}_{\text{in}}$.

Figure C.9 details the acoustic admittance $Y$ for the nozzle geometry of Bell *et al.* [163] as a function of the dimensionless frequency $S$. The equivalent dimensionless frequency $\Omega$ is also indicated at the top of the figure. Results are obtained using both the CFD simulation (●) and the quasi-one-dimensional linear acoustic model, closed using either the IS boundary condition (- - ·) or the QSS boundary condition (····).

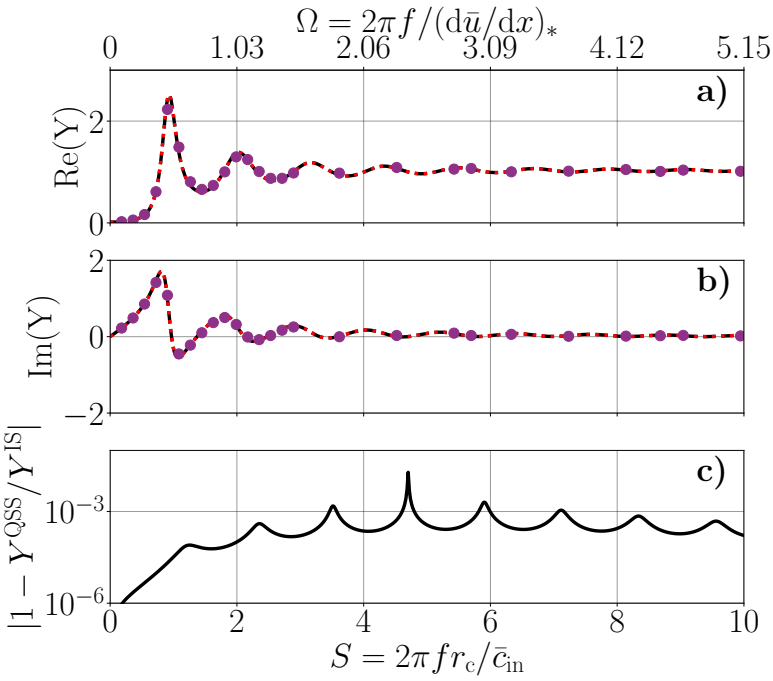


**Figure C.9** (Colour) Real part $\mathrm{Re}(Y)$ **(a)** and imaginary part $\mathrm{Im}(Y)$ **(b)** of the acoustic admittance $Y$ Eq. (C.14), plotted as a function of the dimensionless frequency, $S = 2\pi f\, r_{\text{c}}/\bar{c}_{\text{in}}$ for the nozzle geometry of Bell *et al.* [163]. The corresponding alternative dimensionless frequency $\Omega = 2\pi f/(\mathrm{d}\bar{u}/\mathrm{d}x)_*$ is indicated at the top of the graph. Results from CFD simulations (●) and from the quasi-one-dimensional linear acoustic model using either the IS boundary condition (- - ·) or the QSS boundary condition (····) are shown. The relative deviation between the IS ($Y^{\mathrm{IS}}$) and QSS ($Y^{\mathrm{QSS}}$) boundary conditions is presented in subfigure **(c)**.

A fair agreement is found between CFD and linear-model results for both boundary conditions, in the real part $\mathrm{Re}(Y)$ **(a)** and the imaginary part $\mathrm{Im}(Y)$ **(b)**. To assess the impact of the IS boundary condition on the prediction of $Y$ relative to the QSS condition, the relative deviation $|1 - Y^{\mathrm{QSS}}/Y^{\mathrm{IS}}|$ is plotted in subfigure **(c)**. At low frequencies ($S < 1$) the difference

is negligible, consistent with the quasi-steady behaviour $\mathrm{M}'_* = 0$. At high frequencies ($S > 5$) the error remains below $1 \times 10^{-3}$. For intermediate frequencies ($1 < S < 5$), a few peaks are observed, reaching at most a few per cent.

### Chapter conclusion

A quasi-one-dimensional boundary condition at the critical throat (Eq. (C.5)) is proposed and validated with three nozzle geometries commonly employed in the literature. This formulation generalises the boundary condition originally introduced by Marble and Candel [16]. Whereas Marble and Candel [16] assumed a constant velocity gradient $\mathrm{d}\bar{u}/\mathrm{d}x$ within the nozzle, the present theory requires only the continuity of the first and second derivatives of the cross-sectional area, $\mathrm{dA}/\mathrm{d}x$ and $\mathrm{d}^2\mathrm{A}/\mathrm{d}x^2$, at the throat on the subsonic side.
In cases where a discontinuity in $\mathrm{dA}/\mathrm{d}x$ exists, such as in the nozzle geometry proposed by Goh and Morgans [20], the quasi-one-dimensional approximation must be applied with caution. Moreover, when the quasi-steady critical Mach-number condition, $\mathrm{M}'_* = 0$, is used, the predicted acoustic pressure exhibits a singularity at the throat, a behaviour not observed in CFD simulations. Nevertheless, the predicted inlet reflection coefficient, acoustic admittance, and transmission coefficient are not significantly affected for the geometries considered in this study. This explains the satisfactory agreement reported by Duran and Moreau [22].

Appendix D

# Validation of the entropy-spot injection methodology

*C'est carré-carré chez vous, hein ?*

**Breccan [2]**


## Abstract

This appendix validates the methodology developed to characterise the acoustic response generated by the convection of entropy non-uniformities through a choked-flow nozzle. The procedure is assessed by reproducing the results of Elbakly [159] for an isentropic geometric-throat configuration. A detailed reconstruction of the reference nozzle geometry and operating conditions is performed, and both the quasi-steady-state (QSS) and point-mass (PM) asymptotic acoustic models are applied over a wide range of entropy-spot radii. The comparison between the present CFD results and the reference data demonstrates excellent agreement across both the inertial and quasi-steady regimes. For small entropy spots, the acoustic response follows the inertial scaling predicted by the PM model, while for large spots, it converges toward the QSS regime. These results confirm the accuracy of the entropy-spot injection procedure, the robustness of the implemented numerical framework, and the validity of the methodology used throughout this thesis to quantify indirect noise generation in thermally and geometrically choked flows.


This appendix is a truncation of the following publication, submitted during the PhD:

K. Elbakly, S. Hulshoff, F. Olivon, A. Genot, F. Bake, C. Venner, and L. Hirschberg. "Entropy-patch choked-nozzle interaction: quasi-steady and inertial modeling regimes mapped and limits of linearization established". In: *Proceedings of the 32nd AIAA/CEAS Aeroacoustics Conference*, Bruxelles, Belgium, May 2026.

## Contents


**D.1 Objective and validation methodology . . . . . 162**

D.1.1 Isentropic nozzle geometry . . . . . 162

D.1.2 Numerical set-up . . . 163
D.1.3 Steady-flow fields . . . 164
**D.2 Asymptotic acoustic-response models . . . 165**
D.2.1 Quasi-steady-state acoustic response . . . 165
D.2.2 Inertial acoustic response . . . 166
**D.3 Entropy noise acoustic response . . . 168**

## D.1 Objective and validation methodology

In Chap. 6, a methodology was employed to numerically characterise the acoustic response of a choked-flow nozzle subjected to two-dimensional entropy perturbations. This approach was applied to both thermal- and geometric-throat nozzles. Similar studies have been conducted, notably by Hirschberg [94], Kowalski *et al.* [158], and Elbakly [159]. To validate the proposed methodology detailed in Sec. 6.2, the results of Elbakly [159] were reproduced by applying the present approach to the geometry considered in their study.

### D.1.1 Isentropic nozzle geometry

The isentropic geometric-throat nozzle originally introduced by Hulshoff *et al.* [165] is considered in this study and shown in Fig. D.1. This canonical configuration has since been widely adopted in aeroacoustic investigations [30, 94, 158, 159, 166]. The nozzle consists of three main sections: a rectangular constant-duct inlet of height and width $h_{\text{in}}$, a smooth convergent part with a critical-throat height $h_*$, and a divergent duct. A distinctive feature of this geometry is the sharp angle in the convergent section, which necessitates specific geometric treatment, as detailed in Sec. D.1.1.

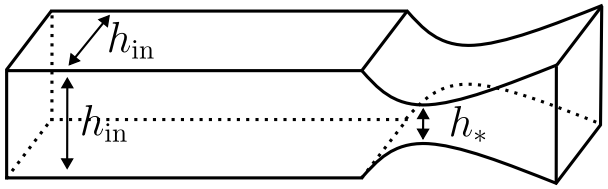


**Figure D.1** Sketch of the geometric-throat configuration from Elbakly [159], featuring a rectangular channel with a sharp-angled inlet nozzle.

This nozzle is fully characterised by two geometric parameters: the contraction ratio $h_*/h_{\text{in}} = 1/3$ and the length ratio $\delta_*/h_{\text{in}} = 1/2$. From the area–Mach-number relation Eq. (4.1), the corresponding inlet Mach number is found to be $\mathrm{M}_{\text{in}} = 0.197$.

#### Smooth convergent section

To construct the smooth convergent section, the Henrici transformation [167] is employed. This method has been described in detail by Hirschberg [94]; only the main steps are recalled here. The objective of the algorithm is to derive a smooth converging profile from a sharp-angle geometry through a Schwarz–Christoffel type conformal mapping. Specifically, a transformation $\zeta \mapsto z$, with $z(\zeta) = x(\zeta) + \mathrm{i}y(\zeta)$, is sought that maps a simple domain of the $\zeta$-plane onto the convergent duct:

$$z(\zeta) = \alpha \left( \ln\left(\frac{1+\tau}{1-\tau}\right) - \frac{1}{b}\ln\left(\frac{b+\tau}{b-\tau}\right)\right) + \beta \ln\left(\frac{\zeta}{b^2}\right), \tag{D.1}$$

with $\tau = \sqrt{(\zeta - b^2)/(\zeta - 1)}$.

Closure of the problem requires the scaling parameter $b$ to be determined numerically in order to satisfy the prescribed contraction length $\delta_*$. The iterative scheme for $b$ is expressed as:

$$b = \begin{cases} \dfrac{y_{\text{in}}}{y_*} + \dfrac{\pi}{2}\dfrac{\delta_*}{y_*}\dfrac{(b-1)}{\ln(b)}, & \text{if } \dfrac{\pi\delta_*}{2y_*} < 2, \\ \exp\left(\dfrac{\pi\delta_*}{2y_*}\dfrac{1-1/b}{1-y_{\text{in}}/(y_* b)}\right), & \text{if } \dfrac{\pi\delta_*}{2y_*} > 2. \end{cases} \tag{D.2}$$

The geometric coefficients $\alpha$ and $\beta$ then follow as:

$$\alpha = \frac{y_{\text{in}} - y_*}{\pi}\left(\frac{b}{b-1}\right), \qquad \beta = \frac{b\,y_* - y_{\text{in}}}{\pi(b-1)}. \tag{D.3}$$

The smoothed convergent profile $z(\zeta)$ is generated by evaluating the mapping at discrete points,

$$\zeta_n = \zeta_0\big(1 + n\sqrt{n}\big), \qquad n = 1, \ldots, N,$$

with $N = 76$ and $\zeta_0 = 0.36$[1]. The resulting profile is then re-oriented according to

$$\tilde{z} = \overline{z}\,\exp(\mathrm{i}\pi),$$

where the overbar denotes complex conjugation.

Finally, the physical coordinates are obtained from the real and imaginary parts:

$$x = \mathrm{Re}(\tilde{z}), \qquad y = \mathrm{Im}(\tilde{z}).$$

**Nozzle geometry**

To the smoothed convergent nozzle, a constant cross-section duct of height $y_{\text{in}}$ is appended over a length $l_c/y_{\text{in}} = 3.5$. Downstream of the critical throat, a divergent section of length $l_d/y_{\text{in}} = 2$ is added, defined as a conical diffuser shaped with a Hermitian cubic spline to avoid abrupt variations in the nozzle slope. The outlet height is imposed as $y_{\text{out}}/y_{\text{in}} = 0.5$. Since the entire nozzle geometry can be expressed in terms of the inlet height $y_{\text{in}}$, the value $y_{\text{in}} = 1$ is adopted following the work of Elbakly [159]. The final nozzle profile is shown in Fig. D.2.

### D.1.2 Numerical set-up

The numerical simulations are performed using the CFD code CEDRE, introduced in Sec. 2.4.

The computational domain is two-dimensional and planar, discretised with approximately $2 \times 10^6$ cells of size $\Delta x/y_{\text{in}} = 1.45 \times 10^{-3}$. A structured mesh is employed for the constant cross-section duct, while an unstructured mesh is used for the convergent–divergent part. This resolution provides adequate spatial discretisation of the injected entropy spot, ensuring at least 30 grid points per radius for spots with $r_s/y_* \geq 0.13$. The discretisation is consistent with that employed by Elbakly [159].

A time step of $\Delta t = 1\times10^{-6}$ s is used, yielding a maximum CFL number of $(\bar{u}_{\text{in}}+\bar{c}_{\text{in}})\Delta t/\Delta x = 0.28$, where $\bar{u}_{\text{in}}$ and $\bar{c}_{\text{in}}$ denote the inlet steady velocity and sound speed, respectively. As described in Sec. 6.2.1, the time step is determined by the inlet velocity $u_{\text{in}}$ and the mesh size, following $\Delta t = \Delta x/u_{\text{in}} = 1 \times 10^{-6}$. The spatial and temporal discretisation schemes are those described in Sec. 2.4.

[1] These values were provided directly by Elbakly [159].

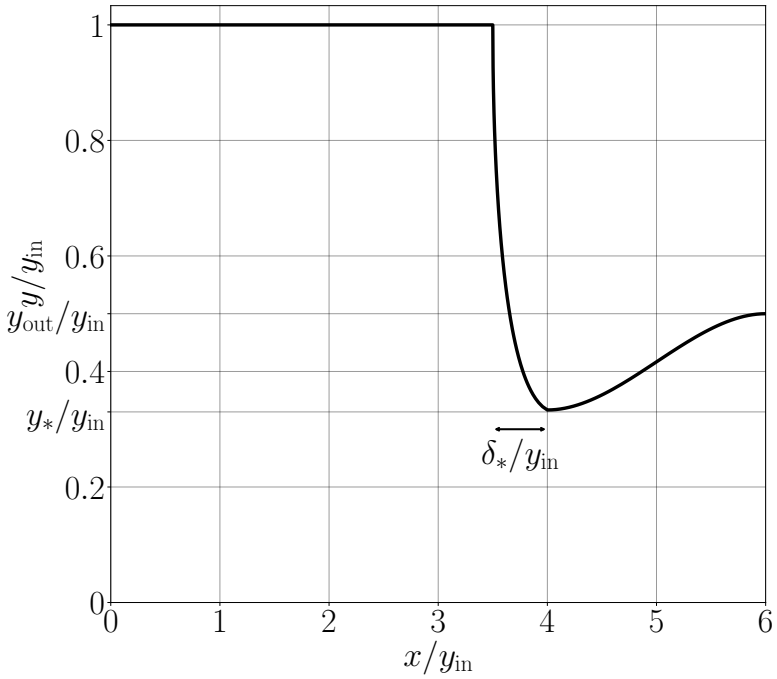


**Figure D.2** Normalised cross-sectional height $y/y_{\text{in}}$ of the nozzle geometry from Elbakly [159] (—), plotted against the normalised longitudinal coordinate $x/y_{\text{in}}$. The contraction ratio $y_*/y_{\text{in}}$ and the length ratio $\delta_*/y_{\text{in}}$ are also indicated.

### D.1.3 Steady-flow fields

The steady base flow is obtained by prescribing an inlet static temperature of $T_{\text{in}} = 300\,\text{K}$, corresponding to a constant heat capacity ratio $\gamma = 1.4$, imposed uniformly throughout the nozzle. Figure D.3 shows the two-dimensional steady-state Mach number field, $\bar{\text{M}}$, within the nozzle of Elbakly [159]. As expected, the Mach number increases from $\bar{\text{M}}_{\text{in}} = 0.19$ at the inlet to a supersonic value of $\bar{\text{M}}_{\text{out}} \approx 1.9$ at the outlet. The sonic line is found to be slightly tilted due to the small length ratio, $\delta_*/y_{\text{in}} = 1/2$.

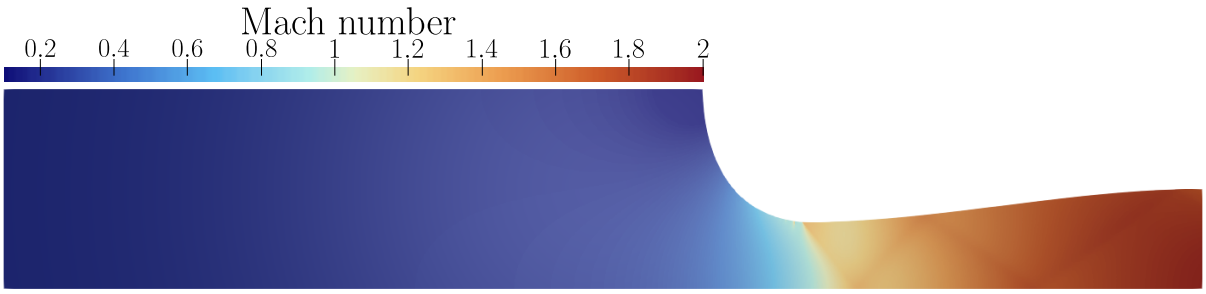


**Figure D.3** (Colour) Two-dimensional steady-state Mach number field obtained from the nozzle geometry of Elbakly [159].

Figure D.4 presents the one-dimensional steady-state profiles of Mach number $\bar{\text{M}}$, static pressure $\bar{p}$, and static temperature $\bar{T}$, along the symmetry axis. The variations of these quantities are not perfectly monotonic; small discrepancies appear in the supersonic region. This behaviour arises from the junction between the smoothed convergent section and the supersonic divergent part, where the derivatives are not matched. The nozzle geometry was retained despite this

mismatch, as the resulting artificial features in the supersonic region do not affect the upstream-propagating acoustic wave. Although the junction could have been further smoothed by slightly increasing the convergent length, such modification might have altered the flow behaviour in the subsonic region.

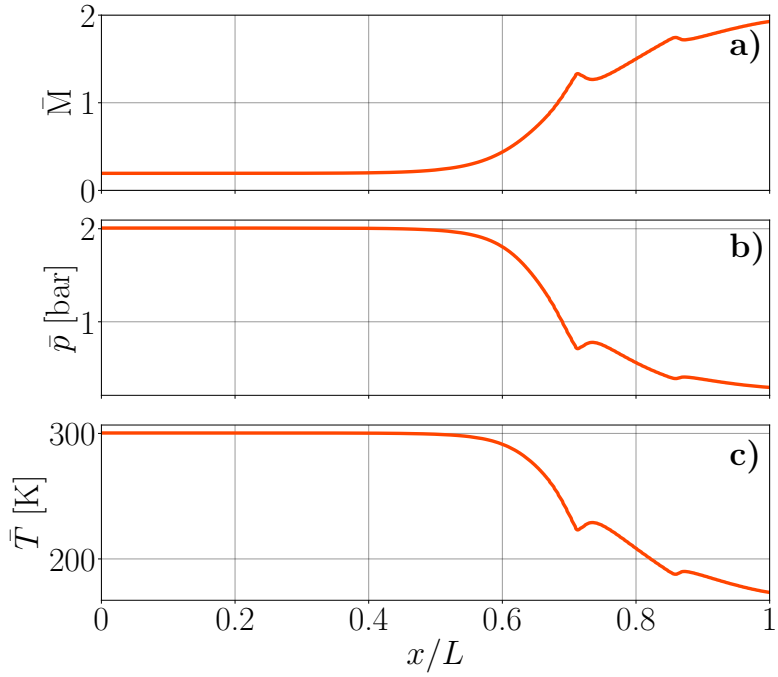


**Figure D.4** (Colour) Steady-state Mach number $\bar{\mathrm{M}}$ **(a)**, static pressure $\bar{p}$ **(b)**, and static temperature $\bar{T}$ **(c)** profiles, as a function of the dimensionless position, $x/L$.

## D.2 Asymptotic acoustic-response models

In the study of Elbakly [159], two models were proposed to describe the acoustic response induced by either a very small or a very large entropy spot. These models are based on the one-dimensional Euler equations (Eq. (2.3)), assuming a linear acoustic response, and are designed to highlight the main mechanisms responsible for the acoustic behaviour of a geometrically-choked flow. For a very large entropy spot, a quasi-steady acoustic response is expected, whereas for a very small entropy spot, the response is assumed to be purely due to inertial effects. These models are described in detail in Sec. D.2.1 and Sec. D.2.2, based on the work of [159].

### D.2.1 Quasi-steady-state acoustic response

For an isentropic flow propagating through a geometric-throat nozzle with a constant heat capacity $c_p$, the linearisation of Eq. (C.1), as derived in Appendix C, yields the following relation upstream of the critical throat:

$$\mathrm{M}' = 0, \tag{D.4}$$

where $\bar{\chi}$ denotes the steady-state quantity and $\chi'$ its fluctuating component. This linear decomposition assumes that the fluctuation amplitude is small compared with the steady quantity, *i.e.*, $\chi' \ll \bar{\chi}$, and that second-order terms are negligible, *i.e.*, $\chi'\chi' = 0$.

In particular, this relation holds at the inlet, *i.e.*, $\mathrm{M}'_{\mathrm{in}} = 0$. The equation can then be rewritten using natural variables as follows:

$$\frac{u'_{\mathrm{in}}}{\bar{u}_{\mathrm{in}}} = \frac{c'_{\mathrm{in}}}{\bar{c}_{\mathrm{in}}} = \frac{1}{2}\frac{T'_{\mathrm{in}}}{\bar{T}_{\mathrm{in}}}. \tag{D.5}$$

Here, Elbakly [159] assumes that the acoustic response generated by the convection of an entropy spot is isobaric, *i.e.*, one can write $T'_{\mathrm{in}}/\bar{T}_{\mathrm{in}} = s'_{\mathrm{in}}/c_p$, from the linearised form of the Gibbs equation (Eq. (2.11)). It then follows that

$$\frac{u'_{\mathrm{in}}}{\bar{u}_{\mathrm{in}}} = \frac{1}{2}\frac{s'_{\mathrm{in}}}{c_p}. \tag{D.6}$$

At the inlet, a uniform flow is assumed, leading to the following acoustic-wave decomposition (see Appendix A for details):

$$\begin{cases} \dfrac{p'_{\mathrm{in}}}{\gamma \bar{p}_{\mathrm{in}}} = P^{+}_{\mathrm{in}} + P^{-}_{\mathrm{in}}, \\ \dfrac{u'_{\mathrm{in}}}{\bar{u}_{\mathrm{in}}} = \dfrac{1}{\bar{\mathrm{M}}_{\mathrm{in}}}\left(P^{+}_{\mathrm{in}} - P^{-}_{\mathrm{in}}\right), \end{cases} \tag{D.7}$$

where $P^{\pm}_{\mathrm{in}}$ are the downstream- and upstream-propagating acoustic waves at the inlet. Since the acoustic response is assumed to be solely due to the convection of the entropy perturbation, $P^{+}_{\mathrm{in}} = 0$, leading to

$$\frac{u'_{\mathrm{in}}}{\bar{u}_{\mathrm{in}}} = -\frac{p'_{\mathrm{in}}}{\gamma \bar{p}_{\mathrm{in}}}. \tag{D.8}$$

Finally, the quasi-steady-state (QSS) acoustic response at the inlet is

$$p'_{\mathrm{in,QSS}} = -\frac{\gamma\, \bar{\mathrm{M}}_{\mathrm{in}}\, \bar{p}_{\mathrm{in}}}{2}\frac{s'_{\mathrm{in}}}{c_p}. \tag{D.9}$$

This model is hereafter referred to as the QSS model. It is noteworthy that the quasi-steady model used here (Eq. (D.9)) differs from that employed in Chap. 6 (Eq. (6.6)) to compare the acoustic response induced by very large entropy spots. In the present case, the convection of the entropy spot is assumed to be isobaric, which leads to a difference from the formulation used in Chap. 6.

### D.2.2 Inertial acoustic response

An isentropic, smoothly varying geometric-throat nozzle with a constant heat capacity $c_p$ is considered. The convection of a small pressure discontinuity $\Delta p$ originating at a source location $x_{\mathrm{s}}$ gives rise to two acoustic waves, as illustrated in Fig. D.5:

$$\Delta p = p^{+}_{\mathrm{s,d}} - p^{-}_{\mathrm{s,u}}, \tag{D.10}$$

where $p^{+}_{\mathrm{s,d}}$ is the downstream-propagating acoustic wave generated downstream of the discontinuity, and $p^{-}_{\mathrm{s,u}}$ is the upstream-propagating wave directed toward the inlet.

Assuming that the pressure discontinuity is sufficiently small, the mass-flow-rate fluctuations satisfy

$$(\rho u)'_{\mathrm{s,d}} = (\rho u)'_{\mathrm{s,u}}. \tag{D.11}$$

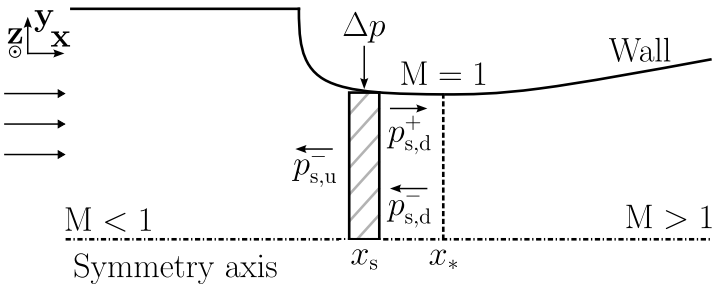


**Figure D.5** Sketch of the downstream- and upstream-propagating acoustic waves generated by the convection of a small pressure perturbation $\Delta p$ in an isentropic geometric-throat nozzle, adapted from Elbakly [159].

Expanding Eq. (D.11) and using

$$\begin{cases} \rho^{\pm} = \dfrac{p^{\pm}}{\bar{c}^2}, \\ u^{\pm} = \pm \dfrac{p^{\pm}}{\bar{\rho}\bar{c}}, \end{cases} \tag{D.12}$$

leads to

$$\begin{cases} p^-_{s,u} = -\dfrac{1+\bar{M}_s}{2}\,\Delta p, \\ p^+_{s,d} = \dfrac{1-\bar{M}_s}{2}\,\Delta p. \end{cases} \tag{D.13}$$

The downstream-propagating acoustic wave $p^+_{s,d}$ is assumed to be reflected at the geometric throat, producing an upstream-propagating acoustic wave in the downstream region $p^-_{s,d}$. Using the quasi-steady-state acoustic-reflection coefficient $R_a$, as described by Marble and Candel [16], one can write

$$R_a = \frac{p^-_{s,d}}{p^+_{s,d}} = \frac{2-(\gamma-1)\bar{M}_s}{2+(\gamma-1)\bar{M}_s}. \tag{D.14}$$

The total acoustic fluctuation upstream of the source is then

$$p'_{s,u} = p^-_{s,u} + R_a\, p^-_{s,d} = -\frac{\Delta p}{2}\left(\left(1+\bar{M}_s\right) - R_a\left(1-\bar{M}_s\right)\right). \tag{D.15}$$

Based on the work of Howe [168], the acoustic power emitted upstream of a sound source can be expressed as follows:

$$|\Phi^-_s| = \frac{A_s}{\bar{\rho}_s \bar{c}_s}\left(1-\bar{M}_s\right)^2 |p'_{s,u}|^2. \tag{D.16}$$

Assuming the flow is isentropic, the conservation of acoustic energy between the sound source ($x_s$) and the inlet ($x_{in}$) yields

$$|p'_{in}| = \sqrt{\frac{\bar{\rho}_{in}\bar{c}_{in}A_s}{\bar{\rho}_s\bar{c}_s A_{in}}}\left[\left(1+\bar{M}_s\right) - R_a\left(1-\bar{M}_s\right)\right]\left(\frac{1-\bar{M}_s}{1-\bar{M}_{in}}\right)\frac{\Delta p}{2}. \tag{D.17}$$

As shown by Curle [169] and Pierce [170], an unsteady force from a wall on the flow acts as a sound source:

$$\Delta p = \frac{F_x}{A_s}, \tag{D.18}$$

where $F_x$ is the force exerted by the walls on the fluid. Using Newton's second law, one obtains

$$F_x = m_e \bar{u}_\mathrm{s} \left.\frac{\mathrm{d}\bar{u}}{\mathrm{d}x}\right|_\mathrm{s}, \tag{D.19}$$

where $m_e$ is the excess mass induced by the pressure discontinuity.

Finally, the inertial acoustic response model, hereafter referred to as the point-mass model (PM), is given by

$$|p'_{\mathrm{in,PM}}| = \sqrt{\frac{\bar{\rho}_\mathrm{in}\bar{c}_\mathrm{in}}{\bar{\rho}_\mathrm{s}\bar{c}_\mathrm{s}\mathrm{A_s}\mathrm{A_{in}}}} \left[\left(1+\bar{\mathrm{M}}_\mathrm{s}\right) - R_a\left(1-\bar{\mathrm{M}}_\mathrm{s}\right)\right] \left(\frac{1-\bar{\mathrm{M}}_\mathrm{s}}{1-\bar{\mathrm{M}}_\mathrm{in}}\right) \frac{m_e}{2}\,\bar{u}_\mathrm{s} \left.\frac{\mathrm{d}\bar{u}}{\mathrm{d}x}\right|_\mathrm{s}. \tag{D.20}$$

To estimate the sound-source position $x_\mathrm{s}$, the methodology of Elbakly [159] is applied. The position at which the quantity

$$\frac{|p'_\mathrm{in}|\,y_\mathrm{in}^3}{m_e\bar{u}_\mathrm{in}^2} = \sqrt{\frac{\bar{\rho}_\mathrm{in}\bar{c}_\mathrm{in}}{\bar{\rho}(x_\mathrm{s})\bar{c}(x_\mathrm{s})\mathrm{A}(x_\mathrm{s})\mathrm{A_{in}}}} \left[\left(1+\bar{\mathrm{M}}(x_\mathrm{s})\right) - R_a(x_\mathrm{s})\left(1-\bar{\mathrm{M}}(x_\mathrm{s})\right)\right] \left(\frac{1-\bar{\mathrm{M}}(x_\mathrm{s})}{1-\bar{\mathrm{M}}_\mathrm{in}}\right) \frac{\bar{u}(x_\mathrm{s})}{2\bar{u}_\mathrm{in}^2} \left.\frac{\mathrm{d}\bar{u}}{\mathrm{d}x}\right|_{x_\mathrm{s}}, \tag{D.21}$$

reaches its maximum is taken as the location where the strongest acoustic emission occurs.

The excess mass density $m_e$ is then numerically estimated by volumetric integration of the density fluctuations, $\rho'_e = (\rho - \bar{\rho})/\bar{\rho}$, over a volume $V$ in the constant-duct region, such that

$$m_e = \int_V \rho'_e \,\mathrm{d}V. \tag{D.22}$$

This numerical integration is performed at a fixed longitudinal position $x_\mathrm{in}$, over the total simulation time $\tau_\mathrm{CFD}$, and across the duct cross-section $\mathrm{A} = y_\mathrm{in}^2$. It has been verified that this method is not sensitive to the sensor position within the constant-duct region.

## D.3 Entropy noise acoustic response

The acoustic response induced by the convection of an entropy spot in a geometric-throat nozzle is now characterised over a wide range of entropy-spot sizes $r_\mathrm{s}$. The methodology used to inject the entropy spot with the CFD code CEDRE is described in Sec. 6.2.1.

Each entropy spot is defined by its normalised radius $r_\mathrm{s}/y_\mathrm{in}$, where $r_\mathrm{s}$ is the entropy-spot radius. The spots are injected at the inlet. The sound-source position is found to be $(x_s - x_*)/\delta_* = 0.3205$, which is very close to the value reported by Elbakly [159]. In this study, the maximum acoustic response $()_\mathrm{max}$ is considered. The acoustic response is measured along the symmetry axis at the inlet. It has been verified that this value is independent of both the transverse and longitudinal positions within the straight-duct section of the nozzle. For the maximum-entropy, the measurement is performed at the transverse height corresponding to the entropy-spot injection location.

Figure D.6 presents the acoustic response of the considered geometric-throat nozzle induced by the convection of circular entropy spots of varying radius $r_\mathrm{s}$. As expected, good agreement is observed between the results obtained with the present methodology and those of Elbakly [159] (QSS: ●, PM: ○).

For very small spot sizes ($r_\mathrm{s}/y_* < 1$), the point-mass model (Eq. (D.20), ■) accurately predicts the acoustic response, indicating that it is mainly driven by the inertial effect of the small excess mass on the surrounding fluid. For large spot sizes ($r_\mathrm{s}/y_* > 10$), the response tends toward the quasi-steady regime (Eq. (D.9), ■), with a normalised value $|p'_\mathrm{max}|_\mathrm{CFD}/|p'_\mathrm{max}|_\mathrm{QSS}$ close to unity.

The injection methodology described in Sec. 6.2.1, along with the procedure used to determine the excess mass $m_e$ is therefore considered valid.

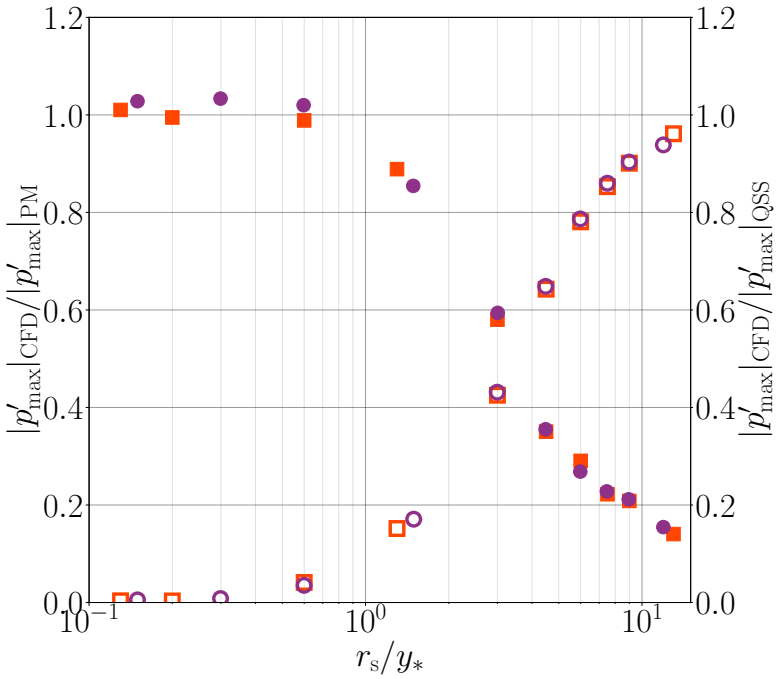


**Figure D.6** (Colour) Normalised acoustic response induced by a circular entropy spot of radius $r_s$ for the nozzle geometry of Elbakly [159]. The acoustic response (CFD) is normalised either by the quasi-steady-state model (QSS: Eq. (D.9), ■) or by the point-mass model (PM: Eq. (D.20), □). The results of Elbakly [159] are also shown (QSS: ●, PM: ○).

### Chapter conclusion

In this appendix, the methodology used to generate and analyse the acoustic response induced by entropy perturbations in a choked-flow nozzle has been validated by comparison with the reference study of Elbakly [159]. The isentropic geometric-throat nozzle geometry was reconstructed, and both the quasi-steady and inertial acoustic-response models were applied over a range of entropy-spot radii to reproduce the asymptotic behaviours.
The results show very good agreement between the normalised acoustic responses obtained from the present simulations and those reported in the literature. For small spots, the point-mass model accurately captures the inertial regime, while for large spots, the quasi-steady-state model correctly describes the asymptotic behaviour of the acoustic response. The consistency between the two asymptotic limits confirms the physical soundness of the proposed injection and measurement procedure.
This validation demonstrates that the numerical methodology developed in this work reliably reproduces the theoretical trends and reference results available in the literature. It thus provides a robust foundation for the detailed investigation of two-dimensional entropy-spot convection and the resulting indirect noise generation presented in Chap. 6.

# Résumé

*Et là, normalement, il me faut une citation latine, mais pfff... j'en ai marre !*
**Le Roi Loth [2]**

## Objectifs et motivations

Les systèmes de propulsion supersonique et hypersonique de type statoréacteur et superstatoréacteur suscitent un intérêt croissant pour les applications de vol atmosphérique à très haute vitesse. Ces moteurs, dépourvus de pièces mobiles, utilisent l'air ambiant comme comburant, ce qui réduit la masse totale embarquée et améliore les performances globales de la propulsion par rapport aux turboréacteurs et aux moteurs-fusées. Dans un statoréacteur, où la combustion reste subsonique dans la chambre de combustion, l'accélération et l'amorçage de l'écoulement (position où le nombre de Mach atteint l'unité) sont généralement imposés par un col géométrique, *i.e.* une contraction géométrique de la tuyère. À l'inverse, dans un superstatoréacteur, la combustion s'effectue en régime supersonique et ne nécessite pas de partie convergente dans la tuyère. Afin d'élargir la plage de fonctionnement des superstatoréacteurs, le concept de statomixte, combinant un mode de combustion subsonique et un mode supersonique, est activement étudié. Le fonctionnement stable d'un tel moteur repose cependant sur un équilibre complexe entre la dynamique de l'écoulement interne, la combustion, les systèmes de chocs à l'entrée, la géométrie de la chambre de combustion, ainsi que la propagation des ondes de pression dans le domaine subsonique du moteur.

Dans ce contexte, les statomixtes à col thermique constituent une solution intéressante. Contrairement aux tuyères géométriquement amorcées, où le col est imposé par une contraction géométrique, l'amorçage résulte ici d'un apport d'énergie volumique distribué dans le conduit divergent, lié à la combustion. La géométrie de la tuyère n'a donc pas besoin d'être modifiée en cours de vol. Modélisée comme une source thermique volumique, la combustion modifie localement les conditions de l'écoulement (pression, température, nombre de Mach, *etc.*), jusqu'à former un col thermique à partir duquel l'écoulement devient supersonique. Ce col thermique joue simultanément le rôle de frontière aérodynamique (transition du régime d'écoulement subsonique à supersonique) et de frontière acoustique, où se produisent des phénomènes de réflexion et de transmission acoustiques. Dans un statomixte, il conditionne directement la transition entre régimes de combustion subsonique et supersonique.

Alors que l'aéroacoustique des tuyères géométriques isentropiques est relativement bien établie, les caractéristiques acoustiques des tuyères à col thermique demeurent très peu documentées. La plupart des travaux fondateurs, tels que ceux de Marble et Candel [16], ont été développés dans le cadre d'écoulements essentiellement isentropiques, avec des conditions aux limites idéalisées au niveau du col géométrique. De plus, ces approches ne tiennent pas compte des effets

d'un apport d'énergie distribué ni de la variabilité locale des propriétés thermodynamiques induite par la combustion. En particulier, le rôle spécifique du col thermique en tant que frontière acoustique, distinct d'un col purement géométrique, n'a été que très peu analysé.

La première motivation de cette thèse est donc de combler ce manque de connaissances en proposant une étude systématique de la réponse aéroacoustique d'une tuyère à col thermique typique d'un statomixte à bas Mach. L'objectif est double :

- d'une part, caractériser la manière dont l'apport d'énergie volumique modifie la réflexion, la transmission et la conversion des ondes acoustiques et entropiques, ainsi que les régimes asymptotiques associés aux basses et hautes fréquences ;
- d'autre part, analyser le rôle spécifique du col thermique en tant que frontière acoustique dans ce type de configuration.

Une seconde motivation réside dans la nécessité de disposer d'outils de modélisation fiables mais peu coûteux, capables de reproduire les résultats de simulations numériques détaillées tout en restant utilisables dans un contexte de conception industrielle. Les simulations CFD à haute fidélité, telles que les LES ou DNS, offrent une description très fine de l'écoulement instationnaire, mais restent coûteuses et difficilement adaptables à des explorations paramétriques étendues. À l'inverse, les modèles linéaires quasi-unidimensionnels, lorsqu'ils sont correctement formulés et munis de conditions aux limites adaptées, peuvent fournir une compréhension physique claire et des tendances paramétriques robustes pour un coût numérique très réduit. Le développement et la validation d'un tel modèle dédié aux configurations à col thermique constituent ainsi un axe majeur de ce travail.

Enfin, un troisième enjeu concerne la compréhension et la quantification du bruit indirect de combustion, issu de la convection de structures entropiques multidimensionnelles dans des écoulements non uniformes. Ce bruit indirect entropique constitue une source importante de bruit et peut contribuer à l'émergence d'instabilités de combustion. Dans les configurations à col thermique, la zone chauffée et l'amorçage de l'écoulement induit introduisent des mécanismes supplémentaires de conversion acoustique–entropie, encore mal connus. L'étude de l'influence conjointe du col thermique, de la distribution de l'apport de chaleur et de la structure des inhomogénéités entropiques sur ce bruit indirect représente un aspect original de ce travail.

Le **Chapitre 1** présente les généralités sur la propulsion aérobie et les statomixtes, ainsi que les principaux mécanismes d'instabilité (instabilités de combustion, bruit indirect). Le reste du manuscrit (**Chapitres 2** à **6**) est organisé autour de la méthodologie développée et des principaux résultats, résumés ci-dessous.

En résumé, les objectifs principaux de la thèse sont :

- développer un cadre de modélisation cohérent pour la réponse aéroacoustique d'une tuyère thermiquement amorcée, incluant une condition aux limites adaptée au col thermique ;
- analyser les mécanismes de conversion acoustique–entropique et leur rôle dans l'amortissement ou l'amplification des ondes acoustiques, en particulier dans les régimes asymptotiques de basse et de haute fréquence ;
- proposer une condition aux limites adaptée au col thermique, permettant d'améliorer la prédiction des coefficients de réflexion et de transmission (acoustiques et entropiques) dans les modèles quasi-unidimensionnels d'acoustique linéaire ;
- introduire et étudier un modèle de couplage thermoacoustique fondé sur une fonction de transfert de flamme (FTF) simplifiée, afin d'identifier les configurations les plus sensibles aux instabilités ;

- fournir des critères d'évaluation de la stabilité globale (amplification maximale, indice de Rayleigh) et identifier les configurations géométriques et de flamme les plus propices au déclenchement d'instabilités.

## Outils et méthodologie (Chapitre 2)

Pour répondre à ces objectifs, une méthodologie fondée sur la complémentarité entre des simulations numériques bidimensionnelles instationnaires et une modélisation quasi-unidimensionnelle d'acoustique linéaire monoharmonique a été mise en place. Le **Chapitre 2** décrit les outils, les hypothèses de modélisation et les cas de référence utilisés dans l'ensemble de la thèse.

**Simulations numériques avec CEDRE :** La première partie de la démarche est constituée de calculs numériques réalisés avec le code de calcul CFD CEDRE de l'ONERA. Ce code résout les équations d'Euler bidimensionnelles compressibles sur des maillages non structurés et permet de modéliser des écoulements transitoires à forte variation de température et de nombre de Mach, en prenant en compte la géométrie complète de la tuyère.

Une géométrie de statomixte, simplifiée mais représentative de configurations réelles, telles que le banc JAPHAR, a été retenue. Elle comprend un diffuseur, une chambre de combustion et une tuyère divergente. Le chauffage induit par la combustion est modélisé par un terme source volumique, dont la localisation et l'intensité sont paramétrables. Cette loi de puissance est calibrée de manière à obtenir, pour différentes distributions de chaleur, des configurations stationnaires à col thermique. Afin de comparer ces configurations à col thermique à une référence plus classique, un modèle de tuyère à col géométrique équivalent, fondé sur l'équivalence du profil de nombre de Mach entre les deux types de tuyères, est proposé et validé.

Les simulations ont été utilisées pour :

- établir un ensemble de configurations à col thermique de base, en faisant varier notamment la position du col, l'intensité de l'apport de chaleur, la distribution spatiale de la puissance volumique et le nombre de Mach d'entrée ;

- imposer différents types de forçages (acoustique et entropique) à l'amont de la tuyère, sous forme d'ondes planes ou de perturbations bidimensionnelles (taches entropiques circulaires ou rectangulaires) ;

- extraire les champs instationnaires de pression, vitesse, densité, température et entropie, afin de calculer les coefficients de réflexion et de transmission acoustique, ainsi que les coefficients de conversion entropie–acoustique ;

- valider les modèles analytiques et quasi-unidimensionnels développés dans les chapitres suivants, en particulier la condition limite au col thermique et les modèles asymptotiques de basse et haute fréquence.

**Modèle quasi-unidimensionnel d'acoustique linéaire :** En parallèle des simulations CFD, un modèle quasi-unidimensionnel d'acoustique linéaire a été développé. Celui-ci repose sur la linéarisation des équations d'Euler quasi-unidimensionnelles autour d'un écoulement stationnaire non uniforme, obtenu soit par un modèle stationnaire quasi-unidimensionnel, soit par projection des champs numériques CEDRE. Les variables acoustiques (pression, vitesse, densité, entropie, *etc.*) sont formulées sous forme complexe harmonique via une transformation de Fourier, ce qui permet de travailler dans le domaine fréquentiel et de caractériser la réponse du système.

Le modèle prend en compte :

- les variations spatiales locales des grandeurs d'écoulement (nombre de Mach, température, vitesse, *etc.*) et des propriétés thermodynamiques (capacité calorifique, rapport des chaleurs spécifiques $\gamma$ dépendant de la température) ;
- l'apport de chaleur distribué, modélisé par un terme source volumique dans l'équation d'énergie, pouvant représenter à la fois un chauffage stationnaire et une composante instationnaire liée aux fluctuations de flamme ;
- la propagation d'ondes acoustiques et entropiques et leur conversion en réponse acoustique dans la zone chauffée et au voisinage du col thermique ;
- un couplage thermoacoustique via une fonction de transfert de flamme (FTF) reprise du modèle cinématique de Dowling (*J. Fluid Mech.* 1999), qui relie les fluctuations de dégagement de chaleur dans l'écoulement aux fluctuations de vitesse au niveau de l'accroche-flamme avec un retard et un filtrage fréquentiel associés à la flamme.

L'ensemble des équations linéarisées est reformulé sous la forme d'un système différentiel de premier ordre pour un vecteur d'état, résolu numériquement par un schéma de Runge–Kutta explicite d'ordre quatre. Une procédure d'itération de type Newton–Raphson est utilisée pour assurer la régularité de la solution au niveau du col critique. Les conditions limites en entrée et en sortie sont formulées en termes d'ondes incidentes et réfléchies, ce qui permet de définir naturellement des coefficients de réflexion, de transmission et de génération de bruit entropique. Une nouvelle condition aux limites associée au col thermique est également proposée.

**Analyse du bruit indirect et structures entropiques :** Enfin, le **Chapitre 2** introduit le cadre méthodologique pour l'étude du bruit indirect : injection d'inhomogénéités d'entropie unidimensionnelles (ondes planes) ou bidimensionnelles (spots entropiques), configuration numérique, et modèles 1D de référence permettant de comparer les résultats thermiquement amorcés à ceux de tuyères géométriques isentropiques.

## Principaux résultats (Chapitres 3 à 6)

### Chapitre 3 - Réponse aéroacoustique d'une tuyère thermiquement amorcée

Le **Chapitre 3** est consacré à la caractérisation de la réponse aéroacoustique d'une tuyère thermiquement amorcée, soumise à un forçage acoustique ou entropique monoharmonique d'onde plane en entrée. Les simulations CFD menées sur plusieurs configurations de col (géométrique ou thermique, plus ou moins éloigné de la chambre de combustion) montrent que le comportement de la tuyère diffère sensiblement de celui d'une tuyère géométrique, en particulier dans le régime des très basses fréquences.

Aux basses fréquences, l'un des résultats marquants est la forte atténuation du coefficient de réflexion acoustique, qui ne tend plus vers le modèle isentropique proposé par Marble et Candel (*J. Sound Vib.* 1977). Cette atténuation s'explique par la conversion partielle de l'onde acoustique incidente en fluctuations entropiques lors de sa convection dans la zone chauffée. Les structures entropiques ainsi générées ne contribuent pas directement à la réflexion acoustique au col, ce qui entraîne une diminution significative de l'amplitude de l'onde qui remonte l'écoulement. Un modèle quasi-stationnaire simple, bâti sur une configuration où un col thermique est placé en fin de conduit à section constante, permet de reproduire ce comportement et de montrer que la réponse basse fréquence est essentiellement contrôlée par la puissance volumique apportée par la région chauffée.

La position et l'intensité de l'apport thermique se sont révélées jouer un rôle important sur l'amplitude du coefficient de réflexion acoustique, notamment à basses fréquences. Lorsque le

col thermique est situé dans la partie divergente de la tuyère, une modification de sa position modifie le profil de Mach et la distribution de température, ce qui se répercute sur les mécanismes de conversion acoustique–entropie. La comparaison avec les résultats du modèle quasi-unidimensionnel (présenté au **Chapitre 4**), utilisant la nouvelle condition au col thermique, confirme ces tendances et valide la capacité du modèle réduit à reproduire les effets de la zone chauffée.

Aux hautes fréquences, en revanche, toutes les configurations étudiées (géométriques ou thermiques) tendent asymptotiquement vers un régime de radiation acoustique d'onde simple, analogue à celui d'un conduit isentropique à section constante. Le coefficient de réflexion décroît, la contribution entropique devient négligeable et l'onde transmise devient prépondérante (l'onde acoustique réfléchie est de plus en plus faible). La fréquence à partir de laquelle ce régime est atteint dépend toutefois de la régularité du profil de Mach stationnaire : des gradients non lisses, en particulier au voisinage du col thermique, retardent l'apparition de ce comportement asymptotique.

### Chapitre 4 - Modèle quasi-unidimensionnel d'acoustique linéaire et condition limite au col thermique

Le **Chapitre 4** introduit le modèle quasi-unidimensionnel d'acoustique linéaire ainsi qu'une nouvelle condition aux limites au niveau du col thermique, qui constituent des contributions majeures de cette thèse. Ce modèle permet de reproduire et d'interpréter, pour un coût numérique réduit par rapport aux simulations CFD, les principales caractéristiques observées dans les simulations numériques.

Une première validation est menée sur des configurations sans apport de chaleur, pour lesquelles les résultats sont confrontés aux solutions analytiques de la littérature pour des tuyères géométriques isentropiques. Le modèle reproduit correctement les coefficients de réflexion et de transmission, ainsi que la transition vers le régime de radiation aux hautes fréquences, ce qui confirme sa robustesse dans le cas de référence géométrique. Ces résultats sont présentés dans l'**Annexe 3** et ont fait l'objet d'un article publié dans le *Journal of Fluid Mechanics*.

Dans un second temps, un apport d'énergie stationnaire est introduit, avec des propriétés thermodynamiques dépendant de la température. Le modèle permet alors d'analyser finement le rôle de la position du col thermique, de l'intensité de l'apport de chaleur et du nombre de Mach d'entrée sur la réponse acoustique et la conversion entropie–acoustique. Les tendances obtenues (fort amortissement à basse fréquence, convergence vers un régime de radiation à haute fréquence, sensibilité à la distribution de température) sont en bon accord avec les simulations CEDRE.

L'un des principaux résultats de ce chapitre concerne la dynamique du col thermique et la condition limite qui lui est associée. Dans les modèles classiques, le col d'une tuyère géométrique est souvent traité comme une position où les fluctuations du nombre de Mach sont nulles ($\mathrm{M}'_* = 0$). Cette hypothèse est remise en question lorsque l'amorçage de l'écoulement est induit par un apport d'énergie distribué.

En analysant les données CFD et en réalisant une étude analytique du système quasi-unidimensionnel, il est montré que la position du col thermique n'est pas fixe mais légèrement fluctuante en réponse aux perturbations issues de l'entrée. Cette mobilité induit des fluctuations du nombre de Mach non négligeables au col, y compris à basse fréquence. La prise en compte explicite de ce phénomène est indispensable pour décrire correctement la conversion entre ondes acoustiques et entropiques à proximité du col. Un modèle quasi-stationnaire pour décrire les coefficients de réflexion acoustique et entropique à basses fréquences dans le cas d'une tuyère divergente où le col thermique est positionné dans cette tuyère est proposé et validé dans l'**Annexe 2**.

Une condition limite originale est donc dérivée, reliant de manière cohérente les fluctuations

de pression, de vitesse et de densité au col. Cette condition repose sur un développement asymptotique local de l'écoulement stationnaire et sur une linéarisation des relations de conservation au voisinage du point critique. Implantée dans le modèle quasi-unidimensionnel, elle est comparée à la condition classique dans divers scénarios.

Les résultats montrent que, pour les tuyères géométriques, la nouvelle condition n'apporte qu'un gain limité en termes de prédiction des coefficients de réflexion, ce qui est cohérent avec la relative validité de l'hypothèse de non-fluctuations du col dans ce cas. En revanche, pour les tuyères thermiquement amorcées, l'amélioration est significative : la prédiction des coefficients de réflexion acoustique, de génération de bruit entropique et de transmission est sensiblement plus fidèle aux résultats CFD. En particulier, la nouvelle condition permet de capturer le fait que, dans la limite de fréquence nulle, le nombre de Mach fluctuant ne tend pas vers zéro, contrairement à ce que suggérerait une condition isentropique standard.

### Chapitre 5 - Instabilités thermoacoustiques dans une tuyère à col thermique

Le **Chapitre 5** étend le modèle quasi-unidimensionnel afin d'étudier les instabilités thermoacoustiques dans une tuyère à col thermique. Pour cela, un modèle de flamme prémélangée dans un tube est introduit, basé sur une fonction de transfert de flamme (FTF) dérivée du modèle cinématique de Dowling (*J. Fluid Mech.* 1999). Le dégagement de chaleur instationnaire est modélisé comme proportionnel aux fluctuations de vitesse localisées aux lèvres de l'accroche-flamme, retardées d'un temps caractéristique et filtrées en fréquence.

Après reformulation du système linéaire pour inclure la FTF et la nouvelle condition au col thermique, l'impact de différents paramètres sur la réponse aéroacoustique est étudié :

- la vitesse de flamme et la hauteur d'accroche-flamme, qui contrôlent le gain et la phase de la FTF ;
- la fréquence propre de la flamme, qui fixe le domaine fréquentiel dans lequel le couplage est le plus efficace.

Deux indicateurs principaux sont utilisés pour évaluer la stabilité thermoacoustique :

- l'amplification maximale de la réponse acoustique, définie comme le rapport entre le maximum du coefficient de réflexion acoustique (ou de génération entropique) et sa valeur dans une configuration de référence sans couplage de flamme ;
- l'indice de Rayleigh, calculé comme l'intégrale volumique du produit entre les fluctuations de dégagement de chaleur et les fluctuations de pression, qui permet de caractériser les fréquences de production ou de dissipation d'énergie acoustique.

Les calculs montrent que le couplage thermoacoustique peut entraîner une amplification substantielle de la réponse acoustique, en particulier pour des vitesses de flamme élevées et pour des rapports de hauteur d'accroche-flamme faibles. Ces configurations, physiquement associées à des flammes rapides et compactes, sont donc les plus susceptibles d'induire des instabilités thermoacoustiques. L'analyse de l'indice de Rayleigh permet de relier ces tendances aux mécanismes locaux de production d'énergie acoustique dans la zone chauffée et au voisinage du col thermique.

### Chapitre 6 - Bruit indirect de combustion : structures entropiques multidimensionnelles

Le **Chapitre 6** est consacré au bruit indirect lié à la convection de structures entropiques dans une tuyère thermiquement amorcée. Deux grandes familles de perturbations sont considérées : les ondes entropiques unidimensionnelles (ondes planes) et les taches entropiques bidimensionnelles.

Pour les ondes entropiques unidimensionnelles, l'analyse faite dans le **Chapitre 3** montre que la réponse acoustique reste principalement contrôlée par l'écoulement moyen et par le nombre de Mach d'entrée. L'apport thermique joue un rôle secondaire dans la mesure où la structure de l'onde reste large devant l'échelle caractéristique de la zone chauffée. Un modèle quasi-stationnaire est proposé et validé pour décrire l'amplification acoustique induite par le chauffage, mettant en évidence un comportement proche de celui d'une tuyère isentropique lorsque la fréquence tend vers zéro. Dans ce régime, le paramètre dominant est le nombre de Mach d'entrée, qui gouverne l'accélération des perturbations d'entropie à travers la zone de fort gradient de vitesse.

À l'inverse, les taches entropiques bidimensionnelles révèlent des comportements plus riches. Lorsque la taille de la tache est grande devant l'échelle de la zone chauffée, la réponse acoustique se rapproche de celle des ondes unidimensionnelles, avec une tendance quasi-stationnaire et une amplification liée à l'apport de chaleur. En revanche, pour des taches de petite taille, la réponse présente un minimum de réponse acoustique fini : contrairement aux tuyères géométriques, la génération de son n'est pas complètement linéairement proportionnelle à la quantité d'entropie injectée lorsque la taille de la tache tend vers zéro. Ce niveau minimal de bruit est une signature du chauffage volumique et de la structure particulière du col thermique, qui introduit une contribution non nulle à la génération de son.

Pour interpréter ces résultats, un modèle unidimensionnel de la littérature, initialement développé pour les tuyères géométriques, est légèrement adapté au cas thermiquement amorcé. La comparaison met en évidence que certains mécanismes de bruit indirect restent dominés par l'inertie de l'écoulement, mais que l'apport thermique introduit une contribution supplémentaire à la génération de son. Cette contribution dépend notamment de la position de l'injection entropique, du nombre de Mach d'entrée et de la localisation du col thermique. Elle ouvre des perspectives de contrôle ou d'atténuation du bruit indirect par une gestion adaptée de la distribution de chaleur et de la topologie des zones de mélange.

## Conclusions

Dans l'ensemble, les résultats de cette thèse montrent que les écoulements à col thermique présentent des comportements acoustiques profondément distincts de ceux observés dans les configurations à col géométrique. L'apport de chaleur distribué modifie simultanément la propagation stationnaire et instationnaire des ondes acoustiques et entropiques, en introduisant de nouveaux mécanismes d'amortissement acoustique, de couplage entropie–acoustique et d'instabilité d'origine thermique. Le modèle quasi-unidimensionnel développé dans ce travail, associé à la nouvelle condition aux limites au niveau du col thermique, fournit un cadre de prédiction robuste et peu coûteux pour décrire ces mécanismes sur un large domaine de conditions de fonctionnement.

Au-delà de ses apports à l'aéroacoustique, ce travail propose des éléments de compréhension physique et des outils de modélisation directement utiles au développement des futurs statomixtes, dont le fonctionnement stable repose sur une maîtrise fine des interactions entre dégagement de chaleur, col thermique et boucle de rétroaction acoustique.

Les conclusions de ce travail sont les suivantes : d'abord, un amortissement acoustique marqué à basse fréquence est mis en évidence, lié à la conversion d'ondes acoustiques en perturbations entropiques dans la zone chauffée. Malgré cet amortissement, il est montré que les configurations à col thermique tendent, aux hautes fréquences, vers un régime de radiation acoustique en onde simple similaire à celui des tuyères géométriques. Par ailleurs, un modèle quasi-unidimensionnel d'acoustique linéaire robuste a été développé, capable de prédire la réponse fréquentielle à partir de l'écoulement porteur stationnaire et de reproduire les résultats CFD sur une large gamme de configurations. Une condition aux limites originale a également été introduite au col thermique, ce qui améliore significativement la prédiction des coefficients de réflexion, de transmission et de

génération de bruit entropie–acoustique dans les écoulements chauffés.

En outre, l'influence du couplage thermoacoustique a été quantifiée au moyen d'une fonction de transfert de flamme simplifiée, ce qui met en évidence une forte sensibilité de la stabilité aux paramètres de flamme (vitesse de flamme) ainsi qu'à la géométrie de l'accroche-flamme. Enfin, l'analyse du bruit indirect pour des structures entropiques multidimensionnelles montre l'existence d'une réponse acoustique minimale non nulle propre aux configurations thermiquement amorcées, absente dans les tuyères isentropiques, soulignant le rôle spécifique du col thermique dans la génération de bruit entropie–acoustique.

## Perspectives

Pour approfondir la compréhension des instabilités de combustion dans les configurations à col thermique, plusieurs pistes de recherche se dégagent naturellement des résultats obtenus dans cette thèse. Ces perspectives visent à affiner la modélisation physique, à étendre le champ d'application des outils développés et à renforcer le lien entre simulations numériques et observations expérimentales.

### Bruit indirect et rôle des structures tourbillonnaires

Une première piste de recherche concerne l'influence de la dynamique bidimensionnelle et tridimensionnelle de l'écoulement sur la génération de bruit indirect. En particulier, la contribution des structures tourbillonnaires cohérentes à la conversion des perturbations entropiques et tourbillonnaires en ondes acoustiques reste largement inexplorée [94]. L'introduction explicite des interactions vortex–acoustique permettrait d'obtenir une description plus complète et plus réaliste des mécanismes gouvernant le bruit indirect dans les écoulements non uniformes et chauffés. Par ailleurs, l'analyse de la réponse à des perturbations entropiques ou tourbillonnaires bidimensionnelles pulsées ou périodiquement injectées offrirait une modélisation plus représentative des conditions instationnaires rencontrées dans les chambres de combustion industrielles.

### Améliorations du modèle acoustique quasi-unidimensionnel

Le modèle acoustique linéaire quasi-unidimensionnel développé dans cette thèse peut être enrichi de plusieurs façons. L'introduction de mélanges gazeux multicomposants permettrait de modéliser le bruit de composition, qui peut jouer un rôle significatif en milieu réactif, comme montré par Gentil *et al.* [84]. De même, l'intégration de cinétiques chimiques simplifiées offrirait la possibilité de représenter plus fidèlement les interactions entre chimie de la combustion et acoustique. La prise en compte d'effets visqueux et non linéaires, à la manière des travaux de Huet et Giauque [23] et Huet *et al.* [26], étendrait encore le domaine de validité du modèle, en particulier dans les régimes où l'approximation linéaire devient insuffisante (surtout à haute fréquence) ou en présence de fluctuations de dégagement de chaleur de forte amplitude.

### Vers des fonctions de transfert de flamme réalistes et un couplage thermoacoustique avancé

Une extension naturelle de ce travail consiste à implémenter des termes sources volumiques stationnaires et des fonctions de transfert de flamme (FTFs) plus réalistes pour décrire le couplage entre dégagement de chaleur instationnaire et fluctuations acoustiques. Des FTFs issues de mesures expérimentales ou extraites de simulations LES permettraient de représenter plus fidèlement le caractère dépendant de la fréquence, non linéaire et spatialement distribué de la dynamique de

flamme. De telles améliorations approfondiraient l'analyse des mécanismes d'instabilité thermoacoustique dans les configurations à col thermique et pourraient révéler des scénarios d'instabilité qui échappent aux formulations simplifiées considérées dans cette thèse. Cet aspect constitue un axe de recherche important.

### Validation expérimentale et extension à des géométries réalistes

Du point de vue applicatif, la validation expérimentale des mécanismes mis en évidence dans ce travail constitue une étape essentielle. La comparaison des prédictions du modèle quasi-unidimensionnel avec des mesures disponibles dans la littérature, telles que celles rapportées par Dessornes et Scherrer [5], permettrait de quantifier sa précision et d'en identifier les limites. En outre, l'étude de l'influence de la géométrie de la tuyère sur les réponses aéroacoustique et thermoacoustique pourrait ouvrir la voie à des stratégies d'optimisation de forme visant à réduire le risque d'instabilités dans les statomixtes à col thermique. L'extension de l'analyse à des géométries tridimensionnelles plus réalistes et à des distributions de dégagement de chaleur plus complexes rapprocherait enfin le cadre de modélisation des conditions opérationnelles rencontrées dans des systèmes propulsifs réels.

En définitive, les outils et résultats développés dans cette thèse fournissent un cadre solide pour la compréhension et la prédiction des phénomènes aéroacoustiques dans les statomixtes à col thermique. Ils constituent une base pour des travaux futurs visant à concevoir des architectures plus robustes vis-à-vis des instabilités thermoacoustiques et à optimiser la distribution de l'apport de chaleur dans les systèmes de propulsion aérobie à haute vitesse.

# List of Figures


1 Examples of ramjet-based missiles. . . . . 1
2 Sketch illustrating the complementary approaches used to understand combustion instabilities in dual-mode ramjet engine combustors. . . . . 2

1.1 Flight altitude versus flight Mach number for several airbreathing engines (adapted from Laux *et al.* [32]). The JAPHAR [5] operating range is also shown. Two dynamic-pressure isolines, corresponding to $q = \rho \mathbf{u}^2/2$, are shown: $q = 20\,\mathrm{kPa}$ and $q = 100\,\mathrm{kPa}$. . . . . 8
1.2 Sketch of the components of a simplified ramjet engine, adapted from Bouchez [9]. . . . . 10
1.3 Sketch of the components of a simplified scramjet engine, adapted from Sen *et al.* [45]. . . . . 11
1.4 Sketch of a simplified dual-mode ramjet engine incorporating a variable-geometry nozzle concept. . . . . 11
1.5 Sketch of a simplified dual-mode ramjet incorporating a thermal throat, adapted from Falempin [52]. . . . . 12
1.6 Photograph of the JAPHAR [5] rig set-up. . . . . 13
1.7 Sketch of the flow couplings occurring in typical airbreathing engines, adapted from Dowling and Mahmoudi [62]. . . . . 14
1.8 Simplified Sketch representation of thermoacoustic coupling, adapted from Candel [86]. . . . . 16

2.1 Sketch of the JAPHAR nozzle geometry used for the experiments by Dessornes and Scherrer [5]. . . . . 25
2.2 Simplified two-dimensional planar sketch of a dual-mode ramjet geometry (not to scale). . . . . 26
2.3 Sketch of the boundary conditions applied in a typical thermally-choked computational domain. A similar approach can be applied to convergent–divergent nozzle geometries. . . . . 28
2.4 Flowchart of the quasi-one-dimensional steady-state volumetric power algorithm used to position a thermal-throat within a divergent nozzle. . . . . 33
2.5 (Colour) Comparison of results from CFD and the algorithm for the same volumetric power distribution: **(a)** Heat-release-rate source term $P_v$, **(b)** Mach number M, and **(c)** static temperature $T$. . . . . 34
2.6 (Colour) Two-dimensional steady-state Mach number field M for the thermal-throat (top) and geometric-throat (bottom) choking cases obtained with the CFD solver. The sonic line is indicated (**- - -**). . . . . 35

3.1 (Colour) Volumetric power source term $P_v$ as a function of the longitudinal coordinate $x/L$ for the different choking configurations considered: $C_{1-6}$. . . 42
3.2 (Colour) Absolute relative error of the global normalised pressure fluctuations $|(\tilde{\varphi} - \tilde{\varphi}_{\text{ref}})/\tilde{\varphi}_{\text{ref}}|$ as a function of mesh size and time-step refinement. . . . . 44
3.3 Sketch of the decomposition of mono-harmonic downstream- and upstream-propagating acoustic waves and entropy waves in a thermally-choked-flow configuration. The subscripts $(_{\text{cu}})$ and $(_{\text{cd}})$ denote quantities evaluated immediately upstream and downstream of the critical throat position, respectively, where $\text{M}(\bar{x}_*) = 1$. . . . . 44
3.4 (Colour) Steady-state flow fields as a function of the normalised longitudinal coordinate $x/L$ for the four choking configurations: $C_{1-4}$. **(a)** Mach number $\bar{\text{M}}$, **(b)** static pressure $\bar{p}$, and **(c)** static temperature $\bar{T}$. Vertical lines indicate the heat-release length $\delta_*/L = 0.38$, located upstream of the critical throat ($\bar{\text{M}} \leq 1$). . . . . 48
3.5 (Colour) Acoustic-reflection coefficient, $R_a = \hat{P}^-_{\text{in}}/\hat{P}^+_{\text{in}}$: **(a)** modulus and **(b)** phase-angle, plotted as a function of the dimensionless frequency, $S_t = f\delta_*/\bar{c}_*$, for the different choking configurations, $C_{1-4}$, which share the same heat-release length, $\delta_*/L = 0.38$. Results from both numerical simulations (markers) and quasi-steady-state models ($QSS_{1-2}$, lines) are shown. . . . . 49
3.6 (Colour) Critical entropy production, $G_s = \hat{\sigma}_*/\hat{P}^+_{\text{in}}$: **(a)** modulus and **(b)** phase-angle, plotted as a function of the dimensionless frequency, $S_t = f\delta_*/\bar{c}_*$, for different choking configurations. Results from numerical simulations (markers) are shown for three thermally choked-flow configurations, $C_1$, $C_2$, and $C_3$, which share the same heat-release length, $\delta_*/L = 0.38$. . . . . 51
3.7 (Colour) Acoustic-transmission coefficient, $T_a = \hat{P}^+_{\text{out}}/\hat{\sigma}_{\text{in}}$: **(a)** modulus and **(b)** phase-angle, plotted as a function of the dimensionless frequency, $S_t = f\delta_*/\bar{c}_*$, for the different choking configurations. Results from numerical simulations (markers) are shown for four thermally choked-flow configurations, $C_{1-4}$, which share the same heat-release length, $\delta_*/L = 0.38$. . . . . 52
3.8 (Colour) Acoustic-reflection coefficient, $R_a = \hat{P}^-_{\text{in}}/\hat{P}^+_{\text{in}}$: **(a)** modulus and **(b)** phase-angle, plotted as a function of the dimensionless frequency, $S_t = f\delta_*/\bar{c}_*$, for the different choking configurations, $C_{1,5,6}$, which share the same normalised power number, $\mathcal{P}_f = 2.80$. Results from numerical simulations (markers) are shown. . . . . 53
3.9 (Colour) Critical entropy production, $G_s = \hat{\sigma}_*/\hat{P}^+_{\text{in}}$: **(a)** modulus and **(b)** phase-angle, plotted as a function of the dimensionless frequency, $S_t = f\delta_*/\bar{c}_*$, for different choking configurations, $C_{1,5,6}$, which share the same normalised power number, $\mathcal{P}_f = 2.80$. Results from numerical simulations (markers) are shown. . . . . 54
3.10 (Colour) Entropy-noise-production coefficient, $R_s = (\hat{P}^-_{\text{in}} - R_a\hat{P}^+_{\text{in}})/\hat{\sigma}_{\text{in}}$: **(a)** modulus and **(b)** phase-angle, plotted as a function of the dimensionless frequency, $S_t = f\delta_*/\bar{c}_*$, for the different choking configurations, $C_{1-4}$, which share the same heat-release length, $\delta_*/L = 0.38$. Results from both numerical simulations (markers) and quasi-steady-state models ($QSS_{1-2}$, lines) are shown. 55
3.11 (Colour) Entropy-noise-production coefficient, $R_s = (\hat{P}^-_{\text{in}} - R_a\hat{P}^+_{\text{in}})/\hat{\sigma}_{\text{in}}$: **(a)** modulus and **(b)** phase-angle, plotted as a function of the dimensionless frequency, $S_t = f\delta_*/\bar{c}_*$, for the different choking configurations, $C_{1,5,6}$, which share the same normalised power number, $\mathcal{P}_f = 2.80$. Results from numerical simulations (markers) are shown. . . . . 56

3.12 (Colour) Entropy-noise-transmission coefficient $T_s = \hat{P}^+_{\text{out}}/\hat{\sigma}_{\text{in}}$ (**(a)**: modulus, **(b)**: phase-angle) plotted as a function of the dimensionless frequency, $S_t = f\delta_*/\bar{c}_*$, for different choking configurations, $\text{C}_{1-4}$, which share the same heat-release length, $\delta_*/L = 0.38$. Results from both numerical simulations (markers) and quasi-steady-state models ($\text{QSS}_{1-2}$, lines) are shown. . . . . 57

3.13 (Colour) Mach-number fluctuations normalised by the static pressure fluctuations $\hat{\text{M}}_*/\hat{P}_*$: **(a)** modulus and **(b)** phase-angle at the steady critical-throat position, plotted as a function of the dimensionless frequency, $S_t = f\delta_*/\bar{c}_*$, for several choking configurations, $\text{C}_{1-6}$. The high-frequency asymptotic isentropic behaviour (●) is shown for the geometric-throat configuration. . . . . 58

3.14 (Colour) Mach-number fluctuations normalised by the entropy fluctuations $\hat{\text{M}}_*/\hat{\sigma}_*$: **(a)** modulus and **(b)** phase-angle at the steady critical-throat position, plotted as a function of the dimensionless frequency, $S_t = f\delta_*/\bar{c}_*$, for several choking configurations, $\text{C}_{1-6}$. The high-frequency asymptotic behaviour (●) is also shown. . . . . 59

4.1 Sketch of a simplified dual-mode ramjet nozzle, with control volume $V$ bounded by the surface $\Gamma$. . . . . 64

4.2 Sketch representation of the boundary-condition treatment for a thermally choked-flow configuration. An analogous decomposition can be applied to a nozzle with a geometric throat. . . . . 71

4.3 Flowchart of the algorithm used to determine the acoustic field. . . . . 74

4.4 (Colour) Modulus **(a)** and phase-angle **(b)** of the normalised critical Mach-number fluctuations due to isentropic acoustic forcing at the inlet, $\hat{\text{M}}_*/\hat{P}_*$, as a function of the dimensionless frequency $\Omega = 2\pi f/(\text{d}\bar{u}/\text{d}x)_*$. Symbols: (○) and (□) denote CFD results for the thermal and geometric throats, respectively; (- - -) and (····) represent the corresponding results from the quasi-one-dimensional linear acoustic model (L) with the GEN boundary condition (Eq. (4.52)). Panel **(c)** shows the relative deviation between CFD and model predictions. . . . . 76

4.5 (Colour) Modulus **(a)** and phase-angle **(b)** of the normalised critical Mach-number fluctuations, $\hat{\text{M}}_*/\hat{\sigma}_*$, due to entropy forcing at the inlet, as a function of the dimensionless frequency $\Omega = 2\pi f/(\text{d}\bar{u}/\text{d}x)_*$. Symbols: (○) and (□) denote CFD results for the thermal and geometric throats, respectively; (- - -) and (····) correspond to the quasi-one-dimensional linear acoustic model (L) with the GEN boundary condition (Eq. (4.52)) for the same configurations. Panel **(c)** shows the relative deviation between CFD and linear model predictions. . 77

4.6 (Colour) Modulus **(a)** and phase-angle **(b)** of the acoustic reflection coefficient, $R_a = \hat{P}^-_{\text{in}}/\hat{P}^+_{\text{in}}$, as a function of the dimensionless frequency, $\Omega = 2\pi f/(\text{d}\bar{u}/\text{d}x)_*$. Symbols: (○) and (□) denote CFD results for the thermal and geometric throats, respectively; (- - -) and (····) correspond to the quasi-one-dimensional linear acoustic model (L) with the GEN boundary condition (Eq. (4.52)) for the same configurations. Panel **(c)** shows the relative deviation between CFD and linear model results. . . . . 78

4.7 (Colour) Modulus **(a)** and phase-angle **(b)** of the entropy-noise-production coefficient, $R_s = \hat{P}^-_{\text{in}}/\hat{\sigma}_{\text{in}}$, as a function of the dimensionless frequency, $\Omega = 2\pi f/(\mathrm{d}\bar{u}/\mathrm{d}x)_*$. Symbols: (○) and (□) denote CFD results for the thermal and geometric throats, respectively; (- - -) and (····) correspond to the quasi-one-dimensional linear acoustic model (L) with the GEN boundary condition (Eq. (4.52)) for the same configurations. Panel **(c)** shows the relative deviation between CFD and linear model results. . . . . 79

4.8 (Colour) Modulus **(a)** and phase-angle **(b)** of the acoustic transmission coefficient, $T_a = \hat{P}^+_{\text{out}}/\hat{P}^+_{\text{in}}$, plotted as a function of the dimensionless frequency, $\Omega = 2\pi f/(\mathrm{d}\bar{u}/\mathrm{d}x)_*$. Symbols: (○) and (□) denote CFD results for the thermal and geometric throats, respectively; (- - -) and (····) correspond to the quasi-one-dimensional linear acoustic model (L) with the GEN boundary condition (Eq. (4.52)) for the same configurations. Panel **(c)** shows the relative deviation between CFD and linear model results. . . . . 80

4.9 (Colour) Modulus **(a)** and phase-angle **(b)** of the entropy-noise-transmission coefficient, $T_s = \hat{P}^+_{\text{out}}/\hat{\sigma}_{\text{in}}$, plotted as a function of the dimensionless frequency, $\Omega = 2\pi f/(\mathrm{d}\bar{u}/\mathrm{d}x)_*$. Symbols: (○) and (□) denote CFD results for the thermal and geometric throats, respectively; (- - -) and (····) correspond to the quasi-one-dimensional linear acoustic model (L) with the GEN boundary condition (Eq. (4.52)) for the same configurations. Panel **(c)** shows the relative deviation between CFD and linear model results. . . . . 81

4.10 (Colour) Relative deviation between CFD and two linear acoustic models employing different critical-throat boundary conditions. $\chi^{\text{CFD}}$ denotes the CFD results, $\chi^{\text{L}}$ the predictions obtained from the linear acoustic model using either the generalised boundary condition (Eq. (4.52)), or the quasi-steady-state (QSS) boundary condition (Eq. (4.51)). The acoustic quantities considered are $\chi = [R_a, R_s, T_a, T_s]$, shown as a function of the dimensionless frequency, $\Omega = 2\pi f/(\mathrm{d}\bar{u}/\mathrm{d}x)_*$ in panels **(a)**–**(d)**, respectively. Results are presented for both choking configurations: thermal throat (- - - and - - -) and geometric throat (···· and -·-·-). . . . . 82

4.11 (Colour) Modulus of the normalised pressure fluctuations $\hat{P}$ as a function of the longitudinal position $x/L$ for a thermally choked-flow configuration, at four acoustic forcing frequencies $\Omega = [0.09, 2.62, 6.12, 10.24]$, in panels **(a)**–**(d)**, respectively. The results are obtained either from the CFD solver (——) or from the linear acoustic model using two boundary conditions: GEN (Eq. (4.52), -·-) and QSS (Eq. (4.51), - - -). . . . . 83

4.12 (Colour) Steady Mach number $\bar{\mathrm{M}}(x)$, static pressure $\bar{p}(x)$, and static temperature $\bar{T}(x)$ as a function of $x/L$ for six different inlet Mach numbers: $\mathrm{M}_{\text{in}} = 0.5$ to 0.75. . . . . 84

4.13 (Colour) Modulus **(a)** and phase-angle **(b)** of the acoustic-reflection coefficient $R_a$ as a function of the dimensionless frequency $\Omega$ for six different inlet Mach numbers: $\mathrm{M}_{\text{in}} = 0.5$ to 0.75. . . . . 85

4.14 (Colour) Modulus **(a)** and phase-angle **(b)** of the entropy-noise-production coefficient $R_s$ as a function of the dimensionless frequency $\Omega$ for six different inlet Mach numbers: $\mathrm{M}_{\text{in}} = 0.5$ to 0.75. . . . . 86

4.15 (Colour) Modulus **(a)** and phase-angle **(b)** of the acoustic-reflection coefficient, $R_a$, as a function of the dimensionless frequency $\Omega = 2\pi f/(\mathrm{d}\bar{u}/\mathrm{d}x)_*$ for the thermal-throat configuration. Results from the linear acoustic model (- - -) are shown alongside CFD results for three distinct forcing amplitudes, $\eta$: 1 % (○), 5 % (☆), and 10 % (▷). . . . . 87

4.16 (Colour) Modulus **(a)** and phase-angle **(b)** of the entropy-noise-production coefficient, $R_s$, as a function of the dimensionless frequency $\Omega = 2\pi f/(\mathrm{d}\bar{u}/\mathrm{d}x)_*$ for the thermal-throat configuration. Results from the linear acoustic model (- - -) are shown alongside CFD results for three distinct forcing amplitudes, $\eta$: 1 % (○), 5 % (☆), and 10 % (▷). . . . . 88

5.1 (Colour) Sketch of the thermoacoustic coupling introduced in the quasi-one-dimensional linear acoustic model used in this chapter. . . . . 93

5.2 (Colour) Sketch adapted from Veynante [144], showing the canonical flame configurations. . . . . 93

5.3 Flame structure in the *Statoréacteur de Recherche*, visualised by the local heat-release rate (HR), reproduced from Roux [145]. Lean and rich premixed flames coexist with a diffusion flame. . . . . 94

5.4 (Colour) Sketch of principle of the $G$-equation (Eq. (5.2)), adapted from Dowling [67]. . . . . 95

5.5 (Colour) Modulus **(a)** and phase-angle **(b)** of the acoustic-reflection coefficient $R_a$ as a function of the dimensionless frequency $\Omega = \omega/(\mathrm{d}\bar{u}/\mathrm{d}x)_*$ for a flame-holder ratio $C_{\mathrm{FH}} = 0.15$ and five flame speeds $\mathcal{S}_f \in 0.4\,\mathrm{m\,s^{-1}}$ to $1.2\,\mathrm{m\,s^{-1}}$. The solid line (—) corresponds to the configuration in which the FTF model (Eq. (5.8)) is not activated. . . . . 101

5.6 (Colour) Modulus **(a)** and phase-angle **(b)** of the entropy-noise-production coefficient $R_s$ as a function of the dimensionless frequency $\Omega = \omega/(\mathrm{d}\bar{u}/\mathrm{d}x)_*$ for a flame-holder ratio $C_{\mathrm{FH}} = 0.15$ and five flame speeds $\mathcal{S}_f \in 0.4\,\mathrm{m\,s^{-1}}$ to $1.2\,\mathrm{m\,s^{-1}}$. The solid line (—) corresponds to the configuration in which the FTF model (Eq. (5.8)) is not activated. . . . . 102

5.7 (Colour) Modulus **(a)** and phase-angle **(b)** of the acoustic-reflection coefficient $R_a$ as a function of the dimensionless frequency $\Omega = \omega/(\mathrm{d}\bar{u}/\mathrm{d}x)_*$ for a flame speed $\mathcal{S}_f = 0.75\,\mathrm{m\,s^{-1}}$ and five flame-holder ratios $C_{\mathrm{FH}} \in 0\,\%$ to $35\,\%$. The solid line (—) corresponds to the configuration in which the FTF model (Eq. (5.8)) is not activated. . . . . 103

5.8 (Colour) Modulus **(a)** and phase-angle **(b)** of the entropy-noise-production coefficient $R_s$ as a function of the dimensionless frequency $\Omega = \omega/(\mathrm{d}\bar{u}/\mathrm{d}x)_*$ for a flame speed $\mathcal{S}_f = 0.75\,\mathrm{m\,s^{-1}}$ and five flame-holder ratios $C_{\mathrm{FH}} \in 0\,\%$ to $35\,\%$. The solid line (—) corresponds to the configuration in which the FTF model (Eq. (5.8)) is not activated. . . . . 104

5.9 (Colour) Modulus of the acoustic-reflection coefficient $R_a$ **(a)** and the entropy-noise-production coefficient $R_s$ **(b)** as a function of the dimensionless flame frequency $\Omega_{\mathcal{F}}$, for a flame-holder ratio $C_{\mathrm{FH}} = 0.15$ and five flame speeds $\mathcal{S}_f \in 0.4\,\mathrm{m\,s^{-1}}$ to $1.2\,\mathrm{m\,s^{-1}}$. The acoustic dimensionless frequency $\Omega = \omega/(\mathrm{d}\bar{u}/\mathrm{d}x)_* = 1$ is also plotted as a coloured circle for comparison. . . . . 105

5.10 (Colour) Modulus of the acoustic-reflection coefficient $R_a$ **(a)** and the entropy-noise-production coefficient $R_s$ **(b)** as a function of the dimensionless flame frequency $\Omega_{\mathcal{F}}$, for a flame speed $\mathcal{S}_f = 0.75\,\mathrm{m\,s^{-1}}$ and five flame-holder ratios $C_{\mathrm{FH}} \in 0\,\%$ to $35\,\%$. The acoustic dimensionless frequency $\Omega = \omega/(\mathrm{d}\bar{u}/\mathrm{d}x)_* = 1$ is also plotted as a coloured circle for comparison. . . . . 106

5.11 (Colour) Normalised amplification ratio of the maximum acoustic response $|R_a|_{\max}/|R_a|_{\max,\mathrm{ref}}$ induced by an inlet acoustic forcing, for flame speeds $\mathcal{S}_f \in 0.4\,\mathrm{m\,s^{-1}}$ to $1.2\,\mathrm{m\,s^{-1}}$ and flame-holder ratios $C_{\mathrm{FH}} \in 0\,\%$ to $35\,\%$. The reference value corresponds to the configuration without the FTF model. . . . . 108

5.12 (Colour) Normalised amplification ratio of the maximum acoustic response $|R_s|_{\max}/|R_s|_{\max,\mathrm{ref}}$ induced by an inlet entropy forcing, for flame speeds $\mathcal{S}_f \in 0.4\,\mathrm{m\,s^{-1}}$ to $1.2\,\mathrm{m\,s^{-1}}$ and flame-holder ratios $C_{\mathrm{FH}} \in 0\,\%$ to $35\,\%$. The reference value corresponds to the configuration without the FTF model. . . . . 109

5.13 (Colour) Rayleigh index $R_I$ (Eq. (5.17)) induced by an inlet acoustic forcing, for flame speeds $\mathcal{S}_f \in 0.4\,\mathrm{m\,s^{-1}}$ to $1.2\,\mathrm{m\,s^{-1}}$ and flame-holder ratios $C_{\mathrm{FH}} \in 0\,\%$ to $35\,\%$. . . . . 110

5.14 (Colour) Non-dimensional flame frequency $\Omega_{\max}$ at which the maximum Rayleigh index occurs $R_I$ as a function of the flame speed $\mathcal{S}_f$ and the flame-holder ratio $C_{\mathrm{FH}}$. . . . . 111

6.1 Sketch of the entropy-spot injection methodology. A similar procedure is used for entropy-slug injection. . . . . 116

6.2 Example of entropy perturbations injection into a thermally choked-flow nozzle: **(a)**: Entropy spot of normalised sized $r_{\mathrm{s}}/y_* = 0.2$ and **(b)** entropy slug of normalised sized $w_{\mathrm{s}}/y_* = 0.2$. The injection centre is located at the centre of the inlet duct in the transverse direction, *i.e.*, $y_0 = y_{\mathrm{in}}/2$. . . . . 116

6.3 (Colour) Absolute relative error of the maximum upstream-propagating acoustic response induced by the injection of a circular entropy perturbation of radius $r_{\mathrm{s}}/y_* = 2 \times 10^{-1}$. . . . . 117

6.4 Two-dimensional normalised fields of entropy (top) and pressure (bottom) fluctuations at four different time instants **(a)**–**(d)** in a thermally choked flow, for a normalised entropy-spot size of $r_{\mathrm{s}}/y_* = 0.25$. The red arrow indicates the circular entropy spot. The green vertical dotted line indicates the onset of the divergent section (and of the heated region), while the red vertical dashed line indicates the steady thermal throat position. . . . . 120

6.5 (Colour) Maximum normalised acoustic response, $|P^-_{\max}/\sigma_{\max}|$, induced by three types of entropy forcing: a one-dimensional planar wave (·●·), a two-dimensional spot (·■·), and a two-dimensional slug (·★·), as a function of the equivalent Strouhal number $S_{t,\mathrm{eq}}$ in a thermally choked nozzle. . . . . 122

6.6 (Colour) Acoustic response $|p'_{\max}|_{\mathrm{CFD}}$ induced by a circular entropy spot of normalised size $r_{\mathrm{s}}/y_*$. The response is normalised, on the left, by the point-mass model $|p'_{\max}|_{\mathrm{PM}}$ (Eq. (6.7), filled markers) and, on the right, by the quasi-steady (QSS) model $|p'_{\max}|_{\mathrm{QSS}}$ (Eq. (6.6), empty markers). Results are shown for the thermally choked configuration (PM: ·■·, QSS: ·⊡·) and the geometrically choked configuration (PM: ·▲·, QSS: ·△·). . . . . 123

6.7 (Colour) Acoustic response $|p'_{\max}|_{\mathrm{CFD}}$ induced by a rectangular entropy slug of normalised size $w_{\mathrm{s}}/y_*$. The response is normalised, on the left, by the point-mass model $|p'_{\max}|_{\mathrm{PM}}$ (Eq. (6.7), filled markers) and, on the right, by the quasi-steady (QSS) model $|p'_{\max}|_{\mathrm{QSS}}$ (Eq. (6.6), empty markers). Results are shown for the thermally choked configuration (PM: ·★·, QSS: ·☆·) and the geometrically choked configuration (PM: ·▼·, QSS: ·▽·). . . . . 125

6.8 (Colour) Acoustic response $|p'_{\max}|_{\mathrm{CFD}}$ induced by a circular entropy spot of normalised size $r_s/y_*$. The response is normalised, on the left, by the point-mass (PM) model $|p'_{\max}|_{\mathrm{PM}}$ (Eq. (6.7), filled markers) and, on the right, by the quasi-steady-state (QSS) model $|p'_{\max}|_{\mathrm{QSS}}$ (Eq. (6.6), empty markers). Results are shown for a thermally choked configuration at three transverse injection positions: $y_0 = 0$ (PM: ·■·, QSS: ·⊡·), $y_0 = y_{\mathrm{in}}/2$ (PM: ·▶·, QSS: ·▷·), and $y_0 = y_{\mathrm{in}}$ (PM: ·◀·, QSS: ·◁·). . . . . 126

6.9 (Colour) Acoustic response $|p'_{\max}|_{\mathrm{CFD}}$ induced by a circular entropy spot of normalised size $r_s/y_*$. The response is normalised, on the left, by the point-mass (PM) model $|p'_{\max}|_{\mathrm{PM}}$ (Eq. (6.7), filled markers) and, on the right, by the quasi-steady-state (QSS) model $|p'_{\max}|_{\mathrm{QSS}}$ (Eq. (6.6), empty markers). Results are shown for a thermally choked configuration at three steady thermal throat positions: $\delta_*/L = 0.32$ (PM: ·▶·, QSS: ·▷·), $\delta_*/L = 0.38$ (PM: ·■·, QSS: ·⊡·), and $\delta_*/L = 0.44$ (PM: ·◀·, QSS: ·◁·). . . . . 127

6.10 (Colour) Acoustic response $|p'_{\max}|_{\mathrm{CFD}}$ induced by a circular entropy spot of normalised size $r_s/y_*$. The response is normalised, on the left, by the point-mass (PM) model $|p'_{\max}|_{\mathrm{PM}}$ (Eq. (6.7), filled markers) and, on the right, by the quasi-steady-state (QSS) model $|p'_{\max}|_{\mathrm{QSS}}$ (Eq. (6.6), empty markers). Results are shown for a thermally choked configuration at three inlet Mach numbers: $\mathrm{M}_{\mathrm{in}} = 0.5$ (PM: ·▶·, QSS: ·▷·), $\mathrm{M}_{\mathrm{in}} = 0.6$ (PM: ·■·, QSS: ·⊡·), and $\mathrm{M}_{\mathrm{in}} = 0.7$ (PM: ·◀·, QSS: ·◁·). . . . . 128

C.1 (Colour) Normalised cross-sectional area $\mathrm{A}/\mathrm{A}_*$ **(a)** and Mach number M **(b)** of the original nozzle geometry from Goh and Morgans [20] (- - -), plotted against the normalised longitudinal coordinate, $\xi = x/L$. The critical choked-throat position $\xi_*$ is also indicated. . . . . 151

C.2 (Colour) Normalised cross-sectional area, $\mathrm{A}/\mathrm{A}_*$ **(a)**, and Mach number, M **(b)**, of the smoothed nozzle geometry from Goh and Morgans [20] (····), plotted against the normalised longitudinal coordinate, $\xi = x/L$. The critical-throat position $\xi_*$ is also indicated. . . . . 152

C.3 Sketch of the generic axisymmetric nozzle geometry proposed by Bell *et al.* [163]. . . . . 152

C.4 (Colour) Normalised cross-sectional area $\mathrm{A}/\mathrm{A}_*$ **(a)** and Mach number M **(b)** of the nozzle geometry from Bell *et al.* [163] (—), plotted against the normalised longitudinal coordinate, $\xi = x/L$. The critical-throat position $\xi_*$ is also indicated. . . . . 153

C.5 (Colour) Modulus $|\hat{\mathrm{M}}_*/\hat{P}_*|$ **(a)**, phase-angle $\arg[\hat{\mathrm{M}}_*/\hat{P}_*]$ **(b)**, and relative deviation $|1-\hat{\mathrm{M}}_*^{\mathrm{IS}}/\hat{\mathrm{M}}_*^{\mathrm{CFD}}|$ **(c)** of the normalised critical Mach-number fluctuations, comparing numerical results $\hat{\mathrm{M}}_*^{\mathrm{CFD}}$ (markers) and analytical results $\hat{\mathrm{M}}_*^{\mathrm{IS}}$ (—, Eq. (C.8)), as a function of the dimensionless frequency, $\Omega = 2\pi f/(\mathrm{d}\bar{u}/\mathrm{d}x)_*$. Results are shown for three nozzle geometries: Bell *et al.* [163] (●), the original geometry of Goh and Morgans [20] (■), and the smoothed version of Goh and Morgans [20] (★). . . . . 155

C.6 (Colour) Modulus of the acoustic pressure fluctuations, $|\hat{p}(x)/\hat{p}_{\mathrm{in}}|$ (**(a)** and **(c)**), as a function of the streamwise position, $\xi = x/L$, for two distinct frequencies, $\Omega = 1$ and $\Omega = 6$. The solution is obtained from the quasi-one-dimensional linear acoustic model (Chap. 4) using either the IS (Eq. (C.5), - - -) or QSS (Eq. (C.3), ····) boundary condition. The relative deviation, $|1-\hat{p}^{\mathrm{QSS}}/\hat{p}^{\mathrm{IS}}|$ (**(b)** and **(d)**, —), between the two boundary-condition solutions is also shown. . . . . 156

C.7 (Colour) Modulus $|R_a|$ **(a)** and phase-angle $\arg[R_a]$ **(b)** of the acoustic-reflection coefficient $R_a$, plotted as a function of the dimensionless frequency, $\Omega = 2\pi f/(\mathrm{d}\bar{u}/\mathrm{d}x)_*$. Results from CFD (markers) and the quasi-one-dimensional linear acoustic model using the IS boundary condition (lines) are shown for each nozzle geometry: Bell *et al.* [163] (●, —), the original geometry of Goh and Morgans [20] (■, - - -), and the smoothed version of Goh and Morgans [20] (★, ····). Subfigure **(c)** shows the relative deviation between the quasi-one-dimensional linear acoustic model using the IS boundary condition (Eq. (C.5)) and that using the QSS boundary condition (Eq. (C.3)). . . . . 157

C.8 (Colour) Modulus $|T_a|$ **(a)** and phase-angle $\arg[T_a]$ **(b)** of the acoustic-transmission coefficient, $T_a$, plotted as a function of the dimensionless frequency, $\Omega = 2\pi f/(\mathrm{d}\bar{u}/\mathrm{d}x)_*$. Results from CFD simulations (markers) and the quasi-one-dimensional linear acoustic model using the IS boundary condition (lines) are shown for each nozzle geometry: Bell *et al.* [163] (●, —), the original geometry of Goh and Morgans [20] (■, - - -), and the smoothed version of Goh and Morgans [20] (★, ····). Subfigure **(c)** shows the relative deviation between the quasi-one-dimensional linear acoustic model using the IS boundary condition (Eq. (C.5)) and that using the QSS boundary condition (Eq. (C.3)). . . . . 158

C.9 (Colour) Real part $\mathrm{Re}(Y)$ **(a)** and imaginary part $\mathrm{Im}(Y)$ **(b)** of the acoustic admittance $Y$ Eq. (C.14), plotted as a function of the dimensionless frequency, $S = 2\pi f\, r_\mathrm{c}/\bar{c}_\mathrm{in}$ for the nozzle geometry of Bell *et al.* [163]. The corresponding alternative dimensionless frequency $\Omega = 2\pi f/(\mathrm{d}\bar{u}/\mathrm{d}x)_*$ is indicated at the top of the graph. Results from CFD simulations (●) and from the quasi-one-dimensional linear acoustic model using either the IS boundary condition (- - ·) or the QSS boundary condition (····) are shown. The relative deviation between the IS ($Y^\mathrm{IS}$) and QSS ($Y^\mathrm{QSS}$) boundary conditions is presented in subfigure **(c)**. . . . . 159

D.1 Sketch of the geometric-throat configuration from Elbakly [159], featuring a rectangular channel with a sharp-angled inlet nozzle. . . . . 162

D.2 Normalised cross-sectional height $y/y_\mathrm{in}$ of the nozzle geometry from Elbakly [159] (—), plotted against the normalised longitudinal coordinate $x/y_\mathrm{in}$. The contraction ratio $y_*/y_\mathrm{in}$ and the length ratio $\delta_*/y_\mathrm{in}$ are also indicated. . . . . 164

D.3 (Colour) Two-dimensional steady-state Mach number field obtained from the nozzle geometry of Elbakly [159]. . . . . 164

D.4 (Colour) Steady-state Mach number $\bar{\mathrm{M}}$ **(a)**, static pressure $\bar{p}$ **(b)**, and static temperature $\bar{T}$ **(c)** profiles, as a function of the dimensionless position, $x/L$. . 165

D.5 Sketch of the downstream- and upstream-propagating acoustic waves generated by the convection of a small pressure perturbation $\Delta p$ in an isentropic geometric-throat nozzle, adapted from Elbakly [159]. . . . . 167

D.6 (Colour) Normalised acoustic response induced by a circular entropy spot of radius $r_\mathrm{s}$ for the nozzle geometry of Elbakly [159]. The acoustic response (CFD) is normalised either by the quasi-steady-state model (QSS: Eq. (D.9), ■) or by the point-mass model (PM: Eq. (D.20), □). The results of Elbakly [159] are also shown (QSS: ●, PM: ○). . . . . 169

# List of Tables


2.1 Air isobaric heat capacity coefficients $\alpha_n$ in $\mathrm{J\,kg^{-1}\,K^{-1}}$ (rounded to $10^{-4}$). . . 24
2.2 Maximum inlet capacities of the ATD 5 test cell, adapted from Dessornes and Scherrer [5]. . . . 24
2.3 Nozzle-inlet conditions corresponding to a flight Mach number of $\mathrm{M} = 3$. . . . 26
2.4 Inlet boundary conditions used to inject downstream-propagating waves. . . . 27

3.1 Presentation of the different choking configurations. . . . 39
3.2 Presentation of the different aero-acoustic coefficients. . . . 45
3.3 Presentation of the two quasi-steady-state analytical models for the acoustic coefficients. . . . 47

B.1 Quasi-steady acoustic-reflection coefficient $R_a$ for three choking configurations (GEO, UNI, THT). Results are reported from CFD simulations ($R_{a,\mathrm{CFD}}$) and from quasi-steady models ($R_{a,\mathrm{MC}}$: Marble and Candel [16]; $R_{a,\mathrm{UNI}}$: Eq. (3.19); $R_{a,\mathrm{GEN}}$: Eq. (B.12)). Values in parentheses indicate the absolute relative error (in %) with respect to the CFD predictions. . . . 145
B.2 Quasi-steady entropy-noise-production coefficient $R_s$ for three choking configurations (GEO, UNI, THT). Results are obtained from CFD simulations ($R_{s,\mathrm{CFD}}$) and from quasi-steady models ($R_{s,\mathrm{MC}}$: Marble and Candel [16]; $R_{s,\mathrm{UNI}}$: Eq. (3.20); $R_{s,\mathrm{GEN}}$: Eq. (B.13)). Values in parentheses indicate the absolute relative error (in %) with respect to the CFD results. . . . 145

# Nomenclature

**Abbreviations**

| | |
|---|---|
| CEDRE | Calcul d'Écoulements Diphasiques Réactifs pour l'Énergétique |
| CFD | Computational Fluid Dynamics |
| CHARME | Solveur des écoulements compressibles multifluides, réactifs, turbulents |
| DNS | Direct Numerical Simulation |
| FDF | Flame Description Function |
| FTF | Flame Transfer Function |
| JAPHAR | Joint Airbreathing Propulsion for Hypersonic Aircraft Research |
| LES | Large Eddy Simulation |
| ONERA | Office National d'Études et de Recherches Aérospatiales |
| PREPHA | Programme de REcherche sur la Propulsion Hypersonique Avancée |
| QSS | Quasi-Steady State |
| RANS | Reynolds-Averaged Navier-Stokes |
| URANS | Unsteady Reynolds-Averaged Navier-Stokes |

**Universal Constants**

| | | |
|---|---|---|
| $\mathcal{R}$ | Universal gas constant ($\approx 8.3145\,\mathrm{J\,mol^{-1}\,K^{-1}}$) | $[\mathrm{J\,mol^{-1}\,K^{-1}}]$ |

**Greek**

| | | |
|---|---|---|
| $\alpha$ | Cross-sectional area variation ($= (\mathrm{dA}/\mathrm{d}x)\,/\mathrm{A}$) | [-] |
| $\Delta t$ | Time step | [s] |
| $\Delta x$ | Longitudinal mesh size | [m] |
| $\Delta y$ | Transverse mesh size | [m] |
| $\delta_*$ | Heat-release-rate length ($= x_* - x_\mathrm{u}$) | [m] |
| $\dot{\omega}_T$ | Chemical heat-release rate | $[\mathrm{J\,s^{-1}\,m^{-3}}]$ |

| | | |
|---|---|---|
| $\eta$ | Normalised fluctuations amplitude | [-] |
| $\gamma$ | Ratio of the heat capacities ($= c_p/c_v$) | [-] |
| $\kappa$ | Heat capacity ratio variation $\left(= (\mathrm{d}\gamma/\mathrm{d}T)/\gamma\right)$ | [-] |
| | Heat capacity variation $\left(= (\mathrm{d}c_p/\mathrm{d}T)/c_p\right)$ | [-] |
| $\Lambda$ | Critical-to-inlet area ratio ($= \mathrm{A}_*/\mathrm{A}_{\mathrm{in}}$) | [-] |
| $\mu$ | Dynamic viscosity | [Pa s] |
| $\Omega$ | Dimensionless frequency ($= 2\pi f/(\mathrm{d}\bar{u}/\mathrm{d}x)_*$) | [-] |
| $\omega$ | Angular frequency ($= 2\pi f$) | [$\mathrm{s}^{-1}$] |
| $\Omega_{\mathcal{F}}$ | Dimensionless flame frequency (Eq. (5.9)) | [-] |
| $\rho$ | Density | [$\mathrm{kg\,m}^{-3}$] |
| $\sigma$ | Normalised entropy fluctuations ($= s'/c_p$) | [-] |
| $\tau$ | Time delay | [s] |

**Latin**

| | | |
|---|---|---|
| A | Cross-sectional area | [$\mathrm{m}^2$] |
| $\dot{m}$ | Mass-flow rate ($= \rho u\mathrm{A}$) | [$\mathrm{kg\,s}^{-1}$] |
| i | Imaginary unit ($= \sqrt{-1}$) | |
| M | Mach number ($= u/c$) | [-] |
| $\mathbf{n}$ | Outer normal vector ($= (n_x,n_y,n_z)$) | |
| $\mathcal{F}$ | Flame function (Eq. (5.8)) | [-] |
| $\mathcal{P}_f$ | Normalised flame-power number (Eq. (3.1)) | [-] |
| $\mathcal{S}_f$ | Flame speed | [$\mathrm{m\,s}^{-1}$] |
| $\mathcal{W}$ | Molar mass of the gas | [$\mathrm{kg\,mol}^{-1}$] |
| $\mathbf{u}$ | Velocity vector ($= (u,v,w)$) | [$\mathrm{m\,s}^{-1}$] |
| $c$ | Sound speed ($= \sqrt{\gamma r T}$) | [$\mathrm{m\,s}^{-1}$] |
| $C_r$ | Contraction ratio ($= (1 - 1/\Lambda)/2$) | [-] |
| $C_{\mathrm{FH}}$ | Flame-holder height ratio ($= y_{\mathrm{FH}}/y_{\mathrm{inj}}$) | [-] |
| $D$ | Normalised density fluctuations ($= \rho'/\bar{\rho}$) | [-] |
| $e$ | Specific internal energy ($= h - p/\rho + u^2/2$) | [$\mathrm{J\,kg}^{-1}$] |
| $f$ | Frequency | [$\mathrm{s}^{-1}$] |
| $G_s$ | Entropy-production coefficient | [-] |

| | | |
|---|---|---|
| $h$ | Specific enthalpy | $[\mathrm{J\,kg^{-1}}]$ |
| $k$ | Wave number ($= \omega/\bar{c}$) | $[\mathrm{m^{-1}}]$ |
| $L$ | Nozzle length | [m] |
| $P$ | Normalised pressure fluctuations ($= p'/(\bar{\gamma}\bar{p})$) | [-] |
| $p$ | Pressure | [Pa] |
| $P_v$ | Volumetric power source term | $[\mathrm{J\,s^{-1}\,m^{-3}}]$ |
| $q$ | Instantaneous heat release | $[\mathrm{J\,kg^{-1}}]$ |
| $r$ | Specific gas constant ($= \mathcal{R}/\mathcal{W}$) | $[\mathrm{J\,K^{-1}\,kg^{-1}}]$ |
| $R_a$ | Acoustic-reflection coefficient | [-] |
| $R_I$ | Rayleigh index (Eq. (5.17)) | [-] |
| $R_s$ | Entropy-noise-production coefficient | [-] |
| $r_s$ | Entropy-non-uniformity characteristic size | [m] |
| $s$ | Entropy | $[\mathrm{J\,K^{-1}}]$ |
| $S_t$ | Strouhal number ($= f\delta_*/\bar{c}_*$) | [-] |
| $T$ | Temperature | [K] |
| $t$ | Time | [s] |
| $T_a$ | Acoustic-transmission coefficient | [-] |
| $T_s$ | Entropy-noise-transmission coefficient | [-] |
| $U$ | Normalised velocity fluctuations ($= u'/\bar{u}$) | [-] |
| $V$ | Control volume | $[\mathrm{m^3}]$ |
| $x$ | Longitudinal position | [m] |
| $Y$ | Acoustic admittance ($= 1/Z$) | [-] |
| $y$ | Transverse position | [m] |
| $Z$ | Acoustic impedance ($= (1 + R_a)/(1 - R_a)$) | [-] |
| CFL | Courant-Friedrichs-Lewy number ($= u_{\mathrm{ref}}\Delta t/\Delta x$) | [-] |

**Mathematical Operators**

| | |
|---|---|
| $\mathrm{D}/\mathrm{D}t$ | Material derivative ($= \partial/\partial t + u\,\partial/\partial x$) |
| $\nabla$ | Nabla |
| $\otimes$ | Dyadic product |

**Subscripts and Superscripts**

| | |
|---|---|
| $()'$ | Fluctuating quantity |
| $()^{+}$ | Downstream-propagating quantity |
| $()^{-}$ | Upstream-propagating quantity |
| $()_{*}$ | Critical-throat quantity |
| $()_{0}$ | Total quantity |
| $()_{\mathrm{in}}$ | Inlet |
| $()_{\mathrm{is}}$ | Isentropic quantity |
| $()_{\mathrm{ref}}$ | Reference value |
| $()_{\mathrm{out}}$ | Outlet |
| $()_{\mathrm{cd}}$ | Critical-downstream position |
| $()_{\mathrm{cu}}$ | Critical-upstream position |
| $()_{\mathrm{FH}}$ | Flame-holder quantity |
| $()_{\mathrm{u}}$ | Upstream |
| $\bar{()}$ | Steady-state quantity |
| $\hat{()}$ | Complex amplitude of the Fourier transform |

# References


[1] P. Jackson. *Le Seigneur des anneaux: Le Retour du roi (Film)*. 2003 (cit. on p. v).

[2] A. Astier. *Kaamelott (TV show)*. 2005 (cit. on pp. v, ix, 1, 7, 37, 61, 91, 113, 131, 147, 161, 171).

[3] Wikipédia. *Air-sol moyenne portée amélioré*. Version ID 228603355. 2025 (cit. on p. 1).

[4] W. Heiser, D. Pratt, D. Daley, and U. Mehta. *Hypersonic airbreathing propulsion*. AIAA, 1994. ISBN: 9781563470356. DOI: 10.2514/4.470356 (cit. on pp. 2, 12, 30, 40).

[5] O. Dessornes and D. Scherrer. "Tests of the JAPHAR dual-mode ramjet engine". In: *Aerosp. Sci. Technol.* 9.3 (2005), pp. 211–221. ISSN: 1270-9638. DOI: 10.1016/j.ast.2005.01.007 (cit. on pp. 2, 8, 12, 13, 24, 25, 40, 134, 179, 181, 189).

[6] T. Poinsot. "Prediction and control of combustion instabilities in real engines". In: *Proc. Combust. Inst.* 36.1 (2017), pp. 1–28. ISSN: 1540-7489. DOI: 10.1016/j.proci.2016.05.007 (cit. on p. 2).

[7] J. Crump, K. Schadow, V. Yang, and F. Culick. "Longitudinal combustion instabilities in ramjet engines: Identification of acoustic modes". In: *J. Propul. Power* 2.2 (1986), pp. 105–109. ISSN: 0748-4658. DOI: 10.2514/3.22852 (cit. on pp. 2, 12).

[8] A. Morgans and D. Yang. "Thermoacoustic instability in combustors". In: *Annu. Rev. Fluid Mech.* 57.1 (2024), pp. 9–33. ISSN: 0066-4189. DOI: 10.1146/annurev-fluid-121021-032828 (cit. on pp. 2, 12).

[9] M. Bouchez. "Statoréacteur: Propulsion aérobie moyenne ou grande vitesse". In: *Techniques de l'ingénieur* (2012). DOI: 10.51257/a-v1-bm3020 (cit. on pp. 2, 9–11, 181).

[10] A. Roux, L. Gicquel, S. Reichstadt, N. Bertier, G. Staffelbach, F. Vuillot, and T. Poinsot. "Analysis of unsteady reacting flows and impact of chemistry description in large eddy simulations of side-dump ramjet combustors". In: *Combust. Flame* 157.1 (2010), pp. 176–191. ISSN: 0010-2180. DOI: 10.1016/j.combustflame.2009.09.020 (cit. on pp. 2, 29, 96, 114).

[11] E. Bekaert. "Dynamique complexe d'écoulements dans les statoréacteurs instables par simulation numérique". Ph.D. thesis. Université de Toulouse, 2025. URL: http://www.theses.fr/2025TLSES076 (cit. on pp. 2, 23).

[12] V. Yang. "Pressure oscillations in liquid-fueled ramjet engines". Ph.D. thesis. California Institute of Technology, 1984 (cit. on p. 2).

[13] F. Culick and T. Rogers. "Modeling pressure oscillations in ramjets". In: *Proceedings of the AIAA/SAE/ASME 16th Joint Propulsion Conference*. Hatford, United States of America, Jan. 1980. URL: https://www.researchgate.net/publication/48925520 (cit. on p. 2).

[14] F. Culick and T. Rogers. "The response of normal shocks in diffusers". In: *AIAA J.* 21.10 (1983), pp. 1382–1390. ISSN: 0001-1452. DOI: 10.2514/3.60147 (cit. on pp. 2, 21).

[15] F. Culick. "Combustion instabilities in liquid-fueled propulsion systems: An overview". In: *Proceedings of the AGARD Conference*. Vol. 450. Jan. 1988, pp. 1–73. URL: https://www.researchgate.net/publication/48926169 (cit. on pp. 2, 12, 16, 17).

[16] F. Marble and S. Candel. "Acoustic disturbance from gas non-uniformities convected through a nozzle". In: *J. Sound Vib.* 55.2 (1977), pp. 225–243. ISSN: 0022-460X. DOI: 10.1016/0022-460X(77)90596-X (cit. on pp. 3, 12, 17, 21, 32, 46, 47, 49, 50, 57, 63, 64, 72, 85, 118, 119, 143–146, 148, 160, 167, 171, 189).

[17] L. Crocco. "Aspects of combustion stability in liquid propellant rocket motors. Part I: Fundamentals. Low frequency instability with monopropellants". In: *J. Am. Rocket Soc.* 21.6 (1951), pp. 163–178. ISSN: 1936-9964. DOI: 10.2514/8.4393 (cit. on pp. 3, 17).

[18] H. Tsien. "The transfer functions of rocket nozzles". In: *J. Am. Rocket Soc.* 22.3 (1952), pp. 139–143. ISSN: 1936-9964. DOI: 10.2514/8.4448 (cit. on pp. 3, 12, 47, 50, 63, 64, 73, 143, 148).

[19] S. Stow, A. Dowling, and T. Hynes. "Reflection of circumferential modes in a choked nozzle". In: *J. Fluid Mech.* 467 (2002), pp. 215–239. ISSN: 0022-1120. DOI: 10.1017/S0022112002001428 (cit. on pp. 3, 63, 70, 148).

[20] C. Goh and A. Morgans. "Phase prediction of the response of choked nozzles to entropy and acoustic disturbances". In: *J. Sound Vib.* 330.21 (2011), pp. 5184–5198. ISSN: 0022-460X. DOI: 10.1016/j.jsv.2011.05.016 (cit. on pp. 3, 150–152, 154, 155, 157, 158, 160, 187, 188).

[21] W. Moase, M. Brear, and C. Manzie. "The forced response of choked nozzles and supersonic diffusers". In: *J. Fluid Mech.* 585 (2007), pp. 281–304. ISSN: 0022-1120. DOI: 10.1017/S0022112007006647 (cit. on pp. 3, 63).

[22] I. Duran and S. Moreau. "Solution of the quasi-one-dimensional linearized Euler equations using flow invariants and the Magnus expansion". In: *J. Fluid Mech.* 723 (2013), pp. 190–231. ISSN: 0022-1120. DOI: 10.1017/jfm.2013.118 (cit. on pp. 3, 16, 17, 21, 32, 46, 63, 64, 70, 143, 148, 149, 158, 160).

[23] M. Huet and A. Giauque. "A nonlinear model for indirect combustion noise through a compact nozzle". In: *J. Fluid Mech.* 733 (2013), pp. 268–301. ISSN: 0022-1120. DOI: 10.1017/jfm.2013.442 (cit. on pp. 3, 133, 178).

[24] M. Huet. "Nonlinear indirect combustion noise for compact supercritical nozzle flows". In: *J. Sound Vib.* 374 (2016), pp. 211–227. ISSN: 0022-460X. DOI: 10.1016/j.jsv.2016.03.028 (cit. on p. 3).

[25] A. Emmanuelli, J. Zheng, M. Huet, A. Giauque, T. Le Garrec, and S. Ducruix. "Description and application of a 2D-axisymmetric model for entropy noise in nozzle flows". In: *J. Sound Vib.* 472 (2020), p. 115163. ISSN: 0022-460X. DOI: 10.1016/j.jsv.2019.115163 (cit. on pp. 3, 4, 63).

[26] M. Huet, A. Emmanuelli, and S. Ducruix. "Influence of viscosity on entropy noise generation through a nozzle". In: *J. Sound Vib.* 510 (2021), p. 116293. ISSN: 0022-460X. DOI: 10.1016/j.jsv.2021.116293 (cit. on pp. 3, 21, 133, 178).

[27] S. Yeddula, J. Guzmán-Iñigo, and A. Morgans. "A solution for the quasi-one-dimensional linearised Euler equations with heat transfer". In: *J. Fluid Mech.* 936 (2022), R3. ISSN: 0022-1120. DOI: 10.1017/jfm.2022.101 (cit. on pp. 4, 63).

[28] S. Yeddula, J. Guzman Inigo, and A. Morgans. "Effect of steady and fluctuating heat transfer on acoustic and entropy transfer functions of a nozzle". In: *Proceedings of the 28th AIAA/CEAS Aeroacoustics Conference*. Southampton, United Kingdom, June 2022, pp. 1–12. DOI: 10.2514/6.2022-2978 (cit. on pp. 4, 21, 38, 63, 92, 93, 149).

[29] M. Huet. "Influence of calorically perfect gas assumption and thermal diffusion on indirect noise generation". In: *Proceedings of the 24th International Congress on Sound and Vibration (ICSV)*. London, United Kingdom, July 2017, pp. 1–8. DOI: 10.25144/24330 (cit. on p. 4).

[30] L. Hirschberg and S. Hulshoff. "Lumped-element model for vortex–nozzle interaction in solid rocket motors". In: *AIAA J.* 58.7 (2020), pp. 3241–3244. ISSN: 0001-1452. DOI: 10.2514/1.J058673 (cit. on pp. 4, 162).

[31] K.-C. Lin, K. Jackson, R. Behdadnia, T. Jackson, F. Ma, and V. Yang. "Acoustic characterization of an ethylene-fueled scramjet combustor with a cavity flameholder". In: *J. Propul. Power* 26.6 (2010), pp. 1161–1170. ISSN: 0748-4658. DOI: 10.2514/1.43338 (cit. on pp. 4, 17).

[32] C. Laux, J.-B. Perrin-Terrin, L. Victor, and S. Starikovskaia. "Foundations of plasma-assisted combustion. Part 2: Mechanisms and applications". In: *Plasma Sources Sci. Technol.* (2025). ISSN: 0963-0252. DOI: 10.1088/1361-6595/ae0f0f (cit. on pp. 8, 181).

[33] A. Thomas. "Some fundamental aspects of ramjet propulsion". In: *J. Jet Propuls.* 27.4 (1957), pp. 381–385. ISSN: 1936-9980. DOI: 10.2514/8.12787 (cit. on p. 9).

[34] F. Falempin and L. Serre. "French flight testing program LEA: Status in 2011". In: *Proceedings of the 17th AIAA International Space Planes and Hypersonic Systems and Technologies Conference*. San Francisco, United States of America, Apr. 2011. DOI: 10.2514/6.2011-2200 (cit. on p. 9).

[35] P. Sacher. *Engineering engine/airframe integration for fully reusable space transportation systems*. Tech. rep. RTOENAVT185. NATO, 2010 (cit. on p. 9).

[36] K. Kedia and A. Ghoniem. "The anchoring mechanism of a bluff-body stabilized laminar premixed flame". In: *Combust. Flame* 161.9 (2014), pp. 2327–2339. ISSN: 0010-2180. DOI: 10.1016/j.combustflame.2014.02.005 (cit. on p. 10).

[37] P. Waltrup, M. White, F. Zarlingo, and E. Gravlin. "History of U.S. Navy Ramjet, Scramjet, and Mixed-Cycle Propulsion Development". In: *J. Propuls. Power* 18.1 (2002), pp. 14–27. ISSN: 0748-4658. DOI: 10.2514/2.5928 (cit. on p. 10).

[38] A. Roux, L. Gicquel, Y. Sommerer, and T. Poinsot. "Large eddy simulation of mean and oscillating flow in a side-dump ramjet combustor". In: *Combust. Flame* 152.1–2 (2008), pp. 154–176. ISSN: 0010-2180. DOI: 10.1016/j.combustflame.2007.06.015 (cit. on pp. 10, 12, 20, 21, 114).

[39] F. Culick and P. Kuentzmann. *Unsteady motions in combustion chambers for propulsion systems*. Tech. rep. AC323AVT039TP103. NATO, 2006 (cit. on p. 10).

[40] D. Mejia, M. Miguel-Brebion, A. Ghani, T. Kaiser, F. Duchaine, L. Selle, and T. Poinsot. "Influence of flame-holder temperature on the acoustic flame transfer functions of a laminar flame". In: *Combust. Flame* 188 (2018), pp. 5–12. ISSN: 0010-2180. DOI: 10.1016/j.combustflame.2017.09.016 (cit. on p. 10).

[41] S. Boulal, A. Genot, J.-M. Klein, Y. Fabignon, A. Vincent-Randonnier, and V. Sabelnikov. "On the hydro-acoustic coupling responsible for the flashback limit-cycle of a premixed flame at a backward-facing step". In: *Combust. Flame* 257 (2023), p. 112999. ISSN: 0010-2180. DOI: 10.1016/j.combustflame.2023.112999 (cit. on pp. 10, 12, 13, 100).

[42] J.-M. Klein, A. Genot, A. Vincent-Randonnier, and A. Mura. "Large-eddy simulation analysis of turbulent flame periodic flashbacks in a backward-facing step (BFS) combustor". In: *Combust. Flame* 280 (2025), p. 114335. ISSN: 0010-2180. DOI: 10.1016/j.combustflame.2025.114335 (cit. on pp. 10, 13, 20, 94).

[43] I. Smith. "The effect of dissociation in rockets, ramjets, and wind tunnels". In: *Proc. Inst. Mech. Eng. Conf. Proc.* 178.8 (1963), pp. 27–32. ISSN: 0367-8849. DOI: 10.1243/PIME_CONF_1963_178_193_02 (cit. on p. 10).

[44] A. Rocamora, J. Labaune, C. Laux, and F. Tholin. "Numerical study of plasma-assisted ignition and stabilisation of a supersonic hydrogen–air combustion in LAERTE facility by a quasi-DC gliding arc". In: *Plasma Sources Sci. Technol.* 34.10 (2025), p. 105002. ISSN: 0963-0252. DOI: 10.1088/1361-6595/ae00ee (cit. on p. 10).

[45] D. Sen, A. Pesyridis, and A. Lenton. "A scramjet compression system for hypersonic air transportation vehicle combined cycle engines". In: *Energies* 11.6 (2018), p. 1568. ISSN: 1996-1073. DOI: 10.3390/en11061568 (cit. on pp. 11, 181).

[46] F. Bartlmä. "Instationäre Strömungsvorgänge bei Überschreiten der kritischen Wärmezufuhr". In: *Z. Flugwiss.* 11 (1963), pp. 160–168. DOI: 10.1007/978-3-7091-8403-5_5 (cit. on p. 11).

[47] C. Delale, G. Schnerr, and J. Zierep. "The mathematical theory of thermal choking in nozzle flows". In: *Z. Angew. Math. Phys.* 44.6 (1993), pp. 943–976. ISSN: 0044-2275. DOI: 10.1007/BF00942759 (cit. on pp. 11, 12).

[48] W. Knuth, P. Gloyer, J. Goodman, and R. Litchfor. *Thermally-choked combustor technology*. Tech. rep. 19960009786. NASA, 1993 (cit. on p. 12).

[49] K. Nakata, K. Ishihara, K. Goto, N. Itouyama, H. Watanabe, A. Kawasaki, K. Matsuoka, J. Kasahara, A. Matsuo, I. Funaki, K. Higashino, J. Braun, T. Meyer, and G. Paniagua. "Experimental investigation of inner flow of a throatless diverging rotating detonation engine". In: *Proc. Combust. Inst.* 39.3 (2023), pp. 3073–3082. ISSN: 1540-7489. DOI: 10.1016/j.proci.2022.08.089 (cit. on p. 12).

[50] E. Curran, W. Heiser, and D. Pratt. "Fluid phenomena in scramjet combustion systems". In: *Annu. Rev. Fluid Mech.* 28.1 (1996), pp. 323–360. ISSN: 0066-4189. DOI: 10.1146/annurev.fl.28.010196.001543 (cit. on p. 12).

[51] K. Nakata, K. Ota, S. Ito, K. Ishihara, K. Goto, N. Itouyama, H. Watanabe, A. Kawasaki, K. Matsuoka, J. Kasahara, A. Matsuo, I. Funaki, K. Higashino, J. Braun, T. Meyer, and G. Paniagua. "Supersonic exhaust from a rotating detonation engine with throatless diverging channel". In: *AIAA J.* 60.7 (2022), pp. 4015–4023. ISSN: 0001-1452. DOI: 10.2514/1.J061300 (cit. on p. 12).

[52] F. Falempin. *Ramjet and dual mode operation*. Tech. rep. RTP-EN-AVT-150. NATO, 2008 (cit. on pp. 12, 181).

[53] J.-M. Klein, A. Genot, A. Vincent-Randonnier, and A. Mura. "Combustion thermoacoustics: On the relevance of some stability criteria". In: *Proceedings of the 9th European Conference for Aeronautics and Space Sciences (EUCASS)*. Lille, France, Sept. 2022, pp. 1–15. DOI: 10.13009/EUCASS2022-4361 (cit. on p. 12).

[54] E. Bekaert, A. Genot, T. Le Pichon, and T. Schuller. "Longitudinal acoustic field in a two-phase ramjet: Numerical simulation and acoustic models". In: *Proceedings of the 3rd International Conference on High-Speed Vehicle Science and Technology (HiSST)*. Busan, South Korea, Apr. 2024, p. 151. HAL: hal-04616255 (cit. on pp. 12, 20, 96).

[55] V. Yang and F. Culick. "Analysis of low frequency combustion instabilities in a laboratory ramjet combustor". In: *Combust. Sci. Technol.* 45.1–2 (1986), pp. 1–25. ISSN: 0010-2202. DOI: 10.1080/00102208608923839 (cit. on pp. 12, 17).

[56] E. George, V. Sabelnikov, and P. Marge. "Self-ignition of ethylene/hydrogen mixtures in unsteady thermal choking conditions: Numerical unsteady RANS investigation". In: *Proceedings of the West-East High Speed Flow Field Conference*. Moscow, Russia, Nov. 2007, pp. 1–12. URL: https://www.researchgate.net/publication/268816532 (cit. on p. 12).

[57] Y. Liu, A. Dowling, N. Swaminathan, R. Morvant, M. Macquisten, and L. Caracciolo. "Prediction of combustion noise for an aeroengine combustor". In: *J. Propul. Power* 30.1 (2014), pp. 114–122. ISSN: 0748-4658. DOI: 10.2514/1.B34857 (cit. on p. 12).

[58] T. Lieuwen and V. Yang. *Combustion instabilities in gas turbine engines: Operational experience, fundamental mechanisms, and modeling*. AIAA, 2005. ISBN: 9781563476693 (cit. on p. 12).

[59] A. Dowling and S. Stow. "Acoustic analysis of gas turbine combustors". In: *J. Propul. Power* 19.5 (2003), pp. 751–764. ISSN: 0748-4658. DOI: 10.2514/2.6192 (cit. on p. 12).

[60] L. Kovásznay. "Turbulence in supersonic flow". In: *J. Aeronaut. Sci.* 20.10 (1953), pp. 657–674. ISSN: 1936-9956. DOI: 10.2514/8.2793 (cit. on p. 13).

[61] B.-T. Chu and L. Kovásznay. "Non-linear interactions in a viscous heat-conducting compressible gas". In: *J. Fluid Mech.* 3.5 (1958), pp. 494–514. ISSN: 0022-1120. DOI: 10.1017/S0022112058000148 (cit. on p. 13).

[62] A. Dowling and Y. Mahmoudi. "Combustion noise". In: *Proc. Combust. Inst.* 35.1 (2015), pp. 65–100. ISSN: 1540-7489. DOI: 10.1016/j.proci.2014.08.016 (cit. on pp. 13, 14, 17, 181).

[63] D. Crighton, A. Dowling, J. Ffowcs Williams, M. Heckl, and F. Leppington. *Thermoacoustic sources and instabilities*. Springer, 1992. ISBN: 9783540197379. DOI: 10.1007/978-1-4471-0399-8_13 (cit. on p. 13).

[64] R. Sujith and S. Pawar. *Thermoacoustic instability: A complex systems perspective*. Springer, 2021. ISBN: 9783030811341. DOI: 10.1007/978-3-030-81135-8 (cit. on p. 14).

[65] T. Lieuwen. "Nonlinear kinematic response of premixed flames to harmonic velocity disturbances". In: *Proc. Combust. Inst.* 30.2 (2005), pp. 1725–1732. ISSN: 1540-7489. DOI: 10.1016/j.proci.2004.07.020 (cit. on pp. 14, 17).

[66] W. Strahle. "On combustion generated noise". In: *J. Fluid Mech.* 49.2 (1971), pp. 399–414. ISSN: 0022-1120. DOI: 10.1017/S0022112071002167 (cit. on p. 14).

[67] A. Dowling. "A kinematic model of a ducted flame". In: *J. Fluid Mech.* 394 (1999), pp. 51–72. ISSN: 0022-1120. DOI: 10.1017/S0022112099005686 (cit. on pp. 14, 95–97, 185).

[68] M. Lighthill. "On sound generated aerodynamically. I. General theory". In: *Proc. R. Soc. Lond. A* 211.1107 (1952), pp. 564–587. ISSN: 0080-4630. DOI: 10.1098/rspa.1952.0060 (cit. on p. 14).

[69] A. Powell. "Theory of vortex sound". In: *J. Acoust. Soc. Am.* 36.1 (1964), pp. 177–195. ISSN: 0001-4966. DOI: 10.1121/1.1918931 (cit. on p. 14).

[70] M. Howe. "Contributions to the theory of aerodynamic sound, with application to excess jet noise and the theory of the flute". In: *J. Fluid Mech.* 71.4 (1975), pp. 625–673. ISSN: 0022-1120. DOI: 10.1017/S0022112075002777 (cit. on pp. 14, 127).

[71] W. Möhring. "On vortex sound at low Mach number". In: *J. Fluid Mech.* 85.4 (1978), pp. 685–691. ISSN: 0022-1120. DOI: 10.1017/S0022112078000865 (cit. on p. 14).

[72] C. Tam and S. Parrish. "The physical processes of indirect combustion noise generation". In: *Int. J. Aeroacoust.* 17.1–2 (2018), pp. 22–35. ISSN: 1475-472X. DOI: 10.1177/1475472X17743628 (cit. on p. 15).

[73] A. Morgans and I. Duran. "Entropy noise: A review of theory, progress and challenges". In: *Int. J. Spray Combust. Dyn.* 8.4 (2016), pp. 285–298. ISSN: 1756-8277. DOI: 10.1177/1756827716651791 (cit. on pp. 15, 21).

[74] F. Bake, N. Kings, A. Fischer, and I. Roehle. "Indirect combustion noise: Investigations of noise generated by the acceleration of flow inhomogeneities". In: *Acta Acust.* 95.3 (2009), pp. 461–469. ISSN: 1610-1928. DOI: 10.3813/AAA.918170 (cit. on p. 15).

[75] K. Knobloch, T. Werner, and F. Bake. "Entropy noise generation and reduction in a heated nozzle flow". In: *Proceedings of the 21st AIAA/CEAS Aeroacoustics Conference*. Dallas, United States of America, June 2015, p. 2818. DOI: 10.2514/6.2015-2818 (cit. on p. 15).

[76] M. Howe. "Indirect combustion noise". In: *J. Fluid Mech.* 659 (2010), pp. 267–288. ISSN: 0022-1120. DOI: 10.1017/S0022112010002466 (cit. on p. 15).

[77] N. Kings and F. Bake. "Indirect combustion noise: Noise generation by accelerated vorticity in a nozzle flow". In: *Int. J. Spray Combust. Dyn.* 2.3 (2010), pp. 253–266. ISSN: 1756-8277. DOI: 10.1260/1756-8277.2.3.253 (cit. on p. 15).

[78] N. Kings. "Indirect combustion noise: Experimental investigation of the vortex sound generation in nozzle flows". Ph.D. thesis. Technische Universität Berlin, 2014 (cit. on p. 15).

[79] J. Ffowcs Williams and M. Howe. "The generation of sound by density inhomogeneities in low-Mach-number nozzle flows". In: *J. Fluid Mech.* 70.3 (1975), pp. 605–622. ISSN: 0022-1120. DOI: 10.1017/S0022112075002224 (cit. on pp. 15, 114).

[80] M. Howe. *Theory of vortex sound*. Cambridge Univ. Press, 2002. ISBN: 9780521812818. DOI: 10.1017/CBO9780511755491 (cit. on p. 15).

[81] L. Magri, J. O'Brien, and M. Ihme. "Compositional inhomogeneities as a source of indirect combustion noise". In: *J. Fluid Mech.* 799 (2016), R4. ISSN: 0022-1120. DOI: 10.1017/jfm.2016.397 (cit. on pp. 15, 23).

[82] L. Magri. "On indirect noise in multicomponent nozzle flows". In: *J. Fluid Mech.* 828 (2017), R2. ISSN: 0022-1120. DOI: 10.1017/jfm.2017.591 (cit. on pp. 16, 63, 149).

[83] M. Ihme. "Combustion and engine-core noise". In: *Annu. Rev. Fluid Mech.* 49.1 (2017), pp. 277–310. ISSN: 0066-4189. DOI: 10.1146/annurev-fluid-122414-034542 (cit. on p. 16).

[84] Y. Gentil, G. Daviller, and S. Moreau. "Combustion noise modelling of thermally perfect and multi-species gas flow in nozzles". In: *J. Fluid Mech.* 1014 (2025), A39. ISSN: 0022-1120. DOI: 10.1017/jfm.2025.10330 (cit. on pp. 16, 21, 63, 133, 149, 178).

[85] B. Zinn. "Pulse combustion: Recent applications and research issues". In: *Symp. (Int.) Combust.* 24.1 (1992), pp. 1297–1305. ISSN: 0082-0784. DOI: 10.1016/S0082-0784(06)80151-7 (cit. on p. 16).

[86] S. Candel. "Combustion dynamics and control: Progress and challenges". In: *Proc. Combust. Inst.* 29.1 (2002), pp. 1–28. ISSN: 1540-7489. DOI: 10.1016/S1540-7489(02)80007-4 (cit. on pp. 16, 181).

[87] D. Durox, T. Schuller, N. Noiray, A.L. Birbaud, and S. Candel. "Rayleigh criterion and acoustic energy balance in unconfined self-sustained oscillating flames". In: *Combust. Flame* 156.1 (2009), pp. 106–119. ISSN: 0010-2180. DOI: 10.1016/j.combustflame.2008.07.016 (cit. on p. 16).

[88] B. Schuermans, J. Moeck, A. Blondé, B. Dharmaputra, and N. Noiray. "The Rayleigh integral is always positive in steadily operated combustors". In: *Proc. Combust. Inst.* 39.4 (2023), pp. 4661–4669. ISSN: 1540-7489. DOI: 10.1016/j.proci.2022.08.035 (cit. on pp. 16, 108, 109).

[89] D. Durox, T. Schuller, N. Noiray, and S. Candel. "Experimental analysis of nonlinear flame transfer functions for different flame geometries". In: *Proc. Combust. Inst.* 32.1 (2009), pp. 1391–1398. ISSN: 1540-7489. DOI: 10.1016/j.proci.2008.06.204 (cit. on p. 17).

[90] T. Schuller, D. Durox, and S. Candel. "A unified model for the prediction of laminar flame transfer functions: Comparisons between conical and V-flame dynamics". In: *Combust. Flame* 134.1 (2003), pp. 21–34. ISSN: 0010-2180. DOI: 10.1016/S0010-2180(03)00042-7 (cit. on pp. 17, 92, 96).

[91] T. Lieuwen. "Modeling premixed combustion–acoustic wave interactions: A review". In: *J. Propul. Power* 19.5 (2003), pp. 765–781. ISSN: 0748-4658. DOI: 10.2514/2.6193 (cit. on pp. 17, 96).

[92] X. Han and A. Morgans. "Simulation of the flame describing function of a turbulent premixed flame using an open-source LES solver". In: *Combust. Flame* 162.5 (2015), pp. 1778–1792. ISSN: 0010-2180. DOI: 10.1016/j.combustflame.2014.11.039 (cit. on p. 17).

[93] T. Schuller, T. Poinsot, and S. Candel. "Dynamics and control of premixed combustion systems based on flame transfer and describing functions". In: *J. Fluid Mech.* 894 (2020), P1. ISSN: 0022-1120. DOI: 10.1017/jfm.2020.239 (cit. on p. 17).

[94] L. Hirschberg. "Low-order modeling of vortex-driven self-sustained pressure pulsations in solid rocket motors". Ph.D. thesis. Université Paris-Saclay, 2019. HAL: tel-02019520 (cit. on pp. 17, 121, 127, 128, 133, 162, 178).

[95] N. Karimi, M. Brear, and W. Moase. "Acoustic and disturbance energy analysis of a flow with heat communication". In: *J. Fluid Mech.* 597 (2008), pp. 67–89. ISSN: 0022-1120. DOI: 10.1017/S0022112007009573 (cit. on pp. 18, 21, 38, 45, 50, 51, 59, 92).

[96] S. Yeddula, R. Gaudron, and A. Morgans. "Acoustic absorption and generation in ducts of smoothly varying area sustaining a mean flow and a mean temperature gradient". In: *J. Sound Vib.* 515 (2021), p. 116437. ISSN: 0022-460X. DOI: 10.1016/j.jsv.2021.116437 (cit. on pp. 18, 38, 92).

[97] Y. Gentil, G. Daviller, S. Moreau, N. Treleaven, and T. Poinsot. "Theoretical analysis and numerical validation of the mechanisms controlling composition noise". In: *J. Sound Vib.* 585 (2024), p. 118463. ISSN: 0022-460X. DOI: 10.1016/j.jsv.2024.118463 (cit. on pp. 21, 149).

[98] T. Poinsot and D. Veynante. *Theoretical and numerical combustion*. 3rd ed. CNRS, 2011. ISBN: 9782746639904 (cit. on pp. 21, 22, 66, 93–95).

[99] V. Rani and S. Rani. "WKB solutions to the quasi 1-D acoustic wave equation in ducts with non-uniform cross-section and inhomogeneous mean flow properties: Acoustic field and combustion instability". In: *J. Sound Vib.* 436 (2018), pp. 183–219. ISSN: 0022-460X. DOI: 10.1016/j.jsv.2018.06.065 (cit. on pp. 21, 63).

[100] W. Li, D. Zhao, X. Chen, Y. Sun, S. Ni, D. Guan, and B. Wang. "Numerical investigations on solid-fueled ramjet inlet thermodynamic properties effects on generating self-sustained combustion instability". In: *Aerosp. Sci. Technol.* 119 (2021), p. 107097. ISSN: 1270-9638. DOI: 10.1016/j.ast.2021.107097 (cit. on p. 21).

[101] E. Bekaert, A. Genot, T. Le Pichon, and T. Schuller. "Low-order models for acoustic modes in a ramjet combustor with inlet shock train". In: *Proceedings of the 9th European Conference for Aeronautics and Space Sciences (EUCASS)*. Lille, France, Sept. 2022, pp. 1–9. DOI: 10.13009/EUCASS2022-6122 (cit. on pp. 21, 94).

[102] F. Williams. *Combustion theory: the fundamental theory of chemically reacting flow systems*. 2nd ed. Perseus Books, 1985. ISBN: 9780201407778 (cit. on p. 23).

[103] R. Fedkiw, B. Merriman, and S. Osher. "High accuracy numerical methods for thermally perfect gas flows with chemistry". In: *J. Comput. Phys.* 132.2 (1997), pp. 175–190. ISSN: 0021-9991. DOI: 10.1006/jcph.1996.5622 (cit. on p. 23).

[104] J. Anderson. *Hypersonic and high-temperature gas dynamics*. AIAA, 2019. ISBN: 9781624105142. DOI: 10.2514/4.105142 (cit. on p. 23).

[105] G Job and F Herrmann. "Chemical potential—a quantity in search of recognition". In: *Eur. J. Phys.* 27.2 (2006), pp. 353–371. ISSN: 0143-0807. DOI: 10.1088/0143-0807/27/2/018 (cit. on p. 23).

[106] Y. Gentil, G. Daviller, and S. Moreau. "Combustion noise modelling re-examined for thermally perfect and multi-species gas flows". In: *Proceedings of the 30th AIAA/CEAS Aeroacoustics Conference*. Rome, Italy, June 2024, pp. 1–19. DOI: 10.2514/6.2024-3328 (cit. on pp. 23, 50).

[107] G. Pelletier, M. Ferrier, A. Vincent-Randonnier, V. Sabelnikov, and A. Mura. "Wall roughness effects on combustion development in confined supersonic flow". In: *J. Propul. Power* 37.1 (2021), pp. 151–166. ISSN: 1533-3876. DOI: 10.2514/1.B37842 (cit. on p. 23).

[108] E. Lemmon, R. Jacobsen, S. Penoncello, and D. Friend. "Thermodynamic properties of air and mixtures of nitrogen, argon, and oxygen from 60 to 2000 K at pressures to 2000 MPa". In: *J. Phys. Chem. Ref. Data* 29.3 (2000), pp. 331–385. ISSN: 0047-2689. DOI: 10.1063/1.1285884 (cit. on p. 24).

[109] K. Kato, T. Kanda, K. Kobayashi, K. Kudo, and A. Murakami. "Downstream ramjet-mode combustion in a dual-mode scramjet engine". In: *J. Propul. Power* 22.3 (2006), pp. 511–517. ISSN: 0748-4658. DOI: 10.2514/1.17547 (cit. on pp. 24, 25).

[110] M. Fotia and J. Driscoll. "Isolator-combustor interactions in a direct-connect ramjet-scramjet experiment". In: *J. Propuls. Power* 28.1 (2012), pp. 83–95. ISSN: 0748-4658. DOI: 10.2514/1.B34367 (cit. on pp. 24, 25).

[111] J. Donohue. "Dual-mode scramjet flameholding operability measurements". In: *J. Propuls. Power* 30.3 (2014), pp. 592–603. ISSN: 0748-4658. DOI: 10.2514/1.B35016 (cit. on pp. 24, 25).

[112] W. Huang and L. Yan. "Numerical investigation on the ram–scram transition mechanism in a strut-based dual-mode scramjet combustor". In: *Int. J. Hydrogen Energy* 41.8 (2016), pp. 4799–4807. ISSN: 0360-3199. DOI: 10.1016/j.ijhydene.2016.01.062 (cit. on pp. 24, 25).

[113] J. Van Der Lee, N. Yokev, and D. Michaels. "Combustion instability due to combustion mode transition in a cavity-stabilized scramjet". In: *J. Propuls. Power* 38.6 (2022), pp. 945–956. ISSN: 1533-3876. DOI: 10.2514/1.B38683 (cit. on pp. 24, 25).

[114] R. Annunziata, N. Bonne, and F. Garnier. "Numerical investigation of engine position effects on contrail formation and evolution in the near-field of a realistic aircraft configuration". In: *Aerosp. Sci. Technol.* 167 (2025), p. 110703. ISSN: 1270-9638. DOI: 10.1016/j.ast.2025.110703 (cit. on p. 26).

[115] S. Boulal, A. Langenais, L. François, P. Bernigaud, and L. Vingert. "Large-scale stochastic dynamics of the afterburning in a supersonic fuel-rich plume: Possible evidence of unconfined deflagration-to-detonation transition". In: *Phys. Fluids* 37.3 (2025), p. 036120. ISSN: 1070-6631. DOI: 10.1063/5.0258100 (cit. on p. 26).

[116] P. Bernigaud, D. Davidenko, and L. Catoire. "A revised model of ammonium perchlorate combustion with detailed kinetics". In: *Combust. Flame* 255 (2023), p. 112891. ISSN: 00102180. DOI: 10.1016/j.combustflame.2023.112891 (cit. on p. 26).

[117] A. Clout, A. Langenais, Y. Dauvois, L. Mieussens, and J. Labaune. "Numerical study and semi-analytical model of rocket motor exhaust backflow in rarefied atmosphere". In: *Phys. Fluids* 37.1 (2025), p. 016119. ISSN: 1070-6631. DOI: 10.1063/5.0250170 (cit. on p. 26).

[118] A. Refloch, B. Courbet, A. Murrone, P. Villedieu, C. Laurent, P. Gilbank, J. Troyes, L. Tessé, G. Chaineray, J. Dargaud, E. Quémerais, and F. Vuillot. "CEDRE software". In: *AerospaceLab J.* 2 (2011), pp. 1–10. ISSN: 2107-6596. HAL: hal-01182463 (cit. on p. 26).

[119] C. Le Touze, A. Murrone, and H. Guillard. "Multislope MUSCL method for general unstructured meshes". In: *J. Comput. Phys.* 284 (2015), pp. 389–418. ISSN: 0021-9991. DOI: 10.1016/j.jcp.2014.12.032 (cit. on p. 26).

[120] E. Toro, M. Spruce, and W. Speares. "Restoration of the contact surface in the HLL Riemann solver". In: *Shock Waves* 4.1 (1994), pp. 25–34. ISSN: 0938-1287. DOI: 10.1007/BF01414629 (cit. on p. 26).

[121] J. Butcher. "Implicit Runge–Kutta processes". In: *Math. Comp.* 18.85 (1964), pp. 50–64. ISSN: 0025-5718. DOI: 10.1090/S0025-5718-1964-0159424-9 (cit. on p. 26).

[122] M. Huet and B. Courbet. *Évaluation analytique et numérique de la non-réflexion des conditions aux limites dans le code CEDRE*. Tech. rep. ONERA, 2016 (cit. on pp. 27, 28).

[123] H. Wang, Q. Yang, and X. Xu. "Effect of thermal choking on ejection process in a rocket-based combined cycle engine". In: *Appl. Therm. Eng.* 116 (2017), pp. 197–204. ISSN: 1359-4311. DOI: 10.1016/j.applthermaleng.2017.01.059 (cit. on pp. 29, 40).

[124] L. Gicquel and A. Roux. "LES to ease understanding of complex unsteady combustion features of ramjet burners". In: *Flow Turbul. Combust.* 87.2 (2011), pp. 449–472. ISSN: 1386-6184. DOI: 10.1007/s10494-010-9306-z (cit. on pp. 29, 94).

[125] A. Shapiro. *The dynamics and thermodynamics of compressible fluid flow. Vol. 1*. 23rd ed. Wiley, 1976. ISBN: 9780471066910 (cit. on pp. 30, 41, 63, 148, 150).

[126] E. Süli and D. Mayers. *An introduction to numerical analysis*. 1st ed. Cambridge Univ. Press, 2003. ISBN: 9780511801181. DOI: 10.1017/CBO9780511801181 (cit. on pp. 31, 70).

[127] F. Olivon, J.-E. Durand, A. Genot, and E. Piot. "High-frequency acoustic propagation in a thermally choked low-Mach dual-mode ramjet". In: *Proceedings of the 30th AIAA/CEAS Aeroacoustics Conference*. Rome, Italy, 2024, pp. 1–15. DOI: 10.2514/6.2024-3114 (cit. on p. 42).

[128] N. Ricker. "Wavelet contraction, wavelet expansion, and the control of seismic resolution". In: *Geophysics* 18.4 (1953), pp. 769–792. ISSN: 0016-8033. DOI: 10.1190/1.1437927 (cit. on p. 42).

[129] L. Geldart and R. Sheriff. *Problems in exploration seismology and their solutions*. Vol. 14. Soc. of Exploration Geophysicists, 2004. ISBN: 9781560801153. DOI: 10.1190/1.9781560801733 (cit. on p. 42).

[130] J. Anderson. *Fundamentals of aerodynamics*. 6th ed. McGraw-Hill Education, 2017. ISBN: 9781259129919 (cit. on pp. 45, 142).

[131] T. Lieuwen. *Unsteady combustor physics*. 2nd ed. Cambridge Univ. Press, 2021. ISBN: 9781108889001. DOI: 10.1017/9781108889001 (cit. on pp. 50–52).

[132] I. Duran and A. Morgans. "On the reflection and transmission of circumferential waves through nozzles". In: *J. Fluid Mech.* 773 (2015), pp. 137–153. ISSN: 0022-1120. DOI: 10.1017/jfm.2015.247 (cit. on pp. 57, 63, 70).

[133] N. Karimi, M. Brear, and W. Moase. "On the interaction of sound with steady heat-communicating flows". In: *J. Sound Vib.* 329.22 (2010), pp. 4705–4718. ISSN: 0022460X. DOI: 10.1016/j.jsv.2010.05.009 (cit. on p. 59).

[134] J. Nan, J. Li, A. Morgans, L. Qin, and L. Yang. "Theoretical analysis of sound propagation and entropy generation across a distributed steady heat source". In: *J. Sound Vib.* 536 (2022), p. 117170. ISSN: 0022-460X. DOI: 10.1016/j.jsv.2022.117170 (cit. on p. 59).

[135] S. Yeddula and A. Morgans. "A semi-analytical solution for acoustic wave propagation in varying-area ducts with mean flow". In: *J. Sound Vib.* 492 (2021), p. 115770. ISSN: 0022-460X. DOI: 10.1016/j.jsv.2020.115770 (cit. on p. 63).

[136] A. Cummings. "Ducts with axial temperature gradients: An approximate solution for sound transmission and generation". In: *J. Sound Vib.* 51.1 (1977), pp. 55–67. ISSN: 0022-460X. DOI: 10.1016/S0022-460X(77)80112-0 (cit. on p. 63).

[137] S. Basu and S. Rani. "Wentzel-Kramers-Brillouin solutions to the nonisentropic Helmholtz equation in a nonuniform duct with mean temperature gradient and mean flow". In: *J. Vib. Acoust.* 145.2 (2023), p. 021002. ISSN: 1048-9002. DOI: 10.1115/1.4054853 (cit. on p. 63).

[138] J. Li and A. Morgans. "The one-dimensional acoustic field in a duct with arbitrary mean axial temperature gradient and mean flow". In: *J. Sound Vib.* 400 (2017), pp. 248–269. ISSN: 0022-460X. DOI: 10.1016/j.jsv.2017.03.047 (cit. on p. 63).

[139] M. Huet, A. Emmanuelli, and T. Le Garrec. "Entropy noise modelling in 2D choked nozzle flows". In: *J. Sound Vib.* 488 (2020), p. 115637. ISSN: 0022-460X. DOI: 10.1016/j.jsv.2020.115637 (cit. on pp. 63, 149).

[140] M. Huet and L. Geiger. "Modeling of indirect combustion noise through a stator". In: *J. Sound Vib.* 540 (2022), p. 117296. ISSN: 0022-460X. DOI: 10.1016/j.jsv.2022.117296 (cit. on p. 63).

[141] S. Boulal, A. Genot, and T. Le Pichon. "Combustion dynamics of a dual-inlet side-dump ramjet combustor". In: *Combust. Flame* 283 (2026), p. 114535. ISSN: 0010-2180. DOI: 10.1016/j.combustflame.2025.114535 (cit. on pp. 88, 114).

[142] G. Bloxsidge, A. Dowling, and P. Langhorne. "Reheat buzz: an acoustically coupled combustion instability. Part 2. Theory". In: *J. Fluid Mech.* 193 (1988), pp. 445–473. ISSN: 0022-1120. DOI: 10.1017/S0022112088002216 (cit. on pp. 92, 95, 96).

[143] S. Ducruix, T. Schuller, D. Durox, and S. Candel. "Combustion Dynamics and Instabilities: Elementary Coupling and Driving Mechanisms". In: *J. Propuls. Power* 19.5 (2003), pp. 722–734. ISSN: 0748-4658. DOI: 10.2514/2.6182 (cit. on p. 93).

[144] D. Veynante. "Flamme de diffusion laminaire". In: *Techniques de l'ingénieur* (1999). DOI: 10.51257/a-v1-be8320 (cit. on pp. 93, 185).

[145] Anthony Roux. "Simulation aux Grandes Echelles d'un statoréacteur". Ph.D. thesis. Institut National Polytechnique de Toulouse, 2009. HAL: tel-04400946 (cit. on pp. 94, 185).

[146] L. Crocco and S.-I. Cheng. *Theory of combustion instability in liquid propellant rocket motors*. Tech. rep. AGARDOGRAPH8. NATO, 1956 (cit. on p. 94).

[147] R. Rajaram and T. Lieuwen. "Acoustic radiation from turbulent premixed flames". In: *J. Fluid Mech.* 637 (2009), pp. 357–385. ISSN: 0022-1120. DOI: 10.1017/S0022112009990681 (cit. on p. 95).

[148] S. Ducruix, D. Durox, and S. Candel. "Theoretical and experimental determinations of the transfer function of a laminar premixed flame". In: *Proc. Combust. Inst.* 28.1 (2000), pp. 765–773. ISSN: 1540-7489. DOI: 10.1016/S0082-0784(00)80279-9 (cit. on pp. 95, 96).

[149] R Balachandran, B Ayoola, C Kaminski, A Dowling, and E Mastorakos. "Experimental investigation of the nonlinear response of turbulent premixed flames to imposed inlet velocity oscillations". In: *Combust. Flame* 143.1 (2005), pp. 37–55. ISSN: 0010-2180. DOI: 10.1016/j.combustflame.2005.04.009 (cit. on pp. 95, 96).

[150] C. O. Paschereit, B. Schuermans, W. Polifke, and O. Mattson. "Measurement of Transfer Matrices and Source Terms of Premixed Flames". In: *J. Eng. Gas Turbine. Power* 124.2 (2002), pp. 239–247. ISSN: 0742-4795. DOI: 10.1115/1.1383255 (cit. on pp. 95, 96).

[151] N. Noiray, D. Durox, T. Schuller, and S. Candel. "A unified framework for nonlinear combustion instability analysis based on the flame describing function". In: *J. Fluid Mech.* 615 (2008), pp. 139–167. ISSN: 0022-1120. DOI: 10.1017/S0022112008003613 (cit. on p. 96).

[152] N. Zettervall and C. Fureby. "A Computational Study of Ramjet, Scramjet and Dual-mode Ramjet Combustion in Combustor with a Cavity Flameholder". In: *Proceedings of the 2018 AIAA Aerospace Sciences Meeting*. Kissimmee, United States of America, Jan. 2018. DOI: 10.2514/6.2018-1146 (cit. on p. 100).

[153] K.-C. Lin, C.-J. Tam, I. Boxx, C. Carter, K. Jackson, and M. Lindsey. "Flame Characteristics and Fuel Entrainment Inside a Cavity Flame Holder of a Scramjet Combustor". In: *Proceedings of the 43rd AIAA/ASME/SAE/ASEE Joint Propulsion Conference & Exhibit*. Cincinnati, United States of America, July 2007. DOI: 10.2514/6.2007-5381 (cit. on p. 100).

[154] D. Micka and J. Driscoll. "Combustion characteristics of a dual-mode scramjet combustor with cavity flameholder". In: *Proc. Combust. Inst.* 32.2 (2009), pp. 2397–2404. ISSN: 1540-7489. DOI: 10.1016/j.proci.2008.06.192 (cit. on p. 100).

[155] O. Kummitha, K. Pandey, and R. Gupta. "CFD analysis of a scramjet combustor with cavity based flame holders". In: *Acta Astronaut.* 144 (2018), pp. 244–253. ISSN: 0094-5765. DOI: 10.1016/j.actaastro.2018.01.005 (cit. on p. 100).

[156] L. Magri, M. P. Juniper, and J. P. Moeck. "Sensitivity of the Rayleigh criterion in thermoacoustics". In: *J. Fluid Mech.* 882 (2020), R1. ISSN: 0022-1120. DOI: 10.1017/jfm.2019.860 (cit. on p. 108).

[157] B.-T. Chu. "On the energy transfer to small disturbances in fluid flow (Part I)". In: *Acta Mech.* 1.3 (1965), pp. 215–234. ISSN: 0001-5970. DOI: 10.1007/BF01387235 (cit. on p. 110).

[158] K. Kowalski, S. Hulshoff, P. Ströer, J. Withag, A. Genot, A. Morgans, F. Bake, K. Venner, M. Sanders, and L. Hirschberg. "Entropy-patch–choked-nozzle interaction: Quasi-steady modeling-regime limits probed". In: *Proceedings of the 30th AIAA/CEAS Aeroacoustics Conference*. Rome, Italy, June 2024, pp. 1–24. DOI: 10.2514/6.2024-3113 (cit. on pp. 114, 162).

[159] K. Elbakly. "Entropy-patch choked-nozzle interaction: Inertial, quasi-steady, linear, and non-linear modeling regimes mapped". Master's thesis. University of Twente, 2025 (cit. on pp. 114, 118, 119, 123, 124, 161–169, 188).

[160] L. Hirschberg, F. Bake, K. Knobloch, S.. Hulshoff, and A. Hirschberg. "Experimental investigations of indirect noise due to modulation of axial vorticity and entropy upstream of a choked nozzle". In: *J. Sound Vib.* 532 (Aug. 2022), p. 116989. ISSN: 0022-460X. DOI: 10.1016/j.jsv.2022.116989 (cit. on p. 118).

[161] R. Gervais and S. Merchant. *The Office (TV show)*. 2005 (cit. on p. 137).

[162] A. Jain and L. Magri. "A physical model for indirect noise in non-isentropic nozzles: Transfer functions and stability". In: *J. Fluid Mech.* 935 (2022), A33. ISSN: 0022-1120. DOI: 10.1017/jfm.2022.27 (cit. on p. 149).

[163] W. Bell, B. Daniel, and B. Zinn. "Experimental and theoretical determination of the admittances of a family of nozzles subjected to axial instabilities". In: *J. Sound Vib.* 30.2 (1973), pp. 179–190. ISSN: 0022-460X. DOI: 10.1016/S0022-460X(73)80112-9 (cit. on pp. 151–155, 157–159, 187, 188).

[164] B. Zinn, W. Bell, B. Daniel, and A. Smith. "Experimental determination of three-dimensional liquid rocket nozzle admittances". In: *AIAA J.* 11.3 (1973), pp. 267–272. ISSN: 0001-1452. DOI: 10.2514/3.6741 (cit. on p. 151).

[165] S. Hulshoff, A. Hirschberg, and G. Hofmans. "Sound production of vortex–nozzle interactions". In: *J. Fluid Mech.* 439 (2001), pp. 335–352. ISSN: 0022-1120. DOI: 10.1017/S0022112001004554 (cit. on p. 162).

[166] L. Hirschberg, S. Hulshoff, J. Collinet, C. Schram, and T. Schuller. "Vortex–nozzle interaction in solid rocket motors: A scaling law for upstream acoustic response". In: *J. Acoust. Soc. Am.* 144.1 (2018), EL46–EL51. ISSN: 0001-4966. DOI: 10.1121/1.5046441 (cit. on p. 162).

[167] P. Henrici. *Applied and computational complex analysis. Vol. 1*. Wiley, 1988. ISBN: 9780471608417 (cit. on p. 162).

[168] M. Howe. *Acoustics of fluid-structure interactions*. Cambridge Univ. Press, 1998. ISBN: 9780521633208. DOI: 10.1017/CBO9780511662898 (cit. on p. 167).

[169] N Curle. "The influence of solid boundaries upon aerodynamic sound". In: *Proc. R. Soc. Lond. A* 231.1187 (1955), pp. 505–514. ISSN: 0080-4630. DOI: 10.1098/rspa.1955.0191 (cit. on p. 167).

[170] A. Pierce. *Acoustics: an introduction to its physical principles and applications*. Springer, 2019. ISBN: 9783030112134. DOI: 10.1007/978-3-030-11214-1 (cit. on p. 167).

RÉPUBLIQUE FRANÇAISE
*Liberté*
*Égalité*
*Fraternité*

Université de Toulouse

**Titre :** Aéroacoustique des tuyères à col thermique dans les statomixtes

**Mots clés :** Aéroacoustique, Statomixte, Col thermique

**Résumé :** Cette thèse étudie la réponse aéroacoustique des tuyères à col thermique, une configuration représentative des statomixtes fonctionnant à la fois en modes statoréacteur et superstatoréacteur. Dans ces moteurs, un apport d'énergie distribué produit par la flamme suffit à amorcer l'écoulement, formant un col thermique jouant à la fois le rôle de frontière aérodynamique et acoustique. Alors que l'aéroacoustique des tuyères géométriques est bien documentée, les configurations où l'amorçage résulte uniquement de l'apport d'énergie ont été beaucoup moins étudiées. L'objectif de cette thèse est de caractériser le comportement acoustique et entropique de ces écoulements et de développer des modèles simplifiés capables de prédire les mécanismes physiques associés.
Une méthodologie combinée a été employée. À l'aide du code CFD CEDRE de l'ONERA, la propagation d'ondes acoustiques et entropiques a été analysée dans une tuyère simplifiée avec un apport d'énergie distribué. En parallèle, un modèle d'acoustique linéaire quasi-unidimensionnel a été développé. Il résout les équations d'Euler linéarisées pour un écoulement non uniforme et non isentropique, avec des propriétés thermodynamiques variables, et intègre une nouvelle condition au col adaptée à l'amorçage thermique. Ce modèle a été validé par comparaison aux simulations CFD, puis utilisé pour une étude paramétrique étendue.
La réponse acoustique à un forçage isentropique a d'abord été caractérisée. Aux très basses fréquences, les écoulements thermiquement amorcés présentent une forte atténuation du coefficient de réflexion acoustique, due à la conversion d'ondes acoustiques en ondes entropiques dans la zone chauffée. Ce comportement diffère fondamentalement des prédictions isentropiques classiques. Un modèle quasi stationnaire a été proposé et validé pour décrire ce régime. Aux hautes fréquences, toutes les configurations amorcées tendent vers un comportement de radiation acoustique en onde simple, bien que la fréquence d'apparition dépende du profil stationnaire du nombre de Mach.
Le bruit indirect généré par la convection de perturbations entropiques a également été étudié. Pour des ondes entropiques unidimensionnelles, l'influence de l'apport thermique reste limitée et la réponse acoustique est principalement gouvernée par l'écoulement moyen. Pour des perturbations bidimensionnelles, telles que des taches entropiques circulaires, le comportement devient plus complexe : les petites structures présentent une réponse acoustique minimale, contrairement aux tuyères géométriques, tandis que les grandes structures retrouvent un régime quasi stationnaire, amplifié par l'apport de chaleur.
Un couplage thermoacoustique simplifié, basé sur un modèle cinématique de réponse de flamme, a ensuite été introduit. Les résultats montrent que les fluctuations de chaleur peuvent amplifier fortement les ondes acoustiques, en particulier pour des vitesses de flamme élevées et de petits accroche-flammes. Une analyse de stabilité fondée sur le taux d'amplification et l'indice de Rayleigh indique que ces configurations sont les plus susceptibles d'engendrer des instabilités, bien qu'elles restent peu probables en pratique.
Dans l'ensemble, ce travail fournit une caractérisation détaillée de la propagation des ondes acoustiques et entropiques, ainsi que du couplage thermoacoustique dans les écoulements thermiquement amorcés. Le modèle quasi-unidimensionnel et la condition au col développés constituent des outils efficaces pour analyser la stabilité des statomixtes et améliorent la compréhension des mécanismes d'instabilité induits par la combustion.

**Title:** Aeroacoustics of thermally choked-flow nozzles in dual-mode ramjets

**Key words:** Aeroacoustic, Dual-mode ramjet, Thermal throat

**Abstract:** This thesis investigates the aeroacoustic response of thermally choked nozzles, a flow configuration representative of dual-mode ramjet engines operating near the ram-to-scram transition. In such systems, distributed heat addition alone is sufficient to choke the flow, forming a thermal throat that acts simultaneously as an aerodynamic and acoustic boundary. While the aeroacoustics of geometrically choked nozzles are well documented, configurations in which choking results purely from heat release have received far less attention. The present work aims to characterise the acoustic and entropy–acoustic behaviour of these flows and to develop low-order models capable of predicting the underlying physical mechanisms.
A combined methodology based on numerical simulations and low-order modelling was employed. Using the ONERA CFD solver CEDRE, the propagation and scattering of acoustic and entropy disturbances were examined in a simplified yet representative dual-mode ramjet nozzle featuring distributed heat release. In parallel, a quasi-one-dimensional linear acoustic model was developed. It solves the linearised Euler equations for non-uniform, heated flows with temperature-dependent thermodynamic properties and incorporates a new boundary condition tailored to the thermal throat. This model was validated against the CFD results and then used for an extensive parametric analysis.
The acoustic response to isentropic forcing was first characterised. At very low frequencies, thermally choked flows exhibit a strong attenuation of the acoustic-reflection coefficient, caused by the conversion of acoustic fluctuations into entropy fluctuations within the heated region. This behaviour differs fundamentally from classical isentropic predictions. An analytical quasi-steady model was proposed and validated to describe this regime. At high frequencies, all choking configurations tend towards a simple-wave acoustic-radiation limit, although the frequency at which this asymptotic regime is reached depends on the shape of the steady Mach-number profile.
The indirect noise generated by entropy perturbations was also examined. For one-dimensional entropy waves, the influence of heat addition remains modest, and the acoustic response is governed mainly by the steady flow. For two-dimensional entropy structures, such as circular spots or slugs, the behaviour becomes more complex. Small-scale entropy perturbations exhibit a finite minimum acoustic response, unlike in geometric nozzles, whereas large-scale structures converge to a quasi-steady regime with enhanced acoustic generation due to heat addition.
A simplified thermoacoustic coupling, based on a kinematic flame-response model, was introduced to account for unsteady heat release. The analysis showed that unsteady heat release can significantly amplify upstream-propagating acoustic waves, especially for fast flames and compact flame-holders. A stability assessment based on the amplification ratio and the Rayleigh index demonstrated that configurations combining high flame speeds with small flame-holder ratios are the most susceptible to thermoacoustic instabilities, although such geometries are unlikely in practical combustors.
Overall, this work provides a detailed characterisation of wave propagation, entropy–acoustic coupling, and thermoacoustic feedback in thermally choked flows. The quasi-one-dimensional model and the thermal-throat boundary condition developed here offer efficient tools for analysing the stability of dual-mode ramjet configurations and contribute to a deeper understanding of the mechanisms governing combustion-induced unsteadiness in airbreathing propulsion systems.